



HAL
open science

Quantitative remote sensing of foliar traits for temperate forest with spectroscopic data

Thierry Gaubert

► **To cite this version:**

Thierry Gaubert. Quantitative remote sensing of foliar traits for temperate forest with spectroscopic data. Engineering Sciences [physics]. Toulouse, ISAE, 2024. English. NNT : 2024ESAE0028 . tel-04758247

HAL Id: tel-04758247

<https://hal.science/tel-04758247v1>

Submitted on 29 Oct 2024

HAL is a multi-disciplinary open access archive for the deposit and dissemination of scientific research documents, whether they are published or not. The documents may come from teaching and research institutions in France or abroad, or from public or private research centers.

L'archive ouverte pluridisciplinaire **HAL**, est destinée au dépôt et à la diffusion de documents scientifiques de niveau recherche, publiés ou non, émanant des établissements d'enseignement et de recherche français ou étrangers, des laboratoires publics ou privés.

Doctorat de l'Université de Toulouse

Délivré par l'ISAE-SUPAERO

Téledétection quantitative des traits foliaires des forêts tempérées à partir de mesures spectroscopiques

Thèse présentée et soutenue, le 11 juin 2024 par

Thierry GAUBERT

École doctorale

SDU2E - Sciences de l'Univers, de l'Environnement et de l'Espaces

Spécialité

Sciences de la terre et des planètes solides

Unité de recherche

ISAE-ONERA PSI Physique Spatiale et Instrumentation

Thèse dirigée par

Xavier BRIOTTET et Susan USTIN

Composition du jury

M. Thomas CORPETTI, Président, CNRS - LETG Rennes

M. Xavier BRIOTTET, Directeur de thèse, ONERA

M. Raul LOPEZ-LOZANO, Rapporteur, INRAE - EMMAH Avignon

Mme Maria Pilar MARTIN, Examinatrice, SpecLab - CCHS Espagne

M. David SHEEREN, Examineur, Institut National Polytechnique de Toulouse / DYNAFOR

Mme Susan USTIN, Co-directrice de thèse, University of California Davis / Institute of the Environment

**QUANTITATIVE REMOTE SENSING OF LEAF TRAITS FOR
TEMPERATE FORESTS FROM SPECTROSCOPIC DATA**

**TÉLÉDÉTECTION QUANTITATIVE DES TRAITS FOLIAIRES
DES FORÊTS TEMPÉRÉES À PARTIR DE MESURES
SPECTROSCOPIQUES**

Thierry Gaubert

Abstract

Forest ecosystems cover around one tenth of the earth's surface. They provide numerous ecological functions and ecosystem services, thanks to their high biodiversity and their role in climate regulation and biogeochemical cycles. However, climate change, linked to global warming, jeopardizes the conservation of these ecosystems by plunging the plant species present into conditions for which they are not adapted. Vegetation in forest ecosystems can be monitored using quantitative remote sensing, by estimating functional traits defined in ecology as indicators of growth, reproduction or survival capacities. More specifically, for plant species, some functional traits, known as leaf traits, are linked to the biochemical composition of foliage and affect the optical properties of vegetation through physical processes. By solving an inverse problem, leaf traits can be retrieved from airborne and spaceborne hyperspectral remote sensing in the 0.4 – 2.5 μm optical range. Hyperspectral sensors, already launched or planned for the next decade, will provide massive data flows, making it possible to monitor forest ecosystems, but requiring automated processing methods. In this context, this thesis targets the development of a generalizable method capable of processing all images of temperate forests from a spatial sensor for the estimation of four leaf traits: leaf concentrations of chlorophylls (C_{ab}), carotenoids (C_{xc}), water (EWT) and dry matter (LMA). To meet this objective, this thesis proposes to test estimation methods at the leaf scale and then at the canopy scale, based on data collected on five forest sites in California, covering several ecosystems and different seasons. At the leaf scale, several trait estimation methods from spectroscopic measures are compared, including physical and statistical approaches, and based on leaf samples collected from the five sites. The main results show that the statistical method based on Gaussian processes regression yields the most accurate estimates whatever the trait. At canopy level, leaf traits are estimated using both a statistical and a hybrid approach, based on AVIRIS acquisitions over the five sites. The statistical approach involves training regression models on AVIRIS hyperspectral data. The hybrid approach consists of training a convolution neural network (CNN) on a synthetic database generated from the DART radiative transfer model. This step shows that statistical approaches perform better than the hybrid approach. Nevertheless, all the methods tested prove ill-suited to extract the effects of leaf traits from canopy-scale reflectance, and estimation errors remain too large to analyze seasonal and intra-specific variation in leaf traits. In order to improve estimation performance, a more in-depth study of the effects of canopy and understory geometry would be required. In addition, it would be necessary to test the predictability of forest health based on leaf trait mapping in order to achieve a comprehensive monitoring of these ecosystems.

Résumé

Les écosystèmes forestiers couvrent environ un dixième de la surface de la terre. Ils assurent de nombreuses fonctions écologiques et services écosystémiques, grâce à leur grande biodiversité et à leur rôle dans la régulation du climat et des cycles biogéochimiques. Cependant, le changement climatique, lié au réchauffement de la planète, met en péril la conservation de ces écosystèmes en plongeant les espèces végétales présentes dans des conditions auxquelles elles ne sont pas adaptées. La végétation des écosystèmes forestiers peut être suivie par télédétection quantitative, en estimant des traits fonctionnels définis en écologie comme des indicateurs des capacités de croissance, de reproduction ou de survie. Plus précisément, pour les espèces végétales, certains traits fonctionnels, connus sous le nom de traits foliaires, sont liés à la composition biochimique du feuillage et affectent les propriétés optiques de la végétation par le biais de processus physiques. En résolvant un problème inverse, les caractéristiques foliaires peuvent être extraites de la télédétection hyperspectrale aéroportée et spatiale dans la gamme optique de 0,4 à 2,5 μm . Les capteurs hyperspectraux, déjà lancés ou prévus pour la prochaine décennie, fourniront des flux de données massifs, permettant de surveiller les écosystèmes forestiers, mais nécessitant des méthodes de traitement automatisées. Dans ce contexte, cette thèse vise le développement d'une méthode généralisable capable de traiter toutes les images de forêts tempérées provenant d'un capteur spatial pour l'estimation de quatre traits foliaires : les concentrations foliaires en chlorophylles (C_{ab}), en caroténoïdes (C_{xc}), en eau (EWT) et en matière sèche (LMA). Pour répondre à cet objectif, cette thèse propose de tester des méthodes d'estimation à l'échelle de la feuille puis à l'échelle de la canopée, à partir de données collectées sur cinq sites forestiers en Californie, couvrant plusieurs écosystèmes et différentes saisons. A l'échelle de la feuille, plusieurs méthodes d'estimation des traits à partir de mesures spectroscopiques sont comparées, incluant des approches physiques et statistiques, et basées sur des échantillons de feuilles collectés sur les cinq sites. Les principaux résultats montrent que la méthode statistique basée sur la régression des processus gaussiens produit les estimations les plus précises quel que soit le caractère. Au niveau de la canopée, les caractéristiques des feuilles sont estimées à l'aide d'une approche à la fois statistique et hybride, basée sur les acquisitions AVIRIS sur les cinq sites. L'approche statistique implique l'apprentissage de modèles de régression sur les données hyperspectrales AVIRIS. L'approche hybride consiste à entraîner un réseau neuronal à convolution (CNN) sur une base de données synthétique générée à partir du modèle de transfert radiatif DART. Cette étape montre que les approches statistiques sont plus performantes que l'approche hybride. Néanmoins, toutes les méthodes testées s'avèrent mal adaptées pour extraire les effets des traits foliaires à partir de la réflectance à l'échelle de la canopée, et les erreurs d'estimation restent trop importantes pour analyser les variations saisonnières et intraspécifiques des traits foliaires. Afin d'améliorer les performances d'estimation, une étude plus approfondie des effets de la géométrie de la canopée et du sous-étage serait nécessaire. En outre, il serait nécessaire de tester la prévisibilité de la santé des forêts sur la base de la cartographie des traits foliaires afin de parvenir à une surveillance complète de ces écosystèmes.

Remerciements

Voilà plus de trois ans que j'ai commencé cette thèse, avec laquelle, comme dans toutes les thèses, il y eu des hauts et des bas. Cette aventure a commencé dans ce contexte particulier de la pandémie de Covid-19, où la distance et la limitation des échanges avec les autres était de mise. C'est pourtant toutes les personnes avec qui j'ai pu échanger qui m'ont aidé depuis le début du parcours et qui, trois ans et demi après, au moment de tourner cette page de ma vie, je tiens à remercier.

Tout d'abord, j'adresse mes sincères remerciements aux membres du jury, Thomas Corpetti et Raul Lopez-Lozano, rapporteurs de cette thèse, pour leur temps consacré à la relecture attentive de ce manuscrit, ainsi que María Pilar Martín et David Sheeren, examinateurs de l'ensemble de mon travail.

Je souhaite ensuite remercier mon équipe encadrante. Je tiens à remercier en particulier Xavier pour sa confiance et avoir partagé sa grande expérience de la recherche, et Susan pour ces échanges, certes compliqués par la distance, mais particulièrement enrichissants. Susan, cela a été un plaisir de te rencontrer durant le séjour de deux mois que j'ai eu la chance de réaliser à Davis. Merci pour ton accueil.

Je souhaite par la même occasion remercier Mui pour son accueil au UC Davis Institute of the Environment, sa joyeuse compagnie au laboratoire et son aide précieuse pour la préparation de la campagne sur les sites d'études. Il me faut également mentionner et remercier les trois étudiants de l'Université de Californie à Davis ; Caden, Thea et Peter ; qui se sont portés volontaires pour venir prêter main forte lors de la campagne terrain. Nos échanges sur les différences entre cultures françaises et américaines ont été particulièrement enrichissants.

Je remercie toute l'équipe du DOTA à l'ONERA pour l'accueil dans ce centre de recherche, leur support technique et conseils, ou encore pour certains d'avoir été des partenaires d'escalades. Je tient à dire un grand merci à Aurélie, avec qui j'ai partagé le bureau, pour son soutien et écoute. Il me tient à cœur de remercier la grande équipe de doctorants, et autres membres de passage du DOTA, ceux qui sont arrivés avant ; Nicolas, Gabriel, Matthieu, Rollin, Killian, Erwan, Arnaud, Romain ; et ceux qui sont arrivés après moi ; Kevin, Benoît, Mathilda et Marianne. Je savais que j'allais rencontrer des collègues mais je n'avais pas conscience qu'autant d'entre eux deviendraient des amis, sans qui l'aventure n'aurait pas eu la même saveur et qui chacun à leur manière, ont contribué à égayer mon quotidien. Mathilda, merci pour ta gentillesse et ton soutien qui ont contribué à rendre plus agréable cette difficile dernière année de thèse. A mes collègues devenus amis, je me souviendrai encore longtemps, du temps passé avec vous lors d'une pause café à l'ONERA ou d'une virée dans les Pyrénées, à la cantine ou autour d'un verre, des fous rires et des débats passionnés. Un immense merci pour ces trois années.

Il me faut également remercier les amis rencontrés bien avant pendant mes études, à la MPSI2 de Fermat ou pendant les trois années d'ENSEEIH, et qui m'ont encore entouré pendant cette thèse. Par chacune de nos retrouvailles, vous m'avez apporté un grand soutien avec vos joies et bonheurs.

Enfin, je souhaite remercier ma famille pour leur amour et leur confiance, et en particulier mes parents, leur soutien est constants depuis toujours, mais il m'a particulièrement été précieux durant ces dernières années parcourues non sans difficultés. J'espère que vous êtes aussi fiers que je le suis du parcours accompli, il fait aussi partie, à ça manière, de votre réussite.

Acknowledgements

It's been over three years since I began this thesis, which, as with all theses, has had its ups and downs. This adventure began in the particular context of the Covid-19 pandemic, where distance and limited exchanges with others were the order of the day. Yet, it's all the people I've been able to talk to who have helped me along the way and whom, three and a half years on, as I turn this page in my life, I'd like to thank.

First of all, I would like to express my sincere gratitude to the members of the jury, Thomas Corpetti and Raul Lopez-Lozano, reviewers of this thesis, for the time they took to carefully review this manuscript, and to María Pilar Martín and David Sheeren, for the assessment of my entire work.

I would also like to thank my supervisory team. In particular, I'd like to thank Xavier for his confidence and for sharing his long research experience, and Susan for these exchanges, which were certainly complicated by distance, but particularly rewarding. Susan, it was a pleasure to meet you during my two-month stay in Davis. Thank you for your warm welcome. At the same time, I'd like to thank Mui for her welcome at the UC Davis Institute of the Environment, her cheerful company in the laboratory and her invaluable help in preparing the field campaign at the study sites. I must also mention and thank the three students from the University of California Davis; Caden, Thea and Peter; who volunteered to come and lend a hand during the field trip. Our exchanges on the differences between French and American cultures were particularly enriching.

I'd like to thank the whole DOTA team at ONERA for the warm welcome they gave me at the research center, their technical support and advices, and for some of them, being climbing partners. I'd like to say a big thank you to Aurélie, with whom I shared the office for three years, for her support and attentiveness. I'd also like to thank the great team of PhD students and other visiting members of DOTA, those who came before; Nicolas, Gabriel, Matthieu, Rollin, Killian, Erwan, Arnaud, Romain; and those who came after me; Kévin, Benoît, Mathilda and Marianne. I knew I was going to meet some colleagues, but I didn't realize that so many of them would become friends, without whom the adventure wouldn't have had the same flavor, and who each in their own way helped to brighten up my daily life. Mathilda, thank you for your kindness and support, which helped to make this difficult last year of thesis work more enjoyable. To my colleagues who have become friends, I'll remember for a long time to come, the time spent with you during a coffee break at ONERA or a trip to the Pyrenees, in the canteen or over a drink, and the laughter and passionate debates. A huge thank you for these three years.

I would also like to thank the friends I met long before during my studies, at MPSI2 of Fermat high-school or during the three years at ENSEEIHT, and who have surrounded me again during this thesis. Each time we met again, you gave me great support with your joys and happiness.

Finally, I'd like to thank my family for their love and confidence, and in particular my parents. Their support has always been constant, but it has been particularly precious to me over the last few years, which have not been without their difficulties. I hope you're as proud as I am of what I've achieved, which is also, in its own way, part of your success.

Contents

Introduction (<i>english</i>)	19
Introduction (<i>français</i>)	25
1 Radiative transfer modeling of forest canopies	31
1.1 Vegetation radiative transfer modeling	32
1.1.1 Leaf radiative transfer modeling	33
1.1.1.1 State-of-the-art	33
1.1.1.2 The PROSPECT model	34
1.1.2 Canopy radiative transfer modeling	35
1.1.2.1 State-of-the-art	35
1.1.2.2 The SAIL model	36
1.1.2.3 DART	36
1.2 Simulation framework	37
1.2.1 Overview of the simulation framework	37
1.2.2 The DART-SFR model	38
1.2.2.1 DART-SFR mock-up	38
1.2.2.2 DART rendering parameters	40
1.3 Sensitivity analyses and spectral signatures	42
1.3.1 Leaf level sensitivity analyses	43
1.3.1.1 Local effects of PROSPECT parameters	43
1.3.1.2 Global effects of PROSPECT parameters	44
1.3.2 Canopy level sensitivity analyses	46
1.3.2.1 Local effects of canopy models parameters	46
1.3.2.2 Global effects of canopy models parameters	47
1.3.3 Conclusions on sensitivity analysis	48
Conclusions	50
2 Methods	51
2.1 Techniques for RTM-based strategies	52
2.1.1 Optimization methods for physical inversions	52
2.1.1.1 Optimization algorithms	52
2.1.1.2 Cost functions	53
2.1.2 Sampling methods	53
2.1.2.1 Random sampling	53
2.1.2.2 Latin Hypercube Sampling (LHS)	53
2.2 Statistical learning techniques	53
2.2.1 Standard Machine Learning Regression Algorithms (MLRAs)	54
2.2.1.1 k-Nearest Neighbors (k-NN) for regression	54
2.2.1.2 Ridge regression	54
2.2.1.3 Partial Least Square Regression (PLSR)	54
2.2.1.4 Gaussian Process Regression (GPR)	55
2.2.1.5 Random Forest Regression (RFR)	55
2.2.2 Deep learning algorithms	55
2.2.3 Training and evaluation strategies	56
2.2.3.1 k-fold cross validation for hyperparameter tuning	56
2.2.3.2 Repeated random sub-sampling validation	57
2.3 Evaluation and validation of models	57
2.3.1 Metrics for accuracy evaluation	57
2.3.1.1 Mean Squared Error (MSE) and derived metrics	57

2.3.1.2	Coefficient of determination	58
2.3.1.3	Bias	58
2.3.1.4	Correlation coefficients	59
2.3.2	Discussions on evaluation and validation of models	59
Conclusion	61
3	Material	63
3.1	The case study	63
3.1.1	California geography and ecosystems	63
3.1.2	HyspIRI Preparation Mission	64
3.2	Description of Sites and Species	64
3.2.1	Study Sites	64
3.2.2	Tree Species	66
3.3	Field data	67
3.3.1	Field campaigns	67
3.3.2	Leaf sampling	68
3.3.2.1	Leaf traits Measurements	68
3.3.2.2	Leaf spectral measurements	70
3.4	Remote sensing data	70
3.4.1	AVIRIS flight lines	70
3.4.2	CSTARS-Canopy dataset	71
3.4.3	Background reflectance spectra	72
3.5	Data statistical analysis	73
4	Estimation at the leaf scale	77
Leaf-scale estimation of oak leaf traits : Comparison of statistical and PROSPECT-based methods		78
Conclusion		113
5	Estimation at the Canopy Scale	115
5.1	Assessment of statistical methods accuracy on the CSTARS-Canopy dataset	116
5.1.1	Methodology	116
5.1.2	Results	117
5.1.3	Summary and conclusion	126
5.2	The Hybrid 1D-CNN Strategy	127
5.2.1	Synthetic dataset generation	127
5.2.2	1D-CNN calibration	128
5.2.2.1	Architecture selection	128
5.2.2.2	1D-CNN training process	129
5.2.3	Evaluation of the 1D-CNN estimator performances	131
5.3	Discussions	137
5.3.1	Discussion on machine learning algorithms	137
5.3.2	Discussion on accuracy of estimations	138
5.3.2.1	Summary and comparison with literature	138
5.3.2.2	Potential sources of errors and uncertainty	139
5.3.2.3	Upscaling leaf trait estimation from leaf to canopy scale	141
Conclusion		142
	Conclusions and Perspectives	143
	Conclusions et Perspectives	147
A	June 2022 field campaign	151
A.1	Fieldwork	151
A.2	Measurements of tree-scale metrics	154
A.3	Plot-scale metrics	155
A.4	Remote sensing data	156
B	Leaf scale estimation for needle-leaf species	159

List of Acronyms

ALA	Average Leaf Angle
ANN	Artificial Neural Network
ASD	Analytical Spectral Device
AVIRIS	Airborne Visible/Infrared Imaging Spectrometer
C_{ab}	Chlorophylls a and b content
CC	Canopy Cover
CNN	Convolution Neural Network
CWT	Continuous Wavelet Transform
C_{xc}	Carotenoids (xanthophylls and carotenes) content
DART	Discrete Anisotropic Radiative Transfer
EBV	Essential Biodiversity Variables
EWT	Equivalent Water Thickness
FWHM	Full Width at Half Maximum
GSD	Ground Sampling Distance
GPR	Gaussian Process Regression
LAD	Leaf Angle Distribution
LAI	Leaf Area Index
LH	Latin Hypercube
LMA	Leaf Mass Area
LUT	Look-Up Table
MLRA	Machine Learning Regression Algorithm
MSE	Mean Square Error
NIR	Near InfraRed
nRMSE	Normalized RMSE
PLSR	Partial Least Square Regression
PROSAIL	PROSPECT and SAIL combination
PROSPECT	PROpriétés SPECTrales
RAMI	RAdiation transfer Model Intercomparison
RFR	Random Forest Regression
RMSE	Root Mean Square Error
rRMSE	Relative Root Mean Square Error
RTM	Radiative Transfer Model

SAA	Sun Azimuth Angle
SAC	Specific Absorption Coefficient
SAIL	Scattering from Arbitrarily Inclined Leaves
SAM	Spectral Angle Mapper
SFR	Simplified Forest Representation
SLA	Specific Leaf Area
SNR	Signal to Noise Ratio
sRMSE	Standardized RMSE
SVM	Support Vector Machine
SVR	Support Vector Regression
SWIR	Short Wave Infrared
SZA	Sun Zenith Angle
TPE	Tree-structured Parzen Estimator
VAA	View Azimuth Angle
VI	Vegetation Index
VZA	View Zenith Angle

List of Figures

1	Map of the temperate forest biomes on the Earth, adapted from Olson et al. 2001.	19
2	(<i>top</i>) Atmospheric transmittance in the optical domain (400 – 2500 nm), the annotation provide the main gases responsible of the atmospheric absorption for each band. (<i>bottom</i>) Typical reflectance spectra of a leaf (blue solid line), the annotations provides the main absorption bands and the related phenomena (from Curran 1989, in green absorption related to pigments, in blue to water, in red and purple to dry matter).	21
1.1	Schematic representation of a dicot leaf (left) and multiple reflections produced by a set of plates (right), adapted from Jacquemoud and Ustin 2019	34
1.2	Schematic representation of the simulation chain from leaf traits to canopy reflectance. White boxes highlight the RTMs parameters. Gray boxes highlight the locked parameters.	37
1.3	Parameters of the composed ellipsoid shape and position.	38
1.4	(a) Schematic representation of the SFR from a nadir point of view with tree crowns in green and soil in pale yellow ; (b) 3D mock-up of the SFR from DART.	39
1.5	Correspondence between the canopy cover (in percent) and the size of the simulated square scene given by its side length (in meters) for several crown radius.	39
1.6	Effect on the size of the simulated scene on the canopy cover. Images represent the surface covered by tree crowns (in green) and soil (in pale yellow) from a nadir point of view. Numbers above the images give the canopy cover in percent.	39
1.7	Average reflectance obtained from 10 rendered images at 3 wavelengths (670, 950 and 1520 nm). Error bars indicate the standard deviations of the reflectance for the 10 images.	41
1.8	Average computation time as function of the Target Ray Mean Density.	41
1.9	MSE (<i>top</i>) and computation time (<i>bottom</i>) as function of the Maximal Scattering Order ($Scat_{max}$)	42
1.10	MSE (<i>top</i>) and computation time (<i>bottom</i>) as function of the Number of Repetition of the scene (N_{rep})	42
1.11	Simulated leaf reflectance (lower lines) and transmittance (upper lines) for different values of PROSPECT-D input parameters. Variations around a standard leaf composition defined by : $[N = 1.8; C_{ab} = 33 \mu g \cdot cm^{-2}; C_{xc} = 8.6 \mu g \cdot cm^{-2}; EWT = 0.0150 cm; LMA = 0.0300 g \cdot cm^{-2}]$ are shown for: (a) C_{ab} ; (b) C_{xc} ; (c) EWT; (d) LMA; and (e) structure parameter N.	44
1.12	Sensitivity of PROSPECT simulated leaf reflectance and transmittance with respect to PROSPECT parameters.	45
1.13	Sensitivity of CWT coefficients of PROSPECT simulated leaf reflectance with respect to PROSPECT parameters.	45
1.14	SAIL canopy reflectance as a function of leaf reflectance (ρ) and leaf transmittance (τ). Canopy reflectance is computed for a 0.3 soil reflectance, $SZA=30^\circ$, and a canopy structure defined by: $LAI = 3$ And $ALA = 45^\circ$	46
1.15	SAIL simulation of canopy reflectance for different values of LAI. Variations for a 0.2 soil reflectance, $SZA = 30^\circ$ and $ALA = 45^\circ$. Leaf optical properties are computed from PROSPECT with a standard leaf composition $[N = 1.8; C_{ab} = 33 \mu g \cdot cm^{-2}; C_{xc} = 8.6 \mu g \cdot cm^{-2}; EWT = 0.0150 cm; LMA = 0.0300 g \cdot cm^{-2}]$. (<i>left</i>) The canopy reflectances are drawn as function of wavelength. Hatched rectangles represent atmospheric absorption bands. (<i>right</i>) Canopy reflectance is given for some wavelengths as a function of LAI	46

1.16	DART-SFR simulation of top-of-canopy reflectance for different values of canopy cover. Variations for a 0.2 soil reflectance, $SZA=30$, $SAA = 225^\circ$, $LAI = 3$ and $ALA = 45^\circ$. Leaf optical properties are computed from PROSPECT with a standard leaf composition [$N = 1.8$; $C_{ab} = 33 \mu\text{g} \cdot \text{cm}^{-2}$; $C_{xc} = 8.6 \mu\text{g} \cdot \text{cm}^{-2}$; $EWT = 0.0150 \text{ cm}$; $LMA = 0.0300 \text{ g} \cdot \text{cm}^{-2}$]. (left) The top-of-canopy reflectances are drawn as function of wavelength. Hatched rectangles represent atmospheric absorption bands. For reference, blue dashed line indicates the reflectance simulated from DART with an homogenous plot of vegetation and the pink dashed line indicates the reflectance simulated by PROSPECT+SAIL, both using the same parameters. (right) Canopy reflectance is given for some wavelengths as a function of Canopy Cover	47
1.17	(a) Illustration of SFR scene segmentation between canopy, sunlit background and shaded background for a canopy cover of 50%; (b) Evolution of the fraction of each element in the scene as a function of canopy cover, for $SZA = 30^\circ$ and $SAA = 225^\circ$	47
1.18	Sobol's total-effect indices for parameters of the SAIL model. Black lines indicate the 95% confidence intervals delivered by Saltelli's algorithm	48
1.19	Sensitivity of PROSAIL simulated canopy reflectance with respect to all PROSAIL parameters. Hatched rectangles represent atmospheric absorption bands.	48
1.20	Sensitivity of CWT coefficients of PROSAIL simulated canopy reflectance with respect to leaf traits. Hatched rectangles represent atmospheric absorption bands.	49
1.21	Sensitivity of PROSPECT - DART-SFR simulated canopy reflectance with respect to all PROSPECT - DART-SFR parameters. Hatched rectangles represent atmospheric absorption bands.	49
1.22	Sensitivity of CWT coefficients of PROSPECT - DART-SFR simulated top-of-canopy reflectance with respect to leaf traits. Hatched rectangles represent atmospheric absorption bands.	49
2.1	Global chart illustrating the main strategies for leaf traits estimation	51
2.2	Flow chart of the repeated random subsampling validation.	57
2.3	Illustration of the behavior of the validation metrics for possible estimation scenarios: (a) unbiased estimation with low variance; (b) unbiased estimation with medium variance; (c) unbiased estimation with high variance; (d) low variance estimation with additive bias; (e) low variance estimation with multiplicative bias; and (f) unbiased low variance estimation with saturation effect for higher values	59
2.4	Diagram illustrating the sources of errors embedded in the estimation strategies and their validation process	60
3.1	Topographic map of California with boundaries California floristic province and AVIRIS boxes, and location of study sites	65
3.2	Timeline of all the AVIRIS acquisitions available on the five study sites (red) and the field campaign (blue)	71
3.3	Schematic diagram of extraction processing of AVIRIS reflectance.	72
3.4	Distribution of selected pixels as a function of temporal shift	72
3.5	Distribution of the four leaf traits for each species.	74
3.6	Scatter plots of the four leaf traits.	75
5.1	Mean leaf traits estimates compared to measured values. Gray vertical lines indicate the range between minimal and maximal estimated values for each sample. Results are given for the MLRA highlighted in Tables 5.2 to 5.5 (for oaks: GPR, GPR, Ridge, RFR; for conifers: Ridge, Ridge, Ridge, RFR; for C_{ab} , C_{xc} , EWT, and LMA respectively)	126
5.2	Distribution of the mean square error validation loss compared to the learning rate (left), and the batch size (right).	128
5.3	Distribution of the mean square error validation loss compared to numbers of convolution layers (left), number of channels (middle) and kernel size of the first layer (right).	129
5.4	Distribution of the mean square error validation loss compared to numbers of dense layers (left), size of the first layer (middle), size of the second layer (right)	129
5.5	Left: Loss evolution for train and validation on synthetic data. Solid lines indicate the mean losses and filled areas indicate the 1st and 9th deciles ; Right: Distribution of best models for validation on synthetic data.	130
5.6	Scatter plot of leaf traits mean estimates compared to input values for validation synthetic data. Gray vertical lines indicate the 1st and 9th deciles of estimated values for each sample.	130

5.7	Top left: Distribution of best models for validation CSTARS-Canopy ; Bottom left: Loss evolution for train and validation on synthetic data and validation CSTARS-Canopy ; Right: Trait-specific loss evolutions for train, validation on synthetic data and validation on CSTARS-Canopy	131
5.8	Mean leaf traits estimates compared to measured values for validation data. Gray vertical lines indicate the 1st and 9th deciles of estimated values for each sample.	136
5.9	Reflectances of extracted AVIRIS pixels compared to reflectances computed with DART-SFR simulations. (<i>top</i>) Reflectances as a function of wavelength, gray area in the background shows the minimal and maximal reflectance simulated by DART-SFR. (<i>bottom</i>) Scatterplot for four pairs of bands, grey dots show the simulated reflectance values	139
5.10	Evolution of the traits estimation errors as a function of the canopy cover, the best retrieval method of each trait is kept to graph each figure.	140
5.11	Evolution of the traits estimation errors as a function of the temporal shift between images and data collection, the best retrieval method of each trait is kept to graph each figure.	141
A.1	Map of SOAP site (coordinates given in meter in the UTM 11N system (EPSG 32611), Google terrain as map background). Orange squares represent sampled forest plots and the blue triangle highlights the location of the base camp.	151
A.2	Map of TEAK site (coordinates given in meter in the UTM 11N system (EPSG 32611), Google terrain as map background). Orange squares represents sampled forest plots and the blue triangle highlight the location of the based camp	152
A.3	Naming convention of subplots numbers and plot grid.	152
A.4	Distribution of DBH for each visited plot.	155
A.5	Species distribution for each plot in proportion of total DBH.	155
A.6	Global Health index distribution by plots in proportion of total DBH.	156
A.7	PRISMA images (RGB extraction) acquired over Soaproot Saddle on 2022-06-11 (<i>left</i>) and Teakettle Experimental Range on 2022-06-23 (<i>right</i>).	156
A.8	RGB representation of PRISMA images correctly georeferenced for the SOAP (<i>left</i>) and TEAK (<i>right</i>). Each cross shows the location of a plot and the extracted pixels (coordinates given in meters in the UTM 11N system (EPSG 32611)).	157
A.9	Reflectance spectra extracted from PRISMA images (one spectrum for each plot).	157
B.1	Influence of gap fraction on measured reflectance ρ_{meas} (lower lines) and transmittance τ_{meas} (upper lines) following equations from Mesarch et al. 1999	159
B.2	Validation plots for C_{ab} for the methods highlighted in Table B.1	159
B.3	Validation plots for C_{xc} for the methods highlighted in Table B.2	160
B.4	Validation plots for EWT for the methods highlighted in Table B.3	160
B.5	Validation plots for LMA for the methods highlighted in Table B.4	161

List of Tables

3.1	The scientific name, common name, four-letter abbreviated species code used in the thesis. Colored cells indicate if the species is present on the site	67
3.2	Dates of the field campaigns (format DD/MM).	68
3.3	Sample distributions for each species, season and site.	69
3.4	List of AVIRIS-C flight lines with associated pixel size, sample number, date and temporal shift.	73
3.5	Basic statistics of the measured foliar traits compared for oak and conifers species .	74
3.6	Correlation matrix for the four leaf traits by pooling all <i>Quercus</i> species (left) and all conifer species (right).	75
5.1	Subsets of species considered for the evaluation of estimation methods. The last columns provide the sites involved	116
5.2	Accuracy metrics expected values of statistical methods for C_{ab} on several subsets of CSTARS-Canopy. The mean m and standard deviation σ of reference data are given in the first column.	118
5.3	Accuracy metrics expected values of statistical methods for C_{xc} on several subsets of CSTARS-Canopy. For reference the mean m and standard deviation σ of reference data are given.	120
5.4	Accuracy metrics expected values of statistical methods for EWT on several subsets of CSTARS-Canopy. For reference the mean m and standard deviation σ of reference data are given.	122
5.5	Accuracy metrics expected values of statistical methods for LMA on several subsets of CSTARS-Canopy. For reference the mean m and standard deviation σ of reference data are given.	124
5.6	Ranges of values used for Latin hypercube generation.	127
5.7	Hyperparameter ranges for the TPE sampling experiment and optimal values found.	128
5.8	Mean values of accuracy metrics for the 1D-CNN estimator for C_{ab} on CSTARS-Canopy. The 5th and 95th percentiles are given in square brackets. For reference, the mean m and standard deviation σ of reference data are given for each CSTARS-Canopy subset.	132
5.9	Mean values of accuracy metrics for the 1D-CNN estimator for C_{xc} on CSTARS-Canopy. The 5th and 95th percentiles are given in square brackets. For reference, the mean m and standard deviation σ of reference data are given for each CSTARS-Canopy subset.	133
5.10	Mean values of accuracy metrics for the 1D-CNN estimator for EWT on CSTARS-Canopy. The 5th and 95th percentiles are given in square brackets. For reference, the mean m and standard deviation σ of reference data are given for each CSTARS-Canopy subset.	134
5.11	Mean values of accuracy metrics for the 1D-CNN estimator for LMA on CSTARS-Canopy. The 5th and 95th percentiles are given in square brackets. For reference, the mean m and standard deviation σ of reference data are given for each CSTARS-Canopy subset.	135
5.12	Non linear correlation (measured by Kendall's Tau) between absolute estimation error and canopy cover.	140
5.13	Non linear correlation (measured by Kendall's Tau) between absolute estimation error and temporal shift.	141
B.1	Performance of methods for the estimation of C_{ab} (in each subcategory, the most accurate method is highlighted in bold).	160

B.2	Performance of methods for the estimation of C_{xc} (in each subcategory, the most accurate method is highlighted in bold).	160
B.3	Performance of methods for the estimation of EWT (in each subcategory, the most accurate method is highlighted in bold).	161
B.4	Performance of methods for the estimation of LMA (in each subcategory, the most accurate method is highlighted in bold).	161

Introduction

Forest ecosystems account for a large proportion of continental land surface, covering around 10% of the earth's surface (FAO 2020). A forest ecosystem is a vegetation type dominated by trees, but various definitions exist worldwide that set specific criteria in terms of size, tree cover, height, and land use. The Food and Agriculture Organization (FAO) of the United Nations defines forests as "land spanning more than 0.5 hectares with trees higher than 5 meters and a canopy cover of more than 10%, or trees able to reach these thresholds in situ" (FAO 2020). Additionally, the FAO excludes land that is predominantly under agricultural or urban land use. This definition is broad enough to cover many types of tree cover, including areas with lower vegetation.

Forest ecosystems play a crucial role in benefiting both climate and biodiversity. This role is especially highlighted in the 2021-2023 IPCC and 2019 IPBES reports. Such as other vegetation-based ecosystems, forests convert solar energy into organic matter through photosynthesis, absorbing carbon dioxide from the atmosphere. Forests ecosystems are the largest supplier of biomass producing 75% of organic matter on continental surfaces and constitute the largest terrestrial carbon sink (Masson-Delmotte et al. 2021). Forest not only plays a role in long-term carbon storage but also has significant positive effects on climate stability (Seymour et al. 2022). Latest research pinpoints the contribution of forests to stabilize local temperatures and rainfall patterns (Pörtner et al. 2022; Seymour et al. 2022). Particularly, forests cool the earth's surface and lower atmosphere through evapotranspiration and the roughness of canopies alter wind and atmospheric mixing. Forests contribute to biodiversity conservation by providing habitats for a wide range of species (Brondizio et al. 2019). Indeed, the plant cover, the biomass created and the different levels of vegetation provide an environment in which a wide variety of species - plants, fungi and animals - can thrive. Forests therefore play a fundamental role in conserving biodiversity. As a result, forests make up a large part of the regions classified as biodiversity hotspots (Myers et al. 2000), which concentrate 44% of vascular plant species and 35% of vertebrate species, and have become priorities for ecosystem conservation because of the pressures they face.

Forest ecosystems cover a wide diversity of biomes. Major biome types can be distinguished on the basis of mean annual rainfall and mean annual temperature (Whittaker 1975). These biomes include tropical moist forests and tropical dry forests around the Equator, boreal forests in sub-arctic climates, and at the mid-latitudes, a wide range of temperate forests (moist temperate, continental temperate, mediterranean, and subtropical forests). Temperate forests are located in mid-latitude regions where different air masses collide and climate is affected by significant seasonal rhythms (Figure 1). Temperate forests are spread along a wide variety of climates following the Köppen-Geiger climate classification and can be classified in three main biomes (Olson et al. 2001): temperate broadleaf and mixed forests, temperate coniferous forest, mediterranean forests and woodlands.

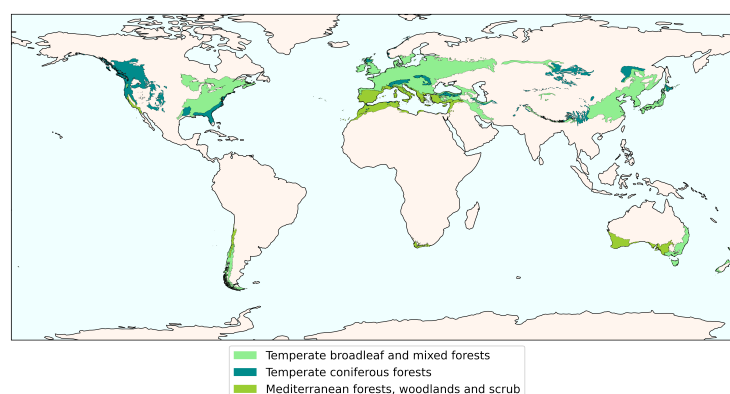


Figure 1: Map of the temperate forest biomes on the Earth, adapted from Olson et al. 2001.

Climate science studies have reached the scientific consensus that Earth is facing global warming driven by anthropic greenhouse gas emissions for at least the past 30 years (Masson-Delmotte et al. 2021; Oreskes 2004). Progress in climate science shed light on the climate change caused by global warming and increase of anthropogenic greenhouse gas concentration in the atmosphere. Climate change not only alters mean temperature and precipitation but also the frequency and intensity of extreme hydro-meteorological events such as droughts and heatwaves. Consequently, climate change jeopardizes the resilience of forest ecosystems. Besides, climate change has been listed by the IPBES as one of the five major threats to biodiversity along with the destruction of natural habitats, overexploitation of species, pollution, and invasive species (Brondizio et al. 2019).

The alteration of temperature and rainfall patterns plunges forest trees directly into conditions to which they are not adapted and in combination with other disturbance factors, pushes forests beyond thresholds of sustainability (Millar and Stephenson 2015). Droughts directly increase water stress in trees and lead to forest desiccation and a reduced resilience to pathogens. Additionally, the elevation of mean temperature and shifts in seasonal timing also ease the spread of pest and disease, as well as invasive species. At the end of the day, climate change has increased the likelihood of tree mortality compared to the mortality levels experienced in the 20th-century (Millar and Stephenson 2015). Cases of sudden and unexpected elevated tree mortality following heat and drought events have already been observed and documented, including in ecosystems that previously were considered tolerant or not at risk of exposure (Hartmann et al. 2022). Extreme hydro-meteorological events also alter fire regimes and intensify fire risk. Wildfire has become a main driver of forest loss, and particularly for temperate forest. For example, wildfires caused 40% of the forest loss in North America over the 2001-2015 period (Curtis et al. 2018).

Climate change alters the physiological processes of forest trees. Consequently, monitoring these physiological processes is a key factor in understanding and assessing the impacts described previously. In ecology, concepts of functional traits have been developed to monitor specifically these physiological processes. Functional traits are defined as any morphological, physiological or phenological feature, measurable at the individual level, which impacts the plant fitness indirectly via its effects on growth, reproduction or survival (Violle et al. 2007).

Subsequently, Essential Biodiversity Variables (EBVs) have been defined by the Group on Earth Observations Biodiversity Observation Network (GEO BON), with the aim of creating a harmonized global observation system to inform scientists and policy-makers (Pereira et al. 2013; GEO BON n.d.). EBVs have been defined on the basis of Essential Climate Variables that guide the Global Climate Observing System (GCOS). EBVs are defined as measurable quantities necessary to study and monitor biodiversity change. They provide a structural, taxonomic and functional description of the environment under study. EBVs include numerous functional vegetation traits. These functional traits are indicators of physiology within the species and within the ecosystem (Pereira et al. 2013).

However, functional traits are not measurable on a large scale, and one solution for covering large areas is the use of remote sensing. Several vegetation functional traits, included in EBVs, have been listed as biodiversity metrics to be observed from space as a priority (Skidmore et al. 2021). Remote sensing “is the science and art of obtaining information about an object, area or phenomenon through the analysis of data acquired by a device that is not in contact with the object, area, or phenomenon under investigation” (Lillesand et al. 2015). The estimation of land physical parameters such as EBVs is part of new trends in remote sensing to move toward quantitative assessments in contrast to qualitative ones.

Among functional traits, several are measurable at the leaf level and are consequently gathered under the name “leaf traits”. Four leaf traits are Chlorophylls a and b content (C_{ab}), carotenoids content (C_{xc}), Equivalent Water Thickness (EWT) and Leaf Mass Area (LMA). They are linked to the plant’s physiological processes and, at ecosystem level, to biogeochemical cycles and are therefore considered as valuable indicators of vegetation’s health and stress levels (Lausch et al. 2016).

- Chlorophylls a and b are the dominant pigments in the leaf. They are the main photosynthetic pigments in leaves and give them their green coloration. They constitute the major part of light-harvesting complexes in photosystems located on thylakoids membranes in the chloroplasts, and therefore play a key role in the conversion of light into chemical energy (Taiz and Zeiger 2010). C_{ab} expresses the mass of chlorophylls a and b per unit of leaf area.
- Carotenoids comprise both carotene and xanthophyll families. Carotenoids are also photosynthetic pigments and are bound with chlorophylls molecules in photosystems (Taiz and

Zeiger 2010). Xanthophylls also provide protection against harmful radiation through the xanthophyll cycle (Demmig-Adams and Adams 1996). C_{xc} expresses the mass of carotenoids per unit of leaf area.

- The leaf water content is an indicator of water management by plant tissues. The EWT is the area-weighted moisture content of the leaf (Riano et al. 2005).
- Other main constituents of the leaf are gathered in the dry matter. The leaf dry matter encompasses a wide range of organic compounds that can be divided in two main groups: nitrogen-based constituents (proteins) and carbon-based constituents (including cellulose, lignin, hemicellulose, starch and sugars) (Féret et al. 2021). The LMA is expressed as the dry mass per unit of leaf area. It is the inverse of Specific Leaf Area (SLA) that is also often used as a leaf functional trait.

Biochemical constituents absorb the energy of light radiation at the microscopic level. Photons are absorbed via the phenomenon of electronic transitions for pigments, or converted into the form of vibrational energy internal to the molecules for water, nitrogen-based and carbon-based constituents. These absorption phenomena involve photons of specific energies. Therefore, foliar biochemistry, and consequently, the four leaf traits impact the leaf optical properties through absorption bands specific to each constituent. The absorption bands are located in the visible range (400 – 750 nm) for C_{ab} and C_{xc} ; in the Near InfraRed range (NIR; 800 – 1400 nm) and the Short Wave InfraRed (SWIR; 1400 – 2500 nm) for EWT and LMA (Figure 2).

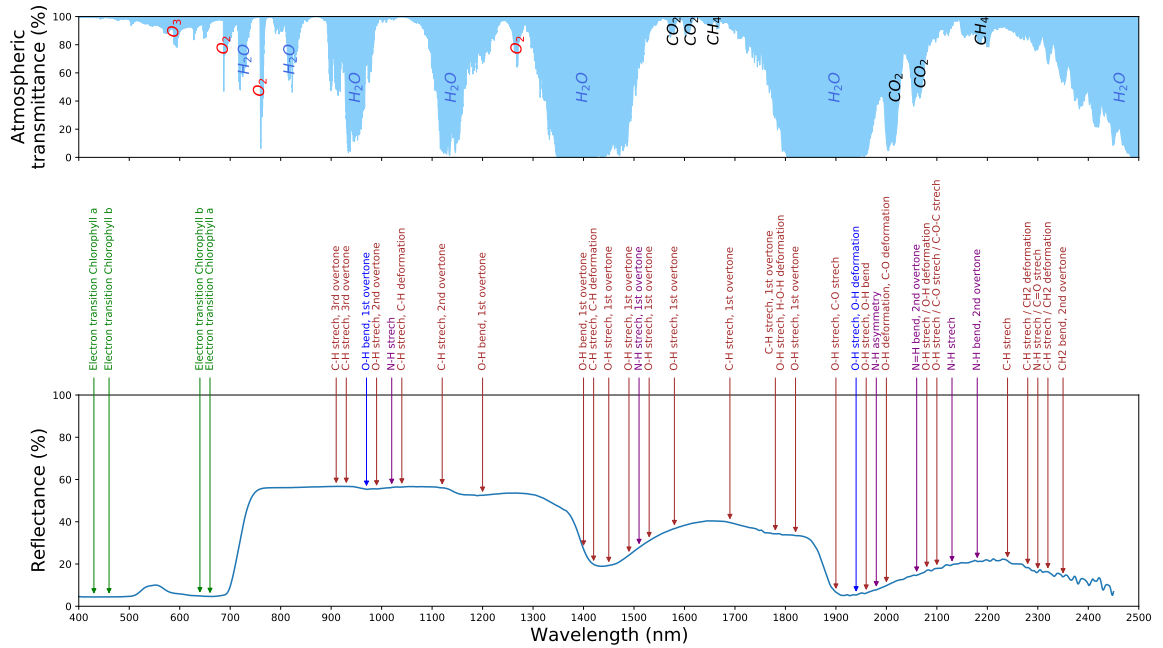


Figure 2: (top) Atmospheric transmittance in the optical domain (400 – 2500 nm), the annotation provide the main gases responsible of the atmospheric absorption for each band. (bottom) Typical reflectance spectra of a leaf (blue solid line), the annotations provides the main absorption bands and the related phenomena (from Curran 1989, in green absorption related to pigments, in blue to water, in red and purple to dry matter).

The absorption bands constitute spectral fingerprints of each leaf trait. In this frame, the analysis of optical measurements with a high spectral resolution can help to quantify leaf traits.

In remote sensing, a concept of instrument called imaging spectrometers has emerged since the 1990s. The emergence of imaging spectroscopy has spawned a wide field of research in the remote sensing realm (Schaeppman 2009; Rast and Painter 2019). Imaging spectroscopy implies that many bands in adjacent wavelengths are measured so that all bands over a specified wavelength interval completely sampled the spectrum. Imaging spectroscopy is often called hyperspectral imaging, but this latter denomination appears unclear because it does not specify that the many bands measured are adjacent. Furthermore, estimation of land physical parameters such as EBV has been cited as one of the main challenges to be overcome in hyperspectral remote sensing

(Bioucas-Dias et al. 2013). Physical parameter estimation is an intermediate step to transform remote sensing measurements into useful estimates. Physical parameters can be estimated using the optical properties transmitted in the atmospheric windows (Figure 2).

In the past, hyperspectral sensors were confined to airborne sensors such as AVIRIS (Green et al. 1998). The development of hyperspectral spaceborne sensors paused since the launch of Hyperion in the 2000s, but more recently, a new wave of spaceborne hyperspectral sensors has found its place in space programs (Ustin and Middleton 2021). This new wave includes sensors recently launched (PRISMA (Cogliati et al. 2021), EnMAP (Guanter et al. 2015), EMIT (Green et al. 2020)), and missions planned for the coming decade (CHIME (Rast et al. 2021), SBG (Green et al. 2022)). These new sensors will generate an unprecedented flow of hyperspectral images of the Earth.

The estimation of land physical parameters, including estimation of leaf traits, from imaging spectroscopy, is part of the inverse problem. In general terms, inverse problems infer parameters of a system from observed data, in contrast to direct problems which simulate the effects given all the parameters (Tarantola 2005; Patow and Pueyo 2003). In vegetation remote sensing modeling, the direct, or forward problem, is a case of radiative transfer. It involves modeling the propagation of light radiation received from the sun through the atmosphere and vegetation to predict observations. Much work has focused on modeling the interaction of light with matter in the case of vegetation leading to the creation of multiple Radiative Transfer Models (RTMs). Formally, the forward problem can be expressed as:

$$Y = f(x, \theta) + n$$

where Y is a set of observations, x is the set of parameters, θ is a set of controllable conditions, and n is an additive noise. f is the function that models the radiative transfer.

The inverse problem, implies to retrieve one or multiple variables of interest from the measurement of the radiance by a sensor. It can be expressed as:

$$\hat{x} = g(Y, \omega)$$

where g is a function parametrized by weights ω , that approximate parameters \hat{x} from the set of observations Y .

Solving the inverse problem therefore depends to a large extent on understanding the direct model. In addition, as with most inverse problems, estimation of leaf traits is an ill-posed problem, meaning that distinct combinations of vegetation characteristics can lead to similar optical measurements, and multiple solutions (Baret and Buis 2008).

Estimation of land physical parameters involves a specific taxonomy of inversion methods. This taxonomy was first introduced in the 2000s (Baret and Buis 2008) and later reintroduced by (Bioucas-Dias et al. 2013) and (Verrelst et al. 2019). The taxonomy considers three inversion strategies: statistical, physical and hybrid. Statistical strategy involves learning statistically the inverse model, *i.e.* the function g , from a set of observations and corresponding measured parameters. The learning phase can be done through simple transformation of the hyperspectral observation or through training of more complex Machine Learning Regression Algorithms (MLRAs). Statistical strategy is also sometimes referred to as a data-driven approach, or empirical approach. Physical strategy tries to invert the RTM, meaning that it is searching for the most likely set of parameters that would provide the observation. Various approaches have been considered, including iterative optimization, look-up-table (LUT), Markov Chain Monte Carlo (MCMC), and genetic algorithms. The physical strategy is reserved for RTM with low computation cost since underlying approaches require numerous calls to the RTM. Hybrid strategy combines aspects of both statistical and physical strategies: it statistically learns an inverse model, *i.e.* the function g , from a set of input-output data generated by forward RTM simulations. The learning phase is typically performed with an MLRA.

However, examining the literature, there is no consensus that appears regarding the strategies to prioritize in the development of leaf traits estimations from space-borne hyperspectral images (Hill et al. 2019). In fact, some authors advocate to focus on hybrid strategies such as Verrelst et al. 2019 while other focus their work on statistical strategies, even for estimation at large scales (*e.g.*, Wang et al. 2020). Most of the studies in the field of leaf traits estimation underline that statistical (or empirical) approaches could theoretically lack of generalization capacities compared to RTM-based methods. Nonetheless, one should noticed that RTM-based methods could also lack generalization capacities if RTM are tune to local conditions, and that shortcomings of statistical methods are becoming less pronounced in recent research results (Hill et al. 2019). Past researches

in this field exhibits two major drawbacks considering the projected requirements of future spaceborne sensors. On the one hand, as emphasized by [Homolová et al. 2013](#) and [Gamon et al. 2019](#), most published studies have focused on a given time period, usually using a single point in time near the center of the growing season, and did not evaluate the reliability of retrieval methods along the whole year. As expected, estimation protocols developed from one season usually fail to reproduce the same accuracy on datasets collected in another season ([Gamon et al. 2019](#)). On the other hand, these studies also usually consider a single or few images, covering limited regions with a single forest ecosystem type and consequently do not provide methods to estimate leaf traits over several sites far from each other containing distinct species. Additionally, only few studies have studied estimation of leaf traits both at the leaf scale and canopy scale on the same site and time period. Thus, the transition from leaf-scale to tree-scale or canopy-scale remains an open question in the literature, and would be highly dependent on the type of trees and the scale of observation. Besides, site and period specific methods would require long processing times compared to the amount of data, or the generation of new simulations, or the measurement of new data in situ. Only few published studies have explicitly targeted a generalizable method to cope with several ecosystems ([Martin et al. 2008](#), [Singh et al. 2015](#), or more recently [Wang et al. 2020](#)). Yet, estimation algorithms are required to produce robust estimates in acceptable processing time in view of operational processing chains ([Verrelst et al. 2019](#)). Moreover, the development of an algorithm related to future spaceborne sensors required to be applied across a wide range of sites and remote sensing scenes. In this frame, it would be preferable to seek more generalized canopy chemistry algorithms to take into account the great variability of temperate forests, and provide an algorithm capable of adapting to variations linked to different ecosystems (species, forest structure) and to spatial-temporal variations in the acquisition (phenology, solar irradiance, latitude). Consequently, current methods are not compatible with the massive hyperspectral data streams that will be provided by new spaceborne sensors in the future. At the end of the day, the field of leaf traits estimation requires more work on the comparison of statistical and RTM-based methods for the development of generalizable estimation methods reliable to use on the diversity of temperate forests along the year. The development of a generalized and, hence, more operational approach would expand the ecological utility of the growing volumes of imaging spectroscopy data, now becoming available. In addition, the reliability and accuracy of estimation methods could be improved understanding the change of scale between the leaves up to the canopy.

Objective of the thesis

In the context of recent and future satellite hyperspectral missions, the objective of the present thesis targets the development of a generalizable method to estimate four leaf traits; namely C_{ab} , C_{xc} , EWT and LMA; from hyperspectral data, robust to the various ecosystems of temperate forests, and temporal changes, including phenological variations of the forest and seasonal illumination variations.

This general problem, imposed by the development of future hyperspectral spaceborne sensors, is based on two underlying scientific challenges and questions. First of all, species from different temperate forest ecosystems have foliage with specific morphological and phenological characteristics linked to their adaptation to climates. Are the estimation methods identified in the literature applicable to foliage of temperate forest species, whatever their characteristics linked to climate and ecosystem? Secondly, species characteristics are also expressed at canopy scale, and influence the signal captured at this scale, as well as landscape variations related to solar illumination and understory. Considering the variations due to canopy structure, the solar illumination and understory, are the estimation accuracies achieved at the leaf scale transferable at the canopy scale?

[Chapter 1](#) of this manuscript focuses on the forward problem. It provides a state-of-the-art of the RTM to model the vegetation at various scales and argues on the selection of three RTMs. It then presents the integration of selected RTMs in the thesis, and conducts sensitivity analyses. This work highlights the link between leaf traits and radiometric quantities.

[Chapter 2](#) introduces the methodology for estimating leaf traits through the three inversion strategies. It reviews the state-of-the-art of methodologies used to estimate leaf traits and details the main algorithms selected in this thesis to build estimation methods.

[Chapter 3](#) describes a dataset that fulfills the criteria required to test the methods presented

in Chapter 2 and meet the challenges set out in this thesis. The dataset encompasses in situ and in-lab data from five sites in California; covering mediterranean, broadleaf, and coniferous mountain forest ecosystems; and seasonal variations. The dataset compiles leaf traits measurements and corresponding radiometric observations from both a portable spectroradiometer and an airborne hyperspectral sensor.

Chapter 4 focuses on estimation of leaf traits at the leaf scale from spectroradiometer measurements presented in Chapter 2, and compares the accuracy of several estimation methods from the state-of-the-art. It aims to assess the robustness of state-of-the-art methods at this scale regarding ecosystem types and seasonal variations of the vegetation from data presented in Chapter 2. State-of-the-art methods gather methods from the three strategies: statistical, physical and hybrid. Physical and hybrid methods are based on a leaf RTM presented in Chapter 1. Statistical and hybrid methods use four MLRAs introduced in Chapter 2. Moreover, the work from Chapter 4 aims to assess the transferability of statistical methods using an open source dataset.

Chapter 5 assesses the capabilities of estimation methods to cope with other interfering factors at the canopy scale; namely canopy structure, solar illumination, and understory impacts. It examines the robustness of statistical methods and a hybrid method to retrieve leaf traits from hyperspectral airborne data. By comparing with the accuracies from Chapter 4, this work aims to highlight the effects of canopy structure, solar illumination and understory; which vary temporally and/or with the ecosystems types; with a view to developing a generalizable estimator for satellite hyperspectral image processing.

Finally, a general conclusion and perspectives are given at the end of the manuscript.

Introduction

Les écosystèmes forestiers représentent une grande partie des terres continentales, couvrant environ 10 % de la surface terrestre (FAO 2020). Un écosystème forestier est un type de végétation dominé par les arbres, mais il existe plusieurs définitions dans le monde qui fixent des critères spécifiques en termes de taille, de couverture arborée, de hauteur et d'utilisation des terres. L'Organisation des Nations Unies pour l'alimentation et l'agriculture (FAO) définit les forêts comme "des terres s'étendant sur plus de 0,5 hectare avec des arbres d'une hauteur supérieure à 5 mètres et un couvert de plus de 10 %, ou des arbres capables d'atteindre ces seuils in situ" (FAO 2020). En outre, la FAO exclut les terres qui sont principalement utilisées à des fins agricoles ou urbaines. Cette définition est suffisamment large pour couvrir de nombreux types de couvert arboré, y compris les zones à végétation basse.

Les écosystèmes forestiers jouent un rôle crucial en faveur du climat et de la biodiversité. Ce rôle est particulièrement mis en évidence dans les rapports 2021-2023 du GIEC et 2019 de l'IPBES. Comme les autres écosystèmes végétaux, les forêts transforment l'énergie solaire en matière organique par la photosynthèse et absorbent le dioxyde de carbone de l'atmosphère. Les écosystèmes forestiers sont le plus grand fournisseur de biomasse, produisant 75 % de la matière organique sur les surfaces continentales et constituant le plus grand puits de carbone terrestre (Masson-Delmotte et al. 2021). Les forêts jouent non seulement un rôle dans le stockage du carbone à long terme, mais ont également des effets positifs significatifs sur la stabilité du climat (Seymour et al. 2022). Les dernières recherches mettent en évidence la contribution des forêts à la stabilisation des températures locales et des régimes de précipitations (Pörtner et al. 2022; Seymour et al. 2022). En particulier, les forêts refroidissent la surface de la terre et la basse atmosphère grâce à l'évapotranspiration, et la rugosité des canopées influe sur les vents et les courants atmosphériques. Les forêts contribuent à la conservation de la biodiversité en fournissant des habitats à un large éventail d'espèces (Brondizio et al. 2019). En effet, le couvert végétal, la biomasse créée et les différents niveaux de végétation constituent un environnement dans lequel une grande variété d'espèces - plantes, champignons et animaux - peuvent prospérer. Les forêts jouent donc un rôle fondamental dans la conservation de la biodiversité. Ainsi, les forêts constituent une grande partie des régions classées comme points chauds de la biodiversité (Myers et al. 2000), qui concentrent 44% des espèces de plantes vasculaires et 35 % des espèces de vertébrés, et sont devenues des priorités pour la conservation des écosystèmes en raison des pressions qu'elles subissent.

Les écosystèmes forestiers couvrent une grande diversité de biomes. Les principaux types de biomes peuvent être distingués sur la base des précipitations et des températures annuelles moyennes (Whittaker 1975). Ces biomes comprennent les forêts tropicales humides et les forêts tropicales sèches autour de l'équateur, les forêts boréales dans les climats subarctiques et, aux latitudes moyennes, un large éventail de forêts tempérées (forêts tempérées humides, tempérées continentales, méditerranéennes et subtropicales). Les forêts tempérées sont situées dans des régions de latitude moyenne où différentes masses d'air s'entrechoquent et où le climat est affecté par des rythmes saisonniers importants. Les forêts tempérées s'étendent sur une grande variété de climats selon la classification climatique de Köppen-Geiger et peuvent être classées en trois biomes principaux (Olson et al. 2001) : les forêts tempérées à feuilles larges et mixtes, les forêts tempérées de conifères et les forêts méditerranéennes.

Les études sur la science du climat ont abouti, depuis au moins 30 ans, à un consensus scientifique selon lequel la Terre est confrontée à un réchauffement climatique dû aux émissions anthropiques de gaz à effet de serre (Masson-Delmotte et al. 2021; Oreskes 2004). Les progrès de la science du climat ont mis en lumière le changement climatique causé par le réchauffement de la planète et l'augmentation de la concentration des gaz à effet de serre anthropiques dans l'atmosphère. Le changement climatique modifie non seulement la température moyenne et les précipitations, mais aussi la fréquence et l'intensité des phénomènes hydrométéorologiques extrêmes tels que les sécheresses et les vagues de chaleur. Par conséquent, le changement climatique

met en péril la résilience des écosystèmes forestiers. En outre, le changement climatique a été répertorié par l'IPBES comme l'une des cinq principales menaces pesant sur la biodiversité, avec la destruction des habitats naturels, la surexploitation des espèces, la pollution et les espèces envahissantes.

L'altération des températures et des précipitations plonge les arbres forestiers directement dans des conditions auxquelles ils ne sont pas adaptés et, en combinaison avec d'autres facteurs de perturbation, pousse les forêts au-delà des seuils de durabilité (Millar and Stephenson 2015). Les sécheresses augmentent directement le stress hydrique des arbres et conduisent à la dessiccation des forêts et à une moindre résistance aux agents pathogènes. En outre, l'élévation de la température moyenne et les changements dans le calendrier saisonnier facilitent la propagation des ravageurs et des maladies, ainsi que des espèces envahissantes. En fin de compte, le changement climatique a augmenté la probabilité de mortalité des arbres par rapport aux niveaux de mortalité enregistrés au XX^{ème} siècle (Millar and Stephenson 2015). Des cas de mortalité élevée, soudaine et inattendue d'arbres à la suite d'épisodes de chaleur et de sécheresse ont déjà été observés et documentés, y compris dans des écosystèmes qui étaient auparavant considérés comme tolérants ou ne risquant pas d'être exposés (Hartmann et al. 2022). Les événements hydrométéorologiques extrêmes modifient également les régimes d'incendie et intensifient le risque d'incendie. Les incendies de forêt sont devenus l'un des principaux facteurs de perte des forêts, en particulier des forêts tempérées. Par exemple, les incendies de forêt ont causé 40 % de la perte de forêts en Amérique du Nord sur la période 2001-2015 (Curtis et al. 2018).

Le changement climatique modifie les processus physiologiques des arbres des forêts. Par conséquent, le suivi de ces processus physiologiques est un facteur clé pour comprendre et évaluer les impacts décrits précédemment. En écologie, les concepts de traits fonctionnels ont été développés pour surveiller spécifiquement ces processus physiologiques. Les traits fonctionnels sont définis comme toute caractéristique morphologique, physiologique ou phénologique, mesurable au niveau individuel, qui a un impact indirect sur l'aptitude de la plante via ses effets sur la croissance, la reproduction ou la survie (Violle et al. 2007).

Par la suite, des variables essentielles de la biodiversité (EBV) ont été définies par le réseau d'observation de la biodiversité du Groupe sur l'observation de la Terre (GEO BON), dans le but de créer un système d'observation mondial harmonisé pour informer les scientifiques et les décideurs politiques (Pereira et al. 2013; GEO BON n.d.). Les EBV ont été définies sur la base des variables climatiques essentielles qui guident le système mondial d'observation du climat (GCOS). Les EBV sont définies comme des quantités mesurables nécessaires à l'étude et au suivi de l'évolution de la biodiversité. Elles fournissent une description structurelle, taxonomique et fonctionnelle de l'environnement étudié. Les EBV comprennent de nombreux traits fonctionnels de la végétation. Ces traits fonctionnels sont des indicateurs de la physiologie de l'espèce et de l'écosystème (Pereira et al. 2013).

Cependant, les traits fonctionnels ne sont pas mesurables à grande échelle, et l'une des solutions pour couvrir de vastes zones est l'utilisation de la télédétection. Plusieurs traits fonctionnels de la végétation, inclus dans les EBV, ont été répertoriés comme des mesures de la biodiversité à observer en priorité depuis l'espace (Skidmore et al. 2021). La télédétection "est la science et l'art d'obtenir des informations sur un objet, une zone ou un phénomène par l'analyse de données acquises par un dispositif qui n'est pas en contact avec l'objet, la zone ou le phénomène étudié" (Lillesand et al. 2015). L'estimation des paramètres physiques terrestres tels que les EBV fait partie des nouvelles tendances de la télédétection qui s'orientent vers des évaluations quantitatives plutôt que qualitatives.

Parmi les traits fonctionnels, plusieurs sont mesurables au niveau des feuilles et sont donc regroupés sous le nom de "traits foliaires". Quatre traits foliaires sont la teneur en chlorophylles a et b (C_{ab}), la teneur en caroténoïdes (C_{xc}), l'épaisseur équivalente de l'eau (EWT) et la surface de la masse foliaire (LMA). Ils sont liés aux processus physiologiques de la plante et, au niveau de l'écosystème, aux cycles biogéochimiques et sont donc considérés comme des indicateurs précieux de la santé de la végétation et du niveau de stress (Lausch et al. 2016).

- Les chlorophylles a et b sont les pigments dominants de la feuille. Elles sont les principaux pigments photosynthétiques des feuilles et leur donnent leur couleur verte. Elles constituent la majeure partie des complexes de capture de la lumière dans les photosystèmes situés sur les membranes des thylakoïdes dans les chloroplastes, et jouent donc un rôle clé dans la conversion de la lumière en énergie chimique (Taiz and Zeiger 2010). C_{ab} exprime la masse de chlorophylles a et b par unité de surface foliaire.

- Les caroténoïdes comprennent les familles du carotène et de la xanthophylle. Les caroténoïdes sont également des pigments photosynthétiques et sont liés aux molécules de chlorophylle dans les photosystèmes (Taiz and Zeiger 2010). Les xanthophylles assurent également une protection contre les rayonnements nocifs grâce au cycle de la xanthophylle (Demmig-Adams and Adams 1996). C_{xc} exprime la masse de caroténoïdes par unité de surface foliaire.
- La teneur en eau des feuilles est un indicateur de la gestion de l'eau par les tissus végétaux. L'EWT est la teneur en eau pondérée de la feuille (Riano et al. 2005).
- Les autres constituants principaux de la feuille sont rassemblés dans la matière sèche. La matière sèche des feuilles comprend un large éventail de composés organiques qui peuvent être divisés en deux groupes principaux : les constituants à base d'azote (protéines) et les constituants à base de carbone (y compris la cellulose, la lignine, l'hémicellulose, l'amidon et les sucres) (Féret et al. 2021). La LMA est exprimée en masse sèche par unité de surface foliaire. C'est l'inverse de la surface foliaire spécifique (SLA) qui est également souvent utilisée comme caractéristique fonctionnelle des feuilles.

Les constituants biochimiques absorbent l'énergie du rayonnement lumineux au niveau microscopique. Les photons sont absorbés par le phénomène des transitions électroniques pour les pigments, ou convertis sous forme d'énergie vibratoire interne aux molécules pour l'eau, les constituants azotés et carbonés. Ces phénomènes d'absorption impliquent des photons d'énergies spécifiques. Par conséquent, la biochimie foliaire, et donc les quatre caractéristiques de la feuille, ont un impact sur les propriétés optiques de la feuille par le biais de bandes d'absorption spécifiques à chaque constituant. Les bandes d'absorption sont situées dans le domaine visible (400 – 750 nm) pour C_{ab} et C_{xc} ; dans le proche infrarouge (NIR ; 800 – 1400 nm) et dans l'infrarouge à ondes courtes (SWIR ; 1400 – 2500 nm) pour l'EWT et le LMA.

Les bandes d'absorption constituent les empreintes spectrales de chaque caractéristique de la feuille. Dans ce cadre, l'analyse des mesures optiques à haute résolution spectrale peut aider à quantifier les caractéristiques des feuilles.

En télédétection, un concept d'instrument appelé spectromètre imageur a émergé depuis les années 1990. L'émergence de la spectro-imagerie a donné naissance à un vaste champ de recherche dans le domaine de la télédétection (Schaepman 2009; Rast and Painter 2019). La spectro-imagerie implique que de nombreuses bandes dans des longueurs d'onde adjacentes soient mesurées de sorte que toutes les bandes sur un intervalle de longueur d'onde spécifié échantillonnent complètement le spectre. La spectroscopie par imagerie est souvent appelée imagerie hyperspectrale, mais cette dernière dénomination n'est pas claire car elle ne précise pas que les nombreuses bandes mesurées sont adjacentes. En outre, l'estimation des paramètres physiques des terres, tels que l'EBV, a été citée comme l'un des principaux défis à relever en matière de télédétection hyperspectrale (Bioucas-Dias et al. 2013). L'estimation des paramètres physiques est une étape intermédiaire pour transformer les mesures de télédétection en estimations utiles. Les paramètres physiques peuvent être estimés en utilisant les propriétés optiques transmises dans les fenêtres atmosphériques.

Dans le passé, les capteurs hyperspectraux étaient limités aux capteurs aéroportés tels qu'AVIRIS (Green et al. 1998). Le développement de capteurs hyperspectraux spatiaux a marqué une pause depuis le lancement d'Hyperion dans les années 2000, mais plus récemment, une nouvelle vague de capteurs hyperspectraux spatiaux a trouvé sa place dans les programmes spatiaux (Ustin and Middleton 2021). Cette nouvelle vague comprend des capteurs récemment lancés (PRISMA (Cogliati et al. 2021), EnMAP (Guanter et al. 2015), EMIT (Green et al. 2020)), et les missions prévues pour la prochaine décennie (CHIME (Rast et al. 2021), SBG (Green et al. 2022)). Ces nouveaux capteurs produiront un flux sans précédent d'images hyperspectrales de la Terre.

L'estimation des paramètres physiques des terres, y compris l'estimation des caractéristiques des feuilles, à partir de la spectro-imagerie, fait partie du problème inverse. De manière générale, les problèmes inverses déduisent les paramètres d'un système à partir des données observées, contrairement aux problèmes directs qui simulent les effets compte tenu de tous les paramètres. Dans la modélisation de la télédétection de la végétation, le problème direct, ou forward, est un cas de transfert radiatif. Il s'agit de modéliser la propagation du rayonnement lumineux reçu du soleil à travers l'atmosphère et la végétation afin de prévoir les observations. De nombreux travaux se sont concentrés sur la modélisation de l'interaction de la lumière avec la matière dans le cas de la végétation, ce qui a conduit à la création de multiples modèles de transfert radiatif (RTM).

Formellement, le problème à terme peut être exprimé comme suit :

$$Y = f(x, \theta) + n$$

où Y est un ensemble d'observations, x est l'ensemble des paramètres, θ est un ensemble de conditions contrôlables, et n est un bruit additif. f est la fonction qui modélise le transfert radiatif.

Le problème inverse implique de récupérer une ou plusieurs variables d'intérêt à partir de la mesure de la radiance par un capteur. Il peut être exprimé comme suit :

$$\hat{x} = g(Y, \omega)$$

où g est une fonction paramétrée par des poids ω , qui approxime les paramètres \hat{x} à partir de l'ensemble des observations Y .

La résolution du problème inverse dépend donc dans une large mesure de la compréhension du modèle direct. En outre, comme pour la plupart des problèmes inverses, l'estimation des caractéristiques des feuilles est un problème mal posé, ce qui signifie que des combinaisons distinctes de caractéristiques de la végétation peuvent conduire à des mesures optiques similaires, et à des solutions multiples (Baret and Buis 2008).

L'estimation des paramètres physiques des terres implique une taxonomie spécifique des méthodes d'inversion. Cette taxonomie a été introduite pour la première fois dans les années 2000 par (Baret and Buis 2008), puis réintroduite par (Bioucas-Dias et al. 2013) et (Verrelst et al. 2019). La taxonomie prend en compte trois stratégies d'inversion : statistique, physique et hybride. La stratégie statistique implique l'apprentissage statistique du modèle inverse, *i.e.* la fonction g , à partir d'un ensemble d'observations et de paramètres mesurés correspondants. La phase d'apprentissage peut être réalisée par une simple transformation de l'observation hyperspectrale ou par l'entraînement d'algorithmes de régression par apprentissage automatique (MLRA) plus complexes. La stratégie statistique est aussi parfois appelée approche fondée sur les données ou approche empirique. La stratégie physique tente d'inverser le RTM, ce qui signifie qu'elle recherche l'ensemble de paramètres le plus susceptible de fournir l'observation. Diverses approches ont été envisagées, notamment l'optimisation itérative, la table de recherche (LUT), la chaîne de Markov Monte Carlo (MCMC) et les algorithmes génétiques. La stratégie physique est réservée aux RTM à faible coût de calcul, car les approches sous-jacentes nécessitent de nombreux appels au RTM. La stratégie hybride combine des aspects des stratégies statistique et physique : elle apprend statistiquement un modèle inverse, *i.e.* la fonction g , à partir d'un ensemble de données d'entrée-sortie générées par des simulations RTM directes. La phase d'apprentissage est généralement réalisée à l'aide d'un MLRA.

Cependant, l'examen de la littérature ne permet pas de dégager un consensus sur les stratégies à privilégier dans le développement de l'estimation des caractéristiques foliaires à partir d'images hyperspectrales spatiales (Hill et al. 2019). En effet, certains auteurs préconisent de se concentrer sur des stratégies hybrides telles que Verrelst et al. 2019, tandis que d'autres concentrent leurs travaux sur des stratégies statistiques, même pour l'estimation à grande échelle (*e.g.*, Wang et al. 2020). La plupart des études dans le domaine de l'estimation des traits foliaires soulignent que les approches statistiques (ou empiriques) pourraient théoriquement manquer de capacités de généralisation par rapport aux méthodes basées sur la RTM. Néanmoins, il convient de noter que les méthodes basées sur les RTM peuvent également manquer de capacités de généralisation si les RTM sont adaptées aux conditions locales, et que les lacunes des méthodes statistiques sont de moins en moins prononcées dans les résultats de recherche récents. Les recherches antérieures dans ce domaine présentent deux inconvénients majeurs compte tenu des exigences prévues pour les futurs capteurs spatiaux. D'une part, comme le soulignent Homolová et al. 2013 et Gamon et al. 2019, la plupart des études publiées se sont concentrées sur une période donnée, en utilisant généralement un seul point dans le temps près du centre de la saison de croissance, et n'ont pas évalué la fiabilité des méthodes d'extraction tout au long de l'année. Comme attendu, les protocoles d'estimation élaborés à partir d'une saison ne parviennent généralement pas à reproduire la même précision sur des ensembles de données collectés au cours d'une autre saison (Gamon et al. 2019). D'autre part, ces études portent généralement sur une seule ou quelques images, couvrant des régions limitées avec un seul type d'écosystème forestier et, par conséquent, ne fournissent pas de méthodes pour estimer les caractéristiques des feuilles sur plusieurs sites éloignés les uns des autres et contenant des espèces distinctes. En outre, seules quelques études ont étudié l'estimation des caractéristiques des feuilles à la fois à l'échelle de la feuille et à l'échelle de la canopée sur le même site et à la même période. Ainsi, le passage de l'échelle de la feuille à l'échelle de l'arbre ou de la canopée reste une question ouverte dans la littérature, et dépendrait

fortement du type d'arbres et de l'échelle d'observation. En outre, les méthodes spécifiques à un site ou à une période nécessiteraient de longs délais de traitement par rapport à la quantité de données, à la génération de nouvelles simulations ou à la mesure de nouvelles données in situ. Seules quelques études publiées ont explicitement ciblé une méthode généralisable pour faire face à plusieurs écosystèmes (Martin et al. 2008, Singh et al. 2015, ou plus récemment Wang et al. 2020). Pourtant, les algorithmes d'estimation sont nécessaires pour produire des estimations robustes dans un temps de traitement acceptable compte tenu des chaînes de traitement opérationnelles (Verrelst et al. 2019). En outre, le développement d'un algorithme lié aux futurs capteurs spatiaux doit être appliqué à un large éventail de sites et de scènes de télédétection. Dans ce cadre, il serait préférable de rechercher des algorithmes de chimie de la canopée plus généralisés pour prendre en compte la grande variabilité des forêts tempérées, et fournir un algorithme capable de s'adapter aux variations liées aux différents écosystèmes (espèces, structure forestière) et aux variations spatio-temporelles de l'acquisition (phénologie, irradiance solaire, latitude). Par conséquent, les méthodes actuelles ne sont pas compatibles avec les flux massifs de données hyperspectrales qui seront fournis par les nouveaux capteurs spatiaux à l'avenir. En fin de compte, le domaine de l'estimation des traits foliaires nécessite davantage de travail sur la comparaison des méthodes statistiques et des méthodes basées sur la RTM pour le développement de méthodes d'estimation généralisables et fiables à utiliser sur la diversité des forêts tempérées tout au long de l'année. Le développement d'une approche généralisée et, par conséquent, plus opérationnelle, élargirait l'utilité écologique des volumes croissants de données de spectro-imagerie, qui deviennent maintenant disponibles. En outre, la fiabilité et la précision des méthodes d'estimation pourraient être améliorées en tenant compte du changement d'échelle entre les feuilles et la canopée.

Objectifs de la thèse

Dans le contexte des missions hyperspectrales satellitaires récentes et futures, l'objectif de la présente thèse est de développer une méthode généralisable pour estimer quatre traits foliaires, à savoir C_{ab} , C_{xc} , EWT et LMA, à partir de données hyperspectrales, robustes aux différents écosystèmes des forêts tempérées, et aux changements temporels, y compris les variations phénologiques de la forêt et les variations saisonnières de l'illumination.

Cette problématique générale, imposée par le développement des futurs capteurs hyperspectraux spatiaux, repose sur deux défis et questions scientifiques sous-jacents. Tout d'abord, les espèces des différents écosystèmes forestiers tempérés ont un feuillage avec des caractéristiques morphologiques et phénologiques spécifiques liées à leur adaptation aux climats. Les méthodes d'estimation identifiées dans la littérature sont-elles applicables au feuillage des espèces des forêts tempérées, quelles que soient leurs caractéristiques liées au climat et à l'écosystème ? Deuxièmement, les caractéristiques des espèces s'expriment également à l'échelle de la canopée, et influencent le signal capturé à cette échelle, ainsi que les variations du paysage liées à l'illumination solaire et au sous-étage. En considérant les variations dues à la structure de la canopée, à l'illumination solaire et au sous-étage, les précisions d'estimation obtenues à l'échelle de la feuille sont-elles transférables à l'échelle de la canopée ?

Le Chapitre 1 de ce manuscrit se concentre sur le problème de l'avant. Il fournit un état de l'art des RTM pour modéliser la végétation à différentes échelles et argumente sur la sélection de trois RTM. Il présente ensuite l'intégration des RTM sélectionnés dans la thèse et effectue des analyses de sensibilité. Ce travail met en évidence le lien entre les caractéristiques des feuilles et les quantités radiométriques.

Le Chapitre 2 présente la méthodologie d'estimation des traits foliaires à travers les trois stratégies d'inversion. Il passe en revue l'état de l'art des méthodologies utilisées pour estimer les traits foliaires et détaille les principaux algorithmes sélectionnés dans cette thèse pour construire les méthodes d'estimation.

Le Chapitre 3 décrit un ensemble de données qui remplit les critères requis pour tester les méthodes présentées au chapitre 2 et relever les défis énoncés dans cette thèse. L'ensemble de données comprend des données in situ et en laboratoire provenant de cinq sites en Californie, couvrant des écosystèmes de forêts méditerranéennes, de feuillus et de conifères de montagne, ainsi que des variations saisonnières. L'ensemble des données compile les mesures des caractéristiques des feuilles et les observations radiométriques correspondantes provenant d'un spectroradiomètre portable et d'un capteur hyperspectral aéroporté.

Le Chapitre 4 se concentre sur l'estimation des caractéristiques des feuilles à l'échelle de la feuille à partir des mesures du spectroradiomètre présentées dans le chapitre 2, et compare la précision de plusieurs méthodes d'estimation de l'état de l'art. Il vise à évaluer la robustesse des méthodes de pointe à cette échelle en fonction des types d'écosystèmes et des variations saisonnières de la végétation à partir des données présentées au chapitre 2. Les méthodes de l'état de l'art regroupent des méthodes issues des trois stratégies : statistique, physique et hybride. Les méthodes physiques et hybrides sont basées sur un RTM foliaire présenté au chapitre 1. Les méthodes statistiques et hybrides utilisent quatre MLRA introduites au chapitre 2. En outre, le travail du chapitre 4 vise à évaluer la transférabilité des méthodes statistiques à l'aide d'un ensemble de données open source.

Le Chapitre 5 évalue les capacités des méthodes d'estimation à faire face à d'autres facteurs d'interférence à l'échelle de la canopée, à savoir la structure de la canopée, l'illumination solaire et les impacts du sous-étage. Il examine la robustesse des méthodes statistiques et d'une méthode hybride pour extraire les caractéristiques des feuilles à partir de données hyperspectrales aéroportées. En comparant les précisions obtenues au chapitre 4, ce travail vise à mettre en évidence les effets de la structure de la canopée, de l'illumination solaire et du sous-étage, qui varient dans le temps et/ou en fonction des types d'écosystèmes, en vue de développer un estimateur généralisable pour le traitement d'images hyperspectrales par satellite.

Enfin, une conclusion générale et des perspectives sont données à la fin du manuscrit en français et en anglais.

Chapter 1

Radiative transfer modeling of forest canopies

As presented in [Introduction](#), the estimation of vegetation traits from optical measurements is a challenging inverse problem. In essence, estimation methods aim to develop an inverse model to the underlying physical process. The propagation of radiation in a medium is described mathematically by the equations of radiative transfer. However these integro-differential equations have proven to be remarkably intractable ([Hapke 2012](#)) and cannot be solved exactly except under very simplifying assumptions. Therefore, computational physics is the only way to obtain an approximate but reasonably accurate solution of the radiative transfer in a complex environment. Computational physics models are essential to understand the forward problem that is how electromagnetic radiation interacts with vegetation elements. They are also a key tool to directly relate observed optical properties to leaf traits and therefore they can guide the development of an estimation method regardless of the chosen strategy. This first chapter focuses on the forward problem and presents the work made on radiative transfer modeling of forest leaves and canopies.

The study of the forward problem has a twofold goal: (i) to understand the link between vegetation composition and its observed optical properties to guide the building of estimation methods; (ii) and to produce reliable simulations of optical properties for the development of physically-based and hybrid estimation strategies. To fulfill these goals, the underlying work consists of the development of a simulation framework that faithfully models the physical processes. The processing chain must be controlled (*i.e.*, it generates outputs that are physically reliable) and configurable (*i.e.*, it exhibits a limited number of parameters that control simulation results, the effects of each parameter are known).

The chapter is structured into four sections, each addressing aspects of the development of the simulation framework/simulation chain and a better understanding of the forward problem for leaf traits estimation.

Firstly, [Section 1.1](#) provides a literature overview of existing RTM for vegetation. This overview is divided in two parts, depending on the scale considered for simulating physical processes. It includes a first part on RTM for simulating physical processes and predicting optical properties at the leaf scale, and a second part on RTM for processes at the canopy scale. From the state-of-the-art, a leaf-scale RTM called PROSPECT, and two canopy-scale RTMs, namely SAIL and DART, are selected for subsequent exploration.

Secondly, [Section 1.2](#) presents the implementations and parametrization of the selected models. This section describes the simulation framework/simulation chain to integrate the RTM and delineates the methodology employed in this thesis to simulate vegetation optical properties.

Following this, [Section 1.3](#) delves into sensitivity analyses conducted on the selected RTM. Various sensibility analyses are conducted, including local sensitivity analyses aiming to discern the influence of key model parameters, and broader variance-based global sensitivity analyses on optical properties and classic transformations. This section aims to identify spectral signatures corresponding to targeted vegetation traits, and to provide assumptions to build inverse models for leaf traits estimation.

Additionally, this section highlights disparities between assumptions from 1D and 3D canopy RTM, and emphasizes their respective applicability and implications for vegetation assessment and the contribution of 3D models compared to 1D models to simulate forest canopies.

Finally, the [conclusion](#) of this first chapter outlines the limitations of RTMs and the simula-

tion framework/simulation chain that may impact the accuracy and reliability of some leaf traits estimation methods.

1.1 Vegetation radiative transfer modeling

A RTM can be defined as the computer realization of radiative transfer processes. A RTM includes a virtual environment (also called scene) that defines the geometry and optical properties (such as scattering, absorption, reflection) of its elements, the light sources, and one or multiple sensors. The RTM defines a computer algorithm that tracks the radiation in this virtual environment to simulate the required quantities, such as the instrument's observed reflectance. For the most simple RTM with strong assumptions, the radiative transfer equations can be analytically solved through the mathematical formalism and the algorithm consists of several equations. For more complex RTM, several strategies have been developed to solve the radiative transfer equations.

RTMs can be distinguished by the scale they aim to simulate physical processes. We can distinguish leaf scale RTMs from canopy-scale RTMs. Leaf-scale RTMs aim to simulate only the optical properties from leaf structure and constituents. They take into account microscopic and macroscopic effects inside the leaves that are respectively the absorption by chemical constituents and the scattering by leaf materials. Canopy-scale RTMs simulate the canopy reflectance from the canopy structure, optical properties of various elements and the illumination conditions. Canopy-scale RTMs primarily simulate the scattering of the light by large vegetation elements, absorption effects are only indirectly simulated through the material properties. Canopy RTMs mostly use spectral invariance (Lewis and Disney 2007), meaning that the computation process is the same for all the wavelengths because the considered elements are too large to scatter differently the rays from distinct wavelengths. The wavelength dependent effects in canopy RTMs comes from absorption of materials (which are precomputed and provided as inputs) and scattering in the atmosphere. State-of-the-art is provided for leaf-scale RTMs in Section 1.1.1 and for canopy-scale RTMs in Section 1.1.2. In spite of this scale consideration, both leaf-scale and canopy-scale RTMs use common methods to solve the radiative transfer equations.

In the state-of-the-art, several taxonomies of RTM can be found. RTM models can be classified in two ways, which partially overlap: RTM can be classified by the way they solve the radiative transfer equations, but also by the complexity of the embedded scene. Regarding the embedded scene complexity, RTM can be divided into one-dimensional (1D) and three-dimensional (3D) models. RTMs that consider horizontally homogeneous and infinite but vertically variable media, such as plate models or N-flux models, are called 1D (Liang 2005). Conversely, 3D RTMs consider both vertical and horizontal variability of the media embedded in the scene. Regarding the strategy to find a solution of the radiative transfer equations, at least five categories can be cited:

- **N-flux models:** N-flux models are derived from the Kubelka–Munk theory (Kubelka and Munk 1931). The models have evolved from two-flux to three-flux and four flux theory (e.g., SAIL ; Verhoef 1984).
- **Geometric optical models:** Analytic models can be derived from simple geometric models of the scene such as the plate model (Allen et al. 1970) or the compact spherical particle models (Melamed 1963).
- **Stochastic approach:** Within stochastic approaches the transfer of photons is simulated through a stochastic process. The stochastic process is often from the Markov chain family that considers several discrete states for the photons and controls the transition probabilities from one state to another.

The two other methods are called ray tracing methods. Ray tracing methods repeatedly sample the light path through the scene. The light path, or photon trajectory, is sampled with basic optical laws (reflection, refraction, and absorption). This is a stochastic process, but more complex than Markov chains. The stochastic process converges toward the solution when a sufficient number of rays have been simulated. Ray tracing methods have as a main advantage their flexibility and are able to simulate a variety of light sources, sensors, radiometric quantities and radiative processes, including in a complex environment. Two kinds of ray tracing methods can be distinguished: discrete ordinates methods and Monte Carlo methods.

- **Discrete ordinates methods:** Discrete ordinates methods solve the radiative transfer problem for a finite number of radiation propagation directions and considering a finite number of voxels to describe the scene (*e.g.*, DART-FT; [Gastellu-Etchegorry et al. 1996](#)).
- **Monte Carlo methods:** Monte Carlo methods consider elements of the scene as triangle meshes. The photon trajectories are not constrained to a spatial grid or predefined directions (*e.g.*, DART-Lux ([Wang et al. 2022](#)), FLIGHT ([North 1996](#)), Raytran ([Govaerts and Verstraete 1998](#))). Monte Carlo methods are considered as the most accurate methods but also the most computationally demanding. Over the last two decades, research into Monte Carlo methods has tremendously increased in the computer graphics field, boosted by the capabilities of video game and film industries.

The choice, design and complexity of an RTM depends on the scientific objective. In the case of a model inversion, an essential first step is to check if the model is well adapted to the vegetation type. The choice of the model could also depend on the selected inversion strategy.

1.1.1 Leaf radiative transfer modeling

1.1.1.1 State-of-the-art

Computer-based leaf models were developed from the late 1960s to the present and have improved our understanding of the interaction of light with plant leaves. Extensive reviews of the computer-based leaf models are provided by several authors ([Baranoski and Rokne 2004](#); [Ustin 2004](#)) and a broad overview of these models was provided in [Jacquemoud and Ustin 2019](#) book, Leaf Optical Properties .

The propagation of light through plant leaves is driven by microscopic and macroscopic interactions that respectively lead to absorption and scattering phenomena. Leaf models embedded varying complexities for the modeling of physics, from the simplest model considering the blade as a single scattering and absorbing layer to the most complicated where all cells are described in detail by their shape, size, position, and biochemical content. Therefore, leaf models are often categorized into different classes following their complexity. By order of increasing complexity, can be quoted plate models, compact spherical particle models, N-Flux models, stochastic approaches, and ray tracing models.

The plate model is a model that approximates the scattering medium by plane-parallel layers. The plate model was first introduced in [Allen et al. 1969](#) and furtherly extended to the generalized plate model by [Allen et al. 1970](#). The generalized plate model simply consists of stacking elementary plates: the leaf is modeled by N uniform compact plates separated by N-1 air spaces to account for intercellular spaces in the leaf mesophyll. This type of problem was first solved for reflectance and transmittance in the 19th century through Stokes glass plate theory ([Stokes 1862](#)), but can be extended to a continuous distribution where N does not need to be an integer. The PROSPECT model was designed based on the generalized plate model in the early 1990s ([Jacquemoud and Baret 1990](#)). The PROSPECT model is now widely used in the remote sensing community.

Some other leaf-scale RTM can be classified as compact spherical particle models. Most of the models are not adapted to model needle-shaped leaves, specifically because they cannot be treated as discrete plane parallel layers. To overcome this issue Melamed's theory ([Melamed 1963](#)) was adapted to simulate reflectance and transmittance of pine needles in the LIBERTY model ([Dawson et al. 1998](#)). Melamed's theory was initially designed for suspended powders and considers a compact layer of spherical particles. It was adapted to pine needles considering that the spherical particles are the needle-leaf cells.

N-flux models are derived from the Kubelka–Munk theory ([Kubelka and Munk 1931](#)). In these models the leaf is considered as a slab of an absorbing and diffusing material. The material is only described by its absorption coefficient and its scattering coefficient.

Stochastic approaches simulate the radiative transfer, as indicated by their name, by a stochastic process. In these approaches, the photons are described by several states (*e.g.*, diffuse reflected radiation, diffuse transmitted radiation, absorbed, ...). The photon state is therefore a discrete random variable, and the transition between the states are deduced from the stochastic process. The `lfmod1` model ([Tucker and Garratt 1977](#)) is an example of stochastic approach and is based on

the Markov chain.

Ray tracing models simulate rays (individual photons) incident on the leaf surface, and their propagation using laws of reflection, refraction and absorption. Ray tracing models provide statistically valid estimates when sufficient numbers of rays have been simulated. They require a detailed description of the leaf, with leaf cells and their structure, and that defines the optical properties of the leaf materials. Ray tracing models are more computationally expensive, but they are the only existing category that can account for the complexity of the internal leaf structure. Their high level of description also allows for the simulation of more detailed optical properties such as the absorption profile of light inside the leaf or the bidirectional reflectance at the blade surface (Jacquemoud and Ustin 2019). Several variants of this strategy have been applied to simulate leaf reflectance and transmittance such as Raytran (Govaerts and Verstraete 1998).

Most of the leaf-scale RTM simulate only the leaf as a Lambertian surface. This approximation can cause inaccurate results for a large variety of plants that have strong specular reflection, particularly because of the presence of wax on their surface (Jacquemoud and Ustin 2019). Some strategies were developed to simulate more accurately the leaf directional effects but studies on this topic are scarce because of the lack of experimental measurements. Additionally, most canopy reflectance models assume leaves as Lambertian surfaces and ignore the directional effects of the leaves. In fact, it is often considered that leaf directional properties only marginally influence the vegetation reflectance that can be measured from an aircraft or a satellite. Therefore, directional leaf RTMs are neither considered nor presented in this thesis.

Considering all the leaf-scale RTMs, the PROSPECT has been selected to simulate leaf-scale optical properties in this thesis for its simplicity to use and its reliability. Details on the PROSPECT RTM are provided in the following section.

1.1.1.2 The PROSPECT model

As detailed in section 1.1.1.1 the PROSPECT model is based on the generalized plate model from Allen et al. 1970, it was first introduced in the early 1990s by Jacquemoud and Baret 1990, and has been the most extensively used radiative transfer model over the past 30 years in the remote sensing community. The PROSPECT model is open-source and was among the first leaf-scale RTM to accurately simulate the directional-hemispherical reflectance and transmittance over the solar spectrum from 400 nm to 2500 nm for various plant leaves. PROSPECT has been extensively validated and is the reference leaf RTM and a cornerstone of all canopy RTM.

The PROSPECT model assumes that leaves can be modeled as a stack of N plates whose optical properties are given by a refractive index and absorption (Figure 1.1). The absorption is computed from the Beer-Lambert law, *i.e.* it is the sum for each leaf constituents of their surface concentration multiplied by the specific absorption coefficients.

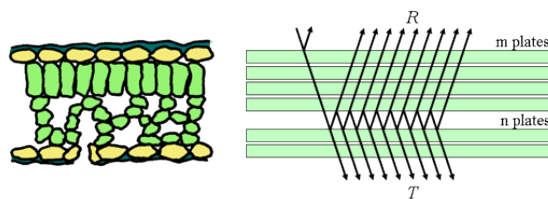


Figure 1.1: Schematic representation of a dicot leaf (left) and multiple reflections produced by a set of plates (right), adapted from Jacquemoud and Ustin 2019

In the PROSPECT model, the leaf structure is fully determined by the structural parameter N . Through the generalized plate model, N can also be a decimal value. The structural parameter N allows to represent the optical effects occurring in the internal leaf structure (multiple reflections and scatterings). Although, it is complex to link this parameter to any precise leaf feature. N is only accessible by fitting PROSPECT to leaf reflectance and transmittance and cause-effect relationships cannot be clearly identified with any other measurable feature. The values of N have been evaluated by some studies and often range between 1 and 2.5 (Jacquemoud et al. 1996; Spaford et al. 2021). The parameter N being the single structure parameter constitutes one of the main advantages of the PROSPECT model.

Over the years, several updated versions of the PROSPECT model were released to include more leaf chemical constituents. The original version of the PROSPECT model (Jacquemoud and Baret 1990) only uses three parameters: N , C_{ab} and EWT. PROSPECT-4 added dry matter (through LMA) and brown pigments as leaf constituents and PROSPECT-5 added carotenoids (through C_{xc}) (Féret et al. 2008). PROSPECT-D added anthocyanins as constituents and updated the pigments specific absorption coefficients and the refractive index (Féret et al. 2017). Finally the PROSPECT-PRO version separated the dry matter between the nitrogen-based constituents (proteins) and the carbon-based constituents (e.g., cellulose and lignin) (Féret et al. 2021). For all the work in this thesis only the PROSPECT-D version is used, and will be simply referred as “PROSPECT”.

The plate model is not adapted to needle-shaped leaves, but PROSPECT has been adapted to simulate the optical properties of conifer needles (Malenovský et al. 2006; Moorthy et al. 2008; Zarco-Tejada et al. 2004). Adaptations consist in the definition of a correction factor to account for the geometry of needle-shaped leaves or a recalibration of the specific absorption coefficients of leaf constituents to improve comparisons between simulated and measured optical properties. Additionally, for C_{ab} estimation, inversions of PROSPECT yielded more accurate estimates than inversions of LIBERTY (Moorthy et al. 2008).

1.1.2 Canopy radiative transfer modeling

1.1.2.1 State-of-the-art

A large diversity of canopy RTMs have been developed over the years. Canopy RTMs are designed for the study of land surface functioning and aim to simulate the radiative transfer near the land surface. They feature several common points. The lower boundary of a forested scene is the Earth surface beneath the vegetation that could be a bare soil or understory layer. The upper boundary is the top of the atmosphere with direct incoming solar radiation. Atmospheric optical properties are determined by the characteristics of aerosol particles, and atmospheric gasses causing multiple scattering and absorption of photons.

The leaf orientation is, in more abstract models, randomly sampled following a distribution function that determine the zenith angle of the leaf surface. Most of the distribution function are not configurable (e.g., spherical, planophile). Conversely, the ellipsoidal distribution (Campbell 1986) admit a single parameter, the average leaf angle (ALA). The ellipsoidal distribution, given its adaptability, is the only one used in this thesis.

Canopy RTM are often divided in two categories regarding the degrees of abstraction for canopy representation, and following the taxonomy: homogeneous and heterogeneous models. This taxonomy is respectively equivalent to the 1D and 3D taxonomy.

For the homogenous models family, the vegetation canopy is assumed to be an unlimited, horizontal turbid medium. The turbid medium is constituted of randomly distributed leaf clumps and gaps in between (Pinty et al. 2001). The canopy structure or canopy architecture is summarized by two descriptors: the LAI (Leaf Area Index) and the LAD (Leaf Angle Distribution). The leaf optical properties are given as input of the canopy RTM. The leaf optical properties are in most cases composed of a Lambertian reflectance and a Lambertian transmittance, but some RTMs admit a specular component of the reflectance (Shultis and Myneni 1988; Malenovský et al. 2007). Thanks to the simplifying assumptions, the radiative transfer equations can be solved analytically for the homogeneous (or 1D) canopy RTMs. Therefore, the execution of homogeneous canopy RTMs is fast, with a low computer resource demand. One way to solve the radiative transfer equations for homogeneous canopy RTMs is through the four flux theory which is an extension of the Kubelka–Munk theory; these RTMs are specifically part of the flux-based RTMs. The SAIL model (Verhoef 1984; Verhoef et al. 2007) is the main canopy flux-based RTM.

Heterogeneous, or 3D, canopy RTMs allow making more flexible assumptions. Here, variations of the vegetation can be admitted in the horizontal planes, and can model discontinuous vegetation canopies. The complexity of the scene varies greatly between canopy RTMs, and even for unique RTM depending on the input parameters. Most simple 3D canopy models extend the homogenous canopy RTMs to meet the assumption of heterogeneous vegetation. GeoSAIL (Huemmerich 2001) and INFORM (Atzberger 2000) models extend the SAIL RTM, modeling tree crowns as geometric primitives and considering the scene as fractions of sunlit vegetation, shadowed vegetation, sunlit soil, and shadowed soil. Ray tracing RTMs allow more detailed structures of the vegetation. On the one hand, discrete ordinates methods, such as DART-FT (Gastellu-Etchegorry et al. 1996)

can admit a high level of detail within the scene, but details need to be in line with the assumptions of the discrete ordinates. On the other hand, Monte Carlo methods can be more flexible. Strong assumptions are embedded in the FLIGHT (North 1996) canopy RTM. But other Monte Carlo methods, such as DART-Lux (Wang et al. 2022) and Raytran (Govaerts and Verstraete 1998), and particularly most recent ones from the computer graphics field, can handle any form of the heterogeneous canopy and arbitrarily complex scenes.

The RAMI (RAdiation transfer Model Intercomparison) initiative was set up in the early 2000s to identify, intercompare and benchmark existing canopy RTMs. For the intercomparison, canopy RTM's outputs are derived from equivalent inputs and are compared. Four phases of the RAMI exercise have been held since the early 2000s (Pinty et al. 2001; Pinty et al. 2004; Widlowski et al. 2007; Widlowski et al. 2013; Widlowski et al. 2015). RAMI-III experiments (Widlowski et al. 2007) evidenced that six RTMs (DART-FT (Gastellu-Etchegorry et al. 1996), drat (Lewis and Disney 2007), FLIGHT (North 1996), Rayspead (Widlowski et al. 2006) and raytran (Govaerts and Verstraete 1998), Sprint3 (Thompson and Goel 1998)) showed good agreement simulating the optical properties of abstract vegetation canopies (homogeneous or geometric primitives). RAMI-IV (Widlowski et al. 2013; Widlowski et al. 2015) improved the vegetation canopy representation toward facet-based description of stems, branches and leaves. However, due to the lack of consistency between RTMs' ability to model vegetation with such details, RAMI-IV did not provide a benchmark result such as RAMI-III.

Considering all the canopy-scale RTMs, two of them have been selected for further study in this thesis. On the one hand, SAIL has been selected for its simplicity to use and its popularity in the remote sensing research community (Berger et al. 2018; Jacquemoud et al. 2009). On the other hand, the DART-Lux model was selected for its flexibility and ability to model accurately heterogeneous vegetation canopies with a wide range of details (Wang et al. 2022). Details on the SAIL and the DART-Lux RTMs are provided in the two following sections.

1.1.2.2 The SAIL model

The SAIL model was initially developed in the mid 1980s (Verhoef 1984) updated with several versions. The last version, named 4SAIL (Verhoef et al. 2007), implements an extended four-flux theory for both the optical and thermal domain.

SAIL has usually been combined with the leaf-scale PROSPECT model. The combination of PROSPECT and SAIL is usually denominated as PROSAIL in the literature. The PROSAIL combination has been used either to solve the forward problem to design vegetation indices or to solve the inverse problem for leaf and canopy traits estimation (Jacquemoud et al. 2009; Berger et al. 2018). Its popularity in the field of remote sensing research is due to its relative simplicity and accuracy.

1.1.2.3 DART

The first version of DART (Discrete Anisotropic Radiative Transfer) was released in the mid 1990s (Gastellu-Etchegorry et al. 1996). Initially the DART RTM only implemented a discrete ordinates method. This version is called DART-FT (for Flux Tracking). In DART-FT, a scene is a 3D matrix of parallel-piped cells (voxels) containing the landscape components (*e.g.*, leaves, trunks, branches, water, soil, atmosphere) characterized by their optical properties (scattering phase functions, and structural parameters).

More recently a new version of DART, called DART-Lux, was released and implements the LuxCoreRender open-source rendering software (Wang et al. 2022). LuxCoreRender is a physically-based rendering software based on Monte-Carlo ray-tracing program (Pharr et al. 2023; *LuxCoreRender – Open Source Physically Based Renderer n.d.*). In DART-Lux, a scene is composed of 3D objects defined by vertices or triangle meshes.

DART offers a high degree of flexibility when it comes to defining scene characteristics. The number of possible parameter combinations is almost infinite. As such, DART should be considered as a software rather than a simple RTM. Although, it is easily possible to define a RTM with clear parameters and a finite number of degrees of freedom from DART.

To fulfill the goals of this thesis, an heterogeneous RTM must be easily configurable regarding the density of crowns. This feature will be controlled by the canopy cover that is intrinsically linked to the stem/crown density. A forest canopy RTM called DART-SFR has been implemented

from DART software in this thesis. The development of the DART-SFR RTM is further presented in this chapter, in the next section (Section 1.2). In this thesis, the denomination “DART” will refer to the whole software while “DART-SFR” will refer to forest canopy RTM.

1.2 Simulation framework

This section focuses on the technical aspect to simulate canopy reflectance from the leaf traits in a controlled and parameterized environment. This step aims to describe how the leaf-scale and canopy-scale RTMs are combined in the simulation framework. The main challenge presented in this section is the definition of a controlled and configurable RTM from DART software: the DART-SFR model. The simulation framework also includes tools to interact with RTMs inputs and outputs. Tools related to inputs include the definition of experimental designs. Tools related to RTMs outputs enable simulation results to be processed and formatted into databases for supply to learning algorithms.

1.2.1 Overview of the simulation framework

The simulation chain to scale leaf traits to canopy reflectance encompasses two steps: the leaf-scale RTM and the canopy scale RTM. The leaf RTM is PROSPECT-D and the canopy RTM is SAIL or DART-SFR. The schematic representation of the simulation chain is given in Figure 1.2.

The PROSPECT-D model is implemented in an open source library, coded in the Python language (Domenzain et al. 2019).

The transfer of simulated leaf optical properties (PROSPECT outputs) as inputs of canopy RTMs are already implemented. Indeed, for the PROSPECT and SAIL combination, a full implementation of PROSAIL is provided in Python language (Domenzain et al. 2019). Regarding the PROSPECT and DART-SFR combination, DART includes implementation of the PROSPECT model and the transfer of leaf optical properties to scene parameters.

The simulation chain admits as input parameters those of the PROSPECT model (leaf traits and PROSPECT leaf structure parameter N), parameters to define the geometry at the canopy level (sun direction, canopy geometry) and other optical properties (soil reflectance) (Figure 1.2).

The selected RTM can include other parameters but these latter are fixed to specific values for the purpose of the study. Locked parameters include at the leaf level contents of anthocyanins and brown pigments because these compounds are considered to be in negligible concentration in the leaf of the species and ecosystems under study. At the canopy level, the view direction is set at nadir (View Zenith Angle VZA set to 0° , and View Azimuth Angle VAA is consequently undefined). For DART-SFR, the atmospheric properties are set to mid latitude summer model (with a visibility of 23 km and a rural aerosol model) (Figure 1.2).

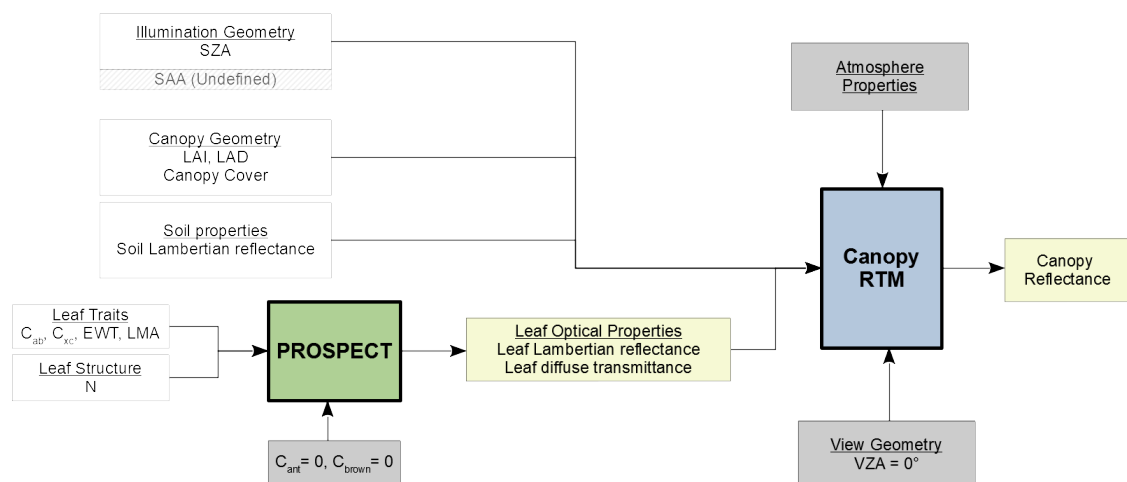


Figure 1.2: Schematic representation of the simulation chain from leaf traits to canopy reflectance. White boxes highlight the RTMs parameters. Gray boxes highlight the locked parameters.

1.2.2 The DART-SFR model

1.2.2.1 DART-SFR mock-up

DART software allows modeling Earth scenes, particularly forest scenes, with an infinite number of possible configurations. For the purpose of the study, the forest scene must be standardized, meaning that it needs to be easily configurable through an acceptable number of parameters. The construction of a configurable scene includes a simplification of the representation at both tree and stand scales.

It is important to notice that the intrinsic size of objects has no influence on the simulated output. Indeed, DART-Lux will compute the optical effect during ray tracing regardless of the objects sizes, therefore, the simulated output will remain the same for any homothety or homogeneous dilation of the scene. That is to say that the simulated reflectance will be the same with a scene of 10 m side length, its shrunk version of side 10 cm, or its enlarged version of size 1 km, as long as ratios between lengths of objects remain the same. Therefore in the following work, length values are given arbitrarily, what matters to reproduce the results is to preserve the ratios between all the lengths.

To model temperate forests canopies, a unique configurable geometry shape for every tree composing the forest has been selected. At the tree scale the tree crowns are simplified through geometric primitives. Here, tree crowns are simplified as composed ellipsoids, which provide realistic shapes and allow relative flexibility. Composed ellipsoids include two half ellipsoids: one for the bottom of the crown and one for the top of the crown. The shape of composed ellipsoids are configured by crown radius, crown height and crown factor as detailed in Figure 1.3. The positions of the composed ellipsoids are partially configured by the height below the crown (Figure 1.3). The full position and shape parameters are given as inputs of DART through a text file. At the tree scale, all the woody elements, which include branches and trunks are neglected to reduce modeling complexity. The crown is only composed as triangles representing the leaves. The orientation of each triangle is randomly sampled for an ellipsoidal leaf distribution.

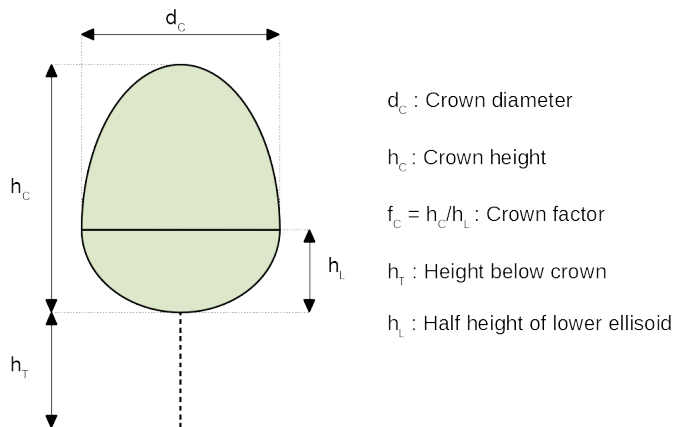


Figure 1.3: Parameters of the composed ellipsoid shape and position.

At the stand scale, it is required to define the density of crowns. All the crowns in the stand have the same shape and dimensions, consequently, it creates a one to one relationship between the crown density and the canopy cover. Thus, the crown density will be controlled by the canopy cover. Besides, the model forest stand should mimic properties of natural stands, meaning that the directional optical properties should be as close as possible from natural stands.

Considering these constraints, the Simplified Forest Representation (SFR) was proposed by [Gastellu-Etchegorry et al. 2003](#) and [Gascon et al. 2004](#) using DART. The SFR considers an elementary stand of four trees without any alignment (Figure 1.4) in a square scene. [Gastellu-Etchegorry et al. 2003](#) showed that this representation provides a Bidirectional Reflectance Factor (BRF) closer to a forest BRF compared to a single tree stand. The forest understory is neglected and the forest floor is represented as a Lambertian surface such as in the homogeneous canopy RTM.

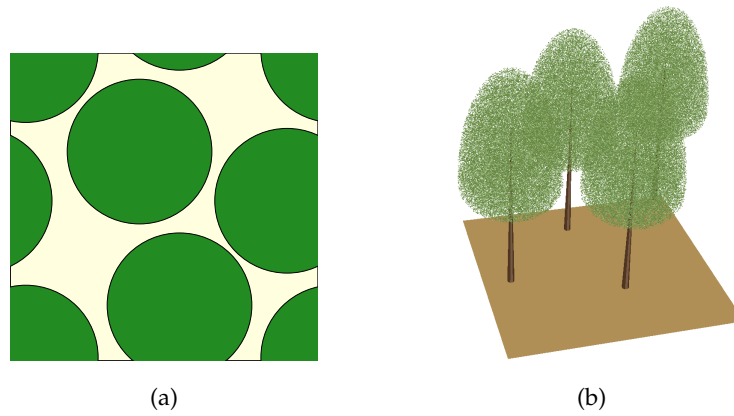


Figure 1.4: (a) Schematic representation of the SFR from a nadir point of view with tree crowns in green and soil in pale yellow ; (b) 3D mock-up of the SFR from DART.

The radius of tree crowns are set to a fixed value and therefore the canopy cover variation is obtained by varying the scene dimensions (Gascon et al. 2004). The x and y coordinates of crown centers are defined as a fraction of the scene side. The larger the scene, the further apart the trees will be and the canopy cover will decrease. Conversely, higher canopy covers are obtained reducing the scene size.

The analytical link between canopy cover and the scene dimensions cannot be found easily, but it can be approximated by computation. For the computation, the projection of the crowns on the (x,y) plane is considered, and the (x,y) plane is meshed with a grid of size 5 cm. The approximation of the canopy cover is given by the number of cells covered by the crowns over the total number of cells. The approximated function between the scene size and the canopy cover is given in Figure 1.5 for several values of tree crown diameter. The effect of the canopy cover variation on the bird-eye view of the SFR scene is schematically represented in Figure 1.6.

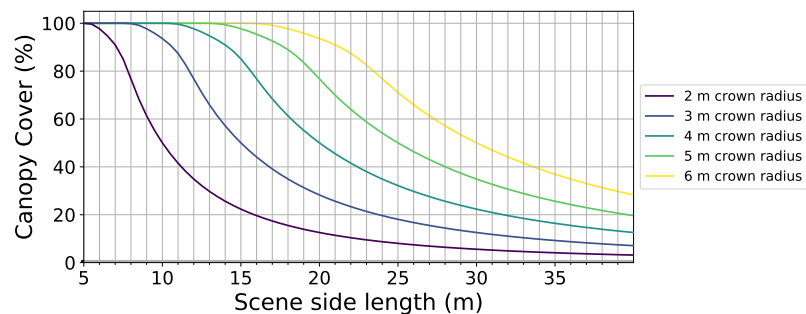


Figure 1.5: Correspondence between the canopy cover (in percent) and the size of the simulated square scene given by its side length (in meters) for several crown radius.

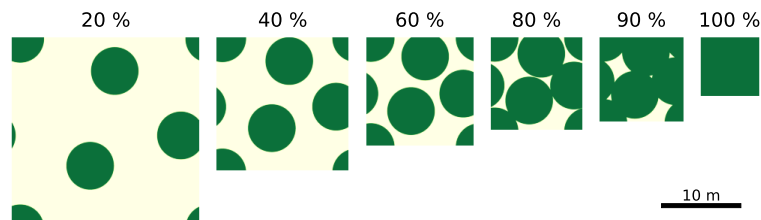


Figure 1.6: Effect on the size of the simulated scene on the canopy cover. Images represent the surface covered by tree crowns (in green) and soil (in pale yellow) from a nadir point of view. Numbers above the images give the canopy cover in percent.

As a result of the impossibility of analytically calculating the link between the scene dimension and the canopy cover CC , only discrete values of the canopy cover will be considered, even though

this parameter is a continuous variable. The step size for canopy cover variation is set to 1%. Thus, 91 text files were generated to define tree positions in mock up from 10% to 100% canopy cover.

1.2.2.2 DART rendering parameters

In addition to geometric and surface optical properties parameters, DART also involves parameters to render images. These parameters are linked to the ray-tracing process. Three main parameters control the image rendering and are under study, two of them are linked to the LuxCoreRender module included in the DART software (Wang et al. 2022):

- Target Ray Mean Density per Pixel is linked to the LuxCoreRender module, and corresponds to the number of photons drawn for each pixel. It is a mean value since the photon drawing is an adaptive process, meaning that more photons are drawn for pixels with a low return rate. The Target Ray Mean Density per Pixel depends on the pixel size, and to overcome this issue it can be converted as Ray Mean Density (d_R ; expressed in m^{-2}) through a simple division by the pixel area.
- The maximal scattering order ($Scat_{max}$; no units) is also linked to the LuxCoreRender module. It corresponds to the number of times each photon can interact with surfaces (reflected or transmitted). The larger the $Scat_{max}$, the more accurate is the rendered image. Conversely, a low $Scat_{max}$ could result in inaccurate modeling of the scattering from the vegetation.
- The number of repetitions of the scene (N_{rep} ; no units) is linked to DART and its way to solve the radiative transfer equations. It corresponds to the number of times a photon can cross the vertical boundaries of the scene. For small scenes, as the SFR scene, a photon is likely scattered towards the side of the scene and would be lost. Increasing N_{rep} partially solves this issue creating virtually a bigger scene which is the repetition of the input scene.

This section aims to assess the impact of these three parameters on the accuracy of simulated spectra with DART-SFR. The main goal is to find input values that yield an admissible error on DART-SFR spectra within an acceptable computation time.

For this study, the SFR scene is defined as in [Subsection 1.2.2.1](#), with parameters set arbitrary to the following values:

- Canopy Cover : 80 % (scene size: 11.75 m)
- Tree crowns as composed ellipsoids
- Crowns as triangle clouds
- Leaf optical properties : PROSPECT simulation ($N = 1.5$, $C_{ab} = 50 \mu\text{g} \cdot \text{cm}^{-2}$, $C_{xc} = 10 \mu\text{g} \cdot \text{cm}^{-2}$, $EWT = 0.012 \text{ cm}$, $LMA = 0.01 \text{ g} \cdot \text{cm}^{-2}$)
- Soil optical properties : lambertian property from DART database (dry grass)
- Sun direction : $\theta = 30^\circ$, $\phi = 225^\circ$ (DART default parameters).
- Pixel size: 0.25m

Target Ray Mean Density (d_R)

Firstly, the influence of d_R is assessed by simulating images with increasing values. The image rendering is based on random sampling (Monte-Carlo process) therefore the reflectances from two simulations with the same parameters may not be exactly the same. In order to take into account the Monte Carlo effects the images are rendered 10 times for the same d_R value. d_R values are sampled on a logarithmic scale from $1.5 \cdot 10^2 \text{ m}^{-2}$ to $3.0 \cdot 10^6 \text{ m}^{-2}$ with 4 points per decade. $Scat_{max}$ and N_{rep} parameters are set to the defaults values (respectively 25 and 1).

Reflectance of all pixels are averaged to obtain the whole image reflectance. Reflectance at three wavelengths are examined: 670 nm in the visible range, 950 nm in the NIR range, and 1520 nm in the SWIR range. Results are shown in [Figure 1.7](#). Additionally, the computation time is recorded for each rendered image. The influence of d_R on the computation time is depicted in [Figure 1.8](#).

The mean simulated reflectance varies little as d_R increases. The range of variation of the mean simulated reflectance is less than 0.001, which is under the accuracy of any instrument. As expected, the standard deviation of simulated reflectances decreases as d_R increases. The

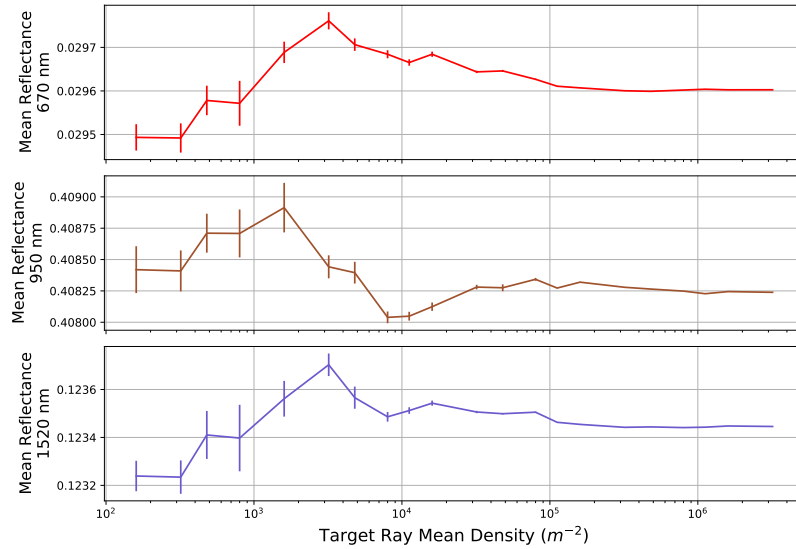


Figure 1.7: Average reflectance obtained from 10 rendered images at 3 wavelengths (670, 950 and 1520 nm). Error bars indicate the standard deviations of the reflectance for the 10 images.

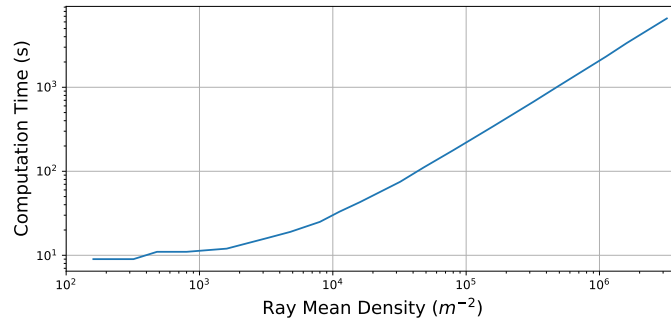


Figure 1.8: Average computation time as function of the Target Ray Mean Density.

mean reflectance converges toward a definite value for d_R values above $5 \cdot 10^4 \text{ m}^{-2}$ (the simulated reflectances are all in a 0.0001 range). d_R has a strong impact on the computation time. Indeed, the computation time increases linearly with Ray Mean Density. Although, for d_R values under $3 \cdot 10^3 \text{ m}^{-2}$, the computation time depends less on d_R and may depend more on other computations from DART. In conclusion, a d_R value of 10^4 m^{-2} seems a proper compromise to reduce the simulations variability and perform the rendering in a reasonable time.

Maximal scattering order ($Scat_{max}$) and number of repetitions of the scene (N_{rep}) The influence of $Scat_{max}$ and N_{rep} is assessed with a distinct experiment. $Scat_{max}$ (resp. N_{rep}) is increased step by step keeping all other parameters at fixed values. For each step, the spectra is compared to an “ideal” image. The ideal image was generated by setting the three parameters to the maximum values allowed in DART ($d_R = 4.0 \cdot 10^6 \text{ m}^{-2}$; $Scat_{max} = 6250$; $N_{rep} = 50$). All the images are generated with a 0.25 m pixel size. Additionally, the computation time is recorded for each rendered image. d_R is set to the default value ($d_R = 100 \text{ m}^{-2}$).

Spectra from simulated images are compared to the ideal spectrum using a MSE (Mean Squared Error). The evolution of the MSE and the computation time according to $Scat_{max}$ value is shown in Figure 1.9. In the same way, Figure 1.10 shows the results for the N_{rep} parameter.

Both $Scat_{max}$ and N_{rep} have little effect on the computation time (Figures 1.9 and 1.10). The computation time is increased approximately by 6 seconds for $Scat_{max}$ over 10^2 compared to the default value ($Scat_{max} = 20$). Higher N_{rep} values increase the computation time by less than 3 seconds compared to the default values ($N_{rep} = 1$). Considering that computation time is more affected by d_R , it is not a determining factor in setting $Scat_{max}$ and N_{rep} values. Observing the evolution of MSE and PSNR according to $Scat_{max}$ and N_{rep} , we can see that the error remains stable after the values $Scat_{max} = 250$ and $N_{rep} = 6$. This behavior is identical for the spectra of the whole scene and also for the three specific material patches.

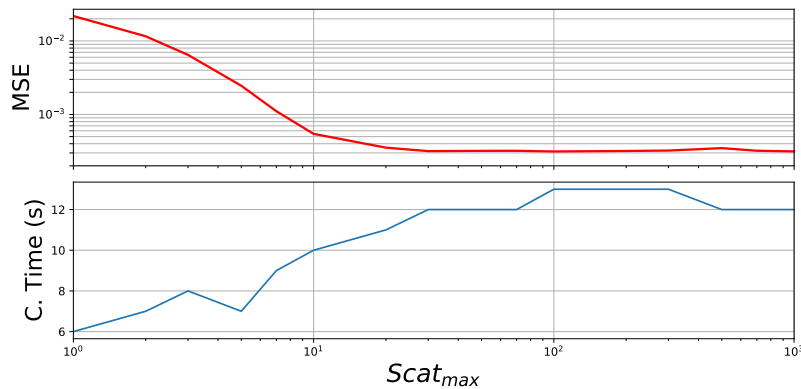


Figure 1.9: MSE (*top*) and computation time (*bottom*) as function of the Maximal Scattering Order ($Scat_{max}$)

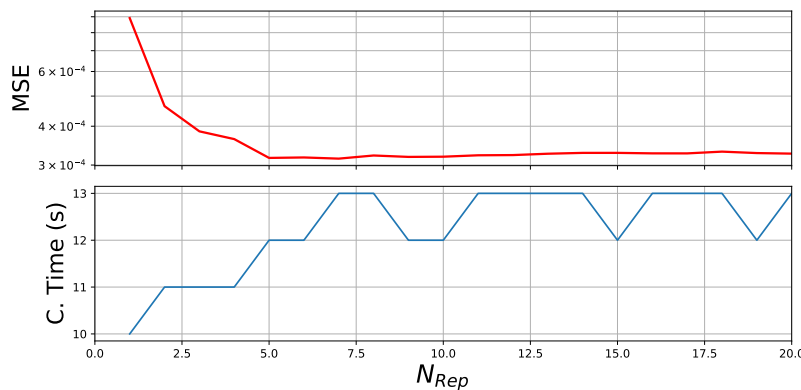


Figure 1.10: MSE (*top*) and computation time (*bottom*) as function of the Number of Repetition of the scene (N_{rep})

In conclusion, the values chosen for simulations with the DART-SFR model are $Scat_{max} = 250$ and $N_{rep} = 6$.

1.3 Sensitivity analyses and spectral signatures

Sensitivity studies were carried out on the selected RTMs: PROSPECT alone, SAIL and its combination with PROSPECT (named PROSAIL), DART-SFR and its combination with PROSPECT. Sensitivity analyses are performed to quantify the sources of variation in leaf optical properties or canopy reflectance. More broadly, sensitivity analyses of the model outputs is a key step for the verification and validation of the forward problem modeling, and provide the insurance that the computational model conforms to theory (Saltelli et al. 2004).

Particularly, sensitivity analyses allow checking the most sensitive spectral range for each parameter, and more specifically from leaf traits. Additionally, sensitivity analyses aim to measure the impact of ancillary parameters such as soil reflectance and foliage inclination on total reflectance, parameters which are not estimated and unknown in practice.

Various strategies have been developed to perform sensitivity analyses and therefore their full taxonomy is complex. However, they can be split into two categories: local methods and global methods. On the one hand, local methods analyze the response of model output by varying model parameters one at a time around a local neighborhood of their central values. The local methods have two main limitations: they vary parameters sequentially and therefore cannot highlight interactions between them ; they explore a small subset of the possible parameter values. Although, local methods provide rapidly easily interpretable results to apprehend the behavior of a model regarding its parameters.

On the other hand, global methods analyze the response of the model output averaged over variation of all parameters exploring a finite region. Global sensitivity analysis aims to overcome

the limitations of local methods and was developed in the late 1980s (Saltelli et al. 2004). Global sensitivity analysis techniques vary the parameters simultaneously in model runs. Therefore they can explore full ranges of the model parameters rather than a local area around a mean value, and analyze the interactions between parameters. Global sensitivity analysis techniques can be subdivided into finer categories according to the strategy used to explore the parameter space and to evaluate their impact on the output.

In this thesis, both a local method and a global method are performed to analyze the sensitivity of the RTM regarding their parameters. Firstly, a local method is performed to study the impact of some parameters: the impact of the PROSPECT parameters on leaf optical properties, the impact of the LAI on the canopy reflectance simulated by PROSAIL, and the impact of the canopy cover on the canopy reflectance simulated by PROSPECT+DART-SFR. Secondly, as a global method, variance-based sensitivity analyses from Sobol's sensitivity indices are performed with Saltelli's algorithm (Saltelli et al. 2010). The variance-based sensitivity analyses are computed thanks to the OpenTURNS python library (Baudin et al. 2017) through Saltelli's Sobol indices experiment. The analysis is performed with Sobol's total effects index for each parameter p ($S_{T,p}$), which measures the contribution to the output variance of p , including all variance caused by its interactions, of any order, with any other input variables. The sensitivity (\mathcal{S}_p) of a parameter p is expressed as the total-effect index for this parameter ($S_{T,p}$) over the sum of the the total-effect indices of all the parameters following equation 1.1 (below).

$$\mathcal{S}_p = \frac{S_{T,p}}{\sum_i S_{T,i}} \quad (1.1)$$

Sensitivities are first computed on the reflectance for each spectral band. In a second step, sensitivities are computed on CWTs (Continuous Wavelet Transform; Mallat 1999) of the reflectance to explore the links between leaf traits and the filtered response of reflectances. The CWT provides a time-scale representation (or more specifically here a wavelength-scale representation) of the signal. The CWT coefficients are computed through the convolution of the signal with the scaled and translated wavelet (scale and translation are further represented in the y-axis and x-axis, respectively). The wavelet used in this section is a Ricker wavelet.

In section 1.3.1 are presented the analyses at the leaf-scale of the PROSPECT model. Section 1.3.2 presents the result at the canopy scale, at first for SAIL and the PROSPECT+SAIL combination and in the second step for DART-SFR and the PROSPECT+DART-SFR combination.

The following distribution are used to perform the sensitivity analyses for each parameters : N: uniform distribution [1 – 2.6] ; C_{ab} : uniform distribution [0 – 120] ; C_{xc} : Chi square distribution ($\nu = 7.7$) ; EWT: Dirichlet distribution ($\theta = [6.3, 550]$) ; LMA ; Log-uniform distribution ($a = -5.5$, $b = -3.8$) ; LAI: uniform distribution [0.05 – 7] ; ALA: uniform distribution [0 – 90] ; CC: uniform distribution [0.1 – 1] ; SZA: uniform distribution [0 – 60] ; SAA: uniform distribution [0 – 360] ; Soil reflectance: normal distribution ($m = 0.18$, $\sigma^2 = 0.13$) truncated at 0 and 1 ; ρ_{leaf} : Beta distribution ($a = 0.57$, $b = 1.27$) ; τ_{leaf} : Beta distribution ($a = 0.64$, $b = 1.37$).

1.3.1 Leaf level sensitivity analyses

1.3.1.1 Local effects of PROSPECT parameters

The local sensitivity analysis, presented in Figure 1.11, illustrates the variations of leaf reflectance and transmittance due to PROSPECT parameters as a function of wavelength. Firstly, the increase in leaf traits induces an increase in absorption, which is characterized by an almost symmetrical decrease in leaf reflectance and transmittance (Figure 1.11 (a) to (d)). Absorption bands specific to each leaf trait can be observed.

C_{ab} alters leaf reflectance and transmittance mainly between 520 and 750 nm, with absorption peaking between 650 and 700 nm. For the absorption peak, there is a saturation effect, including for relatively low C_{ab} values (above $20 \mu\text{g} \cdot \text{cm}^{-2}$). The saturation effect masks C_{ab} variations in this band (650 – 700 nm), so, as Sims and Gamon 2002 point out, wavelengths outside this absorption peak would be used instead for C_{ab} retrieval. Outside the absorption peak, a shift of the red-edge towards longer wavelengths can be noticed as C_{ab} increases, as well as a change in the absorption minimum in green (530 – 570 nm), which increases and is shifted to shorter wavelengths.

C_{xc} affects leaf reflectance and transmittance mainly between 500 and 550 nm. Low C_{xc} is characterized by a minimal absorption around 530 nm. The absorption increases with C_{xc} and shifts the reflectance peak to the 550 nm wavelength.

EWT is characterized by absorption from 900 to 2500 nm, in which some wavelengths are marked by strong absorption peaks (1400 – 1500 nm, 1900 – 2000 nm, and beyond 2500 nm) and secondary absorption peaks (around 950 nm and 1200 nm).

Increasing LMA values induce higher absorption over the 750 – 2500 nm range but LMA does not clearly exhibit identifiable absorption peaks in Figure 1.11 (d). This parameter competes with EWT absorption, *i.e.* LMA absorption is only visible outside EWT absorption peaks. At last, the structure parameter N does not appear to influence leaf absorption, which is consistent with the PROSPECT underlying theory. Specifically, an increase in N seems to redirect the incident energy into reflectance at the expense of transmittance.

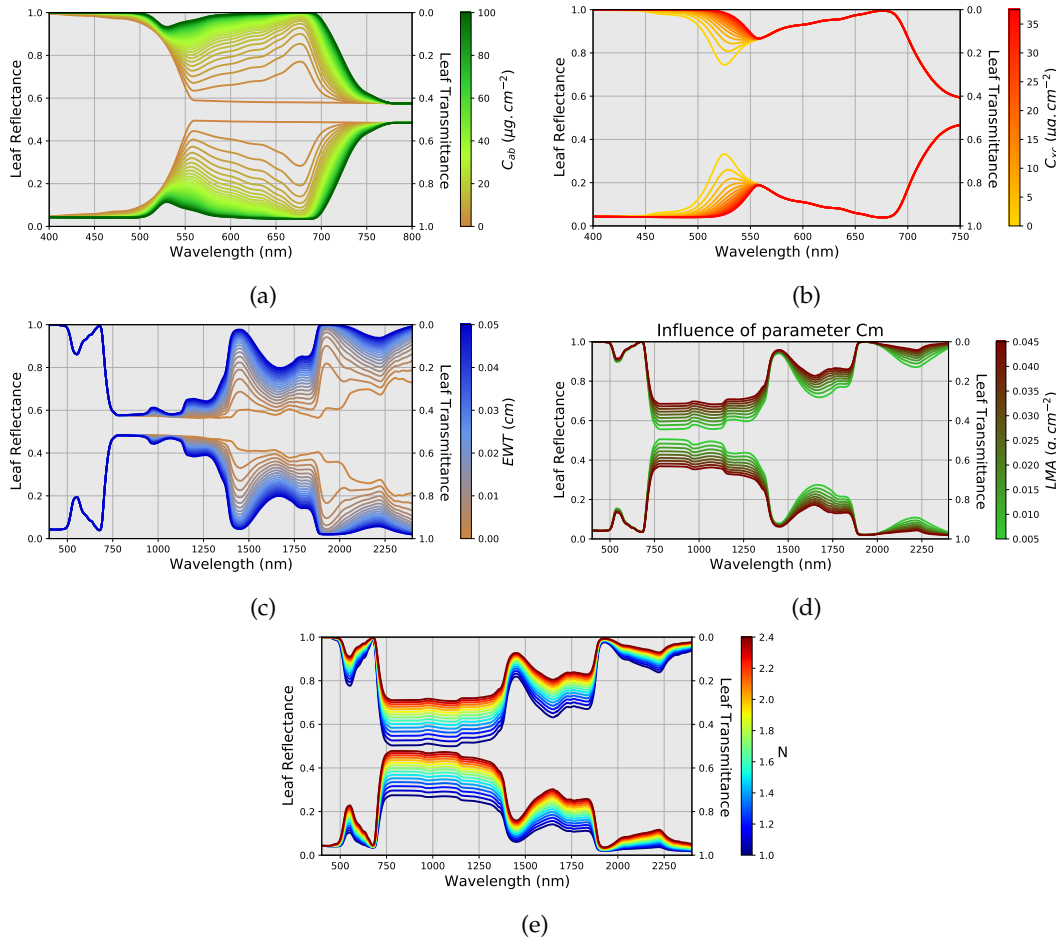


Figure 1.11: Simulated leaf reflectance (lower lines) and transmittance (upper lines) for different values of PROSPECT-D input parameters. Variations around a standard leaf composition defined by : $[N = 1.8; C_{ab} = 33 \mu\text{g} \cdot \text{cm}^{-2}; C_{xc} = 8.6 \mu\text{g} \cdot \text{cm}^{-2}; \text{EWT} = 0.0150\text{cm}; \text{LMA} = 0.0300 \text{g} \cdot \text{cm}^{-2}]$ are shown for: (a) C_{ab} ; (b) C_{xc} ; (c) EWT; (d) LMA; and (e) structure parameter N.

1.3.1.2 Global effects of PROSPECT parameters

For further analysis, a variance-based sensitivity analysis is performed on the PROSPECT model. The size of the experiments is set to 1000, leading to 7000 simulations. Sobol's Total-effect index is computed for each wavelength for both leaf reflectance and transmittance. The sensitivity, expressed as a percentage, for each PROSPECT parameter and for each wavelength is shown in Figure 1.12. Results of the variance-based sensitivity analysis are consistent with the results of the local analysis from section 1.3.1.1. However, it can be seen that C_{ab} also influences short wavelengths below 500 nm (around 40% of the total-effect Sobol indices). N has a significant influence between 750 nm and 1400 nm on reflectance and transmittance variances, with a sensitivity around 70%. EWT is the predominant factor in the SWIR range and followed by N. This indicates that LMA effects could be masked by EWT and N effects.

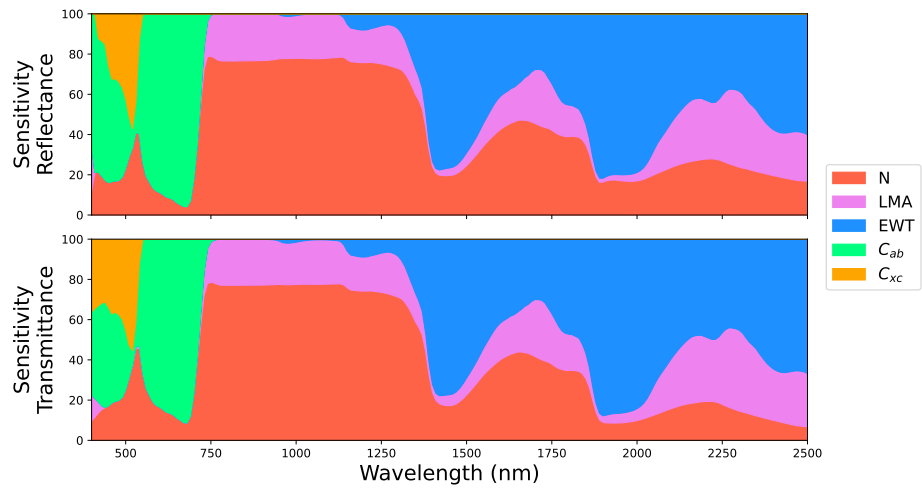


Figure 1.12: Sensitivity of PROSPECT simulated leaf reflectance and transmittance with respect to PROSPECT parameters.

Regarding the variance-based sensitivity analysis on the CWT of leaf reflectance, some CWT coefficients are sensitive to leaf traits, in particular for C_{ab} in the visible range and for EWT in the SWIR range (Sensitivity above 80%). For C_{xc} and LMA, sensitivity of CWT coefficients peaks at 70%. The separations between the effects of leaf traits are clearer than in the previous analysis. In fact, the analysis highlights that the influence of C_{ab} and C_{xc} on leaf reflectance are distinguishable for wavelengths below 550 nm. The same applies for EWT and LMA influence in the SWIR range. Characteristic signatures of leaf traits are noticeable for medium wavelet scales.

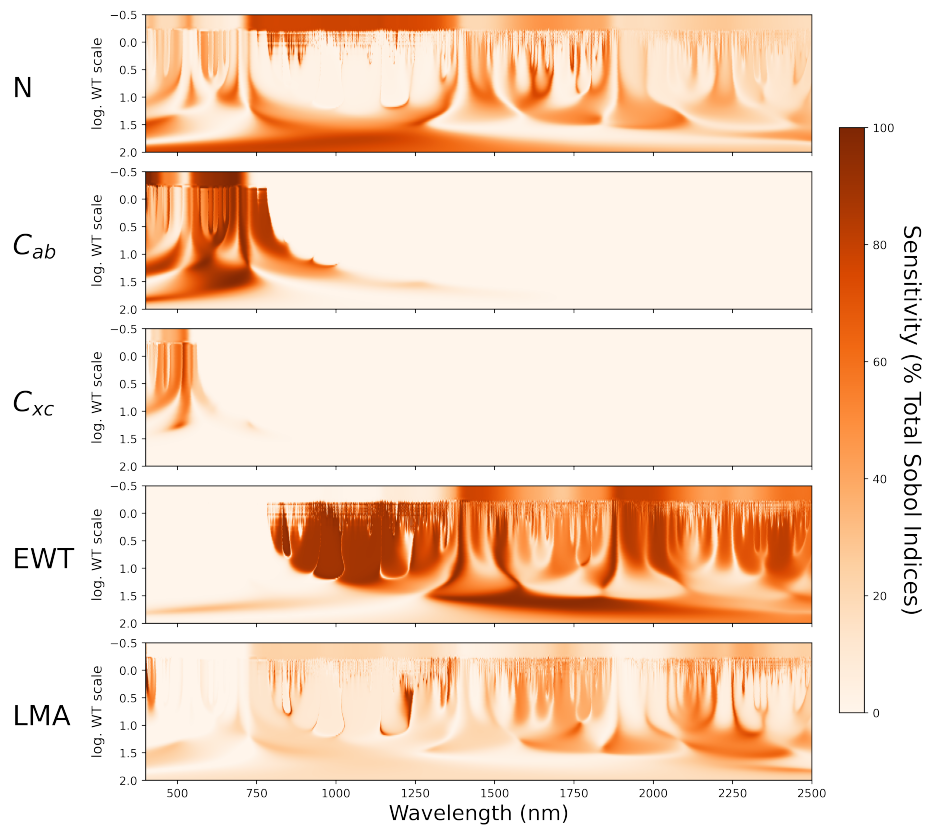


Figure 1.13: Sensitivity of CWT coefficients of PROSPECT simulated leaf reflectance with respect to PROSPECT parameters.

1.3.2 Canopy level sensitivity analyses

1.3.2.1 Local effects of canopy models parameters

At the canopy level, local sensitivity analyses are carried out to explore how leaf transmittance and reflectance, LAI and CC alter the top-of-canopy reflectance. This can be theoretically understandable because a large part of the light is directly reflected by the upper leaves and this stream of light is only subjected to leaf reflectance.

Figure 1.14 shows the effect of leaf transmittance and reflectance on canopy reflectance with SAIL (for a fixed LAI, ALA and soil reflectance). For equal variation, leaf reflectance alters more the canopy reflectance compared to the leaf transmittance.

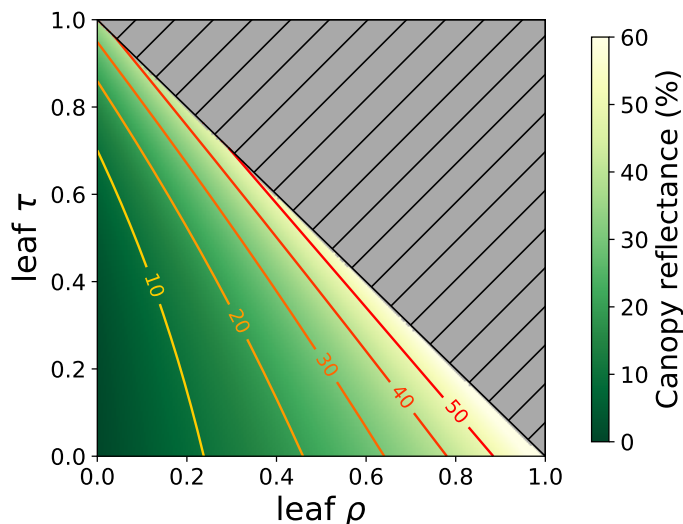


Figure 1.14: SAIL canopy reflectance as a function of leaf reflectance (ρ) and leaf transmittance (τ). Canopy reflectance is computed for a 0.3 soil reflectance, $SZA=30^\circ$, and a canopy structure defined by: $LAI = 3$ And $ALA = 45^\circ$.

Figure 1.15 shows the influence of LAI in the SAIL model for a constant ground reflectance for all wavelengths and equal to 0.2. Decreasing LAI brings canopy reflectance closer to ground reflectance. Examining the effect of LAI for some wavelengths, as LAI increases, canopy reflectance converges asymptotically towards the reflectance corresponding to infinite LAI.

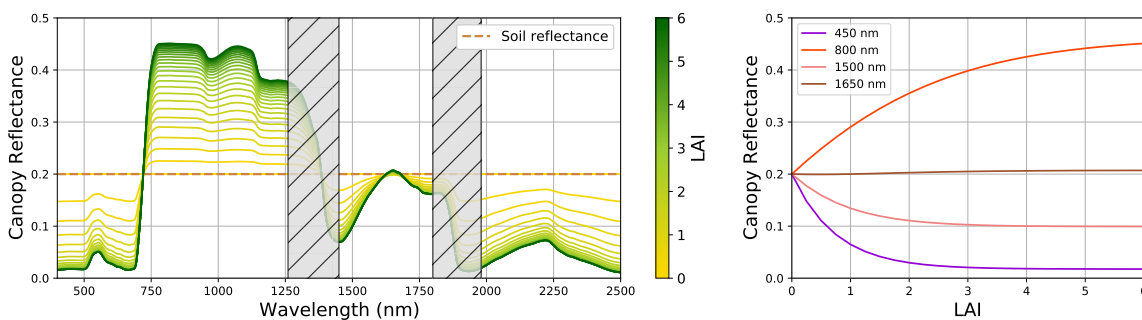


Figure 1.15: SAIL simulation of canopy reflectance for different values of LAI. Variations for a 0.2 soil reflectance, $SZA = 30^\circ$ and $ALA = 45^\circ$. Leaf optical properties are computed from PROSPECT with a standard leaf composition [$N = 1.8$; $C_{ab} = 33 \mu\text{g} \cdot \text{cm}^{-2}$; $C_{xc} = 8.6 \mu\text{g} \cdot \text{cm}^{-2}$; $EWT = 0.0150 \text{ cm}$; $LMA = 0.0300 \text{ g} \cdot \text{cm}^{-2}$]. (left) The canopy reflectances are drawn as function of wavelength. Hatched rectangles represent atmospheric absorption bands. (right) Canopy reflectance is given for some wavelengths as a function of LAI

Figure 1.16 shows the influence of the canopy cover in the DART-SFR model for a constant ground reflectance for all wavelengths and equal to 0.2. As CC decreases, the top-of-canopy reflectance converges toward the ground reflectance. For a CC of 100%, top-of-canopy reflectance matches the canopy reflectance simulated by SAIL, and the top-of-canopy reflectance simulated by DART for an homogeneous plot, both simulated the same parameters. The effect of CC seems

similar to the effects of LAI. However, the behavior of top-of-canopy reflectance is not always monotonic as the canopy cover increases (e.g., at 1650 nm ; Figure 1.16). This could be explained by the fact that as the CC increases, the evolution of sunlit and shaded fractions of the background do not evolve linearly (as shown in Figure 1.17). Particularly, as the CC increases, the scene reaches two tipping points: when the shaded fraction of soil starts to decrease and when the sunlit fraction of soil becomes null (Figure 1.17).

However, the effects of LAI and CC remain similar, and one could expect that a variation of the LAI could be compensated by variation of CC in the DART-SFR RTM.

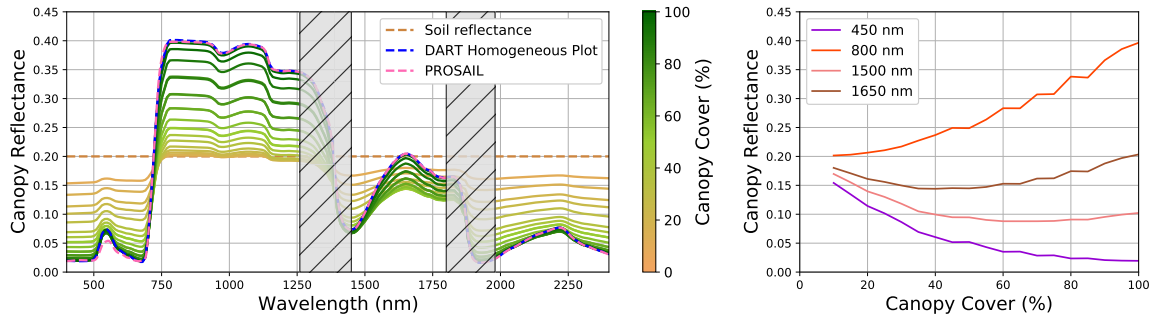


Figure 1.16: DART-SFR simulation of top-of-canopy reflectance for different values of canopy cover. Variations for a 0.2 soil reflectance, $SZA=30$, $SAA = 225^\circ$, $LAI = 3$ and $ALA = 45^\circ$. Leaf optical properties are computed from PROSPECT with a standard leaf composition [$N = 1.8$; $C_{ab} = 33 \mu\text{g} \cdot \text{cm}^{-2}$; $C_{xc} = 8.6 \mu\text{g} \cdot \text{cm}^{-2}$; $EWT = 0.0150 \text{ cm}$; $LMA = 0.0300 \text{ g} \cdot \text{cm}^{-2}$]. (left) The top-of-canopy reflectances are drawn as function of wavelength. Hatched rectangles represent atmospheric absorption bands. For reference, blue dashed line indicates the reflectance simulated from DART with an homogenous plot of vegetation and the pink dashed line indicates the reflectance simulated by PROSPECT+SAIL, both using the same parameters. (right) Canopy reflectance is given for some wavelengths as a function of Canopy Cover

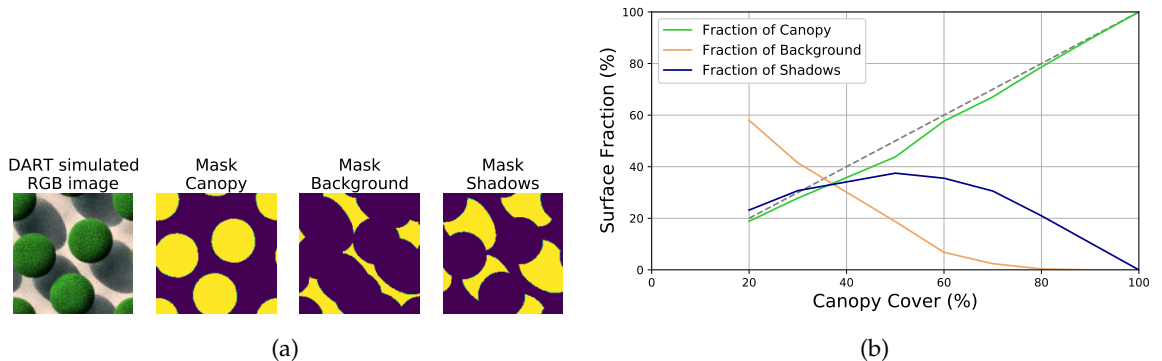


Figure 1.17: (a) Illustration of SFR scene segmentation between canopy, sunlit background and shaded background for a canopy cover of 50%; (b) Evolution of the fraction of each element in the scene as a function of canopy cover, for $SZA = 30^\circ$ and $SAA = 225^\circ$.

1.3.2.2 Global effects of canopy models parameters

The variance-based sensitivity analysis is performed at first on the SAIL model alone with a size of the experiments set to 50000, leading to 700000 simulations. The importance of each parameter is directly examined through Sobol's total effect indices. This analysis confirms the importance of leaf reflectance on canopy reflectance. This parameter is at least twice as important as the other parameters, and six times more important as leaf transmittance (Figure 1.18). The three other parameters that stand out are related to canopy structure (LAI and ALA) and soil reflectance. The illumination geometry (SZA) plays a minor role on the canopy reflectance in SAIL.

Considering the full PROSAIL model, PROSPECT parameters show less importance than canopy structure and soil reflectance. The variance-based sensitivity analysis is performed on the PROSAIL model with the size of the experiments set to 1000, leading to 11000 simulations. Soil reflectance explains around 20% of the variance of the canopy reflectance for all the wavelengths. Canopy structure parameters (LAI and ALA) have a strong impact on canopy reflectance

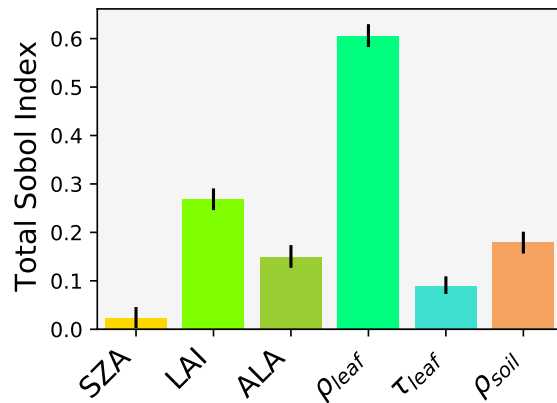


Figure 1.18: Sobol's total-effect indices for parameters of the SAIL model. Black lines indicate the 95% confidence intervals delivered by Saltelli's algorithm

along the whole optical domain (sensitivity around 60%). Regarding leaf traits, each of them explain no more than 20% of the variance of the canopy reflectance. Wavelengths where each leaf trait has the most impact are identical as the one found analyzing the PROSPECT model (section 1.3.1.2, Figure 1.12)

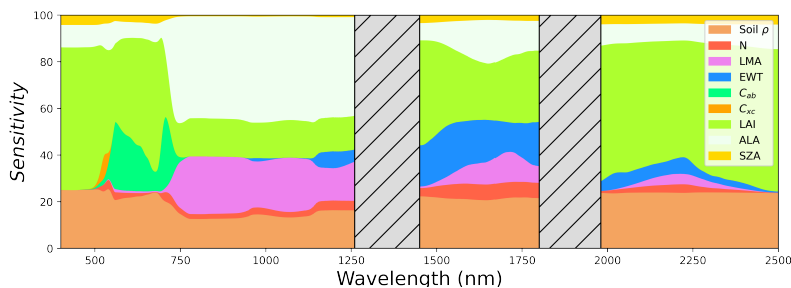


Figure 1.19: Sensitivity of PROSAIL simulated canopy reflectance with respect to all PROSAIL parameters. Hatched rectangles represent atmospheric absorption bands.

The sensitivity analysis is then performed on the CWT coefficients using the same parameters (Figure 1.20). The patterns are similar to the ones from the analysis at leaf level (section 1.3.1.2, Figure 1.13). However, the CWT coefficients are less sensitive with respect to leaf traits. The sensitivity peaks around 70% for C_{ab} and EWT, and 60% for C_{xc} and LMA.

The experiment performed on PROSAIL is now performed on the PROSPECT - DART-SFR model in order to compare the particular effects of homogenous and heterogenous canopies. The variance-based sensitivity analysis is performed on the PROSAIL model with the size of the experiments set to 1000, leading to 13000 simulations and the results are shown in Figure 1.21. With DART-SFR as a canopy model, the prevailing parameter with DART-SFR is the CC which explains at least 20% of the top of canopy variance in the NIR range and up to 40% in the visible and SWIR ranges. Compared to PROSAIL, the influence of LAI and ALA are decreased at the expense of the CC. The sensitivity of top-of-canopy reflectance for C_{ab} and LMA peaks around 20%, which is similar to the sensitivity from PROSAIL. The sensitivity decreases to 10% for EWT and to less than 5% for C_{xc} .

Examining the results of the sensitivity analysis on the CWT coefficients, the same trends as PROSAIL can be found (Figure 1.22). The sensitivity with respect to leaf traits is reduced compared to the leaf level to 60% for C_{ab} , EWT and LMA, and around 50% for C_{xc} . It is also essential to notice that the top-of-canopy reflectance with PROSPECT - DART-SFR is computed with a 10 nm spectral resolution, compared with 1 nm for PROSPECT and PROSAIL. Consequently, the finest spectral signatures are no longer, or less, visible.

1.3.3 Conclusions on sensitivity analysis

Analyses on CWT reveal spectral signatures that cannot be identified from top-of-canopy reflectance analysis alone. The CWT coefficients used to extract these spectral signatures are re-

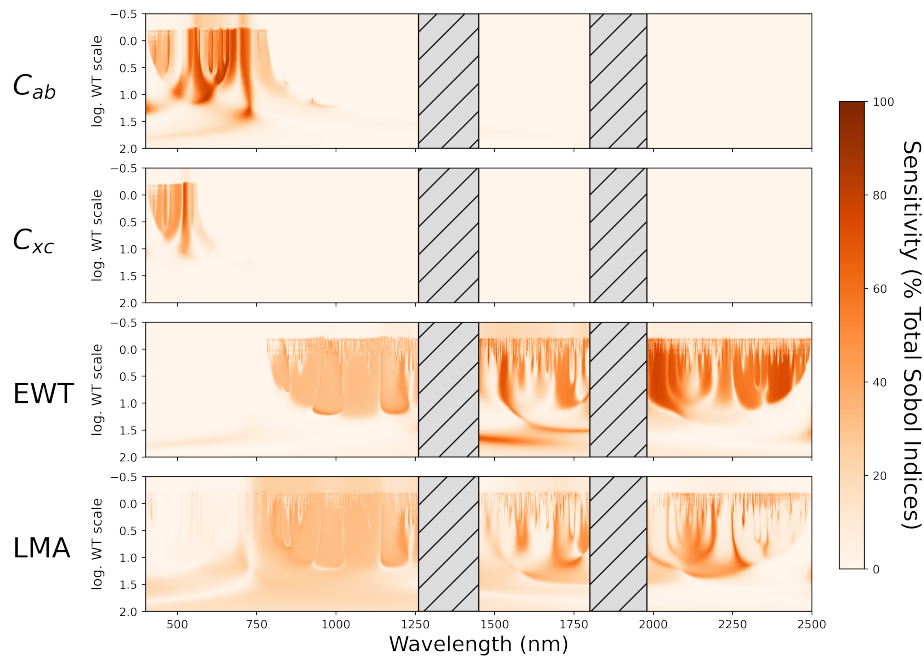


Figure 1.20: Sensitivity of CWT coefficients of PROSAIL simulated canopy reflectance with respect to leaf traits. Hatched rectangles represent atmospheric absorption bands.

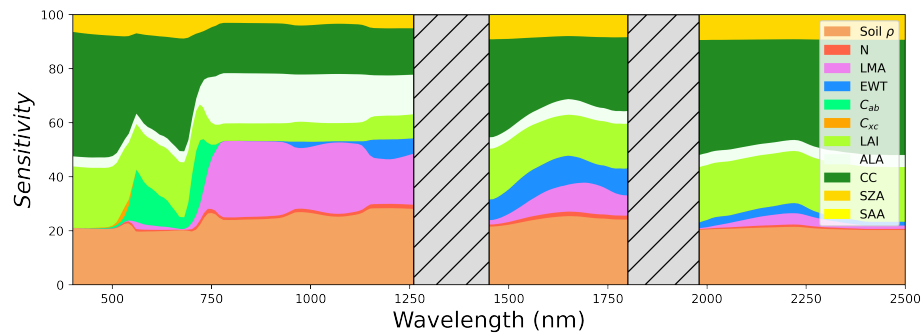


Figure 1.21: Sensitivity of PROSPECT - DART-SFR simulated canopy reflectance with respect to all PROSPECT - DART-SFR parameters. Hatched rectangles represent atmospheric absorption bands.

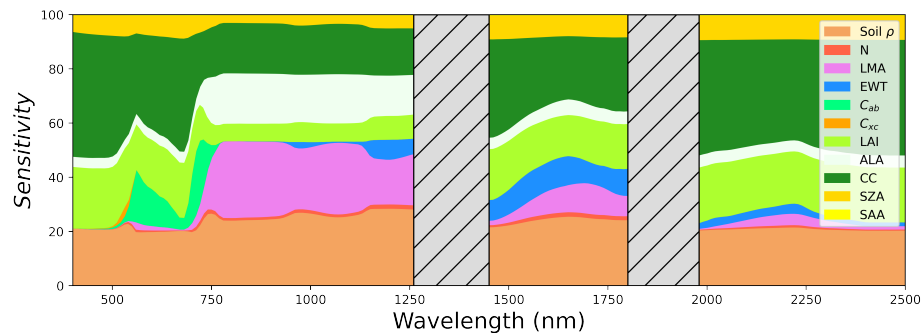


Figure 1.22: Sensitivity of CWT coefficients of PROSPECT - DART-SFR simulated top-of-canopy reflectance with respect to leaf traits. Hatched rectangles represent atmospheric absorption bands.

markably sensitive to leaf traits, even at canopy level. It can be explained by the fact that leaf traits rely on biochemical molecules that have wavelength specific absorption bands that influence the shape of the reflectance spectrum while all other parameters have wavelength independent influence on the entire optical domain. Here, the significant influence of leaf traits on CWT outputs evidence that a well-chosen filter, such as wavelet filters, applied to reflectance spectra may isolate the influence of a specific leaf trait. Moreover, the only a minority of scale and translation combination provide sensitive outputs, highlighting that a leaf-trait-sensitive representation of the

reflectance is sparse or reduce to few values (reduction of the dimension).

Conclusions

The work conducted in this first chapter on radiative transfer modeling led to an overview of existing models from the state-of-the-art. From this overview, a leaf-scale RTM as well as two canopy RTMs have been selected: PROSPECT, SAIL and the DART software. In a second step the selected RTMs were included in a simulation chain. The work on the simulation chain involved the selection of RTMs parameters, the formatting of inputs and outputs data. A major part of the development of the simulation chain was also dedicated to the building of the DART-SFR model from DART and its calibration to produce reliable simulations.

In a third step, RTMs were analyzed using the simulation chain. Sensitivity analyses carried out in this chapter emphasize specific spectral ranges for each leaf trait: 400 – 750 nm for C_{ab} ; 500 – 550 nm for C_{xc} ; 900 – 2500 nm for EWT; and 800 – 2500 nm for LMA. However, the influence of leaf traits on measurable optical properties is partially masked by ancillary parameters. This is particularly noticeable in top-of-canopy reflectance, where variations in vegetation structure have a greater impact than variations in vegetation traits. Additionally, the analyses on CWT of reflectances highlighted the spectral signature of leaf traits. The sensitivity analysis on DART-SFR reveals the importance of the canopy cover effect and the soil reflectance in heterogeneous canopies. An homogenous canopy model such as SAIL is not able to simulate these effects. As a consequence, to simulate heterogeneous temperate forest, DART-SFR will be selected in this work. The results obtained in this chapter would drive the decision for the estimation of leaf traits regardless of the chosen strategy. The building of the simulation chain will ease the development of RTM-based methods. The results from the sensitivity analyses guide the choice of MLRA toward algorithms able to identify the spectral signatures of leaf traits. Indeed, the experiment demonstrated that a proper MLRA, for inversion at the canopy level, should be able to build a representation of the hyperspectral signal robust to variations of the canopy geometry and illumination conditions. The use of CWT highlighted that convolution filters are able to extract sensitive features from reflectance spectra. In this frame, MLRAs that act as, or include convolution filters (such as CNN) are promising algorithms to estimate leaf traits from hyperspectral data.

Nevertheless, the selected RTM under their current status exhibit some limitations. Firstly, the limitation of the considered models is the simulation of mixed canopies, *i.e.* canopies with spatial variation in leaf traits or LAI. It is also often not possible to simulate species-specific properties, and complex details of the trees, such as branches usually are not taken into account. Particularly, conifers remain difficult to model faithfully due to the complexity of their shoots. Secondly, current RTMs provide a unique solution to a set of parameters, while in fact many natural landscapes can match these parameters and have distinct reflectances. Indeed, a finite set of parameters cannot describe completely any forest landscape, therefore RTMs may be required to provide, as outputs, probability distributions to account for the hidden parameters. The resolution of these limitations is out of the scope of this thesis, but it will be necessary to take them into account to analyze the estimation performances of the tested methods, and to provide new leads for future investigations.

Chapter 2

Methods

This chapter introduces the underlying methodologies for leaf traits estimation. It reviews the state-of-the-art of methodologies and underlying algorithms used to estimate leaf traits. Moreover, the chapter details the algorithms selected in this thesis to build estimation methods.

As presented in the [Introduction](#), the estimation of land physical parameters, and particularly estimation of leaf traits, through hyperspectral remote sensing are a case of inverse problem. The forward or direct problem is a case of radiative transfer and has been detailed in [Chapter 1](#). It can be expressed as:

$$Y = f(x, \theta) + n$$

where f is the function that models the radiative transfer; *i.e.* a RTM; Y is a set of observations, x is the set of parameters, θ is a set of controllable conditions, and n is an additive noise.

Meanwhile, estimation of leaf traits from hyperspectral data, *i.e.* the inverse problem, can be expressed as:

$$\hat{x} = g(Y, \omega)$$

where g is a function parametrized by weights ω , that approximate parameters \hat{x} from the set of observations Y .

A specific taxonomy of strategies to solve the inverse problem was developed and considers three classes: statistical, physical and hybrid ([Baret and Buis 2008](#); [Bioucas-Dias et al. 2013](#); [Verrelst et al. 2019](#)). All these strategies involve underlying algorithms and techniques from various domains including statistics, machine learning and data mining, optimization. The main step involved for each strategies is illustrated in [Figure 2.1](#).

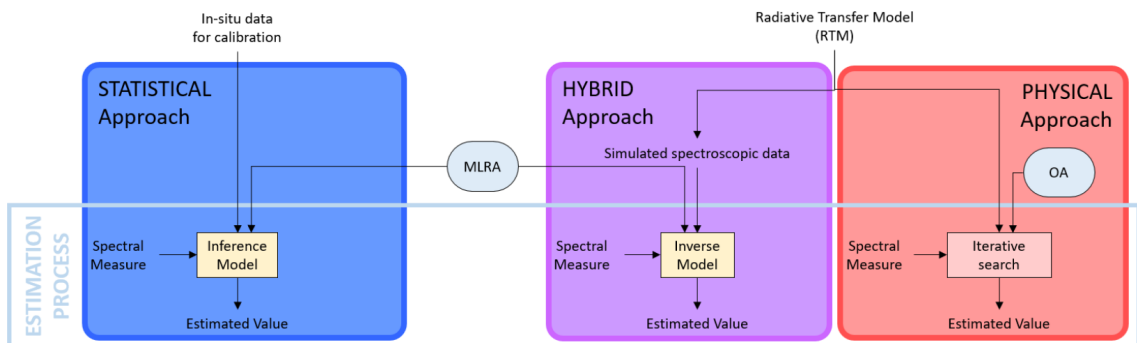


Figure 2.1: Global chart illustrating the main strategies for leaf traits estimation

Statistical strategies, also often called empirical strategies or data-driven methods in the literature, are based on the statistical learning of the inverse model, *i.e.* the function g . The learning phase is done with a set of observations with corresponding measured parameters, and often performed through MLRAs that can embed various degrees of complexity. Various MLRAs have been used in the literature to fulfill this goal. Training and validation steps of MLRAs involve techniques from machine learning.

Physical and hybrid strategies rely on the inversion of an RTM, and can therefore be described as RTM-based strategies. Physical strategies rely exclusively on RTM and search for parameters which provide the simulation result closest to the observation. These strategies therefore involve two elements: an algorithm to search for the proper parameter values, and a cost function to

measure the distance between an RTM simulation and the observation. Search strategies include iterative optimization, Markov Chain Monte Carlo (MCMC), and genetic algorithms.

Hybrid strategies combine aspects of both statistical and physical strategies and learn an inverse model, *i.e.* the function g , typically from an MLRA. The MLRA learns from a set of input-output data generated by forward RTM simulations and called a synthetic database. Consequently, hybrid strategies share the same issue with statistical strategies regarding training and validation of MLRAs. Additionally, they require sampling techniques to generate synthetic databases.

Statistical and hybrid strategies protocols provide estimators (or inference models) after the training phase of the MLRA, *i.e.* a computation rule, while physical strategies imply to repeat the process each time a new sample is presented (Figure 2.1).

To address all the aspects of the methodology for estimation of leaf traits and validation of estimation models this chapter is structured into three sections. Each section provides an overview of the state-of-the-art and a focus on the selected algorithms and methods for the development of estimation models in Chapter 4 and Chapter 5.

Firstly Section 2.1 presents the techniques related to RTM-based methods and focuses on optimization algorithms and sampling strategies.

Secondly, Section 2.2 provides an overview of the MLRAs used in statistical and hybrid strategies and details the selected MLRAs that will be used in Chapter 4 and Chapter 5. Following this, the section presents the techniques used to train and validate MLRAs.

Finally, Section 2.3 introduces the selected metrics to assess accuracy, validate and compare estimation models, and then provides a discussion on these metrics.

Look-Up-Table (LUT) based methods are complicated to categorize. While LUT-based methods have been categorized as hybrid methods since Bioucas-Dias et al. 2013, their behavior and protocol fall more into the domain of hybrid methods. Indeed, one could argue that LUT-based methods are equivalent to a hybrid method using a k-nearest neighbors (k-NN) regression algorithm (Hastie et al. 2009) for several reasons. As hybrid strategies, LUT-based strategy requires generating a synthetic database from a RTM (the LUT) gathering spectra $(X_i)_{i \in 1, \dots, N}$ and corresponding values of the target feature $(Y_i)_{i \in 1, \dots, N}$. LUT-based strategy and k-NN regression follow the same process of a local interpolation: for a sample x , the algorithm finds a predefined number k of training samples $(\tilde{x}_i)_{i \in 1, \dots, k}$ closest in distance to the new point x . The distance function is predefined and is often the euclidean distance. Then, the target feature value y is predicted from the $(\tilde{y}_i)_{i \in 1, \dots, k}$ features corresponding to the $(\tilde{x}_i)_{i \in 1, \dots, k}$ samples in the training database. The prediction is often performed by computing the mean of the $(\tilde{y}_i)_{i \in 1, \dots, k}$ set, but other aggregate functions could be used. Therefore in this chapter, the LUT-based strategy is presented in Section 2.2 as a k-NN regression algorithm to build a hybrid method.

2.1 Techniques for RTM-based strategies

2.1.1 Optimization methods for physical inversions

2.1.1.1 Optimization algorithms

Iterative optimization inversion is a classical technique to invert models. Given an observation s_{obs} the technique searches for the model inputs that provide the output s_{sim} the most similar as possible from s_{obs} . To do this, the technique consists in updating iteratively the values of the input variables of the model until the output s_{sim} closely fits the corresponding measurements s_{obs} (Baret and Buis 2008). The similarity, or the goodness of fit, between measured and simulated reflectance spectra is quantified by a cost function. In other words, the input variables are updated by an optimization algorithm to minimize the cost function. The algorithm stops when convergence is reached.

The iterative optimization inversion method requires numerous calls to the RTM function, and is therefore reserved for RTMs with a low computational cost. In the general case, RTMs are not differentiable functions, or at least their Jacobian matrix is not analytically calculable. Therefore the optimization algorithms are often from the family of the quasi-Newton methods because they avoid the computation of the Jacobian or Hessian matrices (for example Féret et al. 2011 and Féret et al. 2019). Additionally, optimization algorithms that admit constraints are preferred in order to limit input variables in their physically acceptable range. However, the exact algorithm used is not clearly identifiable for most of the studies. For example Spafford et al. 2021 and Wang et al. 2023 cited that they used functions from Matlab but these functions implement several algorithms as options. Consequently, the underlying optimization algorithm used remains unknown.

In [Chapter 4](#), the Powell’s algorithm ([Powell 1964](#)) implemented in the `scipy.optimize` python module is used.

2.1.1.2 Cost functions

Optimization algorithms require a cost function to minimize and that define the goodness of fit between the RTM output and the corresponding measurement. The cost function could depend on the type of measurements and the chosen RTM for inversion as the cost function may account explicitly for measurements and model uncertainties ([Baret and Buis 2008](#)). For vegetation RTM, and when no prior information is available, the cost function is usually defined as the Euclidean distance (defined by the L2 norm) between simulated spectrum R_{sim} and measured spectrum R_{meas} , but other functions have also been proposed ([Baret and Buis 2008](#)). The cost function defined by the Euclidean distance can also be weighted according to the wavelengths (with a weight W_λ ; [Féret et al. 2019](#)) and the general form of the cost function can be written following equation 2.1 for a measured reflectance R_{meas} .

$$C = \sum_{\lambda=\lambda_1}^{\lambda_n} W_\lambda (R_{sim,\lambda} - R_{meas,\lambda})^2 \quad (2.1)$$

2.1.2 Sampling methods

The building of hybrid methods requires the synthesis of a large number of simulations gathered in a synthetic dataset. Those simulations are obtained with various input values of the RTM parameters. The distribution of the input values is done through the sampling of the space of input variables. Several sampling schemes have already been tested and described in previous studies for RTM inversions ([Féret et al. 2011](#)). Two main sampling schemes are used in the quantitative remote sensing literature.

2.1.2.1 Random sampling

Values of the variables of interest can be sampled from a multidimensional probability distribution. This approach may take into account the dependencies between variables. For example [Féret et al. 2011](#) sampled PROSPECT parameters using a multivariate normal distribution to take into account covariance between leaf constituents.

Numerous numerical libraries are available to generate samples from probability distributions, but most of them only include standard probability distributions which are not bounded and could provide values in unrealistic ranges. Although, standard probability distributions can easily be truncated by drawing samples with the acceptance-rejection sampling method. More recently the `openturns` Python library has been released ([Baudin et al. 2017](#)) and enables generating samples for a wide variety of marginal and conditional distributions.

2.1.2.2 Latin Hypercube Sampling (LHS)

The Latin Hypercube Sampling (LHS) is a sampling method for multidimensional distributions but with independent input variables. The LHS applies a stratified sampling strategy enabling to better cover the domain of variations of the input variables with a limited number of simulations ([McKay et al. 1979](#); [Stein 1987](#)). For each variable, it is required to define a sampling probability distribution. The sampling procedure is based on dividing the range of each variable into several intervals of equal probability, thus, LHS maintains properties of marginal probability distribution for each variable. LHS has the advantage of requiring a much smaller sample number than simple random sampling to cover all the considered space of input variables.

LHS scheme can be built with `pyDOE` Python library or `openturns` Python library ([Baudin et al. 2017](#)).

2.2 Statistical learning techniques

For both statistical and hybrid strategies the resolution of the inverse problem, modeled by the approximation of the function g , is a supervised learning task. Indeed, both strategies attempt to learn g by examples, *i.e.* a set of observations gathering inputs and corresponding outputs of g . The learning algorithm predicts outputs for each input and modifies the input/output relationship in response to differences between original and predicted outputs; this process is

called the learning or training phase. Moreover, it is a regression task as the outputs of the approximated function are continuous variables rather than discrete variables (as in classification).

Numerous algorithms have been proposed in the realm of machine learning for regression. The use of several Machine Learning Regression Algorithms (MLRA) have been investigated for land parameter estimation in remote sensing.

2.2.1 Standard Machine Learning Regression Algorithms (MLRAs)

This thesis focuses on the comparison of four MLRA, namely Gaussian Process Regression (GPR), Partial Least Square Regression (PLSR), Random Forest Regression (RFR) and Ridge Regression (Ridge), in Chapter 4 and Chapter 5. The implementations of these MLRA used in Chapter 4 and Chapter 5 are the ones from the `scikit-learn` python library (Pedregosa et al. 2011).

Additionally, the LUT-based methods presented here as a k-NN regression algorithm, will be only used in Chapter 4.

2.2.1.1 k-Nearest Neighbors (k-NN) for regression

The k-Nearest Neighbors (k-NN) regression algorithm is a local interpolation method. To predict the target feature \hat{y} corresponding to a set of features x , this approach consists in: finding the k training samples $(\tilde{x}_i)_{i \in 1, \dots, k}$ closest from x according to a distance function; then predict the \hat{y} from the $(\tilde{y}_i)_{i \in 1, \dots, k}$ features corresponding to the $(\tilde{x}_i)_{i \in 1, \dots, k}$ samples in the training database using an aggregate function. The aggregation function is usually the statistical mean, but other aggregate functions could be used such as the median value. The distance function is usually the euclidean distance, which is equivalent to the mean square error. The euclidean distance between observed features and a sample of the training database is given by equation 2.2.

$$MSE = \frac{1}{n} \sum_{\lambda=\lambda_1}^{\lambda_n} (R_{simu,\lambda} - R_{meas,\lambda})^2 \quad (2.2)$$

Other distance functions can be used. For example the Spectral Angle Mapper (SAM) measures the collinearity and presents the advantage of not being sensitive to the intensity of the signals. The definition of SAM is linked to the dot product of two vectors such as described in equation 2.3.

$$SAM = \left[\frac{\sum_{\lambda=\lambda_1}^{\lambda_n} R_{simu,\lambda} R_{meas,\lambda}}{\sqrt{\sum_{\lambda=\lambda_1}^{\lambda_n} R_{simu,\lambda}^2} \sqrt{\sum_{\lambda=\lambda_1}^{\lambda_n} R_{meas,\lambda}^2}} \right] \quad (2.3)$$

2.2.1.2 Ridge regression

Ridge regression is a regularized ordinary least square linear regression. Ridge regression is a parametric model and finds a linear relationship between the input and the output. To address the overfitting issue, the cost function is regularized by the norm of the model weights as detailed in equation 2.4.

$$C = \|Y - w^T X\|_2^2 + \alpha \|w\|_2^2 \quad (2.4)$$

where α is the regularization hyperparameter and controls the amount of shrinkage for the model weights.

The proper value of α is a compromise between a model with no regularization ($\alpha = 0$) equivalent to an ordinary least square linear regression, and a too regularized model where the weights are zeros (value of α is too large). The value of the regularization hyperparameter α is usually determined with cross-validation.

2.2.1.3 Partial Least Square Regression (PLSR)

The Partial Least Square Regression (PLSR) is a linear parametric model (Wold et al. 2001). The PLSR algorithm is designed and well suited for problems where there is multicollinearity among the features, and thus, is widely used in chemometrics, particularly to quantify relationships between biochemicals and their spectral properties. The algorithm seeks to maximize the covariance between inputs and target values, projecting the inputs onto orthogonal components (also called latent vectors). Such as Ridge regression, PLSR is a form of regularized linear regression where

the strength of the regularization is controlled by the number of components. If too many components are kept, PLSR can overfit the training data. Thus, the number of components is determined with cross-validation.

2.2.1.4 Gaussian Process Regression (GPR)

Gaussian Process Regression (GPR) is a kernel-based machine learning algorithm (Rasmussen and Williams 2005). GPR is a Bayesian approach and is a non-parametric algorithm, meaning that it does not make any assumptions about the functional form of the underlying relationship between the input and output variables. With GPR, the approximation of the target function is built with a gaussian stationary process with a prior covariance specified by a kernel object. In the fitting process, the gaussian process is then constrained from training samples optimizing the kernel hyperparameters by maximizing the log-marginal-likelihood. In gaussian process regression, the kernel embeds prior information and should be selected according to the regression problem. Several types of kernels have been proposed, including some kernels that are more specific for certain types of data such as periodic kernels for problems with periodic signals. The most common kernel in GPR application is the Radial Basis Function (RBF) kernel defined for two data points x_i and x_j by the equation 2.5 and parameterized by a length scale $\gamma > 0$.

$$K_{RBF}(x_i, x_j) = \exp\left(-\frac{\|x_i - x_j\|_2^2}{2\gamma^2}\right) \quad (2.5)$$

2.2.1.5 Random Forest Regression (RFR)

Random Forest Regression (RFR) is an ensemble method derived from the decision tree algorithm (Breiman 2001). With RFR, a set of decision trees are built from a bootstrap sampling of the training data. The prediction of the ensemble is given as the averaged prediction of all the individual decision trees. This strategy injects randomness in the fitting process and leads to more robust predictions than decision trees.

2.2.2 Deep learning algorithms

Deep learning is a subset of machine learning specifically involving algorithms known as artificial neural networks (ANN). The name deep learning comes from the structure of ANN with successive layers of interconnected nodes (the artificial neurons) that extract increasingly abstract features from the data (Goodfellow et al. 2016). The first ANN architecture and quintessential example of deep learning is the multilayer perceptron (MLP), also known as feedforward deep network. The MLP consists of multiple layers of neurons, organized in a feedforward manner. Each neuron in one layer is connected to every neuron in the following layer, forming a directed graph without cycles. ANN can deal with complex issues creating highly nonlinear functions. Indeed, it has been formally demonstrated that neural networks are universal function approximators (Hornik et al. 1989), that is to say, a neural network can approximate any function, as long it is deep and expressive enough.

The training of a neural network is not very different from a standard machine learning algorithm. They use the same principle: during training the weights of a neural network are modified in order to minimize the prediction error defined by a cost function with a gradient descent (Goodfellow et al. 2016). In deep learning the cost function is usually named “loss”. The weights are updated by optimizers that compute new weights values with backpropagation of the gradient. The standard gradient descent is usually too computationally expensive considering the number of weights and number of samples, therefore the loss minimization is done through a stochastic gradient descent.

A convolutional neural network (CNN) is a type of deep learning algorithm composed of layers that perform convolution operations. CNNs were originally designed specifically for processing and analyzing visual data, with automatic features learning from images to classify them accurately (LeCun et al. 2010). CNN architectures can be modified and adapted for various tasks and domains by adjusting the number of layers, filter sizes, and other parameters to suit the specific requirements of the problem at hand. CNNs have demonstrated remarkable performance in various tasks in computer vision and image processing such as image classification, object detection, facial recognition, and image segmentation. More specifically, CNNs are increasingly being applied to remote sensing problems (Kattenborn et al. 2021).

CNNs consist of multiple layers, including convolutional layers and fully connected layers (Goodfellow et al. 2016). Convolutional layers apply convolution operations to the input data. Each layer consists in multiple filters (also called kernels) that scan across the input signal to perform a discrete convolution and produce a feature map. The convolution outputs are linear combinations of a portion of the input where the weights are the filter ones. The filter's weights are learned during the training process to extract meaningful features from the input data. Typically, multiple filters are used in each convolutional layer, allowing the network to learn different features at each layer. Convolution layers are usually followed by the activation function to introduce non-linearity and a pooling layer to reduce the dimensionality of the feature maps. Convolution layers are followed by fully connected layers that are similar to layers from traditional neural networks (MLP). Between the last pooling layer and the fully connected layers, the data are typically reshaped into a one-dimensional vector by a flattening layer.

CNN may cope with the non-linearity of the remotely sensed observed physical processes. Besides, 1D-CNNs could analyze the one-dimensional imaging spectroscopy signals, enabling processing the whole spectrum at the same time. However, CNNs have been little used in imaging spectroscopy analysis for land biophysical parameter estimation. Some studies can be found for soil analysis (Kawamura et al. 2021; Ng et al. 2019; Shen and Viscarra Rossel 2021), and many fewer studies can be found for vegetation analysis and they are all very recent (Cherif et al. 2023; Pullanagari et al. 2021; Shi et al. 2022; Annala et al. 2020).

2.2.3 Training and evaluation strategies

For both statistical and hybrid strategies, the model training and fitting processes remain the same. For MLRAs with hyperparameters, the optimal values of their respective hyperparameters are determined with a cross validation (CV).

The evaluation strategy differs for statistical and hybrid strategies, mainly due to the difference in the number of samples to train and test the models. Indeed, for hybrid methods, synthetic datasets can be arbitrarily large because increasing the dataset size only requires RTM simulations. It is consequently easy to get large datasets for both the train and test phase with synthetic data. In a hybrid strategy, the trained MLRA can be then tested on a dataset with actual measurements to assess its accuracy.

For statistical methods both train and test phases are done on actual measurements which are costly to obtain, and therefore a small size dataset. Thus, the results may be more sensitive to the train/test split of the dataset. Some can minimize the effect of small dataset in the results such as the repeated random sub-sampling validation (section 2.2.3.2).

Moreover, machine learning algorithms are developed for variables with similar ranges of variations. Therefore the preliminary step before training a MLRA is to scale the training features to lie in similar ranges of values. Here, two scalers are distinguished: the standard scaler and the min-max scaler. The standard scaler scales the data by removing the mean (centering) and dividing by the standard deviation. Scaled data have a null mean and a unit variance. The min-max scaler linearly scales the data such that the minimal and maximal values are 0 and 1.

2.2.3.1 k-fold cross validation for hyperparameter tuning

The hyperparameter tuning can be performed in a simple hold-out evaluation on the training set, but this strategy has two main disadvantages. The hold-out divides the dataset in three parts (train, validation and test), thus reducing the number of training and test samples. It may also provide an hyperparameter value too specific to the train subset leading to overfitting. The k-fold cross validation (CV) provides a solution to these disadvantages (Hastie et al. 2009).

In the k-fold cross validation, a test set should still be held out for final evaluation, but the validation set is no longer needed. The train dataset is split in a number k of subsets, known as folds. The same procedure is applied for each of the k folds: the model is fitted using the remaining $k - 1$ folds as training data and the resulting model is evaluated on the selected fold. Then, the k results for each fold can be averaged to produce a single performance measure. It is usually suggested to set $k = 5$ or $k = 10$ (Hastie et al. 2009).

The procedure can assess the performance of several hyperparameter values and find the best one (hyperparameter tuning). There are several underlying methods for hyperparameter tuning, including grid search and random search. Grid search is the simplest method for hyperparameter tuning. A grid of hyperparameter values is defined and the model is trained and evaluated for each combination of hyperparameters in the grid. The combination of hyperparameters that results in the best performance is selected as the optimal set of hyperparameters values. For the

Random search, the same procedure is followed except that the hyperparameters are randomly sampled from a specified distribution instead of defining a grid.

2.2.3.2 Repeated random sub-sampling validation

The hold-out evaluation or a single run of a k-fold cross-validation procedure may result in a noisy estimate of model performance. Indeed, different splits of the data may result in very different performance results.

To overcome this issue, the repeated random sub-sampling validation, also known as Monte Carlo cross-validation, creates repeated random splits of the dataset into train and test subsets in order to provide an expected error that is independent from the train/test split. The flow chart in Figure 2.2 depicts the main steps of this evaluation strategy.

For each repetition of random split, the model is fitted from the train subset, including the hyperparameters tuning through a k-fold CV (model selection). Then, the predictions (y_{pred}) are made from the features of the test subset (x_{test}) and compared to target values of the test subset (y_{test}). The comparison between y_{pred} and y_{test} provides the test error, this error is conditional on the train subset of this repetition. The process is repeated an arbitrary number of times (T), and the expected error is computed by averaging all the T conditional errors.

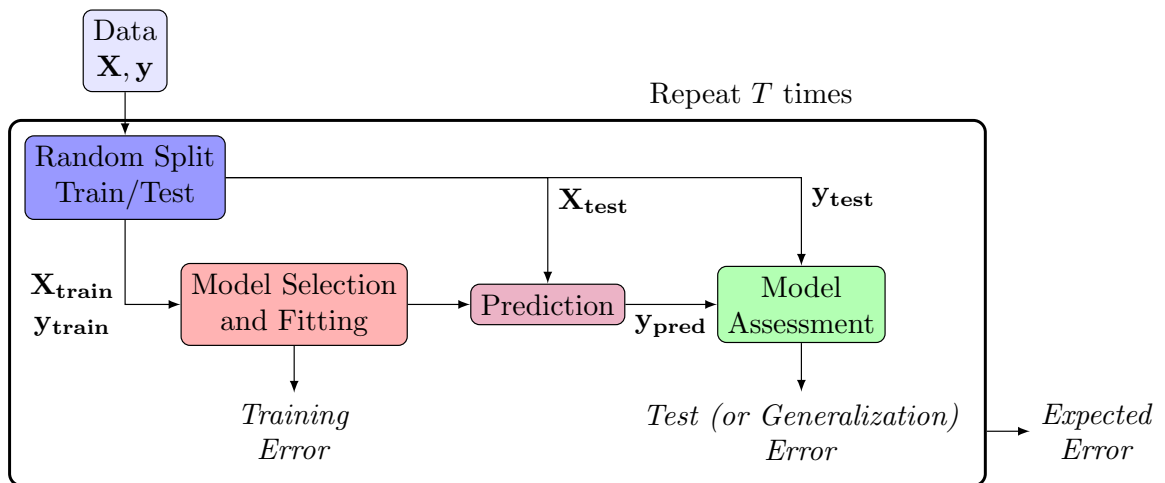


Figure 2.2: Flow chart of the repeated random subsampling validation.

2.3 Evaluation and validation of models

Evaluation is an essential step in the development of a model for biophysical parameter estimation in remote sensing. A review of the metrics used in the literature for validation of biophysical parameter estimation was published by Richter et al. 2012 and showed that a consequent number of metrics are used in the remote sensing literature. In this thesis, accuracy of estimation models are evaluated using mainly three metrics: the coefficient of determination (R^2), the root mean squared error (RMSE), and the bias (BIAS). Additionally, other metrics for the discussions are used: nRMSE, sRMSE, Kendall's Tau.

This section provides the definition of all the validation metrics used in this thesis.

2.3.1 Metrics for accuracy evaluation

Metrics for accuracy evaluation compare a set of measured values to the set of corresponding estimates. In this section, the vector of the measured values (also called reference values) will be denoted as $v = (v_1, v_2, \dots, v_N)^T$ and the vector of the estimates as $\hat{v} = (\hat{v}_1, \hat{v}_2, \dots, \hat{v}_N)^T$

2.3.1.1 Mean Squared Error (MSE) and derived metrics

The Mean Square Error (MSE), as its name suggests, is defined by the average of the squared errors following equation 2.6.

$$MSE(\hat{v}, v) = \frac{1}{N} \sum_{i=1}^N (\hat{v}_i - v_i)^2 \quad (2.6)$$

From the MSE are derived other metrics such as the Root Mean Square Error (RMSE) which is by definition the square root of the MSE (equation 2.7). The RMSE is the most frequently used metrics by far (Richter et al. 2012).

$$RMSE = \sqrt{MSE} \quad (2.7)$$

The RMSE has the advantage of being expressed in the same unit as the variable under study. From the RMSE, can be defined other metrics with no unit: the relative RMSE (rRMSE; equation 2.8) which is the RMSE divided by the mean of reference values m ; the standardized RMSE (sRMSE; equation 2.9) which is the RMSE divided by the standard deviation σ of reference values; the normalized RMSE (nRMSE; equation 2.10) which is the RMSE divided by the range of reference values.

$$rRMSE = \frac{RMSE}{m} \quad (2.8)$$

$$sRMSE = \frac{RMSE}{\sigma} \quad (2.9)$$

$$nRMSE = \frac{RMSE}{\max(v) - \min(v)} \quad (2.10)$$

2.3.1.2 Coefficient of determination

The coefficient of determination R^2 , is the second most frequently used metric (Richter et al. 2012) and is given following equation 2.11.

$$R^2(\hat{v}, v) = 1 - \frac{\sum_{i=1}^N (\hat{v}_i - v_i)^2}{\sum_{i=1}^N (\hat{v}_i - \bar{v})^2} \quad (2.11)$$

The coefficient of determination is also linked to the MSE reduced by the variance of reference data, and by definition to the sRMSE (equation 2.12). The coefficient of determination represents the proportion of variance explained by the independent variables in the model. R^2 is an indicator of the goodness of fit and therefore a measure of how well unseen samples are likely to be predicted by the model, through the proportion of explained variance.

$$R^2(\hat{v}, v) = 1 - \frac{MSE}{var(v)} \quad (2.12)$$

The best possible value for R^2 is 1, and it can be negative because the model can be arbitrarily worse. It is important to note that the coefficient of determination for estimation validation should not be confused with the coefficient of determination for linear regression which is the squared Pearson correlation coefficient, and only ranges between 0 and 1.

2.3.1.3 Bias

The bias indicates the difference between averages of reference values and estimates. It is also equivalent to the mean of errors and is computed following equation 2.13.

$$BIAS(\hat{v}, v) = \frac{1}{N} \sum_{i=1}^N (\hat{v}_i - v_i) \quad (2.13)$$

One should notice that the bias is not a commutative metric. Bias is in this thesis always computed with respect to reference values in order to get a negative value (respectively positive value) if the variable is underestimated (respectively overestimated).

2.3.1.4 Correlation coefficients

Correlation coefficients can indicate the match between reference values and estimates. They range between -1 and 1 , indicating a perfect correlation when its absolute is close to 1 , and no correlation when it is close to 0 . The most commonly known correlation coefficient is the Pearson's correlation coefficient r . But it only indicates linear correlation and conceals potential non-linear effects. Two main non-linear correlation coefficients have been introduced in statistics: Spearman's rank correlation coefficient (Spearman's ρ) and Kendall rank correlation coefficient (Kendall's τ). Both of them assess how well the relationship between two variables can be described using a monotonic function. Spearman's ρ is the usual Pearson correlation coefficient applied to the rank variables. Kendall's τ computation examines all the pairs $((v_i, \hat{v}_i); (v_j, \hat{v}_j))$ and checks their concordance, *i.e.* if either both $v_i > v_j$ and $\hat{v}_i > \hat{v}_j$ holds or both $v_i < v_j$ and $\hat{v}_i < \hat{v}_j$. Kendall's τ is computed from the number of concordant pairs and the number of discordant pairs following equation 2.14.

$$\tau(\hat{v}, v) = \frac{N_{\text{concordant pairs}} - N_{\text{discordant pairs}}}{\frac{1}{2}N(N-1)} \quad (2.14)$$

From Kendall's τ the fraction of concordant pairs f_c can be deduced: $f_c = \frac{\tau+1}{2}$

2.3.2 Discussions on evaluation and validation of models

The metrics for validation of models do not emphasize the same trends in the estimations. MSE and R^2 are both sensitive to the bias and variance of the errors (Figure 2.3 (a) to (e)). But without looking at a plot of estimated vs. reference values it is difficult to distinguish if the model shortcomings originate from a bias effect or a variance effect. By definition, the bias metric is only sensitive to the bias of estimates and expresses specific information about it. Correlation coefficients are altered by the variance of estimates errors (Figure 2.3 (a) to (c)), but the bias has almost no effect on them (Figure 2.3 (d) and (e)). Moreover, non-linear correlation coefficients highlight to what extent the estimates are ordered in the same sequence as the reference data. Estimation models that obtain low MSE but achieve non-linear correlation coefficient close to 1 can be corrected, such as in the case of saturation effect (Figure 2.3 (f))

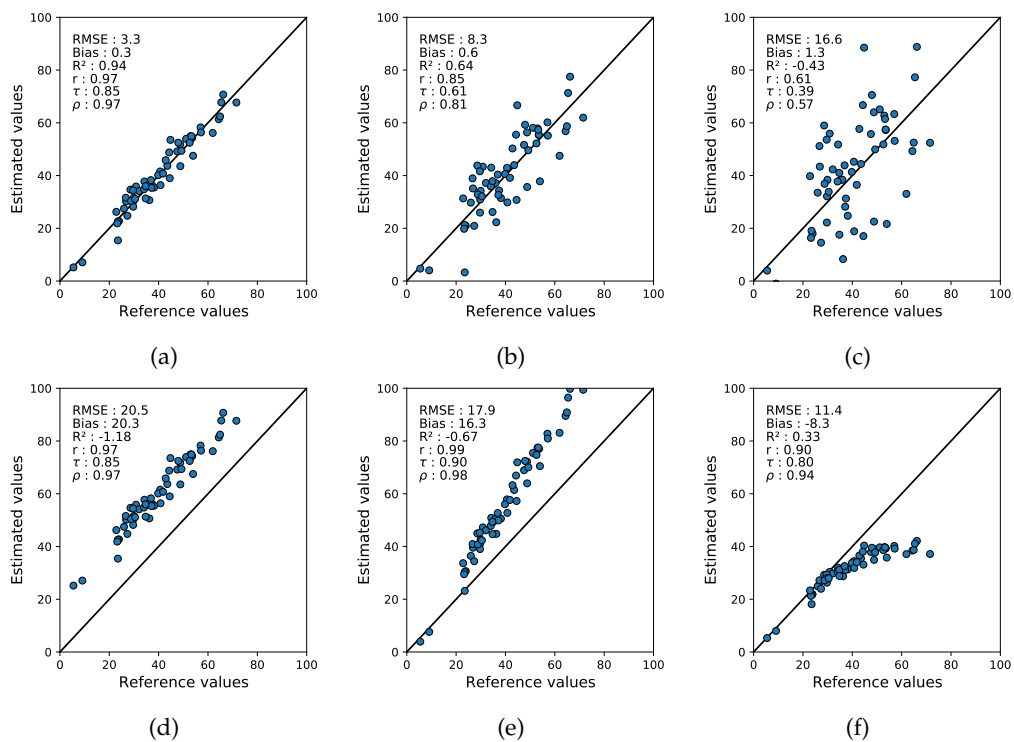


Figure 2.3: Illustration of the behavior of the validation metrics for possible estimation scenarios: (a) unbiased estimation with low variance; (b) unbiased estimation with medium variance; (c) unbiased estimation with high variance; (d) low variance estimation with additive bias; (e) low variance estimation with multiplicative bias; and (f) unbiased low variance estimation with saturation effect for higher values

Validation metrics can also highlight the gain of information that is provided by the optical measurements compared to the prior information contained only in the reference data. Typical values of the MSE and coefficient of determination R^2 can be derived for two scenarios where estimates are only derived using prior information from the basic statistics of the reference values.

Average guess. In the average guess assumption, all the estimates are set to the empirical mean of the reference data : $\forall i, \hat{v}_i = \bar{v}$. In this case, the MSE and R^2 can be computed easily : $MSE = var(v)$ and $R^2 = 0$.

Random normal guess. In the random normal guess assumption, all the estimates are drawn from a normal distribution $\hat{v}_i \stackrel{iid}{\sim} \mathcal{N}(\mu, \sigma^2)$ where $\mu = \bar{v}$ and $\sigma^2 = var(v)$ the empirical variance of reference values. In this case the expected value of the MSE is:

$$\mathbb{E}[MSE] = 2\sigma^2$$

The expected value of the coefficient of determination is $\mathbb{E}[R^2] = -1$

Thus, critical values of the coefficient of determination are $R^2 = -1$ and $R^2 = 0$.

Besides, the computed metrics contain in practice errors that are due to measurements of reference data (Figure 2.4). Indeed, while the estimation process intent to retrieve the actual value of leaf traits (blue arrow in Figure 2.4) it is not possible to directly access these values and the validation is performed on measured data, which contains errors that affect the evaluation metrics. Other sources of errors can be exhibited for hybrid methods specifically. The inverse model built for a hybrid method contains the approximation errors of the RTM, and could additionally lack adaptability to the measures reflectance that embedded the sensor noise.

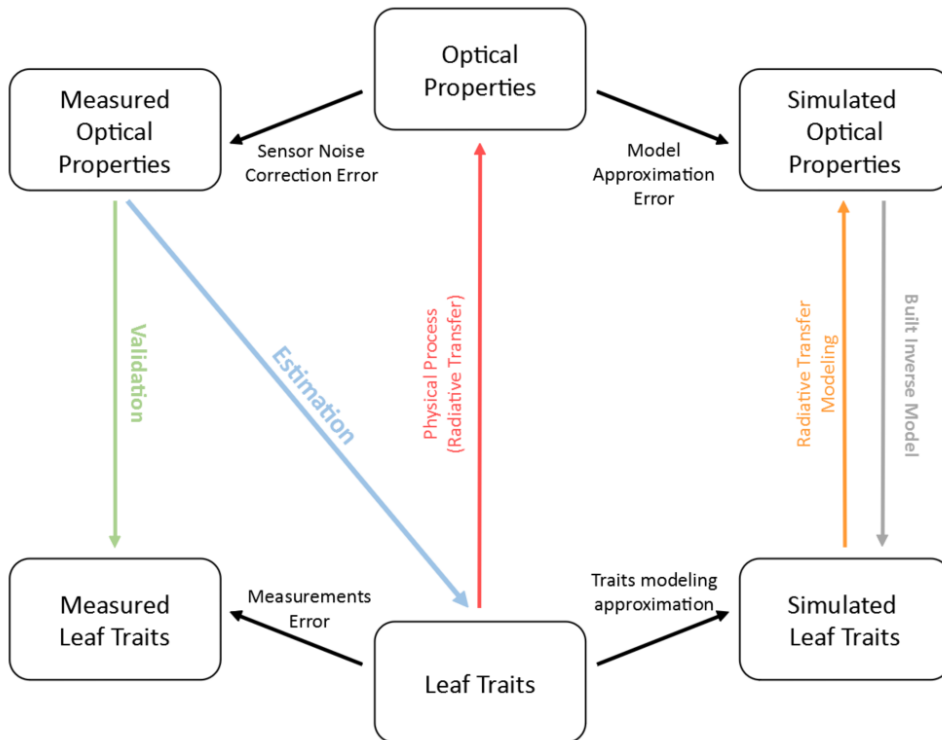


Figure 2.4: Diagram illustrating the sources of errors embedded in the estimation strategies and their validation process

Conclusion

In conclusion, the state-of-the-art provides algorithms and techniques from the fields of statistics, machine learning and optimization to define a protocol for building and validating an estimation model. From the state-of-the-art several algorithms and techniques are selected to perform estimation of leaf traits in this thesis. Optimization algorithms are selected to perform inversion of the PROSPECT model by iterative optimization inversion. Two protocols for the generation of data are selected to synthesize datasets from RTM for hybrid strategies (LHS as random sampling). Four MLRA are selected to build statistical and hybrid strategies, namely Ridge regression, PLSR, GPR, RFR. Additionally, techniques from machine learning have been presented to calibrate and evaluate the MLRA-based estimations.

Besides, another MLRA, the 1D-CNN, is introduced. The architecture of such models with convolution layers may extract specific features from the top-of-canopy reflectance that are sensitive to leaf traits as the CWT coefficients presented in [Chapter 1](#).

The estimation models that will be built from the fundamental components presented in this chapter will require data collected in situ in order to validate them. [Chapter 3](#) will propose data collected in situ in association with in-lab and hyperspectral measurements to validate the estimation protocols.

Chapter 3

Material

This chapter introduces all the measurements and data gathered and processed as reference data to evaluate the accuracy of estimation methods presented in [Chapter 2](#). In this chapter, the study area is introduced as well as the HypsIRI Preparation Mission context that enabled the acquisition of reference data in section 3.1. Then the study sites and species are described in greater detail in section 3.2. section 3.3 presents the protocols for measurements and processing of reference field data. section 3.4 presents the acquisition and processing of airborne hyperspectral images. A statistical analysis of the reference data is provided in section 3.5.

3.1 The case study

3.1.1 California geography and ecosystems

California is an eco-climatic region with a Mediterranean climate. It offers a diversity of micro-climates due to its complex topography and its location between the Pacific Ocean and the Great Basin of the United States, with a mountainous region and semi-arid high plateaus. In botanical geography, California constitutes a floristic region whose eastern part is formed by the Sierra Nevada mountain range covered by vast forests. The California floristic province is part of the Mediterranean biome, characterized by a temperate climate with long, dry and hot summers and mild, wet winters with precipitation occurring mainly from October to May. Moreover, it constitutes an area of major interest in terms of global biodiversity since it is part of the 25 regions defined by Norman Myers as "Biodiversity hotspots" ([Myers et al. 2000](#)). The California floristic province biodiversity hotspot covers a major part of the state of California, the south-west part of Oregon and north-west part of Baja California in Mexico. It spans from west to east including the Pacific coastline, the California coastal mountain ranges, the California central valley and the Sierra Nevada mountains up to the ridge line. From north to south, the hotspot stretches from the Klamath Mountains and the southern Cascade Range to the Sierra de Juarez in Baja California ([Figure 3.1](#)).

The WWF (World Wide Fund for Nature) identifies several ecoregions in the California Floristic Province including the California Interior Chaparral and Woodlands and the Sierra Nevada Forests ([Olson et al. 2001](#); [WWF 2023b](#)). The California Interior Chaparral and Woodlands ecoregion surrounds California's Central Valley and includes the foothills of the Sierra Nevada Forests ecoregion in the east. The Sierra Nevada Forests ecoregion lies between the California Interior Chaparral and Woodlands ecoregion to the west and the Great Basin Shrub Steppe ecoregion to the east. The Sierra Nevada runs 640 km from north to south and 100 km east to west. The mountains increase gradually in height from north to south, peaking at Mount Whitney at 4,421 m elevation above sea level.

The Sierra Nevada and its foothills exhibit a substantial elevation gradient that induces a high diversity of climates and vegetation types in the area. The western slopes of the Sierra Nevada, including its foothills, are heavily influenced by the Mediterranean climate of California. Precipitation occurs mostly from fall through spring and ranges from 510 to 2,030 mm and winters are relatively mild. On the western slopes, the annual rainfall spatial distribution mirrors the elevation gradient: roughly, the climate is wetter as the elevation increases. Precipitation peaks between 1,500 and 2,400 m elevation and diminishes upslope toward the ridgeline on the east.

The gradients of elevation and climatic conditions create a succession of various ecosystems and vegetation types. The multiplicity of ecosystems present in this relatively small area also increases the number of ecotones, reinforcing the region's high biodiversity. On the foothills of the Sierra Nevada, oak woodland and chaparral are the most widespread and characteristic natural communities as part of the California Interior Chaparral and Woodlands ecoregion. Valleys are dominated by foothill pine (*pinus sabiniana*), blue oak (*quercus douglasii*), and chaparral species, other distinctive oaks in this ecoregion are coast live oak (*quercus agrifolia*), canyon live oak (*quercus chrysolepis*), valley oak (*quercus lobata*), and interior live oak (*quercus wislizeni*) (Sawyer and Keeler-Wolf 1995; Earth 2023a). Above the foothills, a succession of vegetation zones can be observed, from montane through subalpine to alpine. The montane zone features ponderosa pine (*pinus ponderosa*) at lower elevations, along with California black oak (*quercus kelloggii*), incense cedar (*calocedrus decurrens*), and some other trees. Above this is a mixed-conifer forest with ponderosa pine, Jeffrey pine, Douglas-fir, white fir, sugar pine. Above the mixed-conifer forests, in the zone of deepest snow, are simpler forests dominated by white fir and then red fir. Above these forests is the subalpine zone with extensive stands of lodgepole pine with interspersed mountain meadows and montane chaparral. Jeffrey pine, western white pine, mountain juniper, whitebark pine, and quaking aspen also occupy this zone. Mountain hemlock, whitebark pine, foxtail pine, and limber pine occur at the upper limit of the subalpine zone. Above timberline, the alpine zone contains alpine meadows, talus slopes, and rocky outcrops. (Arno 1973; North et al. 2016; Sawyer and Keeler-Wolf 1995; WWF 2023a; Earth 2023b)

The Californian Sierra Nevada is home to a large number of monitored and/or protected forest sites. Indeed, about 52% of the land in the Sierra Nevada Mountains is owned by the US government through the National Park Service, the US Forest Service and the Bureau of Land Management. The state of California owns about 27 million acres in and surrounding the Sierra-Cascades mountain region in California. More particularly, a large number of forest sites are studied for scientific purposes and to understand forest ecosystems.

3.1.2 HypsIRI Preparation Mission

In preparation for the HypsIRI hyperspectral satellite mission (now replaced by the Surface Biology and Geology mission, often shorten to SBG), NASA has supported and carried out several annual hyperspectral airborne campaigns over California to demonstrate the important scientific applications research that is uniquely enabled by HypsIRI-like data sets. These campaigns involve the Airborne Visible/Infrared Imaging Spectrometer sensor (AVIRIS; Green et al. 1998).

AVIRIS is an instrument developed by NASA at the Jet Propulsion Laboratory (JPL). AVIRIS was flown on a NASA Lockheed ER-2 research aircraft over large diverse regions. The ER-2 research aircraft was flown at an altitude of around 20 km (Lee et al. 2015). Considering this altitude and the 1 milliradian instantaneous field of view of the sensor, AVIRIS provides images with a ground resolution around 14m for the HypsIRI Airborne Campaign. Data sets from AVIRIS purpose was to simulate measurements similar to the projected HypsIRI-VSWIR instrument and were collected at regular intervals to obtain seasonal coverage.

In the frame of this HypsIRI Airborne Campaign, regions overflown with AVIRIS were delimited in five boxes. Among them, two boxes included overflight of the Sierra Nevada and its foothills: Tahoe box and Yosemite box (Figure 3.1; Lee et al. 2015). This set of hyperspectral images constitutes a unique and unprecedented dataset in the field of hyperspectral remote sensing.

3.2 Description of Sites and Species

3.2.1 Study Sites

In this thesis, five sites are studied located on the west-side of the Sierra Nevada Mountains and its foothills: Tonzi Ranch (TONZ), San Joaquin Experimental Range (SJER), Blodgett Forest (BLOF), Soaproot Saddle (SOAP) and Teakettle experimental Range (TEAK). They are highly instrumented sites and belong to the Ameriflux network¹ (US-Ton, US-CZ1, US-Blo, US-xSP, US-CZ2, US-xTE, US-CZ4). Moreover, three of these sites belong to the National Ecological Observatory Network (NEON): SJER, SOAP and TEAK. These five sites are spread across latitudes varying between 37°

¹<https://ameriflux.lbl.gov/>

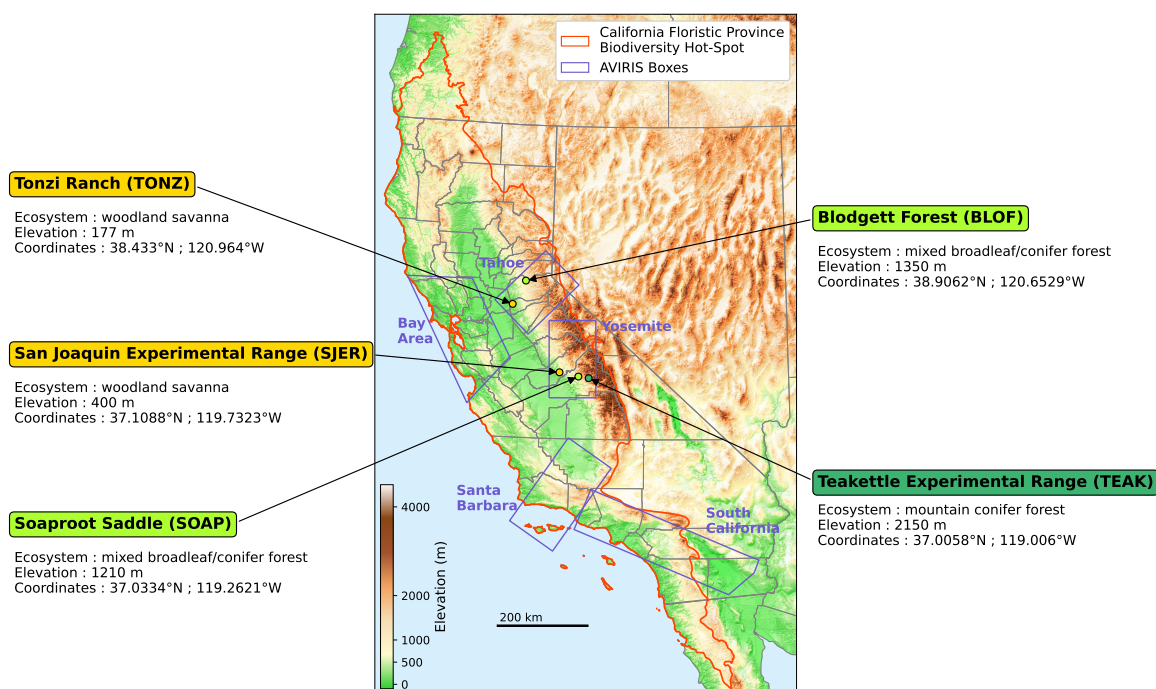


Figure 3.1: Topographic map of California with boundaries California floristic province and AVIRIS boxes, and location of study sites

and 39°, and the most distant sites are separated by about 250 km. They are also distributed along an elevation gradient, from lower to mid-elevations of the Sierra Nevada West slopes, with elevation ranging from 150 m to 2300 m above sea level (Figure 3.1). All these five study sites are included in the areas flown over by the AVIRIS instrument since 2013, as reference sites of the HypSIRI preparatory mission. TONZ and BLOF are located in the Tahoe box while SJER, SOAP and TEAK are located in the Yosemite box (Figure 3.1).

TONZ and SJER are the lower elevation sites located in the foothills of the Sierra Nevada and are part of the California Interior Chaparral and Woodlands ecoregion. TONZ and SJER mean annual temperature and precipitation are 15.8°C and 559 mm, 16.5°C and 485 mm, respectively (Ma et al. 2016), consistent with their more northern and southern locations in the Sierra Nevada range. TONZ and SJER are grass-oak-pine woodland savannas. Both TONZ and SJER experience cattle grazing. TONZ is privately owned land while SJER is state-owned land managed jointly by the California State University’s Agricultural Foundation and the U.S. Forest Service. The woodland savannas of TONZ and SJER are mainly composed of two vegetated active layers (excluding to first order the presence of occasional shrubs): an understory of annual grass species and an overstory dominated by two species, blue oaks (*Quercus douglasii*) and gray pines (*Pinus sabiniana*). For example, on TONZ, blue oaks account for about 40 % of the overstory, and gray pines are sparsely spread (3 trees/ha). For SJER, in addition to blue oaks, interior live oaks (*Quercus wislizeni*) are part of the canopy mix.

BLOF, SOAP and TEAK are located on the west slopes of the Sierra Nevada mountains and are part of the Sierra Nevada Forest ecoregion. BLOF and SOAP are mid-elevation sites and are located at the elevation limit between oak forest and Sierra mixed conifer forest.

BLOF is managed by UC Berkeley from the Blodgett Forest Research Station to improve the understanding and management of commercial forest types. On BLOF, temperature ranges from 0°C to 9°C in winter and from 14°C to 32°C in summer, with an average annual precipitation of 1651 mm (Blodgett Forest Research Station 2023). BLOF is mainly covered by a productive mixed conifer forest and to a lesser extent by oak forest.

SOAP is part of the U.S. Forest Service’s Major Land Resource Area. The annual temperature and rainfall average 13.4°C and 900 mm respectively (NEON 2023b). SOAP is composed of mixed mid-elevation conifer forests over a complex terrain of coarse hills, steep slopes and narrow drainage basins. The SOAP overstory is dominated by ponderosa pine (*pinus ponderosa*) and incense cedar (*Calocedrus decurrens*), with co-dominant canyon live oaks (*Quercus chrysolepis*) and black oaks (*Quercus kelloggii*) mainly located on lower elevations in the site.

TEAK is managed by the U.S. Forest Service and partially encompasses the Pacific Southwest Research Station's Teakettle Experimental Forest in the southern part of the area (NEON 2023a; North et al. 2016). TEAK is located at higher elevation (ranging in elevation from 1,900 to 2,807 m). Mean annual temperature is 8°C and mean annual precipitation is 1222.5 mm. The varied terrain is typical of the Sierra Nevadas, with rugged mountains, meadows and prominent granite outcrops. TEAK receives substantial snowfalls in the winter and the vegetation is a montane conifer forest dominated white fir (*Abies concolor*) and red fir (*Abies magnifica*). Along with fir species, the forest also features pine species adapted to mountain climates : Jeffrey pine (*Pinus jeffreyi*) at lower elevation and lodgepole pine (*Pinus contorta*) in the upper areas.

3.2.2 Tree Species

Eleven species are under study, including four North American oak species and seven North American conifer species (four pine species, two fir species, and one cypress species). This section describes each species under study, nevertheless, more details about their characteristics can be found in the the California Native Plant Society database ² and UC Jepson eFlora database ³. Species will be further referred with their species code from the USDA Plant Database (USDA PLANTS Database 2021) which consist of 4 letters from the binomial nomenclature: the two first letters of the genus and the two first letters of the specific epithet. Moreover, for oak species evergreen and deciduous species will be identified by superscript (e) or (d), respectively. A summary of site species names and their presence on the sites is given in Table 3.1.

The four oak species under study are endemic to California, namely blue oak (*Quercus douglasii* ; QUDO^(d)), interior live oak (*Quercus wislizeni* ; QUWI^(e)), black oak (*Quercus kelloggii* ; QUKE^(d)), and canyon live oak (*Quercus chrysolepis*; QUCH^(e)).

QUDO^(d), commonly called blue oak are broadleaf deciduous trees, up to 18 m tall, that are generally found in a ring bordering the Central Valley, in the lower reaches of the Sierra Nevada foothills, the San Francisco Bay Area and both the North of South Coast Range, between 150 m and 600 m elevation. QUDO^(d) are distributed on dry and well drained slopes, prefer full sun exposure and are drought tolerant. Their dull blue-green deciduous leaves are oblong (length from 3 to 8 cm), with wavy or slightly lobed margins and are pubescent below.

QUWI^(e), commonly called interior live oak, is a broadleaf evergreen tree, up to 22 m tall, present in foothills and hot/dry canyons, being most abundant in the lower elevations of the Sierra Nevada, but also widespread in the Pacific Coast Ranges at elevation from sea level to 1500 m. Its evergreen alternate leaves are thick, leathery, small (2–5 cm), flat, generally elliptical, but shiny, lighter green below, and may have either toothed or smooth margins.

QUCH^(e), called canyon live oak, grows up to 30 m tall, and is the most widely distributed oak in California. QUCH^(e) is a broadleaf evergreen species and occurs from 30 m to 2800 m in mountainous regions, growing close to creeks and drainage swales, in moist cool microhabitats (Sierra Nevada, Coast Ranges, etc.). Its leaves are flat, elliptical to oblong extending to an acute leaf tip (length from 2.5 to 8 cm), green dark and glossy above with spines, dull golden and hairy below.

QUKE^(d), commonly known as the California black oak, is a broadleaf deciduous tree growing up to 35 m height. It occurs in pure or mixed stands, growing in a wide range of mixed evergreen forests, oak woodlands, and coniferous forests distributed from the foothills and lower mountains of California to elevations between 30 m and 2600 m. Its wide deciduous leaves are deeply lobed (length from 10 to 20 cm) with acute tips, dark and shiny green on top and pale and noticeably fuzzy underneath.

For conifers, all the seven North American species are evergreen as they are part of *Pinus*, *Abies*, and *Calocedrus* genera.

The four pine species are the gray pine (*Pinus sabiniana* ; PISA), ponderosa pine (*Pinus ponderosa* ; PIPO), sugar pine (*Pinus lambertiana* ; PILA), and Jeffrey pine (*Pinus jeffreyi* ; PIJE).

PISA, commonly called gray pine or foothill pine, is a native and endemic tree that grows equally in northern, southern and central California. It tends to grow in places with poor soils, at elevations from 0 to 1300 m and reach a height of 25 m at maturity. The needles grow in fascicles of three and are long gray-green and drooping needles (they usually grow between 20 and 30 cm).

²<https://calscape.org>

³<https://ucjeps.berkeley.edu/eflora>

PIPO, commonly known as ponderosa pine, is a widespread and variable pine native to western North America. PIPO grows in the upper foothills up to the mid-height peaks of the Sierra Nevada. Mature individuals can reach the height of 70 m. The needles are long (12 to 26 cm), thin (under 2 mm), and grow in bundles of three.

PILA, commonly known as the sugar pine, is the tallest and most massive pine tree. It is native to the mountains of the Pacific coast of North America, from Oregon through California to Baja California. Commonly growing to 40–60 m, PILA is distributed at mid-elevation between 500 and 1,500 m above sea level. This pine grows needles between 5 and 11 cm in bundles of five.

PIJE, named Jeffrey Pine in honor of its documenter John Jeffrey, is an endemic pine from the California floristic province. PIJE is a large tree, reaching 25 to 40 m and is closely related to PIPO. PIJE grows widely at 1,500 to 2,100 m elevation, and up to 2900 in the southern mountain ranges. The needles, in bundles of three, are waxy pale gray-blue-green, 12 to 23 cm long, and thick.

The two fir species under study are the white fir (*Abies concolor* ; ABCO), and the red fir (*Abies magnifica* ; ABMA).

ABCO, commonly known as white fir, is a native North American fir species distributed in the mountainous areas of California, Oregon, Idaho and Colorado. ABCO grows in the moderate elevation mix conifer forest and up to 3,200 m elevation in the red fir forest. ABCO trees grow to 25-60 meters tall. The leaves are needle-like, twisted upward and flattened, 2.5-6 cm long and 2 mm wide by 0.5-1 mm thick, green to waxy pale blue-green above, and with two waxy pale blue-white bands of stomata below.

ABMA, called red fir, is an endemic fir species from the California floristic province. ABMA is a high altitude tree that grows up to 40-60 m tall. The leaves are needle-like, 2-3.5 centimeter long, and waxy blue-green with a sharp acute tip that bends upward.

From the *Calocedrus* genus, the California incense cedar (*Calocedrus decurrens* ; CADE) is a native tree from the western North America from the cypress family. It grows from lower to high elevation up to 2,500 m. Such as other species from the cypress family, CADE foliage grows in flat sprays with scale-like leaves.

Scientific name	Abbreviation	Common Name	TONZ	SJER	BLOF	SOAP	TEAK
<i>Abies concolor</i>	ABCO	white fir					
<i>Abies magnifica</i>	ABMA	red fir					
<i>Calocedrus decurrens</i>	CADE	incense cedar					
<i>Pinus jeffreyi</i>	PIJE	jeffrey pine					
<i>Pinus lambertiana</i>	PILA	sugar pine					
<i>Pinus ponderosa</i>	PIPO	ponderosa pine					
<i>Pinus sabiniana</i>	PISA	grey pine					
<i>Quercus chrysolepsis</i>	QUCH ^(e)	canyon live oak					
<i>Quercus douglasii</i>	QUDO ^(d)	blue oak					
<i>Quercus kelloggii</i>	QUKE ^(d)	black oak					
<i>Quercus wislizeni</i>	QUWI ^(e)	interior live oak					

Table 3.1: The scientific name, common name, four-letter abbreviated species code used in the thesis. Colored cells indicate if the species is present on the site

3.3 Field data

3.3.1 Field campaigns

On the five study sites, several field campaigns and data collections took place in 2013 and 2014. These data collections are part of the project entitled “Identification of Plant Functional Types By Characterization of Canopy Chemistry Using an Automated Advanced Canopy Radiative Transfer Model” (principal investigator: Susan Ustin ; CSTARS lab, University of California, Davis, NASA grant #NNX12AP87G). This project was one of the 14 proposals funded over three years by NASA to support participation in the HypSPiRI Preparatory Airborne Activities, Associated Science and Application Research (Lee et al. 2015; NASA 2011). The main objective of the CSTARS lab with this proposal was to assess the consistency between plant functional types and biochemical diversity at the canopy, and aims to address the HypSPiRI mission to monitor changes in physiological functioning. The third and last sub-objective was to “Test the potential for complete automation of the radiative transfer model inversion to retrieve canopy chemistry products from HypSPiRI spectra”.

To this aim, leaves were collected from the field for chemical analysis. Additionally, reflectance and transmittance were measured on leaves for chemical analysis using an integrating sphere and an ASD Fieldspec-3 spectrometer. For chemical analysis, the project targeted physiologically active canopy chemistry components that are relevant for fluxes of carbon and water with the atmosphere, namely: chlorophyll a and b, carotenoids, water and ligno-cellulose dry matter (NASA 2011).

Between 4 or 5 field campaigns occurred in 2013 and 2014 for each site. They took place at three times of the year, approximating seasons (*i.e.*, spring, summer and fall) to capture the variation linked to the phenology. The dates of the field campaigns are detailed in Table 3.2.

Table 3.2: Dates of the field campaigns (format DD/MM).

Site	2013		Spring	2014	
	Summer	Fall		Summer	Fall
TONZ	11/06	24/09	15/04 - 17/04	06/06 - 08/06	06/10 - 08/10
SJER	16/06 - 20/06	06/11 - 11/11	09/04 - 11/04	11/06 - 16/06	21/10 - 23/10
BLOF	-	30/09 - 03/10	21/04 - 23/04	01/06 - 04/06	04/11 - 06/11
SOAP	16/06 - 20/06	06/11 - 11/11	11/04 - 13/04	11/06 - 16/06	27/10 - 30/10
TEAK	16/06 - 20/06	06/11 - 11/11	-	11/06 - 16/06	27/10 - 30/10

Each field campaign was split into three main steps that are detailed in the further subsections: leaf collection, leaf traits measurements, leaf reflectance and transmittance measurements.

A total of 290 trees were sampled during the field campaigns, including 114 oaks trees, 101 pines, 56 firs, and 19 CADE (Table 3.3). The number of sampled trees is variable considering the species, site, and season. Several reasons explain the differences of sampled trees: (i) some species are only present on one site and are therefore less sampled; (ii) priority was given to deciduous species in spring and fall campaigns to capture their more pronounced phenological variations compared to evergreen species.

3.3.2 Leaf sampling

Between 10 and 20 plots were distributed across each study site to cover the full variation in species composition and canopy density. Species and plots sampled during each season varied by site. Plots dominated by deciduous species were measured in all three seasons in order to analyze the temporal evolution of the vegetation while plots dominated by evergreen species were measured at most during two seasons.

In each plot, one or several open grown trees were selected, *i.e.* trees that were not too tall to access leaves from the extended pole clipper (about 6 m) and that were in a more open location so that the foliage was not likely shadowed by other nearby taller trees. The location of each sampled tree was recorded with a Trimble Geo7X GPS unit. Two sets of 15 leaves/needles were collected from the upper and sunlit portion of the canopy from the selected individuals with a tree trimmer. For evergreen species, which keep their leaves for several years, new leaves were not collected with the assumption that previous years leaves made up the majority of canopy regardless of the season. A similar assumption was made for conifers and only needles from the 2nd or 3rd year were collected. The first set of leaves/needles was placed in a sterilized and previously weighed plastic bag for water and dry matter content estimation while the second set of leaves was placed in foil packets, to avoid the light from reaching them for spectral measurements and pigment extraction. Both sets were stored on blue ice in coolers until they arrived at the lab where they were placed in a lab refrigerator. Leaf measurements were conducted less than 48 hours after they were removed from the plant.

3.3.2.1 Leaf traits Measurements

C_{ab} , C_{xc} , EWT and LMA are four leaf functional traits expressed as the mass contained per unit of leaf area. Therefore, the measurement protocol of leaf traits involves the measure of the leaf area and the respective mass of each family of compounds.

To derive leaf area (further noted A), on both leaf sets, all the leaves and needles were scanned with 150 dpi using a white background to amplify the contrast between leaves and background. Then, leaf areas were derived by delineating the leaves from the background in the scans. Addi-

Table 3.3: Sample distributions for each species, season and site.

Species	Season	TONZ	SJER	BLOF	SOAP	TEAK	TOTAL
ABCO	Spring			5			5
	Summer			5		8	13
	Fall			5	4	12	21
	Total			15	4	20	39
ABMA	Spring						
	Summer					7	7
	Fall				1	9	10
	Total				1	16	17
CADE	Spring						
	Summer						
	Fall			10	9		19
	Total			10	9		19
PIJE	Spring						
	Summer					9	
	Fall					12	
	Total					21	21
PILA	Spring						
	Summer						
	Fall				1	1	2
	Total				1	1	2
PIPO	Spring			5			5
	Summer			5	5		10
	Fall			10	13	1	24
	Total			20	18	1	39
PISA	Spring	5					5
	Summer	5	10				15
	Fall	5	10				15
	Total	15	20				35
QUCH	Spring				5		5
	Summer				2		2
	Fall				12		12
	Total				19		19
QUDO	Spring	5	5				10
	Summer	8	9				17
	Fall	9	8				17
	Total	22	22				44
QUKE	Spring			6	5		11
	Summer			4	9		13
	Fall				7		7
	Total			10	21		31
QUWI	Spring		3				3
	Summer		8				8
	Fall		9				9
	Total		20				20

tionally, the leaf or needle thickness was measured with a caliper.

To determine mass of leaf pigments from the second set of leaves/needles, samples were frozen in liquid nitrogen immediately after the spectral measurements. They were stored frozen for a short time and then lyophilized. The pigments extraction was done with 90% acetone (14 mL) for 48 hours. Each vial contains one sample (5 leaves from one individual). Three replicates were taken from each vial. Lambda 25 UV/Vis spectrophotometer were used with concentrations for chlorophylls and carotenoids of 23 mg/mL and 8 mg/mL. A detailed explanation of the lab protocol is explained in the work of [Lichtenthaler 1987](#). Then, the mass of chlorophylls a and b ($m_{chlorophylls}$) and the mass of carotenoids ($m_{carotenoids}$) were derived from concentrations measured

in the solutions and used to compute the C_{ab} and C_{xc} values following equations 3.1 and 3.2.

$$C_{ab} = \frac{m_{Chl\ a\&b}}{A} \quad (3.1)$$

$$C_{xc} = \frac{m_{xc}}{A} \quad (3.2)$$

To derive EWT and LMA from the first set of leaves, the Ziplock bags for leaf water samples were weighed empty and then they were weighed again with leaves. Leaves were dried at 60°C for a minimum of 48 hours in an oven. Dry and fresh weights (respectively m_{dry} and m_{fresh}) were used to compute LMA and EWT following equations 3.3 and 3.4.

$$EWT = \frac{m_{fresh} - m_{dry}}{A} \frac{1}{\rho_{water}} \quad (3.3)$$

$$LMA = \frac{m_{dry}}{A} \quad (3.4)$$

One could notice that the density of water ($\rho_{water} = 1 \text{ g} \cdot \text{cm}^{-3}$) is a factor in the computation of EWT. Therefore EWT is expressed as a length, its values are given in cm. The EWT can be seen as the thickness of a volume of water occupying a specific area, and for this very reason EWT is actually an equivalent thickness.

3.3.2.2 Leaf spectral measurements

From the second set of leaves/needles, directional-hemispherical reflectance and transmittance were measured from each individual using an ASD FieldSpec Pro (1-2 nm sampling interval, with 3-10 nm resolution) attached to a Li-cor 1800-12 integrating sphere with a 6 V, 10 W, 3100 K illumination source (LI-COR 1983). For broadleaf species, five leaves were randomly selected as sample replicates. For conifers species, since needles did not cover the entire sample port of the LI-1800, three sample replicates were created by arranging leaves as close together as possible with no overlap (*i.e.*, minimizing gaps between leaves) and sealing the ends of the leaves using either black rubber gaskets or black electric tape.

The spectra were collected in radiance from 350 to 2500 nm. The protocol also involves the measurements of the reference material illumination I_r and stray radiation illumination I_d . Reflectance R_s and transmittance T_s of samples are derived using the equation provided by the manufacturer and described below (equations 3.5 and 3.6; LI-COR 1983). The manufacturer also provides the intrinsic reflectance of the sphere reference material R_r .

$$R_s = \frac{(I_s - I_d)R_r}{I_r - I_d} \quad (3.5)$$

$$T_s = \frac{I_s R_r}{I_r} \quad (3.6)$$

where I_s is the measured sphere output when the sample is illuminated and I_r is the measured sphere output when the reference material is illuminated. The five processed spectra per sample were averaged. Then, a Savitzky-Golay filter (Savitzky and Golay 1964) was applied to smooth the SWIR part of the spectrum (1600 – 2500 nm).

The leaf traits measurement associated with the corresponding directional-hemispherical reflectance and transmittance constitute the CSTARS-Leaf dataset.

3.4 Remote sensing data

3.4.1 AVIRIS flight lines

AVIRIS is an hyperspectral airborne imaging sensor developed by NASA at the JPL (Jet Propulsion Laboratory, Pasadena, California). AVIRIS is a whiskbroom scanner with an instantaneous field of view of 1 mrad and a total field of view of 34°. AVIRIS features 224 contiguous bands in the optical range from 365 nm to 2,500 nm. The bands are split on two sensors: one for the visible and near infrared range and one for the short wave infrared range. The FWHM (Full Width at Half Maximum) is around 10 nm for each band (Green et al. 1998).

AVIRIS is loaded on the NASA ER-2 aircraft and was flown at an altitude of 20 km, and provides images with a GSD of approximately 14-15 m (Table 3.4). AVIRIS was flown around noon and images were acquired at nadir to avoid as much as possible the directional effects. In the frame of the HypSIRI Preparation mission, at least three sets of flights were scheduled each year from 2013 to 2015 in each flight box. The flights took place in spring, summer and fall to capture the phenological variations of the vegetation. A total of 47 images were acquired over the five study sites and cover at least 30% of the site area during the years 2013 and 2014 (Figure 3.2).

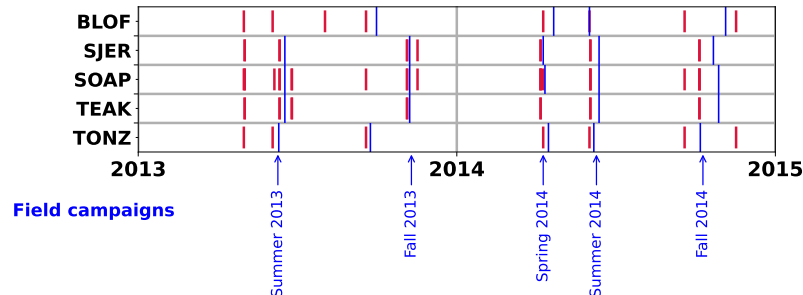


Figure 3.2: Timeline of all the AVIRIS acquisitions available on the five study sites (red) and the field campaign (blue)

The NASA JPL processed the raw AVIRIS data to provide ortho-corrected reflectance images. The processing steps includes: (i) the radiometric calibration to convert image in luminance values, (ii) the geometrical orthorectification based on a geometric lookup-table methodology for data rendering and employing a full three-dimensional ray tracing and a 30m spatial resolution digital elevation model for complete orthorectification, and (iii) the atmospheric correction performed with the ATmosphere REMoval Algorithm (ATREM) to provide images of scaled surface reflectance (Gao et al. 1993).

Images that were acquired more than one month before or after a field campaign were removed from the flight line list. Images of the Tahoe box from September 2014 were also removed from the list because of the presence of a wildfire and the spread of its smoke over the study area, which would have required revision of the applied atmospheric correction. A total of 38 flight lines were selected to extract spectral data.

3.4.2 CSTARTS-Canopy dataset

The 38 ortho-corrected reflectance images were downloaded from the AVIRIS data portal⁴. Visual inspection of the images from the AVIRIS data portal downloaded showed that they often exhibit a spatial shift up to 2 pixels (about 30m). To reduce the uncertainty linked to georeferencing, the images were processed with the gefolki algorithm (Brigot et al. 2016) to provide a more consistent georeferencing. Images were georeferenced to Maxar Technology RGB images, and resampled at the same GSD of the AVIRIS image, extracted from Google Earth service. AVIRIS images were not spatially resampled in order to minimize the spatial shift uncertainty associated with such processes.

Then, for each image, GPS positions of sampled trees of the site and the season were associated with the image. For each GPS position, the closest pixel in the image was identified and the reflectance data was extracted (Figure 3.3). Two occurrences of the AVIRIS sensor were built by the JPL and both were used in the HypSIRI Preparation Mission. Both payloads were built with the same features, although, for feasibility reasons, they have slightly different center wavelengths and FWHM for each band (e.g., center wavelengths could differ by 1 nm). Therefore, in order to standardize the spectral data, the reflectance data were spectrally resampled with a third order spline interpolation on a standard grid (201 bands, from 400 nm to 2500 nm, every 10 nm).

On average, between 7 and 8 pixels were extracted for one image (Table 3.4). A total of 292 pixels and reflectance data associated with ground measurements were extracted from the AVIRIS images. Since the areas covered by some flight lines overlap, multiple pixels from the same day and distinct images could be associated with a single sampled individual.

This dataset with AVIRIS reflectance data associated with in-lab measurements of leaf traits is further denominated the CSTARTS-Canopy dataset in Chapter 5.

⁴<https://aviris.jpl.nasa.gov/dataportal/>

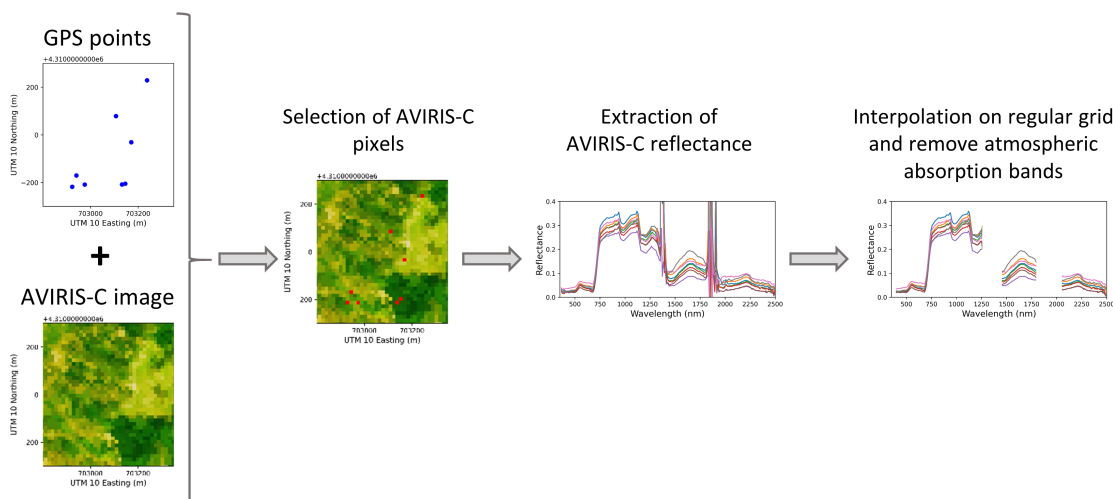


Figure 3.3: Schematic diagram of extraction processing of AVIRIS reflectance.

The temporal shift between the image acquisition and field sampling ranges from -22 days to 13 days (Table 3.4). On average AVIRIS images were acquired earlier than the field sampling date (average temporal shift of -5.3 days, with a standard deviation of 8.4 days). Indeed, most of the pixels were acquired before leaf collection in the field (Figure Figure 3.4). The difference of dates between leaf collections and AVIRIS acquisition is due to feasibility reasons. In fact, due to travel time into different forest sites it was not possible to access multiple sites on the same day, and it was not possible to have multiple crews at each site due to lack of equipment and lack of staff.

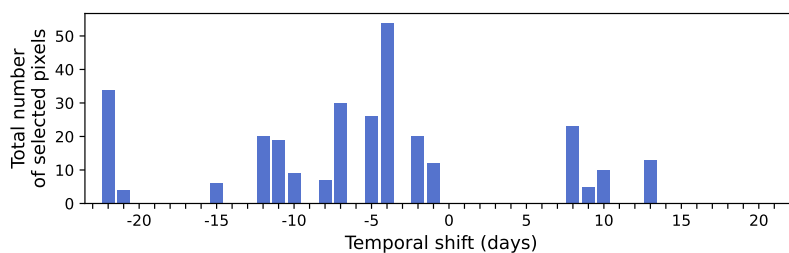


Figure 3.4: Distribution of selected pixels as a function of temporal shift

In the CSTARs-Canopy dataset the assumption is made that the time between image acquisition and in-field collection caused minimal changes to the leaf traits. Additionally, there was any rainfall between leaf collection and AVIRIS acquisition that could alter the EWT. Besides, to build the CSTARs-Canopy dataset, the assumption that the collected twigs and leaves are representative of the entire individual.

3.4.3 Background reflectance spectra

In addition, soil reflectance spectra were extracted from hyperspectral images to simulate canopy reflectance with canopy RTMs (see Chapter 1 for details on canopy RTM parameters). This step involves finding areas without tree cover and large enough to cover an entire pixel of a hyperspectral image.

Soil reflectance spectra were extracted from two types of images: AVIRIS images and NIS (NEON imaging spectrometer) images. The NIS is supported and operated by NEON, and is flown every two years over NEON sites at vegetation maximum greenness (Musinsky and Thibault n.d.). NIS is a pushbroom sensor and has a 1 mrad instantaneous field of view at nadir providing GSD of 1 m for the typical flight altitude (1000m above ground level). NIS features 426 bands, covering wavelengths from 380 nm to 2510 nm with a 5 nm spectral resolution and a 7.5 nm FWHM (Gallery et al. n.d.).

AVIRIS images have a GSD of 14 m, and were therefore only used to extract soil spectra at sites with a low canopy cover. Indeed, for TONZ and SJER, which have low canopy covers,

Table 3.4: List of AVIRIS-C flight lines with associated pixel size, sample number, date and temporal shift.

Site	Name	Pixel Size (m)	Number of Selected Pixels	Date of flight (YYYY-MM-DD)	Date of sampling (YYYY-MM-DD)	Temporal shift (days)
BLOF	f130919t01p00r12	14.9	8	2013-09-19	2013-10-01	-12
	f140410t01p00r13	14.7	11	2014-04-10	2014-04-22	-12
	f140602t01p00r15	14.9	12	2014-06-02	2014-06-03	-1
	f141117t01p00r14	14.6	13	2014-11-17	2014-11-04	13
SJER	f130612t01p00r09	14.8	12	2013-06-12	2013-06-19	-7
	f131105t01p00r15	14.5	10	2013-11-05	2013-11-07	-2
	f140407t01p00r09	14.5	4	2014-04-07	2014-04-11	-4
	f140603t01p00r17	14.6	7	2014-06-03	2014-06-11	-8
	f141006t01p00r09	14.6	6	2014-10-06	2014-10-21	-15
SOAP	f130606t01p00r05	14.5	4	2013-06-06	2013-06-16	-10
	f130612t01p00r07	14.0	9	2013-06-12	2013-06-16	-4
	f130612t01p00r14	14.0	3	2013-06-12	2013-06-16	-4
	f130626t01p00r07	14.0	6	2013-06-26	2013-06-16	10
	f130626t01p00r09	14.0	4	2013-06-26	2013-06-16	10
	f131105t01p00r10	13.8	3	2013-11-05	2013-11-09	-4
	f131105t01p00r11	13.7	15	2013-11-05	2013-11-09	-4
	f131117t01p00r06	14.1	12	2013-11-17	2013-11-09	8
	f140407t01p00r07	13.7	8	2014-04-07	2014-04-12	-5
	f140407t01p00r18	14.1	8	2014-04-07	2014-04-12	-5
	f140410t01p00r18	15.1	5	2014-04-10	2014-04-12	-2
	f140603t01p00r10	14.0	9	2014-06-03	2014-06-14	-11
	f140603t01p00r12	13.9	2	2014-06-03	2014-06-14	-11
	f140603t01p00r21	14.2	8	2014-06-03	2014-06-14	-11
	f141006t01p00r07	13.8	16	2014-10-06	2014-10-28	-22
f141006t01p00r16	14.2	18	2014-10-06	2014-10-28	-22	
TEAK	f130612t01p00r06	14.3	5	2013-06-12	2013-06-17	-5
	f130612t01p00r15	14.3	9	2013-06-12	2013-06-19	-7
	f130626t01p00r06	14.5	5	2013-06-26	2013-06-17	9
	f130626t01p00r08	14.3	11	2013-06-26	2013-06-18	8
	f131105t01p00r08	14.1	11	2013-11-05	2013-11-09	-4
	f131105t01p00r09	14.3	5	2013-11-05	2013-11-07	-2
	f140603t01p00r09	14.4	1	2014-06-03	2014-06-15	-12
	f140603t01p00r11	14.2	5	2014-06-03	2014-06-13	-10
	f141006t01p00r06	14.3	4	2014-10-06	2014-10-27	-21
TONZ	f130604t01p00r12	14.9	3	2013-06-04	2013-06-11	-7
	f130919t01p00r13	14.9	5	2013-09-19	2013-09-24	-5
	f140410t01p00r14	14.6	6	2014-04-10	2014-04-17	-7
	f140602t01p00r16	15.0	9	2014-06-02	2014-06-06	-4

soil reflectance spectra could be extracted from AVIRIS images. For SOAP and TEAK, larger treeless areas correspond to rocky outcrops and their reflectance is not representative of soils under the canopy. These sites required to select smaller treeless areas in zones with a higher canopy cover whose reflectance spectra could only be extracted from NIS images with 1 m GSD. The NIS images used in this step were acquired in June 2017. For BLOF, the high canopy cover and lack of hyperspectral images with a small GSD on the site imply that reliable soil reflectance spectra cannot be obtained. Since BLOF has a geology similar to SOAP and TEAK, soil reflectance spectra from these latter sites will also be used for BLOF canopy simulations.

3.5 Data statistical analysis

The measurements presented in this chapter can be analyzed statistically regarding species. They provide prior information regarding the range of variations of leaf traits.

Mean statistics for each leaf trait are given in Table 3.5 and more detailed distributions per species are given in Figure 3.5.

Table 3.5: Basic statistics of the measured foliar traits compared for oak and conifers species

	C_{ab} ($\mu\text{g}\cdot\text{cm}^{-2}$)	C_{xc} ($\mu\text{g}\cdot\text{cm}^{-2}$)	EWT (cm)	LMA ($\text{g}\cdot\text{cm}^{-2}$)
Mean	33.7 / 62.6	8.7 / 16.3	0.0112 / 0.0367	0.0124 / 0.0321
Standard Dev.	13.2 / 23.2	2.9 / 5.0	0.0026 / 0.0062	0.0043 / 0.0059
Min.	0.5 / 19.3	2.0 / 6.3	0.0051 / 0.0223	0.0045 / 0.0179
Max.	68.4 / 136.0	17.8 / 31.4	0.0202 / 0.0527	0.0215 / 0.0539

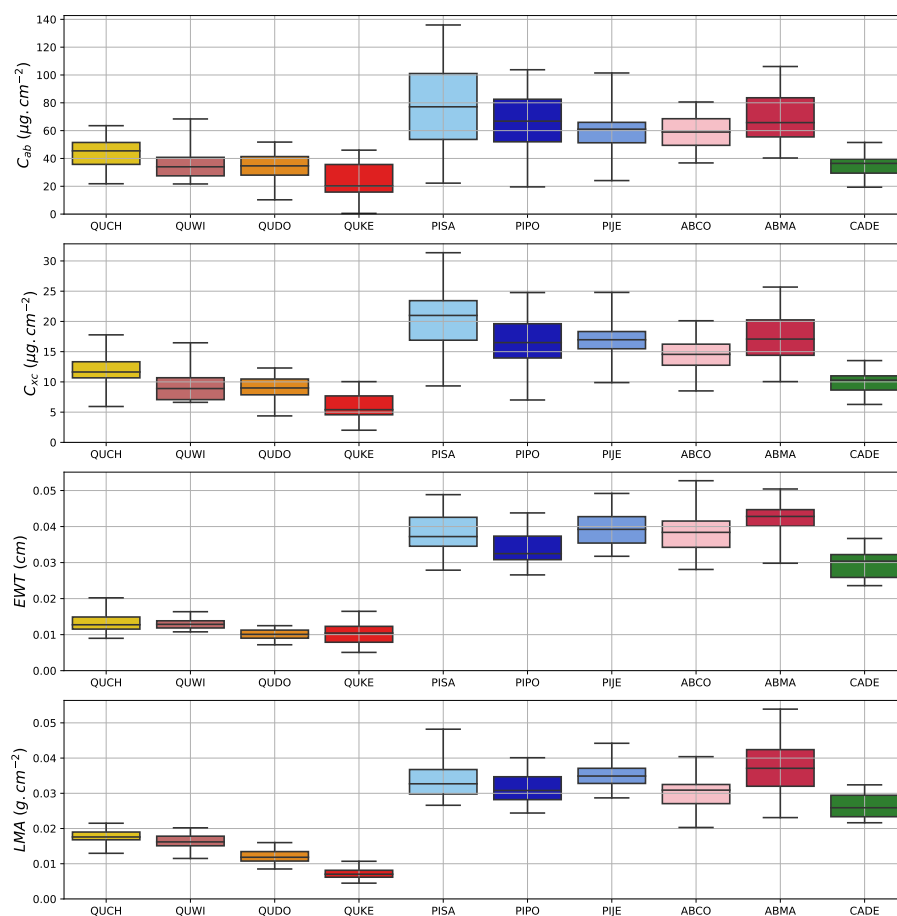


Figure 3.5: Distribution of the four leaf traits for each species.

Statistical analysis shows that leaf traits distribution are different for broadleaf and conifer species. For example, pigments contents are almost twice higher for conifers, and almost three times higher for EWT and LMA. Detailed distributions by species from Figure 3.5 and standard deviations from Table 3.5 highlights that leaf traits values are more restricted for oak species. The two by two leaf traits scatter plot representation (Figure 3.6) confirms that oaks and conifers leaf traits distributions are distinct, and that the conifer distributions of leaf traits are more spread than the oak ones.

For oak species, evergreen species tend to have higher values of leaf traits than deciduous species (Figure 3.5). Inter-species discrepancy is particularly visible for LMA where each species appears to have a specific range of values.

For conifer species, pine and fir species exhibit similar distributions of leaf traits. CADE is the only species that stands out among conifers with leaf trait values intermediate between oaks and firs.

Figure 3.6 emphasizes the correlation between leaf traits. Table 3.6 give the correlation between leaf traits values, for oak species and conifer species respectively. C_{ab} and C_{xc} show the highest correlation (0.91 for oak, 0.95 for conifers) and are both correlated to LMA (correlation over 0.5). EWT is less correlated to other leaf traits and more particularly for oak species (around 0.22 with pigments-related traits for oak compared to 0.4 for conifer species). More generally, traits are more correlated for conifer species than for oak species (except between C_{xc} and EWT).

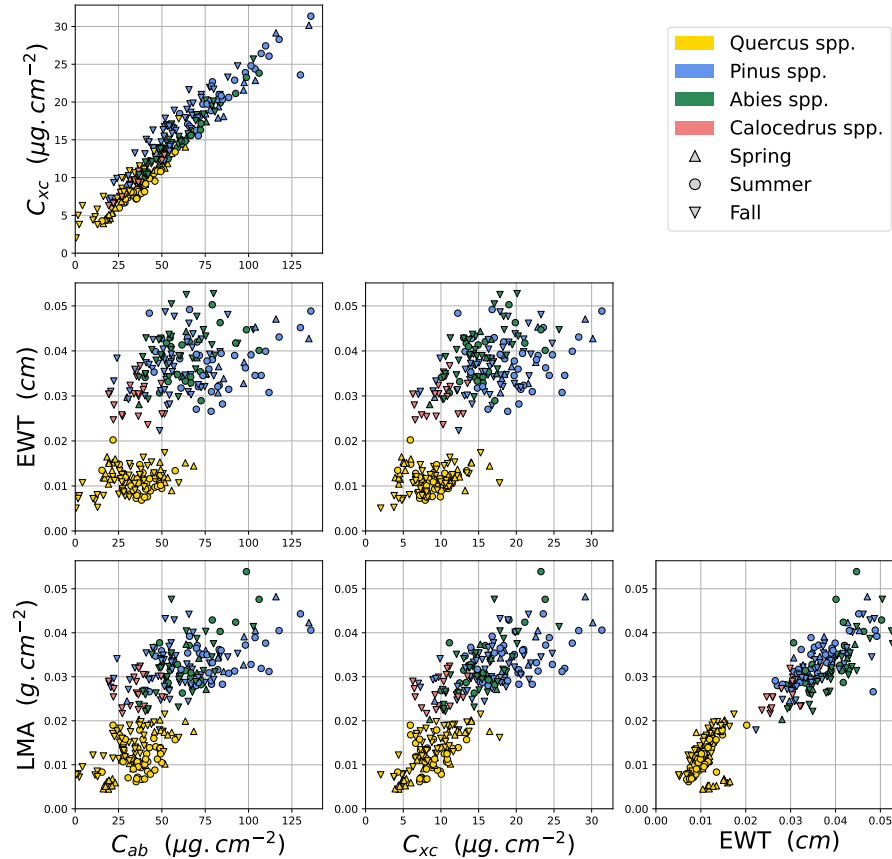


Figure 3.6: Scatter plots of the four leaf traits.

Table 3.6: Correlation matrix for the four leaf traits by pooling all *Quercus* species (left) and all conifer species (right).

	C_{ab}	C_{xc}	EWT	LMA
C_{ab}	1.00	0.91	0.20	0.49
C_{xc}		1.00	0.24	0.67
EWT			1.00	0.48
LMA				1.00

	C_{ab}	C_{xc}	EWT	LMA
C_{ab}	1.00	0.95	0.38	0.57
C_{xc}		1.00	0.46	0.63
EWT			1.00	0.74
LMA				1.00

For oak species, the average leaf thickness, regardless of the species, is 0.29 mm. Although leaf thickness shows discrepancies between species similar as LMA. Indeed, average leaf thickness per species follow the same trend as LMA with the smallest for QUKE^(d) (0.24 mm) followed by QUDO^(d) (0.28 mm), QUWI^(e) (0.32 mm) and QUCH^(e) (0.35 mm). In fact, leaf thickness is slightly correlated to LMA (0.68), but with higher correlation than EWT (0.56). As expected, leaf thickness is even more correlated to leaf surface weight (sum of LMA and EWT; 0.73) that represents the quantity of matter per unit area of leaf, all types of compounds included.

Chapter 4

Estimation at the leaf scale

This Chapter focuses on leaf scale estimation of leaf traits. The work on this topic regarding the studied oak species has been published in a peer-reviewed article "[Estimation of Oak Leaf Functional Traits for California Woodland Savannas and Mixed Forests: Comparison between Statistical, Physical, and Hybrid Methods Using Spectroscopy](#)", Gaubert et al. 2024, which is inserted in this chapter. The following paragraph introduces the overall thesis approach for leaf traits estimation at the leaf scale that lead to the publication of the article. After the article, a conclusion is added in this manuscript to summarize the main results and how the article fits in with this thesis.

As seen in [Chapter 1](#) the remotely sensed signal acquired at the top of a tree canopy is to first order influenced by leaf reflectance and transmittance. From this point of view, understanding how the leaf traits can be estimated at the leaf scale from leaf reflectance and transmittance is a key step to further perform accurate estimations at the canopy scale.

Several methods from three classes of estimation strategies presented in the [Chapter](#) and [Chapter 2](#) have been developed to estimate leaf traits from leaf reflectance and transmittance. However, the accuracy of estimation methods have been compared only by a few authors, more particularly considering methods from distinct classes of strategies ([Féret et al. 2019](#); [Wang et al. 2023](#)). In addition, most studies focused on one or two leaf trait retrieval and at the peak vegetation growth with mature leaves. Studies considering data collected at different stages of the phenological cycle are scarce in the literature ([Noda et al. 2021](#)).

Therefore, this study focuses on the estimation of the four leaf traits from laboratory directional-hemispherical leaf reflectance and transmittance measurements and aims to compare the performances of estimation methods taken from the state-of-the-art (statistical, physical and hybrid; [Chapter](#)). In this Chapter, physical and hybrid methods are based on the PROSPECT leaf radiative transfer model (presented in [Chapter 1](#)) and therefore are referred as PROSPECT-based methods. PROSPECT-based methods include inversion of PROSPECT from iterative algorithms and LUT-based inversion. For LUT-based methods, two distance functions (spectral angle mapper and euclidean distance) and two sampling schemes (Latin hypercube sampling and Multivariate gaussian sampling ; [Chapter 2](#)) were tested. For statistical and hybrid methods, the four distinct MLRA described in [Chapter 2 Section 2.2](#) were used to build estimators and compared: Ridge, PLSR, GPR, and RFR. Additionally, for statistical methods, the MLRAs were trained either on the CSTAR-Leaf database or on an independent database from the state-of-the-art (ANGERS) in order to assess the transferability of such methods. Considering all these features, a total of 17 estimation strategies were compared.

To compare the strategies under study, the data from the CSTAR-Leaf dataset, presented in [Chapter 3](#) and gathering the leaf traits measurements and directional-hemispherical leaf reflectance and transmittance measurements, is used in this article to evaluate the accuracy of the selected methods. Although the CSTAR-Leaf dataset also included measurements of conifers leaf traits and needles optical properties, the peer-reviewed article focuses on estimation of leaf traits for oak species and excluded the conifer samples for several reasons. As a matter of fact, the PROSPECT model has been calibrated and validated on broadleaves species ([Féret et al. 2017](#)) and therefore simulating the optical properties of other functional groups, such as conifers, is potentially outside the validity domain of PROSPECT. Thus, to compare only the estimation methods performance it is required to restrict the study to samples that are in the validity domain of PROSPECT to avoid as much as possible the potential misrepresentation of this RTM. In addition,

measuring tools are not adapted to the shape of conifer needles (Yáñez-Rausell et al. 2014). As a result, the leaf directional-hemispherical reflectance and transmittance measurement protocol required to be adapted to cope with conifer leaves. In this protocol, adapted from Mesarch et al. 1999 the conifer leaves (needles) are stacked into bundles for optical measurements and require an additional processing step to correct the effects of gaps between the leaves. This protocol provides spectral measurements with less controlled uncertainties. Consequently, for these reasons conifer samples were excluded from the study. Nevertheless, tests that were carried out on conifer samples are presented in Appendix B.

For simplicity, the article refers to the oak samples of the CSTARS-Leaf dataset as “CSTARS dataset” or “our dataset”. Also for simplicity’s sake, the expression “CSTARS-Leaf dataset” will only refer to the oak samples in the rest of this Chapter.

As detailed in Chapter 3 the CSTARS-Leaf dataset gathers samples from 114 deciduous and evergreen oak trees collected over three seasons (spring, summer and fall) and from four out of the five study sites of the thesis where the oaks species are present (TONZ, SJER, BLOF, SOAP).

The objective of the peer-reviewed article is threefold:

1. Compare all the estimation methods performances on the CSTARS-Leaf dataset and identify the most suitable one for each trait and for all of them.
2. Explore the transferability statistical approaches when MLRA are trained on an independent dataset (here ANGERS) containing distinct species from other ecosystem types.
3. Study the distribution of the PROSPECT structural parameter N values, retrieved by iterative inversions, for the oak specimens included in the CSTARS-Leaf database and study its seasonal, intra- and inter-specific variability.

Leaf-scale estimation of oak leaf traits : Comparison of statistical and PROSPECT-based methods

The article is divided with the following structure: Section 1 introduces the context of the study, the targeted leaf traits and the state-of-the-art methods. Section 2 describes the data collection and processing performed to build the CSTARS-Leaf dataset and further details the tested methods. Finally, the results are shown in Section 3 and are followed by discussions in Section 4.



Article

Estimation of Oak Leaf Functional Traits for California Woodland Savannas and Mixed Forests: Comparison between Statistical, Physical, and Hybrid Methods Using Spectroscopy

Thierry Gaubert ^{1,*}, Karine Adeline ¹, Margarita Huesca ², Susan Ustin ³ and Xavier Briottet ¹¹ ONERA/DOTA, Université de Toulouse, F-31055 Toulouse, France² Faculty of Geo-Information Science and Earth Observation (ITC), University of Twente, 7522 NH Enschede, The Netherlands³ Institute of the Environment, University of California Davis, Davis, CA 95616, USA

* Correspondence: thierry.gaubert@onera.fr

Abstract: Key leaf functional traits, such as chlorophyll and carotenoids content (C_{ab} and C_{xc}), equivalent water thickness (EWT), and leaf mass per area (LMA), are essential to the characterization and monitoring of ecosystem function. Spectroscopy provides access to these four leaf traits by relying on their specific spectral absorptions over the 0.4–2.5 μm domain. In this study, we compare the performance of three categories of estimation methods to retrieve these four leaf traits from laboratory directional-hemispherical leaf reflectance and transmittance measurements: statistical, physical, and hybrid methods. To this aim, a dataset pooling samples from 114 deciduous and evergreen oak trees was collected on four sites in California (woodland savannas and mixed forests) over three seasons (spring, summer and fall) and was used to assess the performance of each method. Physical and hybrid methods were based on the PROSPECT leaf radiative transfer model. Physical methods included inversion of PROSPECT from iterative algorithms and look-up table (LUT)-based inversion. For LUT-based methods, two distance functions and two sampling schemes were tested. For statistical and hybrid methods, four distinct machine learning regression algorithms were compared: ridge, partial least squares regression (PLSR), Gaussian process regression (GPR), and random forest regression (RFR). In addition, we evaluated the transferability of statistical methods using an independent dataset (ANGERS Leaf optical properties database) to train the regression algorithms. Thus, a total of 17 estimations were compared. Firstly, we studied the PROSPECT leaf structural parameter N retrieved by iterative inversions and its distribution over our oak-specific dataset. N showed a more pronounced seasonal dependency for the deciduous species than for the evergreen species. For the four traits, the statistical methods trained on our dataset outperformed the PROSPECT-based methods. More particularly, statistical methods using GPR yielded the most accurate estimates (RMSE = 5.0 $\mu\text{g}\cdot\text{cm}^{-2}$; 1.3 $\mu\text{g}\cdot\text{cm}^{-2}$; 0.0009 cm; and 0.0009 $\text{g}\cdot\text{cm}^{-2}$ for C_{ab} , C_{xc} , EWT, and LMA, respectively). Among the PROSPECT-based methods, the iterative inversion of this model led to the most accurate results for C_{ab} , C_{xc} , and EWT (RMSE = 7.8 $\mu\text{g}\cdot\text{cm}^{-2}$; 2.0 $\mu\text{g}\cdot\text{cm}^{-2}$; and 0.0035 cm, respectively), while for LMA, a hybrid method with RFR (RMSE = 0.0030 $\text{g}\cdot\text{cm}^{-2}$) was the most accurate. These results showed that estimation accuracy is independent of the season. Considering the transferability of statistical methods, for the four leaf traits, estimation performance was inferior for estimators built on the ANGERS database compared to estimators built exclusively on our dataset. However, for EWT and LMA, we demonstrated that these types of statistical methods lead to better estimation accuracy than PROSPECT-based methods (RMSE = 0.0016 cm and 0.0013 $\text{g}\cdot\text{cm}^{-2}$ respectively). Finally, our results showed that more differences were observed between plant functional types than between species or seasons.

Keywords: oak ecosystems; leaf functional traits; seasonality; inversion methods; PROSPECT; machine learning; spectroscopy



Citation: Gaubert, T.; Adeline, K.; Huesca, M.; Ustin, S.; Briottet, X. Estimation of Oak Leaf Functional Traits for California Woodland Savannas and Mixed Forests: Comparison between Statistical, Physical, and Hybrid Methods Using Spectroscopy. *Remote Sens.* **2024**, *16*, 29. <https://doi.org/10.3390/rs16010029>

Academic Editor: Markus Immitzer

Received: 4 October 2023

Revised: 12 December 2023

Accepted: 14 December 2023

Published: 20 December 2023



Copyright: © 2023 by the authors. Licensee MDPI, Basel, Switzerland. This article is an open access article distributed under the terms and conditions of the Creative Commons Attribution (CC BY) license (<https://creativecommons.org/licenses/by/4.0/>).

1. Introduction

Oak trees from the *Quercus* genus comprise around 500 species, including both deciduous and evergreen species. They are mostly distributed in the Northern Hemisphere from cool temperate to tropical climates, and their numbers are the greatest in North America and China. According to the Red List of Oak 2020 report and analyses of over 430 species studied worldwide, about 31% of oak species are estimated to be threatened and globally, 41% are considered to be of conservation concern [1]. They are mainly endangered by land use change due to agriculture and urbanization expansion, as well as logging and global climate change, which is leading to a decrease in water availability and increase in fires, pests, and diseases. However, oak trees are of high ecological and economic importance since they provide food (acorns) and habitat for fauna, serve as carbon sinks, and are used for timber, furniture, fuel, dyes, and tannins [2]. They are present in 18 out of the 36 biodiversity hotspots recognized by the Critical Ecosystem Partnership Fund (CEPF), which feature a rich biodiversity but experience severe habitat loss. About 89 oak species exist in the United States and 20 are present in California, of which 7 are endemic [3]. Oak trees are distributed between oak woodland savannas and oak forest ecosystems, the former representing about 50,000 km² while the latter 27,000 km² [4]. Most are threatened due to population increase and demand for wood and fuel; management plans have been drawn up for the six regions of California to preserve oak resources, promote stand regeneration, and prevent fire propagation [5].

Optical remote sensing is a widely used technology to observe large-scale terrestrial landscapes with high temporal revisit. Remote sensing has been used to observe oak ecosystems: for instance, for monitoring the spatio-temporal land cover change of a cork oak forest due to anthropogenic disturbance [6], for assessing the post-fire recovery of a mixed pine–oak forest [7], for estimating tree cover over an evergreen oak woodland [8], and for identifying pest-infected oak trees [9]. The remotely sensed signal acquired at the top of a tree canopy is to a certain extent influenced by canopy structure, but primarily by leaf reflectance and transmittance. These optical properties have been demonstrated to be the expression of plant functions and strategies [10]. The latter can be explained through the definition of plant traits and plant functional traits, which can be upscaled from the individual to the ecosystem level. A plant trait is any morphological, physiological, or phenological feature measurable without reference to the environment, while a functional trait is any trait that impacts fitness indirectly via its effects on growth, reproduction, and survival [11].

Among the optically relevant traits at the leaf level, chlorophyll a and b content (C_{ab}), carotenoid content (C_{xc}), equivalent water thickness (EWT), and leaf mass area (LMA) are often studied since they have been proven to be valuable indicators to assess vegetation health and stress levels [12].

Due to their biochemical (C_{ab} , C_{xc} , EWT) or morphological nature (LMA), they have become fundamental for monitoring environmental function and structure in order to improve our understanding of physiological vegetation processes and global biogeochemical cycles [13]. Monitoring leaf traits would also provide insight into vegetation resilience against the increased impact of global climate change. As such, their accurate and quantitative estimation is targeted for a precise monitoring of essential biodiversity variables over space and time [14]. C_{ab} and C_{xc} are leaf photosynthetic pigments that intervene in light harvesting and its conversion into chemical energy. C_{xc} include xanthophylls and carotenes, and also contribute to photoprotection [13,15,16]. EWT is correlated with the amount of water per leaf area and thus with water management by plant tissues. EWT is therefore a determining factor for thermal regulation, drought resistance, and flammability [17]. LMA is the inverse of the specific leaf area (SLA) and is a key indicator of resource allocation and plant strategies since it aggregates a wide range of organic compounds that can be separated into nitrogen-based constituents (proteins) and carbon-based constituents (including cellulose, lignin, hemicellulose, starch, and sugars) [18,19]. All of these four traits have specific spectral absorption features over the visible and near-infrared to short-wave infrared

range (VSWIR) or 0.4–2.5 μm range [20]: pigments absorb light mainly in the visible range from 400 to 750 nm, while both EWT and LMA absorb light in the near-infrared (NIR) and more strongly in the short-wave infrared range (SWIR).

In situ and laboratory measurements provide the most accurate estimations of leaf traits. However, considering the high costs and time consumption of laboratory analysis and the spatial limitations of field leaf sampling, estimating these traits using these techniques over large ecosystems is unrealistic. An alternative that has been increasingly and broadly used is leaf spectroscopy with the measurement of leaf optical properties (LOPs: leaf reflectance and transmittance) from VSWIR spectroradiometers [20]. In general, these estimation methods can be classified into three main categories: statistical methods, physical methods, and hybrid methods [21]. The first category uses a training dataset composed of concurrent leaf traits and LOP measurements to build regression models with a machine learning regression algorithm (MLRA). Applying the trained regression model upon LOP enables estimating the associated leaf trait values. Physical methods rely on LOP measurements and LOP simulations from radiative transfer models (RTMs) which relate leaf traits to LOP with a mechanistic description of the physical scattering processes that drives interactions between light and leaf constituents. Then, an inversion method is performed to estimate leaf traits by finding the best fit between the measured and simulated LOP among strategies including iterative optimization based on minimization algorithms [22] or look-up table (LUT) building [23]. The last category, called hybrid methods, combines aspects of both statistical and physical strategies. Hybrid methods build an inverse model with an MLRA trained on a synthetic dataset constituted by LOP simulations generated with an RTM [24]. On the one hand, physical and hybrid methods are RTM-based methods, i.e., they depend on the ability of the RTM to accurately simulate the physical processes by which LOPs are derived from leaf traits. On the other hand, statistical methods mainly depend on the properties of the training dataset and the MLRA fitting protocol.

Several RTMs with different levels of complexity to model leaf structure exist: from simplified 1D descriptions to very accurate 3D ones. The PROSPECT model is the most widely used leaf-scale RTM and has numerous versions, accounting for a large variety of leaf compounds (see ref. [25] for the original version, ref. [26] for versions 4 and 5, ref. [27] for version D, and ref. [18] for version PRO). It simulates directional-hemispherical LOPs from biochemical and morphological variables (including C_{ab} , C_{xc} , EWT, and LMA) and a unique structure parameter based on the generalized plate model (structure parameter N) [28]. Many research studies have used the PROSPECT model to estimate leaf traits for trees with computational efficiency from many optical databases and over a large variety of worldwide species [22,29,30]. Most studies have focused on leaf trait retrieval from mature and sunlit leaves at peak vegetation growth, but few do so throughout the whole phenological cycle, tackling seasonal variations and vertical crown heterogeneity, which affects plant light conditions [31–34] and which depends on the plant functional type, which for trees is either deciduous or evergreen [13]. Also, studies have mainly been conducted on a diversity of tree genera and a mix of species either in one particular ecosystem type [35] or in as many ecosystems worldwide as possible [30], in order to draw global conclusions on performance accuracy. Generally, this work has been conducted using one leaf trait estimation method category but little research has been conducted using all the three aforementioned categories [33] or on species from the same genus for comparison purposes [36]. This is because complete datasets encompassing all these variation sources (e.g., leaf position, seasonality, species, functional group, geographical areas, etc.) are complex to collect, and choosing the most appropriate estimation method requires having representative datasets. In addition, assessing the transferability of these methods trained on one dataset and applied to an independent one continues to be challenging and still requires research to achieve a global mapping of leaf traits. This has been recently investigated by Wang et al. [30], who demonstrated a good transferability of PROSPECT-based estimation methods in contrast to statistical methods based on partial least squares regressions. Moreover, to our knowledge,

hybrid methods have not been tested and compared to physical or statistical methods, although they could provide more stable inverse models than physical methods. Also, several studies have highlighted the need for prior information on the N leaf structure parameter for PROSPECT to achieve better leaf trait estimation performance [37]. The seasonal and intra-/interspecific variability in this parameter has been poorly studied but has been demonstrated to change between species and between different strategies for light environments (i.e., sun or shade), even within a single functional type [34]. The correlation of N with leaf thickness has already been emphasized [31], but previous studies have not yielded much knowledge on the cause of N discrepancy. Indeed, N simulates several optical effects occurring inside the leaf but does not represent a single concrete physical parameter of leaves. Hence, the interpretation of its value and variations is a thorny issue since cause–effect relationships cannot be clearly identified. Interpreting the variations in N, one is restricted to making assumptions based on the correlations of N with other variables. Secondly, we study the variations in N between species and seasons to provide a more detailed distribution of N. These more detailed distributions could be used in future studies as prior knowledge on N for simulating accurate optical properties, or to estimate leaf traits with LUT-based methods or hybrid methods, both at the leaf and canopy scales. For oak trees, some or all of the four traits (mainly C_{ab}) have been estimated for a given species [34,38,39], a selection of species [40], or a large variety of species within the genus [36] at the leaf level, while some have been estimated at the canopy level [24,41]. But to our knowledge, no study has simultaneously estimated all the four traits at the leaf level for several oak species, compared the three estimation method categories between seasons and sites sharing the same ecosystem type, and investigated variations in N.

Thus, the present study aims to estimate four leaf traits (C_{ab} , C_{xc} , EWT, and LMA) of oak trees by comparing statistical and PROSPECT-based methods (physical and hybrid) with the use of a unique dataset collected over three seasons (spring, summer and fall), measuring leaves of four oak species (including both deciduous and evergreen functional types) present in two ecosystems (woodland savannas and mixed broadleaf/conifer forests) along an elevation and a latitudinal gradient in the Sierra Nevada Range, California, USA. More specifically, the tackled scientific goals are (1) to study the distribution of the PROSPECT structural parameter N's values in our oak-specific dataset and its seasonal, intra- and interspecific variability; (2) to compare all the estimation methods and identify the most suitable one for each trait and for all of them; and (3) to explore the transferability of the statistical approach when trained on an independent dataset (here, the freely available ANGERS dataset [42], which expands the data to trees others than oaks). Finally, this study will bring new insights into the most appropriate estimation methods and their retrieval performance achieved for trees within the same genus (here, *Quercus*), and how these results can potentially be transferred to other oak species in comparison to more generalized datasets such as ANGERS.

Section 2 describes the datasets and further details the tested methods. Results are shown in Section 3 and are followed by discussions in Section 4.

2. Materials and Methods

2.1. Experimental Dataset

2.1.1. Oak Species and Study Sites

Four endemic Californian oak species were selected for our study, namely blue oak (*Quercus douglasii*), interior live oak (*Quercus wislizeni*), black oak (*Quercus kelloggii*), and canyon live oak (*Quercus chrysolepis*) [3]. More information, including their spatial distribution, leaf characteristics, and their respective acronyms (QUWI^(e), QUKE^(d), QUCH^(e), QUDO^(d)) that will be used throughout this article, is given in Figure 1, and on the websites of the California Native Plant Society (<https://calscape.org>; accessed on 18 September 2023) and UC Jepson eFlora (<https://ucjeps.berkeley.edu/eflora>; accessed on 18 September 2023). Superscript ^(d) (respectively ^(e)) in the species acronyms denote if the species is deciduous (respectively evergreen). QUDO^(d), commonly called blue oak, is a broadleaf deciduous tree

up to 18 m tall that is generally found in a ring bordering the Central Valley, in the lower reaches of the Sierra Nevada foothills, the San Francisco Bay Area, and both the Northern and Southern Coast Range, at between 150 m and 600 m elevation. QUDO^(d) is distributed on dry and well-drained slopes, prefers full sun exposure, and is drought-tolerant. Its dull blue-green deciduous leaves are oblong (length from 3 to 8 cm), with wavy or slightly lobed margins, and are pubescent below. QUWI^(e), commonly called interior live oak, is a broadleaf evergreen tree, up to 22 m tall, present in foothills and hot/dry canyons, being most abundant in the lower elevations of the Sierra Nevada but also widespread in the Pacific Coast Ranges at an elevation from sea level to 1500 m. Its evergreen alternate leaves are thick, leathery, small (2–5 cm), flat, generally elliptical, but shiny, lighter green below, and may have either toothed or smooth margins. QUCH^(e), called canyon live oak, grows up to 30 m tall and is the most widely distributed oak in California. QUCH^(e) is a broadleaf evergreen species and occurs in mountainous regions at an elevation from 30 m to 2800 m, growing close to creeks and drainage swales, in moist cool microhabitats (Sierra Nevada, Coast Ranges, etc.). Its leaves are flat, elliptical to oblong extending to an acute leaf tip (length from 2.5 to 8 cm), green dark and glossy above with spines, dull golden and hairy below. QUKE^(d), commonly known as the California black oak, is a broadleaf deciduous tree growing up to 35 m in height. It is found in pure or mixed stands, growing in a wide range of mixed evergreen forests, oak woodlands, and coniferous forests distributed from the foothills and lower mountains of California to elevations between 30 m and 2600 m. Its wide deciduous leaves are deeply lobed (length from 10 to 20 cm) with acute tips, dark and shiny green on top and pale and noticeably fuzzy underneath.

The study sites and their associated data collections between 2013 and 2014 are part of NASA's HypSIRI Preparatory Science initiative [44] and were collected by the CSTARS lab (University of California, Davis, CA, USA). The four sites are located at lower to medium elevations on the west side of the Sierra Nevada mountains and their foothills, in California, USA, with latitudes varying between 37° and 39° (250 km separate the most distant sites) and an elevation gradient between 200 m and 1500 m above sea level (Figure 1): Tonzi Ranch site (TONZ), San Joaquin Experimental Range site (SJER), Blodgett Forest site (BLOF) and Soaproot Saddle site (SOAP). They are highly instrumented sites and belong to the Ameriflux network (<https://ameriflux.lbl.gov/>; US-Ton, US-CZ1, US-Blo, US-xSP). TONZ and SJER are grass–oak–pine woodland savannas composed mainly of two vegetated active layers (excluding the presence of occasional shrubs): an understory of annual grass species and an overstory dominated by QUDO^(d) (40% cover) with sparse gray pines (*Pinus sabiniana*; 3 trees/ha) for TONZ and a mix of QUDO^(d), QUWI^(e), and gray pines for SJER. Both TONZ and SJER experience cattle grazing, TONZ on privately owned land and SJER on state-owned land managed jointly by the California State University's Agricultural Foundation and the US Forest Service. The major difference is that TONZ is classified as a woody savanna in the IGBP (International Geosphere–Biosphere Programme) ecosystem surface classification since its mean forest canopy cover is between 30% and 60% (specifically 47%), while SJER is classified as a savanna since its cover is lower (equal to 30%). Their mean annual temperature and precipitation are 15.8 °C and 559 mm and 16.5 °C and 485 mm, respectively [45]. BLOF is mainly covered by a productive mixed conifer forest and to a lesser extent by an oak forest. BLOF is managed by UC Berkeley from the Blodgett Forest Research Station to improve the understanding and management of commercial forest types. The temperature ranges from 0 °C to 9 °C in winter and from 14 °C to 32 °C in summer, with an average annual precipitation of 1651 mm [46]. SOAP is part of the US Forest Service's Major Land Resource Area. SOAP is composed of mixed mid-elevation conifer forests over a complex terrain of coarse hills, steep slopes, and narrow drainage basins. The SOAP overstory is dominated by ponderosa pine (*Pinus ponderosa*) and incense cedar (*Calocedrus decurrens*), with co-dominant QUCH^(e) and QUKE^(d). The annual temperature and rainfall average 13.4 °C and 900 mm, respectively [47]. Finally, all sites experience a Mediterranean-type climate with hot and dry summers, with precipitation occurring mainly from October to May.

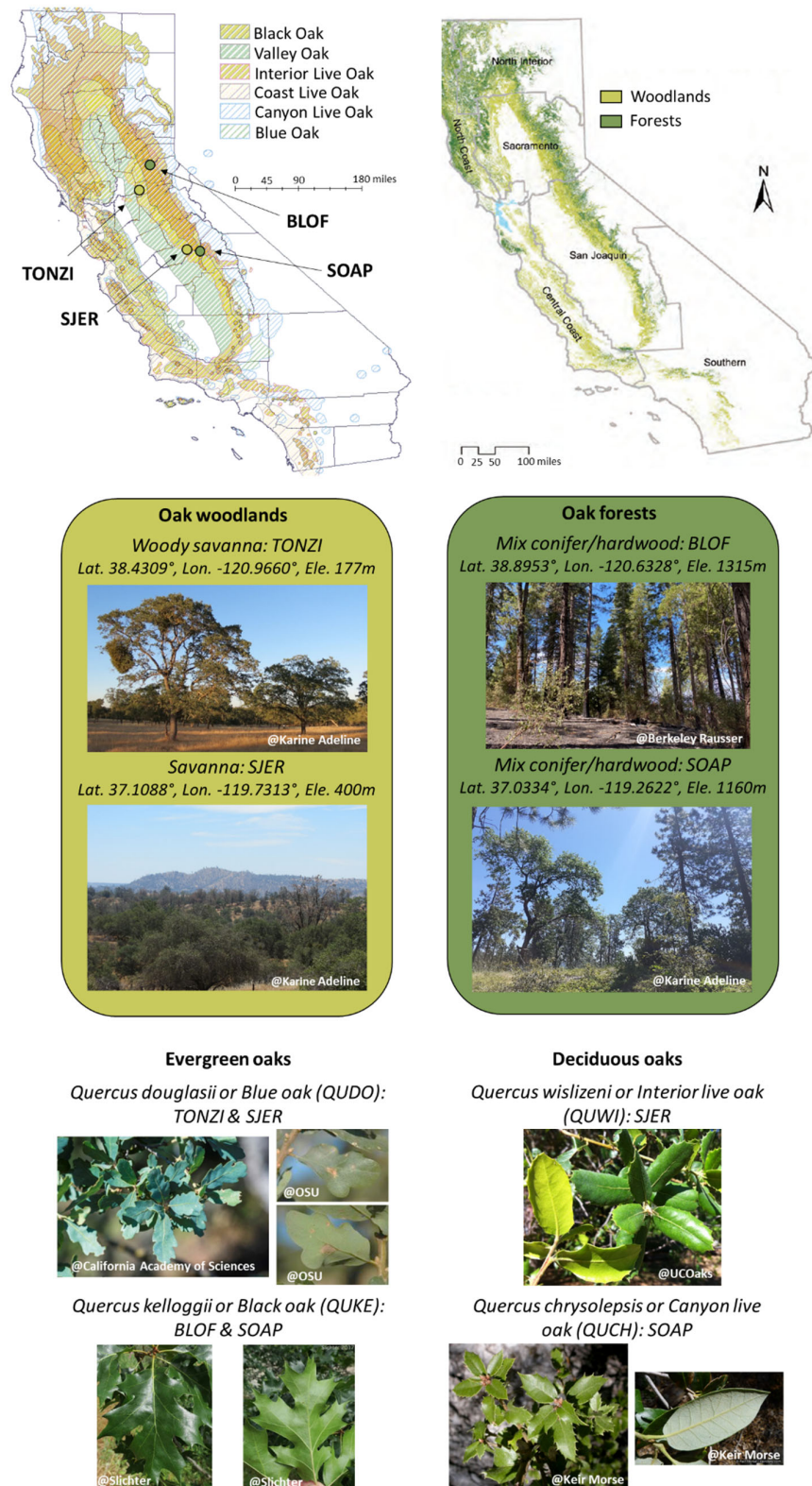


Figure 1. (Top): distribution map of six endemic California oak species (adapted from [43]) and oak ecosystem types, woodlands (including savannas) and forests (adapted from [4]). (Middle): descriptive photos of the four study sites with their geographic coordinates. (Bottom): photos of the leaves (adaxial and abaxial side) of the four studied oaks with their scientific name, common name, acronym in brackets (following the USDA Plant Database, <https://plants.usda.gov/>), and sites where they were sampled.

2.1.2. Leaf Sampling

The dataset contains a total of 114 leaf samples collected during 5 field campaigns in 2013 and 2014 over 3 seasons (i.e., spring, summer and fall) (Table 1). The number of sampled trees per site and per season is given in Table 2. QUDO^(d) is the species with the highest number of samples, with 44 trees, followed by QUKE^(d) with 31 trees. QUCH^(e) and QUWI^(e) are only present on one site and therefore fewer trees were sampled (circa 20 trees).

Table 1. Dates of field campaigns (format DD/MM).

Site	2013		2014		
	Summer	Fall	Spring	Summer	Fall
BLOF	-	30/09	22/04	02/06	04/11
SJER	19/06	07/11	11/04	11/06	21/10
SOAP	16/06	09/11	12/04	14/06	28/10
TONZ	11/06	24/09	17/04	06/06	06/10

Table 2. Sample distribution for each species, season, and site.

Species	Season	BLOF	SJER	SOAP	TONZ	Total
QUKE ^(d)	Spring	6	-	5	-	11
	Summer	4	-	9	-	13
	Fall	-	-	7	-	7
	Total	10	-	21	-	31
QUCH ^(e)	Spring	-	-	5	-	5
	Summer	-	-	2	-	2
	Fall	-	-	12	-	12
	Total	-	-	19	-	19
QUDO ^(d)	Spring	-	5	-	5	10
	Summer	-	9	-	8	17
	Fall	-	8	-	9	17
	Total	-	22	-	22	44
QUWI ^(e)	Spring	-	3	-	-	3
	Summer	-	8	-	-	8
	Fall	-	9	-	-	9
	Total	-	20	-	-	20
TOTAL				114		

Around 4 to 10 plots were distributed along each study site to cover the full variation in species composition and canopy density. Species and plots sampled during each season varied by site. Plots dominated by deciduous species were measured in all three seasons in order to analyze the temporal evolution of the vegetation while plots dominated by evergreen species were measured at most during two seasons.

In each plot, a representative tree (not too big, not too small) with accessible leaves was selected. Two sets of leaves were collected from the upper and sunlit portion of the canopy from five selected individuals per species (five samples) with a tree trimmer. For evergreen species, new leaves were not collected with the assumption that previous years' leaves made up the majority of the canopy regardless of the season. The first set of leaves was placed in a sterilized and previously weighed plastic bag for water and dry matter content estimation, while the second set of leaves was placed in foil packets (to avoid the light from reaching them) for spectral measurements and pigment extraction. Both sets were stored on blue ice in coolers until they arrived at the lab, where they were placed in a

lab refrigerator. Leaf measurements were conducted less than 48 h after they were removed from the plant.

2.1.3. Leaf Spectral Measurements

From the second set of leaves, leaf directional-hemispherical reflectance and transmittance [48] were measured in five randomly selected leaves from each individual (or sample) using an ASD FieldSpec Pro (1–2 nm sampling interval, with 3–10 nm resolution) attached to a Licor 1800-12 integrating sphere with a 6 V 10 W 3100 K illumination source [49]. The spectra were collected in radiance from 350 to 2500 nm. The protocol also involved the measurements of the reference material illumination I_r and stray radiation illumination I_d . Reflectance R_s and transmittance T_s of samples were derived using the equation provided by the manufacturer and described below [49]. The manufacturer also provides the intrinsic reflectance of the sphere reference material R_r .

$$R_s = \frac{(I_s - I_d)R_r}{I_r - I_d} \quad (1)$$

$$T_s = \frac{I_s R_r}{I_r} \quad (2)$$

where I_s is the measured sphere output when the sample is illuminated and I_r is the measured sphere output when the reference material is illuminated.

The five processed spectra per sample were averaged. Then, a Savitzky–Golay filter was applied to smooth the SWIR part of the spectrum (1600–2500 nm).

2.1.4. Leaf Trait Measurements

C_{ab} , C_{xc} , EWT, and LMA are four leaf functional traits expressed as the mass contained per unit of leaf area. Therefore, the measurement protocol of leaf traits involves measuring the leaf area and the respective mass of each family of compounds.

To derive leaf area (further noted A), in both leaf sets, all the leaves were scanned with 150 dpi using a white background to amplify the contrast between the leaves and the background. The leaves were placed far enough apart to avoid overlapping or contact between them. A supervised classification was then applied using the support vector machine implemented in ENVI 5.0 software. Two ROIs (regions of interest) were used to define the training areas. One ROI represents the white background, and the other ROI represents the leaf. The results from the leaf class were converted to a vector shapefile, each vector representing an individual leaf. Finally, the area of each vector (i.e., each leaf) was estimated using ArcGIS 10.1 software. Additionally, leaf thickness was measured with a caliper.

To determine the mass of leaf pigments from the second set of leaves, leaf samples were frozen in liquid nitrogen immediately after the spectral measurements. They were stored frozen for a short time and then lyophilized. Pigment extraction was conducted with 90% acetone (14 mL) for 48 h. Each vial contained one sample (5 leaves from one individual). Three replicates were taken from each vial. A PerkinElmer Lambda 25 UV/Vis spectrophotometer was used with concentrations of chlorophylls and carotenoids of 23 mg/mL and 8 mg/mL (PerkinElmer, Waltham, MA, USA). A detailed explanation of the lab protocol is explained in the work of Lichtenthaler et al. [50,51]. Then, the mass of chlorophylls a and b ($m_{chlorophylls}$) and the mass of carotenoids ($m_{carotenoids}$) were derived from concentrations measured in the solutions and used with leaf area A to compute the C_{ab} and C_{xc} values following Equations (3) and (4).

$$C_{ab} = \frac{m_{chlorophylls}}{A} \quad [\mu\text{g}\cdot\text{cm}^{-2}] \quad (3)$$

$$C_{xc} = \frac{m_{carotenoids}}{A} \quad [\mu\text{g}\cdot\text{cm}^{-2}] \quad (4)$$

To derive EWT and LMA from the first set of leaves, ziplock bags with leaf water samples were weighed empty and then they were weighed again with leaves. Leaves were dried at 60 °C for a minimum of 48 h in an oven. Dry and fresh weights (respectively, m_{dry} and m_{fresh}) were used with leaf area A to compute LMA and EWT following Equations (5) and (6).

$$EWT = \frac{m_{fresh} - m_{dry}}{A} \rho_{water} \quad [\text{cm}] \quad (5)$$

$$LMA = \frac{m_{dry}}{A} \quad [\text{g} \cdot \text{cm}^{-2}] \quad (6)$$

One could notice that the density of water (ρ_{water}) is a factor in the computation of EWT. Therefore, EWT is expressed as a length, its values are given in cm, and for this very reason, EWT is actually an equivalent thickness.

Mean statistics for each leaf trait are given in Table 3 and more detailed distributions per species are given in Figure 2. Globally, evergreen species tend to have higher values of leaf traits than deciduous species (Figure 2). Interspecies discrepancy is particularly visible for LMA, where each species appears to have a specific range of values. Table 4 gives the correlation between leaf trait values, all species considered. C_{ab} and C_{xc} show the highest correlation (0.92) and are both correlated to LMA (over 0.5). EWT is the least correlated to other leaf traits (around 0.25 with pigments-related traits and 0.43 with LMA).

Table 3. Basic statistics of CSTARs dataset (ours) compared to ANGERS dataset for the four leaf traits.

ANGERS/CSTARs	C_{ab} ($\mu\text{g} \cdot \text{cm}^{-2}$)	C_{xc} ($\mu\text{g} \cdot \text{cm}^{-2}$)	EWT (cm)	LMA ($\text{g} \cdot \text{cm}^{-2}$)
Mean	33.6/33.9	8.7/8.7	0.0112/0.0116	0.0124/0.0052
Standard Dev.	13.2/21.7	2.8/5.1	0.0026/0.0049	0.0043/0.0036
Min.	0.8/0.5	0.0/2.0	0.0044/0.0050	0.0017/0.0045
Max.	106.7/68.4	25.3/17.8	0.0340/0.0202	0.0331/0.0215

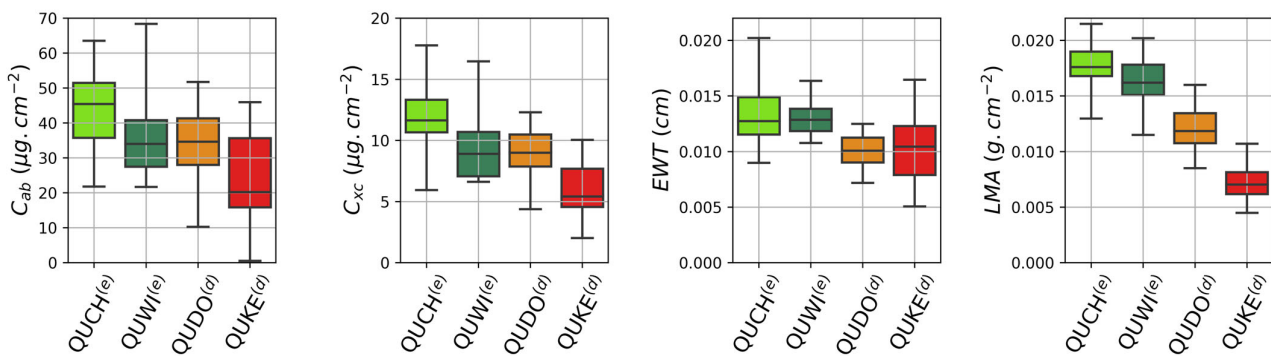


Figure 2. Boxplot of leaf trait values pooled by tree species. Whiskers indicate minimal and maximal values.

Table 4. Correlation matrix for the four leaf traits obtained by pooling all species, sites, and seasons.

	C_{ab}	C_{xc}	EWT	LMA
C_{ab}	1.00	0.92	0.24	0.52
C_{xc}		1.00	0.26	0.66
EWT			1.00	0.43
LMA				1.00

Average leaf thickness, regardless of species, is 0.29 mm, although it shows discrepancies between species, similar to LMA. Indeed, average leaf thickness per species follows the same trend as LMA; the smallest values are those for QUKE^(d) (0.24 mm) followed by QUDO^(d) (0.28 mm), QUWI^(e) (0.32 mm), and QUCH^(e) (0.35 mm). In fact, leaf thickness is slightly correlated to LMA (0.68), but with a higher correlation than EWT (0.56).

As expected, leaf thickness is even more correlated to leaf surface weight (sum of LMA and EWT; 0.73), which represents the quantity of matter per unit area of leaf, all types of compounds included.

Finally, our dataset is further named the CSTARTS dataset and comprises both leaf spectra and leaf traits.

2.2. Supplementary Dataset

ANGERS is a dataset collected at INRA in June 2003 in Angers (France) [26,42]. ANGERS contains 276 samples from 43 plant species. Samples contain joint measurements of leaf biochemistry (including C_{ab} , C_{xc} , EWT, and LMA) and spectral measurements (directional-hemispherical reflectance and transmittance between 400 and 2450 nm). ANGERS is freely available on the Opticleaf website (<http://opticleaf.ipgp.fr/index.php?page=database>; accessed on 1 September 2023). In ANGERS, 4 oak samples are present: 2 from *Quercus palustris* (deciduous) and 2 from *Quercus ilex* L. (evergreen). These data were used as a reference to calibrate the specific absorption coefficients of chlorophylls and carotenoids in PROSPECT (versions 5 and D) [26,27]. The main statistics computed for leaf traits (Table 3) are compared with those of our dataset.

2.3. Estimation Methods

Two strategies were selected for the physical category (Section 2.3.2): iterative optimization (Section 2.3.2.1 Iterative Optimization Inversion) and LUT-based inversions (Section 2.3.2.2 LUT-Based Inversion). Statistical strategies are presented in Section 2.3.3 and hybrid strategies in Section 2.3.4. The organization chart of all tested methods is given in Figure 3.

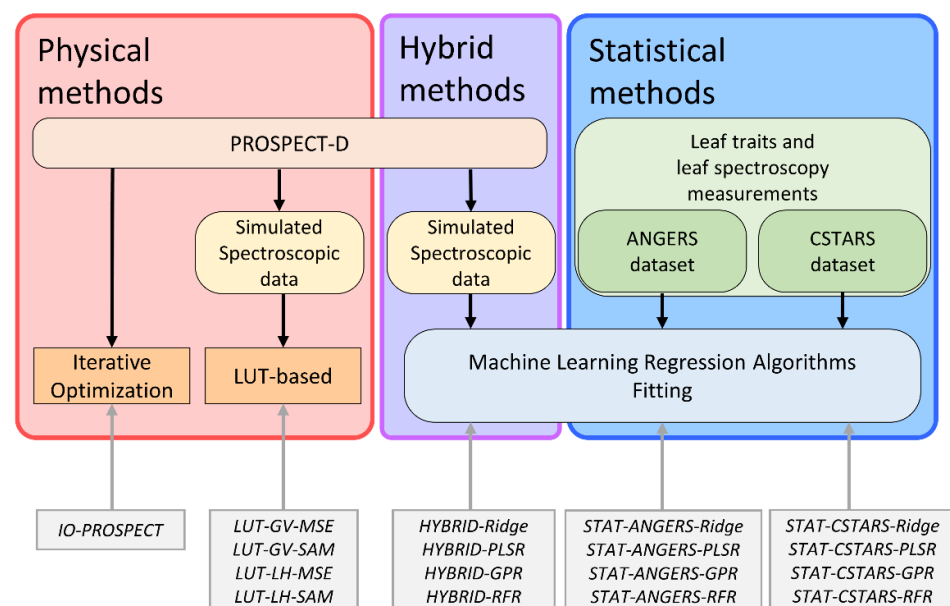


Figure 3. Organization chart of methods. For detailed description of the used acronyms, please refer to the following subsections.

For both statistical and hybrid strategies, the same four MLRAs were used. These MLRAs are presented in Section 2.3.3: ridge regression (Section 2.3.3.1), partial least squares regression (Section 2.3.3.2), Gaussian process regression (Section 2.3.3.3), and random forest regression (Section 2.3.3.4). All estimation strategies were implemented in Python language. Version D of PROSPECT [27] was used for PROSPECT-based methods (physical and hybrid methods) implemented in Python language (<https://github.com/jgomezdans/prosail> (accessed on 1 September 2023); DOI: 10.5281/zenodo.2574925).

All the methods estimate the traits separately, except IO-PROSPECT. The IO-PROSPECT method uses all the spectral bands in the [400–2500] nm range (see Section 2.3.2.1 Iterative Optimization Inversion). For all the other methods, leaf traits are estimated separately, and prior selection of spectral ranges from LOPs is important since only parts of the spectrum are sensitive to the targeted leaf traits. The selection of spectral ranges is further explained in Section 2.3.1.

2.3.1. Selection of Spectral Ranges Adapted for Each Leaf Trait

Sun et al. [52] conducted a sensitivity analysis to determine which spectral ranges are altered by a given trait. C_{ab} have a dominant effect between 500 and 750 nm. C_{xc} alters reflectance and transmittance spectra only between 450 and 550 nm and plays a dominant role in an even narrower band around 500 nm. EWT dominates leaf spectra variations at wavelengths above 1400 nm. EWT also alters leaf reflectance and transmittance at shorter wavelengths between 900 and 1400 nm since liquid water has absorption bands around 950 nm and 1200 nm. LMA alters leaf reflectance and transmittance in the near-infrared and short-wave infrared regions, although its effects are never dominant at wavelengths in the optical domain. Thus, in our study we used the following spectral ranges: [450–760] nm for C_{ab} , [450–560] nm for C_{xc} , [900–2400] nm for EWT, and [750–2400] nm for LMA.

2.3.2. Physical Methods

2.3.2.1. Iterative Optimization Inversion

The inversion of PROSPECT based on iterative optimization consists in minimizing the residual error between measured and PROSPECT predicted spectra. This method is further named IO-PROSPECT.

This minimization is performed through cost function C and an optimization algorithm that explores the input parameter space of the PROSPECT model. As an optimization algorithm, we used the modified Powell's algorithm [53] implemented in the *scipy.optimize* Python module. Cost function C is here defined as the Euclidean distance between spectra and the computed sum of the squared error for all considered n wavelengths λ .

$$C = \sum_{\lambda=\lambda_1}^{\lambda_n} \left[\left(R_{pred, \lambda} - R_{meas, \lambda} \right)^2 + \left(T_{pred, \lambda} - T_{meas, \lambda} \right)^2 \right] \quad (7)$$

Five parameters are considered as inputs by the optimization algorithm during the minimization process: the four leaf traits (C_{ab} , C_{xc} , EWT, LMA) and the structural parameter N . Thus, for IO-PROSPECT, and only for this method in our study, the four leaf traits and the structural parameter N are estimated simultaneously. Moreover, to keep all parameters in a realistic range of values during the optimization process, we added constraints to parametrize Powell's algorithm. We considered the following minimal and maximal values in the minimization process: [0–5] for N , [0.0–50.0] $\mu\text{g}\cdot\text{cm}^{-2}$ for C_{ab} , [0.0–50.0] $\mu\text{g}\cdot\text{cm}^{-2}$ for C_{xc} , [0.00–0.07] cm for EWT, and [0.00–0.07] $\text{g}\cdot\text{cm}^{-2}$ for LMA. Powell's algorithm was initialized with known average values of leaf traits: 1.8 for N , 40 $\mu\text{g}\cdot\text{cm}^{-2}$ for C_{ab} , 10 $\mu\text{g}\cdot\text{cm}^{-2}$ for C_{xc} , 0.015 cm for EWT, and 0.015 $\text{g}\cdot\text{cm}^{-2}$ for LMA.

In the minimization process, all the wavelengths available between 400 nm and 2400 nm were considered. Although the cost function can include wavelength-dependent weights [37], we chose to grant the same weights for all the wavelengths.

2.3.2.2. LUT-Based Inversion

LUT synthetic spectra were generated with PROSPECT-D following two sampling schemes as already described in previous studies [54].

- Sampling #1: In this first approach, parameter values are generated through a Latin hypercube (LH) sampling scheme built with *pyDOE* Python library. LH sampling enables generating random samples that are evenly distributed over the parameter space. LH sampling maintains the properties of a uniformly distributed sampling but

has the advantage of requiring a much smaller sample number than simple uniform random sampling to cover all the considered space. For each variable, we define a specific sampling range: [0.8–3.5] for N , [0.0–100.0] $\mu\text{g}\cdot\text{cm}^{-2}$ for C_{ab} , [0.0–30.0] $\mu\text{g}\cdot\text{cm}^{-2}$ for C_{xc} , [0.00–0.05] cm for EWT, and [0.00–0.05] $\text{g}\cdot\text{cm}^{-2}$ for LMA.

- **Sampling #2:** In this second approach, the four leaf trait values (C_{ab} , C_{xc} , EWT, and LMA) are generated as a Gaussian vector (GV). This approach aims to take into account actual correlations between the constituents. The traits are sampled as a Gaussian random vector where the mean vector is derived from the empirical average in Table 4 and the covariance matrix between four variables is derived from an empirical covariance matrix of the measured samples (Table 3). This sampling scheme is designed to reduce the number of unrealistic optical properties that are likely simulated with LH (sampling #1). This sampling scheme introduces prior information on the values of the parameters. To keep the sampled values in a realistic range, we truncated the multivariate Gaussian with the following bounds: [0.0–100.0] $\mu\text{g}\cdot\text{cm}^{-2}$ for C_{ab} , [0.0–30.0] $\mu\text{g}\cdot\text{cm}^{-2}$ for C_{xc} , [0.00–0.05] cm for EWT, and [0.00–0.05] $\text{g}\cdot\text{cm}^{-2}$ for LMA. Samples were drawn from the truncated law with the acceptance–rejection method. N parameter values were drawn from a uniform law between 0.8 and 3.5 and independent from the multivariate Gaussian law of leaf traits.

For both sampling schemes, the number of PROSPECT simulations is 10,000.

The LUT-based approach consists in finding the trait values that minimize the distance function between the measured spectrum and the computed spectra in the LUT. Two functions are used as distance measures to retrieve the optimal solution within the LUT: the mean square error (MSE) and spectral angle mapper (SAM). Both distances are computed for all the $n = 2101$ wavelengths λ between $\lambda_1 = 400$ nm and $\lambda_n = 2400$ nm. The distances are computed separately between measured reflectance R_{meas} and computed reflectance R_{simu} and between measured transmittance T_{meas} and computed transmittance T_{simu} .

The mean square error is defined for two vectors as the normalized squared Euclidean norm of their difference as in Equation (8) below.

$$MSE = \frac{1}{2n} \sum_{\lambda=\lambda_1}^{\lambda_n} \left[(R_{simu,\lambda} - R_{meas,\lambda})^2 + (T_{simu,\lambda} - T_{meas,\lambda})^2 \right] \quad (8)$$

The SAM between two vectors is defined from their dot product. As described in Equation (9), we sum the SAM for reflectance and for transmittance as the distance measure.

$$SAM = \left[\frac{\sum_{\lambda=\lambda_1}^{\lambda_n} R_{simu,\lambda} R_{meas,\lambda}}{\sqrt{\sum_{\lambda=\lambda_1}^{\lambda_n} R_{simu,\lambda}^2} \sqrt{\sum_{\lambda=\lambda_1}^{\lambda_n} R_{meas,\lambda}^2}} \right] + \left[\frac{\sum_{\lambda=\lambda_1}^{\lambda_n} T_{simu,\lambda} T_{meas,\lambda}}{\sqrt{\sum_{\lambda=\lambda_1}^{\lambda_n} T_{simu,\lambda}^2} \sqrt{\sum_{\lambda=\lambda_1}^{\lambda_n} T_{meas,\lambda}^2}} \right] \quad (9)$$

LUT-based methods are further named LUT-SS-FFF, where SS is the sampling scheme used (LH or GV) and FFF the distance function (MSE or SAM).

This inversion problem is ill posed, meaning that multiple sets of PROSPECT parameters can yield similar spectra. To alleviate this ill-posedness and increase estimation robustness, the mean trait values corresponding to the set of q best-matching spectra were considered as the final solution.

The optimal number of best-matching cases q^* used for the inversion was determined on a per-variable basis. q^* is the value of q that minimizes the RMSE between field data and estimations. Therefore, inversions were performed considering several values for q :

$$\{1, 2, 3, 5, 8, 10, 15, 20, 30, 50, 75, 100, 150, 200, 300, 500, 750, 1000, 1500, 2000\}$$

The optimal values obtained for each sampling method and distance function are given in Table 5.

Table 5. Optimal q^* values of LUT-based strategies for each sampling scheme and distance function.

	C_{ab}	C_{xc}	EWT	LMA
LUT-GV-MSE	200	750	3	1000
LUT-GV-SAM	500	1500	3	50
LUT-LH-MSE	8	3	2	2000
LUT-LH-SAM	150	2000	2	200

2.3.3. Statistical Methods

Statistical methods differ by training dataset and MLRA used to build the statistical relationship between LOPs and reference leaf trait values. In this study, we focus on the comparison of four MLRAs, namely Gaussian process regression (GPR), partial least square regression (PLSR), random forest regression (RFR), and ridge regression (Ridge). We consider two training datasets, namely ANGERS and CSTARTS. The training and evaluation strategies are slightly different for the ANGERS or CSTARTS datasets and are detailed in Section 2.3.3.5 Training Strategies. These methods are further named STAT-*DDDDDD-*Algo** where *DDDDDD* is the dataset used as training data (ANGERS or CSTARTS) and *Algo* is the MLRA used (GPR, PLSR, RFR or Ridge). We implement the statistical methods from the Python *scikit-learn* library.

2.3.3.1. Ridge Regression

Ridge regression is a regularized ordinary least squares linear regression. Ridge regression is a parametric model that finds a linear relationship between the input and the output: $y_i = w^T x_i$. To address the overfitting issue, cost function is regularized by the L2 norm of the model weights w , as detailed in Equation (10):

$$C = \|Y - w^T X\|_2^2 + \alpha \|w\|_2^2 \quad (10)$$

where α is the regularization hyperparameter. α controls the amount of shrinkage for the model weights. Ridge uses an L2 norm, while other regularized algorithms such as LASSO use an L1 norm. Penalization with an L1 norm would result in a sparse model with few non-zero coefficients, equivalent to a selection of spectral bands. However, in this study, we want to keep most of the coefficients as non-zero values to obtain a model that accounts for all the spectral band information and is more robust to wavelength-independent noise.

2.3.3.2. Partial Least Squares Regression

PLSR is a linear parametric model [55]. The PLSR algorithm is designed and well suited for problems where there is multicollinearity among the features and is thus widely used in chemometrics, particularly to quantify relationships between biochemicals and their spectral properties. The algorithm seeks to maximize the covariance between inputs and target values projecting the inputs onto l orthogonal components (also called latent vectors). Like ridge regression, PLSR is a form of regularized linear regression where the strength of regularization is controlled by the number of components l . If too many components are kept, PLSR can overfit the training data. Thus, the number of components l is determined with cross-validation (see Section 2.3.3.5 Training Strategies).

2.3.3.3. Gaussian Process Regression

Gaussian Process Regression (GPR) is a kernel-based machine learning algorithm [56]. GPR is a Bayesian approach and a non-parametric algorithm, meaning that it does not make any assumptions about the functional form of the underlying relationship between the input and output variables.

With GPR, the approximation of the target function is built with a Gaussian stationary process, with prior covariance specified by a kernel object. In the fitting process, the Gaussian process is then constrained from the training samples optimizing the kernel hyperparameters by maximizing the log marginal likelihood.

We used an implementation based on Algorithm 2.1 from [56]. As the kernel, we used the sum of a radial basis function (RBF) kernel and a white kernel. The first kernel helps to deal with non-linearity while the latter specifies the noise level in the targets.

The RBF kernel is defined for two samples x_i and x_j by length scale parameter γ following Equation (11).

$$K_{RBF}(x_i, x_j) = \exp\left(-\frac{\|x_i - x_j\|_2^2}{2\gamma^2}\right) \quad (11)$$

The white kernel is defined for two samples x_i and x_j by noise level parameter σ following Equation (12).

$$K_w(x_i, x_j) = \sigma \text{ if } x_i = x_j \text{ else } 0 \quad (12)$$

γ and σ are the two parameters that are optimized during the fitting of GPR.

2.3.3.4. Random Forest Regression

Random forest regression (RFR) is an ensemble method derived from a decision tree algorithm [57]. With RFR, a set of n_{trees} decision trees are built from a bootstrap sampling of the training data. The prediction of the ensemble is given as the averaged prediction of all the individual decision trees. This strategy injects randomness into the fitting process and leads to more robust predictions than decision trees.

Here, we chose $n_{trees} = 500$, which is considered enough to reach a good prediction accuracy but is not the optimal number of trees.

2.3.3.5. Training Strategies

The model training and fitting processes were the same for both the STAT-CSTARS and STAT-ANGERS categories. For all algorithms, a different final calibrated model was built for each leaf trait, accounting for all the spectral bands included in the spectral range, which is trait-dependent (see Section 2.3.1). Reflectance and transmittance measurements were scaled by removing the mean and scaling to unit variance. For PLSR and ridge regression, the optimal values of their respective hyperparameters were determined with a five-fold cross validation (5-CV) and using an exhaustive grid search (for ridge: $\alpha \in \{2^{-16}; 2^{-15}; \dots; 2^{10}\}$, for PLSR: $l \in \llbracket 1; 15 \rrbracket$).

Evaluation strategies differed for STAT-CSTARS and STAT-ANGERS. For STAT-ANGERS, all the data were used for training. Then, for the test, the trained model was applied on the full CSTARS dataset to estimate leaf trait values and compute the validation metrics (see Section 2.4). For STAT-CSTARS, data were randomly split into train (75%) and test (25%) datasets. This process was repeated 10 times in order to build 10 trained models for each of the 4 studied MLRAs. Each time, we evaluated the trained model on the remaining 25% of the CSTARS dataset to compute the validation metrics (Section 2.4). Finally, for each validation metric, the 10 values were averaged to compute their expected values.

2.3.4. Hybrid Methods

The tested hybrid methods use MLRAs presented in the previous subsection (Section 2.3.3: GPR, PLSR, RFR, or ridge). For the hybrid methods, MLRAs were trained on synthetic datasets generated with the PROSPECT-D model. Here, the synthetic dataset was built using a GV random sampling scheme (Sampling #2) in order to minimize the number of unrealistic sets of traits and to cover the subspace of realistic parameter values with fewer points.

MLRAs were trained using the training protocol detailed in Section 2.3.3.5 for the ANGERS dataset.

To train the MLRAs, the influence of training dataset size was tested by considering several sizes of the synthetic training dataset (250, 500, 1000, 1500, 2000, 2500, 5000,

and 10,000 samples). The trained MLRAs were then tested on another independently generated GV-sampled PROSPECT-D synthetic dataset comprising 1000 samples. These preliminary results showed that with more than 1000 samples, there was no additional significant improvement in RMSE. Therefore, we only used 1000 samples from the synthetic dataset, which constituted a reasonable trade-off between computation time and performance estimation.

The hybrid methods are further named Hybrid-*Algo* where *Algo* is the MLRA used (GPR, PLSR, RFR, or Ridge).

2.4. Validation Metrics

The performance of the calibrated models on the CSTARS dataset was evaluated using the coefficient of determination (R^2), root mean squared error (RMSE), and bias (BIAS).

If v denotes the vector of n measured values and \hat{v} is the vector of n estimated values, these scoring metrics can be computed with Equations (13)–(15).

$$RMSE(\hat{v}, v) = \sqrt{\frac{1}{n} \sum_{i=1}^n (\hat{v}_i - v_i)^2} \quad (13)$$

$$R^2(\hat{v}, v) = 1 - \frac{\sum_{i=1}^n (\hat{v}_i - v_i)^2}{\sum_{i=1}^n (v_i - \bar{v})^2} = 1 - \frac{RMSE}{Var(v)} \quad (14)$$

$$BIAS(\hat{v}, v) = \frac{1}{n} \sum_{i=1}^n (\hat{v}_i - v_i) \quad (15)$$

3. Results

3.1. Variability in PROSPECT N Structural Parameter

The parameter N has a major influence on LOPs simulated by the PROSPECT model since an increase in N tends to increase leaf reflectance and lower leaf transmittance. For example, Figure 4 highlights that a variation of 0.5 in N implies an increase in reflectance of 0.1 in the NIR region.

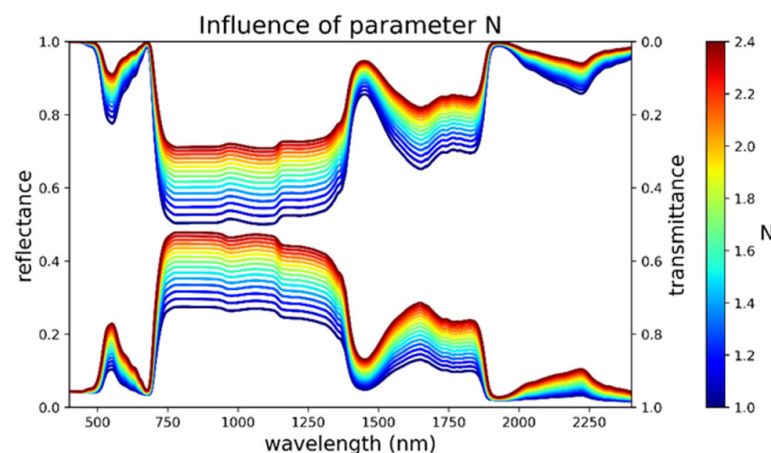


Figure 4. Influence of the leaf structural parameter N on PROSPECT simulations for the following leaf composition: $C_{ab} = 33 \mu\text{g}\cdot\text{cm}^{-2}$, $C_{xc} = 8.7 \mu\text{g}\cdot\text{cm}^{-2}$, EWT = 0.015 cm, and LMA = $0.015 \text{ g}\cdot\text{cm}^{-2}$.

All estimated N values for each sample (i.e., tree) in the CSTARS dataset are within the range 1.0–2.4 (Figure 5). Globally, QUKE^(d) has the lowest N median value while QUCH^(e) has the highest N, with an absolute difference of 0.6. In comparison, QUDO^(d) and QUWI^(e) have comparable median values. The range of N values for QUKE^(d) and QUWI^(e) is 0.8, whereas it is 0.6 for QUDO^(d) and QUCH^(e). These results show the inter- and intraspecies

variability in N can be larger than 0.5 and would be mirrored by the variability in LOPs. No site dependency is observed for N for the QUKE^(d) and QUDO^(d) species (Table 6).

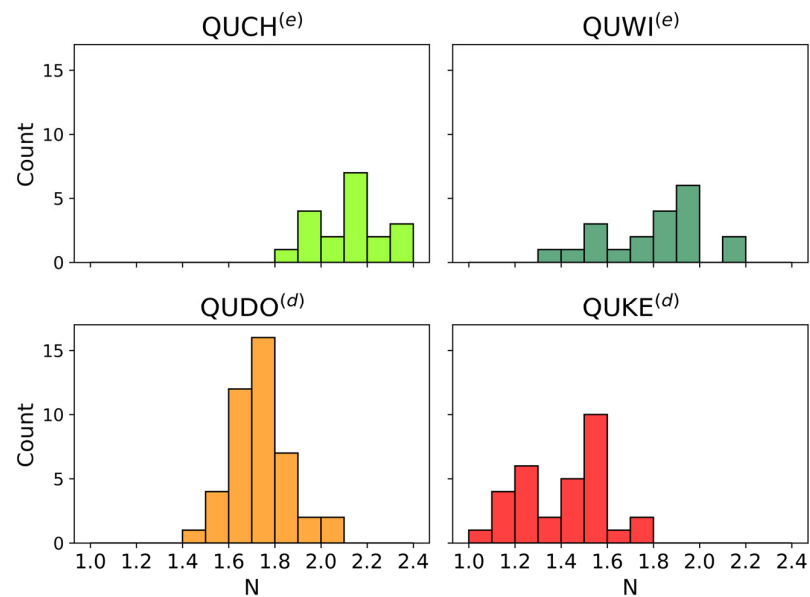


Figure 5. Histograms of estimated PROSPECT leaf structural parameter N values for each species and per plant functional type (light and dark green: evergreen, orange and red: deciduous).

Table 6. Basic statistics of estimated PROSPECT leaf structural parameter N by species and sites.

Species	QUCH ^(e)	QUWI ^(e)	QUKE ^(d)			QUDO ^(d)		
Site	SOAP (n = 19)	SJER (n = 20)	BLOF (n = 10)	SOAP (n = 21)	All (n = 31)	SJER (n = 22)	TONZ (n = 22)	All (n = 44)
Mean	2.13	1.81	1.27	1.48	1.42	1.79	1.68	1.74
Std.	0.14	0.23	0.17	0.15	0.18	0.11	0.11	0.12
Med.	2.12	1.85	1.21	1.58	1.46	1.78	1.69	1.73
Min.	1.85	1.37	1.04	1.19	1.04	1.62	1.46	1.46
Max.	2.36	2.18	1.54	1.77	1.77	2.05	1.93	2.06

For deciduous species, N has a seasonal influence since its value increases from spring to fall. But it is small for QUDO^(d), with median N values from 1.67 in spring to 1.76 in the fall. In contrast, it is large for QUKE^(d), with median variations from 1.22 to 1.60 (Figure 6). For evergreen species, no seasonal trend is clearly noticeable, mainly due to the lack of data in summer for QUCH^(e) and spring for QUWI^(e).

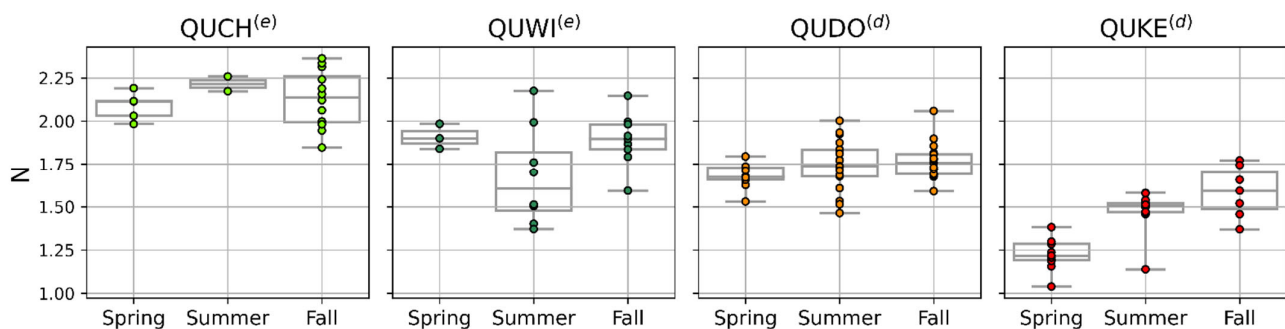


Figure 6. Boxplot representation of PROSPECT leaf structural parameter N distribution for all species. Whiskers depict minimal and maximal values.

Estimated values of N are highly correlated with LMA (Pearson correlation coefficient equals 0.82; see Figure 7). For comparison, the three other leaf traits (C_{ab} , C_{xc} , and EWT) show less correlation with estimated N (respectively, 0.39, 0.56, and 0.25). Moreover, estimated N is less correlated with leaf thickness (0.59) and leaf surface weight (sum of EWT and LMA; 0.69) than with LMA.

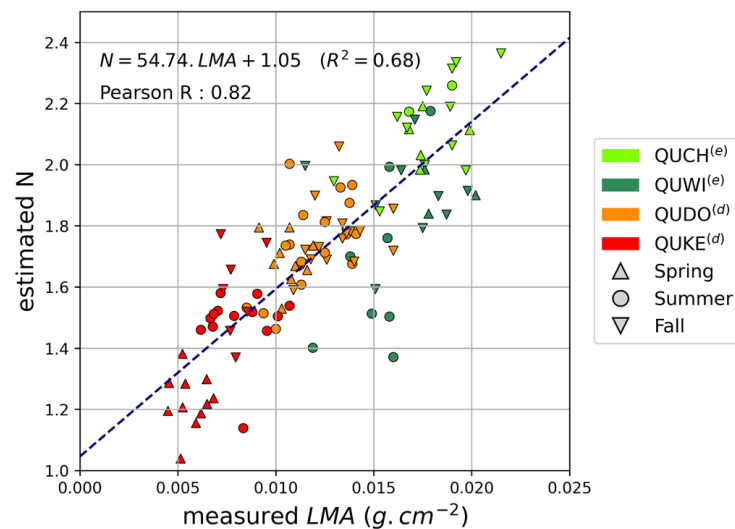


Figure 7. Comparison between measured LMA and estimated values of PROSPECT leaf structural parameter N.

3.2. Leaf Trait Estimations

This section is divided into four subsections, each one describing the results for one leaf trait. For each leaf trait, all the accuracy metrics of all methods are compared for the whole CSTARS dataset. Detailed metric values by species and season are given for the two methods with the best accuracy (with the exception of C_{xc} due to comparable performance of two methods). Additionally, scatterplots compare estimates to measured leaf trait values for the most accurate method within each subcategory (cf. gray blocks in Figure 3). Two representations are chosen to display these scatterplots, the first by species and the second by season, in order to highlight potential specific or seasonal trends.

3.2.1. Chlorophyll Content

Higher accuracy was obtained for the STAT-CSTARS category, regardless of the chosen MLRA, with mean performance giving an RMSE equal to $5.7 \mu\text{g}/\text{cm}^2$, R^2 around 0.77, and a bias under $0.3 \mu\text{g}/\text{cm}^2$ (Table 7). In this category, STAT-CSTARS-GPR yielded the most accurate estimates. For STAT methods, using the ANGERS dataset instead of CSTARS worsened RMSE performance by a factor of two on average.

For PROSPECT-based methods, IO-PROSPECT was the second best among all the methods considered, with bias still under $5.0 \mu\text{g}/\text{cm}^2$. LUT-based and hybrid inversions led to mitigating results. The accuracy of LUT-based methods was sensitive to the sampling strategy used to build the LUT (average RMSE for GV of $8.9 \mu\text{g}/\text{cm}^2$, average RMSE for LH of $14.5 \mu\text{g}/\text{cm}^2$). For hybrid methods, similar accuracy was obtained using non-linear methods (GPR, RFR) on the one hand and linear methods (PLSR, ridge) on the other, the former achieving better performance.

The influence of species and seasons on the results of the two most accurate methods (STAT-CSTARS and IO-PROSPECT) is analyzed in Table 8. For IO-PROSPECT, evergreen oaks (QUCH^(e), QUWI^(e)) deliver the best estimates whatever the season and have a low absolute bias (less than $2 \mu\text{g}/\text{cm}^2$). On the contrary, performance for deciduous oaks is inferior by a factor of two in terms of RMSE and has a significant bias. This plant functional type trend is not observed for STAT-CSTARS-GPR, which presents excellent biases whatever the species and season, under $2 \mu\text{g}/\text{cm}^2$ globally. Spring and fall have a

better performance than summer for both methods. In general, QUDO^(d) and QUCH^(e) estimates are overestimated whatever the method, except for STAT-CSTARS (Figure 8). For fall and QUKE^(d), particularly low C_{ab} contents are observed and not correctly estimated (either over- or underestimated), except for IO-PROSPECT (Figure 8). This may highlight the limitations of PROSPECT in some cases and those of the training datasets (ANGERS, CSTARS) when dealing with extreme values.

Table 7. Performance of methods for the estimation of C_{ab} (in each subcategory, the most accurate method is highlighted in bold).

Category	Method	RMSE ($\mu\text{g}/\text{cm}^2$)	R^2	Bias ($\mu\text{g}/\text{cm}^2$)
Physical	IO-PROSPECT	7.8	0.64	4.9
	LUT-GV-MSE	8.0	0.63	4.9
	LUT-GV-SAM	8.0	0.63	5.5
	LUT-LH-MSE	13.5	−0.05	11.5
	LUT-LH-SAM	14.3	−0.19	12.4
Hybrid	Hybrid-Ridge	11.3	0.26	9.2
	Hybrid-PLSR	11.8	0.19	9.5
	Hybrid-GPR	9.0	0.53	5.8
	Hybrid-RFR	8.6	0.57	5.8
Statistical	STAT-ANGERS-Ridge	12.9	0.04	11.7
	STAT-ANGERS-PLSR	10.3	0.39	8.7
	STAT-ANGERS-GPR	9.4	0.49	6.3
	STAT-ANGERS-RFR	11.5	0.24	7.0
	STAT-CSTARS-Ridge	6.4	0.71	0.3
	STAT-CSTARS-PLSR	5.8	0.76	0.2
	STAT-CSTARS-GPR	5.0	0.83	b
STAT-CSTARS-RFR	5.7	0.78	0.1	

Table 8. Detailed results of STAT-CSTARS-GPR/IO-PROSPECT for C_{ab} .

		RMSE ($\mu\text{g}/\text{cm}^2$)	R^2	Bias ($\mu\text{g}/\text{cm}^2$)
Species	QUCH ^(e)	6.4/4.3	0.71/0.88	1.0/0.6
	QUWI ^(e)	4.6/4.5	0.80/0.87	0.9/1.8
	QUDO ^(d)	4.6/9.9	0.76/−0.20	1.1/8.1
	QUKE ^(d)	3.0/9.4	0.73/0.36	0.3/7.1
Season	Spring	3.7/7.0	0.93/0.78	−1.2/3.4
	Summer	5.8/9.2	−0.02/−0.15	1.2/6.2
	Fall	4.8/7.0	0.81/0.73	2.1/4.7

3.2.2. Carotenoid Content

Same as C_{ab} , STAT-CSTARS methods perform better than all other methods regardless of the chosen MLRA, with mean performances of RMSE = 1.4 $\mu\text{g}/\text{cm}^2$, R^2 around 0.71, and a bias under 0.1 $\mu\text{g}/\text{cm}^2$ (Table 9). STAT-CSTARS-GPR yields the most accurate estimates for C_{xc} . Then, both IO-PROSPECT and non-linear hybrid methods provide the second most accurate results (RMSE around 2.0 $\mu\text{g}/\text{cm}^2$, R^2 around 0.5, bias around 0.5 $\mu\text{g}/\text{cm}^2$). Like for C_{ab} , non-linear hybrid methods perform better than linear ones. LUT-based inversions

perform the worst (RMSE higher than $3.2 \mu\text{g}/\text{cm}^2$, GV still better than LH). STAT-ANGERS RMSE performance is inferior by a factor of more than 2 compared to STAT-CSTARS methods and by a factor of 1.5 compared to hybrid methods. Results are highly dependent on MLRA: they are better for non-linear methods (RMSE lower than $3.0 \mu\text{g}/\text{cm}^2$) than for linear ones (RMSE over $5.0 \mu\text{g}/\text{cm}^2$). Whatever the MLRA, estimates are biased (bias ranging from 1.5 to $5.1 \mu\text{g}/\text{cm}^2$).

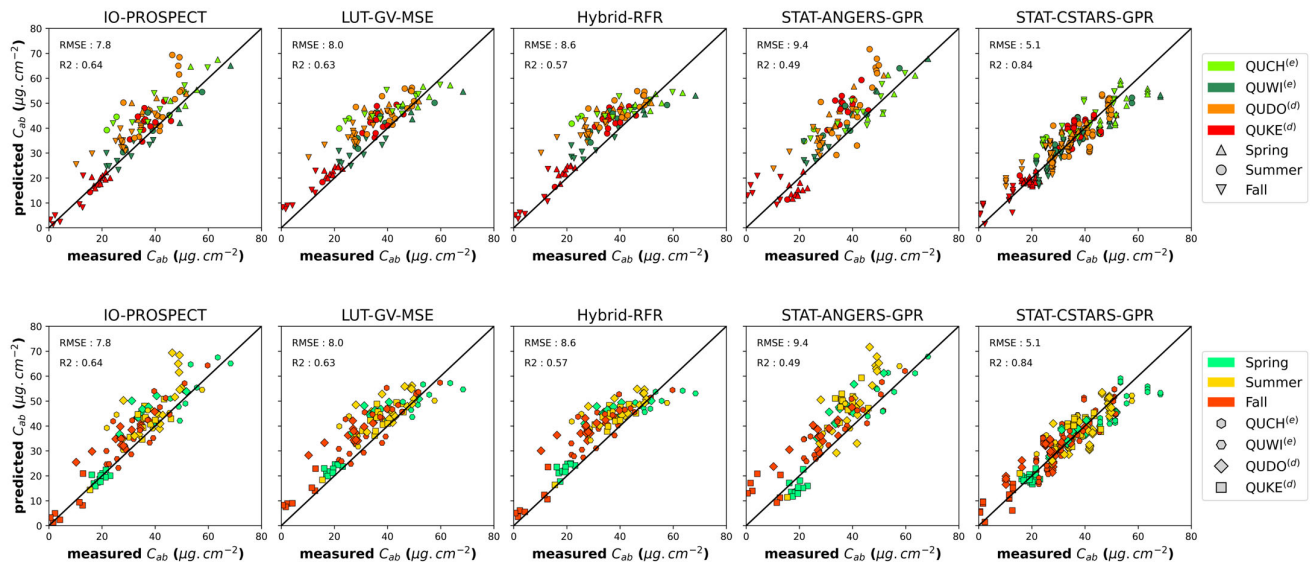


Figure 8. Validation plots for C_{ab} for the methods highlighted in Table 7: per species (top) and per season (bottom).

Table 9. Performance of methods for the estimation of C_{xc} (in each subcategory, the most accurate method is highlighted in bold).

Category	Method	RMSE ($\mu\text{g}/\text{cm}^2$)	R ²	Bias ($\mu\text{g}/\text{cm}^2$)
Physical	IO-PROSPECT	2.0	0.5	0.4
	LUT-GV-MSE	2.1	0.46	0.3
	LUT-GV-SAM	2.7	0.08	0.7
	LUT-LH-MSE	4.7	−1.75	4.3
	LUT-LH-SAM	3.6	−0.56	2.4
Hybrid	Hybrid-Ridge	2.3	0.36	0.5
	Hybrid-PLSR	2.3	0.37	0.0
	Hybrid-GPR	2.0	0.52	0.1
	Hybrid-RFR	2.0	0.52	0.6
Statistical	STAT-ANGERS-Ridge	5.0	−2.13	4.6
	STAT-ANGERS-PLSR	5.6	−2.83	5.1
	STAT-ANGERS-GPR	3.0	−0.09	2.0
	STAT-ANGERS-RFR	2.8	0.06	1.5
	STAT-CSTARS-Ridge	1.4	0.70	0.1
	STAT-CSTARS-PLSR	1.4	0.69	0.1
	STAT-CSTARS-GPR	1.3	0.75	0.1
	STAT-CSTARS-RFR	1.4	0.70	0.1

Analyzing the three most accurate methods, STAT-CSTARS-GPR, HYBRID-GPR, and IO-PROSPECT, their species-dependent performance is less obvious in comparison with C_{ab} (Table 10). On the one hand, when using HYBRID-GPR, there are more non-linear variations in C_{xc} estimates for evergreen oaks, with underestimations of C_{xc} above $13 \mu\text{g}/\text{cm}^2$ (Figure 9). A similar comment can be made for LUT-GV-MSE. On the other hand, STAT-CSTARS-GPR seems to have more homogeneous and robust variations whatever the species, which is indicated by R^2 values between 0.5 and 0.7 while those of HYBRID-GPR are globally lower than 0.2 (Figure 9, Table 10). IO-PROSPECT behaves similarly to STAT-CSTARS-GPR, except that the absolute bias and RMSE are higher. Seasonally, HYBRID-GPR and IO-PROSPECT have similar performance. Taking into account R^2 and bias, the three methods all had the worst results in summer.

Table 10. Detailed results of STAT-CSTARS-GPR/HYBRID-GPR/IO-PROSPECT for C_{xc} .

		RMSE ($\mu\text{g}/\text{cm}^2$)	R^2	Bias ($\mu\text{g}/\text{cm}^2$)
Species	QUCH ^(e)	1.9/2.6/2.3	0.47/0.19/0.37	0.8/−0.8/0.3
	QUWI ^(e)	1.3/2.5/2.2	0.69/0.17/0.32	0.2/−1.4/−1.5
	QUDO ^(d)	1.0/1.4/1.9	0.63/0.23/−0.46	0.4/0.1/0.5
	QUKE ^(d)	0.7/1.8/1.8	0.75/0.12/0.16	0.0/1.6/1.5
Season	Spring	1.1/2.2/2.2	0.90/0.60/0.62	0.1/−0.1/0.9
	Summer	1.5/1.7/2.0	0.21/0.18/−0.17	0.6/0.3/0.9
	Fall	1.2/2.0/1.9	0.72/0.57/0.62	0.5/0.0/−0.4

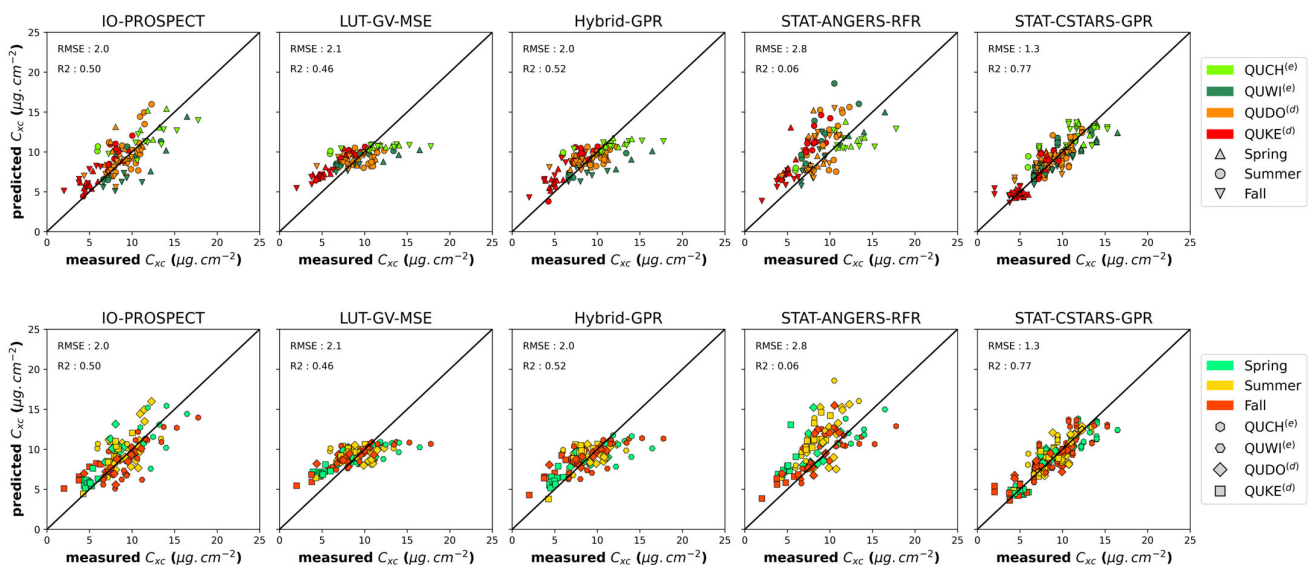


Figure 9. Validation plots for C_{xc} for the methods highlighted in Table 9: per species (top) and per season (bottom).

3.2.3. Equivalent Water Thickness

Accurate estimates and excellent performance are obtained with STAT-CSTARS (RMSE $< 0.0015 \text{ cm}$), without bias, while STAT-ANGERS is second best, also with a very low bias ($< 0.0007 \text{ cm}$ in absolute values) except for when RFR is used (RMSE $\leq 0.0018 \text{ cm}$) (Table 11). Unexpectedly, for both STAT-ANGERS and STAT-CSTARS, GPR, ridge, and PLSR achieved quite similar results. Thus, it can be inferred that the relationship between spectral data and EWT is almost linear. IO-PROSPECT, LUT-based, and hybrid methods give RMSE estimations which are half as accurate as those provided by statistical methods (0.0033--

0.0070 cm) and with higher biases (0.0018–0.0063 cm). Globally, IO-PROSPECT and LUT-based methods perform similarly for EWT. Hybrid methods delivered the highest biases.

The two best methods, STAT-CSTARS-GPR and STAT-ANGERS-Ridge, are further compared in Table 12. For STAT-CSTARS-GPR, RMSE is in the range 0.009–0.0015 cm, with a bias less than 0.0006 cm in absolute value. The highest RMSE is obtained for QUCH^(e), and the highest bias is obtained for QUDO^(d). One can note that the R² of QUWI^(e) is much lower (0.31). For STAT-ANGERS-Ridge, QUDO^(d), QUCH^(e), and QUWI^(e) estimates have a similar RMSE (~0.0013 cm) with a bias less than 0.006 cm. In comparison, performance for QUKE^(d) is inferior by almost a factor of two and with a larger bias (−0.0018 cm) when using the STAT-ANGERS-Ridge model. As such, non-specific species dependency is observed for the two methods. Then, considering each method by season, their RMSEs are similar and bias performance is low, with the spring season performing a bit worse.

Table 11. Performance of methods for the estimation of EWT (in each subcategory, the most accurate method is highlighted in bold).

Category	Method	RMSE (cm)	R ²	Bias (cm)
Physical	IO-PROSPECT	0.0035	−0.73	0.0018
	LUT-GV-MSE	0.0037	−0.90	0.0020
	LUT-GV-SAM	0.0034	−0.63	0.0019
	LUT-LH-MSE	0.0034	−0.66	0.0017
	LUT-LH-SAM	0.0033	−0.50	0.0018
Hybrid	Hybrid-Ridge	0.0070	−5.93	0.0063
	Hybrid-PLSR	0.0069	−5.66	0.0061
	Hybrid-GPR	0.0052	−2.84	0.0030
	Hybrid-RFR	0.0043	−1.56	0.0029
Statistical	STAT-ANGERS-Ridge	0.0016	0.66	−0.0001
	STAT-ANGERS-PLSR	0.0018	0.52	−0.0007
	STAT-ANGERS-GPR	0.0018	0.53	0.0004
	STAT-ANGERS-RFR	0.0048	−2.29	0.0036
	STAT-CSTARS-Ridge	0.0009	0.87	0.0001
	STAT-CSTARS-PLSR	0.0010	0.83	0.0000
	STAT-CSTARS-GPR	0.0009	0.87	0.0001
	STAT-CSTARS-RFR	0.0015	0.62	0.0000

Table 12. Detailed results of STAT-CSTARS-GPR/STAT-ANGERS-Ridge for EWT.

		RMSE (cm)	R ²	Bias (cm)
Species	QUCH ^(e)	0.0015/0.0014	0.76/0.71	−0.0002/0.0004
	QUWI ^(e)	0.0010/0.0012	0.31/0.35	0.0003/0.0004
	QUDO ^(d)	0.0009/0.0012	0.58/0.33	0.0006/0.0006
	QUKE ^(d)	0.0012/0.0022	0.83/0.52	−0.0003/−0.0018
Season	Spring	0.0013/0.0017	0.67/0.22	0.0002/−0.0006
	Summer	0.0010/0.0017	0.88/0.57	0.0002/−0.0001
	Fall	0.0010/0.0013	0.86/0.78	0.0003/0.0001

All methods that rely on PROSPECT (physical and hybrid) seem to have a multiplicative bias whatever the species (Figure 10). The same trend is present for three species (QUCH^(f), QUDO^(d), and QUWI^(e)), leading to an overestimation of EWT as EWT values increase. For QUKE^(d) only, EWT is underestimated for values over 0.010 cm and under this threshold, EWT is accurately estimated. Notice that the cases with EWT over 0.010 cm are almost exclusively samples collected in spring. In contrast, statistical methods have almost no bias, which is more of an additive nature.

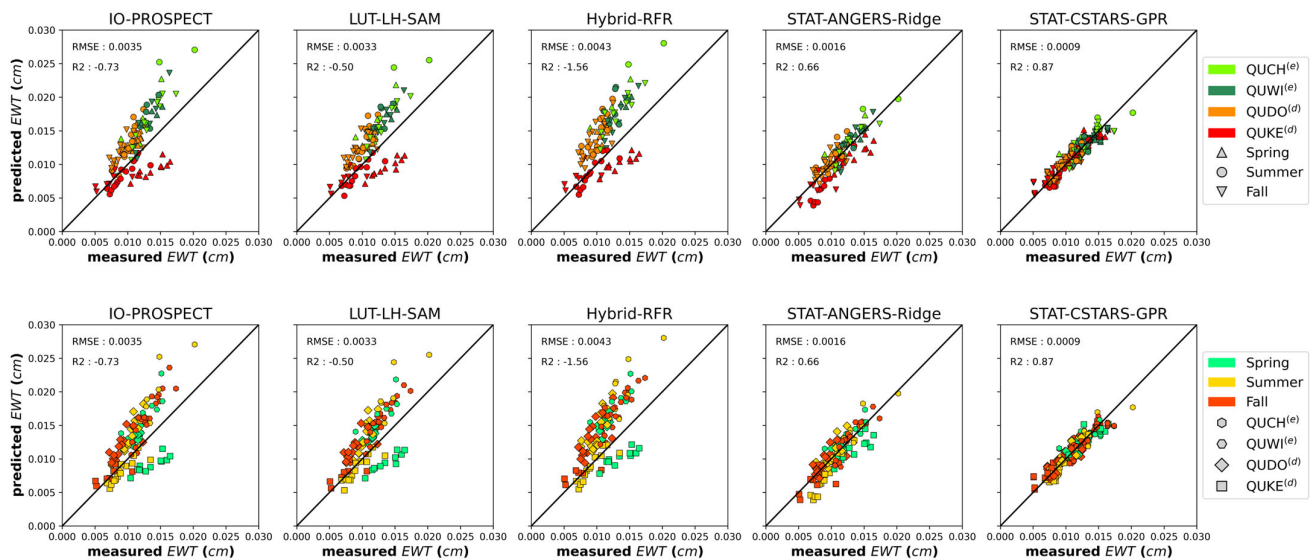


Figure 10. Validation plots for EWT for the methods highlighted in Table 11: per species (**top**) and per season (**bottom**).

3.2.4. Dry Matter Content

Consistent with EWT estimations, STAT-CSTARS provides the most accurate estimates, followed by STAT-ANGERS with the use of GPR, PLSR, and ridge (RMSE = 0.0009 g/cm², R² = 0.95, and no bias for the former; mean RMSE = 0.0014 g/cm², mean R² = 0.9, and mean bias 0.0005 g/cm² for the latter; Table 13). For STAT-ANGERS, PLSR and ridge have a lower RMSE, but PLSR is more reliable since it reduces the bias by a factor of two compared to ridge. The use of RFR leads to the lowest performances. For STAT-ANGERS, RMSE is increased by a factor of three and bias is five times greater than in the case of the other MLRAs. IO-PROSPECT, LUT-based, and hybrid methods yielded more biased estimations (bias is always higher than 0.0020 g·cm⁻², except for hybrid-RFR, for which it was 0.0014 g/cm²) and lower accuracy than statistical methods (RMSE is around two times higher for the most accurate PROSPECT-based methods). For LUT-based methods, choosing SAM as a cost function instead of MSE improves accuracy (RMSE is reduced by a factor of two).

Table 13. Performance of methods for the estimation of LMA (in each subcategory, the most accurate method is highlighted in bold).

Category	Method	RMSE (g/cm ²)	R ²	Bias (g/cm ²)
Physical	IO-PROSPECT	0.0055	−0.64	0.0038
	LUT-GV-MSE	0.0038	0.20	0.0017
	LUT-GV-SAM	0.0021	0.76	0.0014
	LUT-LH-MSE	0.0049	−0.29	0.0037
	LUT-LH-SAM	0.0030	0.52	0.0026
Hybrid	Hybrid-Ridge	0.0071	−1.72	0.0071
	Hybrid-PLSR	0.0069	−1.61	0.0041
	Hybrid-GPR	0.0062	−1.12	0.0038
	Hybrid-RFR	0.0030	0.5	0.0014

Table 13. Cont.

Category	Method	RMSE (g/cm ²)	R ²	Bias (g/cm ²)
Statistical	STAT-ANGERS-Ridge	0.0013	0.91	−0.0006
	STAT-ANGERS-PLSR	0.0013	0.91	−0.0003
	STAT-ANGERS-GPR	0.0016	0.86	0.0005
	STAT-ANGERS-RFR	0.0044	−0.04	−0.0024
	STAT-CSTARS-Ridge	0.0009	0.95	0.0000
	STAT-CSTARS-PLSR	0.0009	0.95	0.0000
	STAT-CSTARS-GPR	0.0009	0.95	0.0000
	STAT-CSTARS-RFR	0.0013	0.90	0.0000

For deciduous species (QUDO^(d) and QUKE^(d)), both the STAT-CSTARS-GPR and STAT-ANGERS-Ridge methods showed similar performance, with better estimates than global RMSE (RMSE < 0.0009 g·cm^{−2}; Table 14). In contrast, for evergreen species, the performance of STAT-CSTARS-GPR and STAT-ANGERS-Ridge is worse. Moreover, evergreen species exhibit poorer performance in terms of RMSE and R². LMA for evergreen species is underestimated with STAT-ANGERS-Ridge (Figure 11) and estimates show a negative bias over 0.001 g·cm^{−2}. No specific seasonal trend is noticed for both methods.

Table 14. Detailed results of STAT-CSTARS-GPR/STAT-ANGERS-Ridge for LMA.

		RMSE (g/cm ²)	R ²	Bias (g/cm ²)
Species	QUCH ^(e)	0.0011/0.0017	0.60/0.20	−0.0001/−0.0012
	QUWI ^(e)	0.0012/0.0023	0.64/−0.04	−0.0003/−0.0020
	QUDO ^(d)	0.0008/0.0007	0.79/0.81	0.0002/−0.0001
	QUKE ^(d)	0.0007/0.0007	0.82/0.80	−0.0000/−0.0002
Season	Spring	0.0008/0.0013	0.98/0.94	0.0001/−0.0005
	Summer	0.0009/0.0014	0.92/0.83	0.0001/−0.0006
	Fall	0.0011/0.0013	0.91/0.89	−0.0001/−0.0007

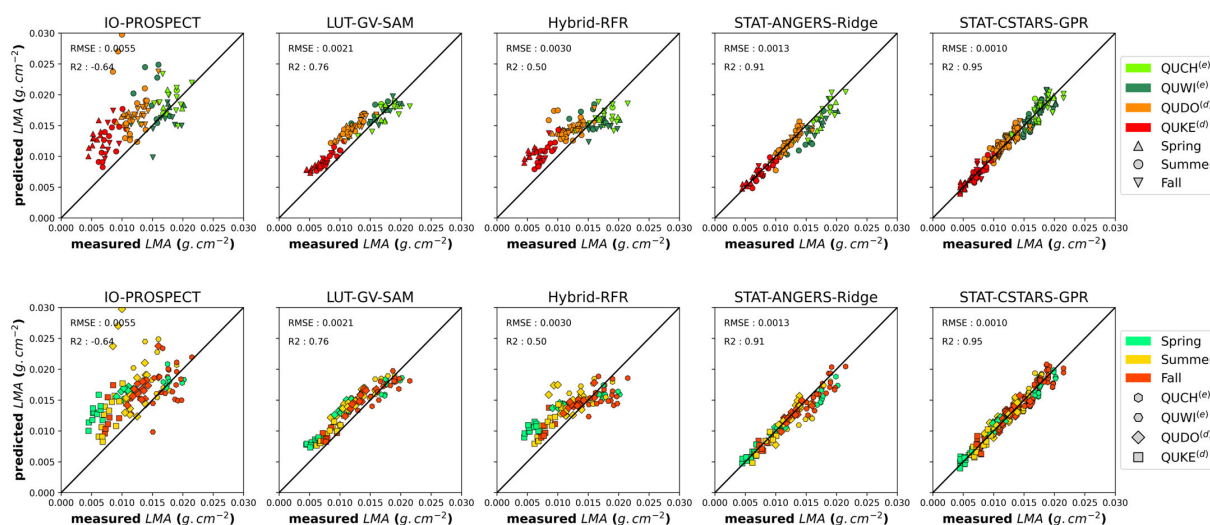


Figure 11. Validation plots for LMA for the methods highlighted in Table 13: per species (**top**) and per season (**bottom**).

Globally, for statistical methods, linear MLRAs (ridge and PLSR) produce similar or better estimations than the two non-linear methods (GPR, RFR), and there are fewer significant differences between linear and non-linear methods with the use of the CSTARS dataset (STAT-CSTARS category).

4. Discussion

4.1. Variability in the PROSPECT Structure Parameter *N*

Considering the estimated *N* values, our study highlights the high interspecific and intraspecific variability in *N*. *N* has also a seasonal evolution in the four species of the same genus. Estimated global values of *N* range between 1 (minimum value for QUKE^(d)) and 2.4 (maximum value for QUCH^(e)), which is in line with previous studies. Indeed, Jacquemoud et al. [25] mentioned that, for dicotyledon leaves, *N* is usually in the range of 1.5–2.5 in experimental datasets and Spafford et al. [37] found a range of 1–2.5 for PROSPECT simulations in order to encompass a large variety of species. Below, variations in *N* are further discussed based on their interspecific variability (Section 4.1.1), intraspecific variability (Section 4.1.2), and influence on PROSPECT LOP simulations and leaf trait estimations (Section 4.1.3).

4.1.1. Interspecific Variability in *N*

In our results, intraspecific variations in *N* are noticeable. Evergreen oak species (QUWI^(e) and QUCH^(e)) exhibit higher *N* values than deciduous oaks regardless of the season. Particularly, QUKE^(d) has a much lower mean *N* (1.42) compared to other species (1.74, 1.81, and 2.13 for QUDO^(d), QUWI^(e), and QUCH^(e), respectively).

Analyzing the statistical link between *N* values and measurable parameters provides more interpretability of *N* variability. Indeed, the interspecific trend of *N* follows the interspecific trend of LMA exactly (2.1.3). This trend is confirmed by the high correlation between *N* and LMA (Pearson's *R* = 0.82; Figure 7). While Demarez et al. [31] emphasized that *N* is correlated to leaf thickness, we found that *N* is less correlated to this latter parameter (Pearson's *R* = 0.59) than to LMA. Moreover, compared to LMA, *N* shows less correlation to leaf surface weight (0.69) while this latter factor is more strongly linked to leaf thickness. Considering this, interspecific variations in *N* may be driven by LMA variations. And particularly, *N* being more correlated to LMA than to thickness means that *N* may be more related to the nature of leaf material than to its quantity.

The specificity of leaf surface, such as the presence of wax or a complex cuticle structure, is not simulated in the PROSPECT model. Therefore, we question whether the

structural parameter N can compensate for effects due to cuticles and pubescence when modeling leaf reflectance. In our dataset, evergreen oaks QUWI^(e) and QUCH^(e) have a hard cuticle, leading to high specular reflection (as seen in Figure 1), and QUCH^(e) leaves are pubescent on the abaxial side. QUDO has a quite hard leaf compared to QUKE^(d), which is consistent with plant adaptation strategies for hot, low foothill habitats (i.e., woodland savannas). Considering these properties, N values might be higher for QUCH^(e), QUWI^(e), and QUDO^(d) compared to QUKE^(d) to compensate for their complex surface properties.

4.1.2. Intraspecific Variability in N

We also observe intraspecific variations in N . N dynamic range is 0.6 for QUCH^(e) and QUDO^(d) and reaches 0.8 for QUKE^(d) and QUWI^(e). Several factors can drive these intraspecific variations and are discussed hereafter.

The N parameter is expected to change over the course of the year following the phenological evolutions of a given species. Our dataset, collected at three different phenophases during the year, provides insight into this evolution. However, few studies actually provide information that can be compared with our results about N distribution for a given species and even less throughout a phenological cycle. Considering deciduous plants, phenological variations in N show an increase from spring to fall, as observed in forests [31,34] and crops [58]. For instance, Noda et al. [34] found that N ranges between 1 (from budburst in mid-May) and 1.4 (before leaf fall at the end of October) for leaves of *Quercus Crispula*. In our oak dataset, the same seasonal tendencies were observed for QUDO^(d) (from 1.67 to 1.76) and QUKE^(d) (from 1.22 to 1.60).

For evergreen species, QUCH^(e) and QUWI^(e), we found no particular seasonal trend for N with our dataset. However, during field sampling, priority was not given to evergreen species due to their smaller variations in leaf functional traits, and therefore we lack data throughout the year for QUCH^(e) and QUWI^(e) (respectively, in summer and spring). Moreover, for evergreen species, new leaves that grew in the years of sampling were not collected due to the assumption that previous years' leaves make up the majority of the canopy. Therefore, during the leafing out period of evergreen oaks in spring, when one could expect the highest discrepancy compared to previous year's generation, the new leaf generation was not sampled. This may explain why QUCH^(e) and QUWI^(e) show similar values of N and leaf traits in spring, summer, and fall. However, the two generations of leaves are less distinguishable in summer, and some new-generation leaves might have been collected in summer. This could explain why QUWI^(e) N values are more variable for summer.

Jacquemoud et al. [22] provided a hypothesis to explain the increase in N from spring to fall, which was at least observed in deciduous species [31,34]. They stated that N estimated for dry leaves is higher than N estimated for fresh ones, probably due to an increase in multiple scattering due to the loss of water. However, our results show that N is strongly correlated to LMA. In addition, N exhibited almost no correlation with EWT and particularly leaves with lower N values could have high EWT values, around the average (e.g., QUKE^(d) leaves in spring, see Figure 12). Therefore, N variations throughout the phenological cycle may be driven by the content of dry matter, which only increases during the leaf's lifetime and may not be driven by water loss. Furthermore, other intraspecific variabilities in N that were observed might only be compelled by factors of LMA variation.

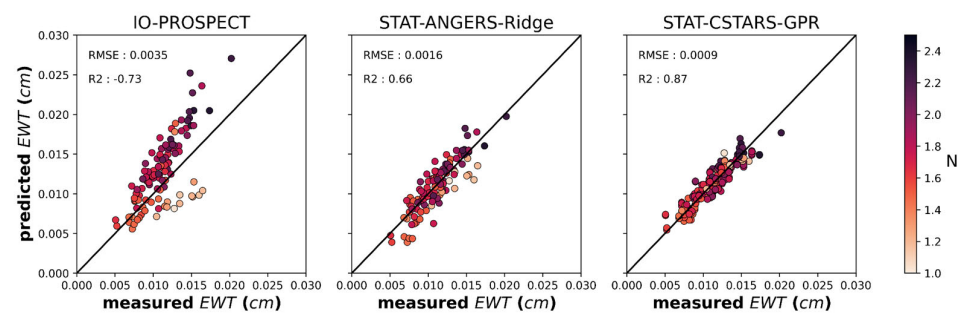


Figure 12. Validation plots for EWT for IO-PROSPECT, STAT-ANGERS-Ridge, and STAT-CSTARS-GPR. Color indicates the value of PROSPECT structural parameter N estimated through PROSPECT-IO. Spring leaves of QUKE^(d) with a value of N below 1.2 are clearly identifiable in the IO-PROSPECT method plot.

In addition, other sources of variations in the N parameter include leaf position within the highly heterogeneous vertical profile of the tree canopy and if the leaf developed in the shade or in the sun [31,34]. This could lead to a 5–10% rise in intraspecific variability [31]. In our dataset, it was sometimes impossible to collect leaves at the very top of the canopy, so for some of the 20 m and taller trees, leaves were collected from a part of the canopy that received less sunlight instead. Thus, this is another factor of N variation in our study that could have artificially increased intra- and interspecific variabilities in N .

4.1.3. Limitations of the PROSPECT Structure Parameter N and Its Impact on Leaf Trait Estimations

Generally, the N parameter has a substantial influence on the spectral shape of LOPs (cf. Figure 4). Ceccato et al. [59] conducted a sensitivity study showing that the N parameter can explain about 40% of the output. Thus, a precise estimation of N may therefore be required to accurately estimate leaf traits. In addition, assessing the performance of PROSPECT for leaf trait estimation at the extremes of the observed N values (close to 1 or 3) has not been explored; therefore, limitations of the PROSPECT model for these values remain partially unknown.

Spafford et al. [37] assessed the impact of retrieving the N value prior to estimating leaf traits with a method similar to IO-PROSPECT. They developed a correlation function between N and reflectance in the NIR band (wavelengths where pigments do not absorb) and used this correlation to accurately estimate the N parameter in isolation. Leaf traits were estimated with better accuracy than without the prior retrieval of the N value. However, their conclusion stated that with the knowledge of both leaf directional-hemispherical reflectance and transmittance, the use of optimized spectral subdomains yielded better accuracy without using the prior estimation of N . In our study, we did not use any previously estimated N value. Despite this fact, our results highlighted a large intraspecific variability in this parameter; therefore, one should not use a single previously estimated N value by species but rather estimate N each time, as in [37].

Moreover, Pacheco-Labrador et al. [60] found better estimations for the pigments and EWT of *Quercus Ilex* leaves with IO-PROSPECT by removing trichomes from the surfaces of the leaves. Their work indicates qualitatively that leaf surface impacts the leaf trait estimation accuracy of PROSPECT-based methods. In fact, the PROSPECT model does not simulate any specificity of leaf surface, while most plant leaves display a waxy surface or a complex cuticle structure. This shortcoming has been emphasized by several studies. Furthermore, for C_{ab} estimation with PROSPECT, taking into account leaf surface reflection by adding an additional surface layer into the PROSPECT model or changing pigment-specific absorption coefficients demonstrated better performance, especially for leaves covered by heavy wax or hard cuticles [61,62]. But these results have barely been investigated for other leaf traits (i.e., C_{xc} , EWT, and LMA) and the concurrent impact of N values has not been studied to our knowledge.

In our dataset, QUWI^(e) and QUCH^(e) have a hard cuticle, leading to high specular reflection (as seen in Figure 1). In particular, QUCH^(e) leaves are pubescent on the abaxial side. However, despite the fact that these features (presence of hairs, hard cuticle, asymmetry between adaxial and abaxial leaf surfaces) are not taken into account in the PROSPECT model, our estimations for all leaf traits are quite acceptable because they are globally only slightly poorer than those obtained for deciduous oaks (Figures 8–11) by PROSPECT-based methods. Even though QUKE^(d) possesses waxy leaf surfaces on the upper side (adaxial; as seen in Figure 1), QUKE^(d) samples in spring exhibited low N values, between 1 and 1.4. In this range, a variation in N implies higher changes in simulated spectral variations in NIR and SWIR (Figure 4) where EWT is spectrally sensitive. These may be the two main reasons explaining the inaccurate estimations of EWT we obtained for QUKE^(d) spring samples (see Figure 12 and Section 4.2 for further discussions on EWT estimation).

4.2. Comparison of Leaf Trait Estimation Methods

Estimation methods were tested for four leaf traits and to varying degrees, trends in the results are specific for each leaf trait. However, it is possible to identify trends common to all four leaf traits and to draw general conclusions; these are discussed below in Section 4.2.1. The specificity of results related to leaf pigment contents, EWT, and LMA are further discussed in Section 4.2.2, Section 4.2.3, and Section 4.2.4 respectively.

4.2.1. Estimation Method Considerations Common to All Four Variables

Globally, STAT-CSTARS methods showed greater accuracies, as expected, since the training and test data came from the same dataset which potentially included the same specific errors and bias. However, the four selected MLRAs yielded different estimation accuracies, with GPR providing the most accurate estimates for all the traits. Its performance is further used as a reference as it achieved the greatest retrieval performance in comparison with the other methods.

PROSPECT-based methods estimated leaf traits with less accuracy than STAT-CSTARS methods. Compared with STAT-ANGERS methods, the advantage of statistical methods is less clear, particularly for pigment content estimation. The transferability of statistical methods is further discussed in Section 4.3.

IO-PROSPECT was globally more accurate than the other PROSPECT-based methods. In our study, IO-PROSPECT presented limitations only in LMA estimation, which are discussed further in Section 4.2.4. For C_{ab} , C_{xc} , and EWT, LUT-based and HYBRID methods yielded equally or less accurate estimates. Our assumption is that LUT-based and HYBRID methods are both built on synthetic datasets generated with PROSPECT and are therefore dependent on the sampling strategy used. This is particularly noticeable when comparing LUT-GV and LUT-LH used for the same trait. Conversely, IO-PROSPECT and other iterative inversions of PROSPECT use direct simulations with only the required parameter values. Moreover, LUT-based methods are difficult to calibrate since they involve three main parameters (sampling scheme, distance function, and q) whose effects remain unclear. For example, the optimal q was selected from our dataset, but this could be considered overfitting, and the results we obtained with LUT-based methods should be considered less reliable. In addition, LUT-based methods are not clearly more efficient than IO-PROSPECT, particularly when using a LUT with many samples. Thus, we consider that iterative inversions of PROSPECT should be chosen over LUT-based methods. HYBRID methods build estimators from an MLRA and a synthetic dataset. They can overfit on synthetic data and become less resilient to noise or other spectral measurements errors.

In our study, for both statistical and hybrid methods, we compared estimators built with four MLRAs: ridge, PLSR, GPR, RFR. However, it may not be possible to draw an unambiguous conclusion regarding the most appropriate choice of MLRA. For statistical methods, Yang et al. [63] compared different MLRAs trained on leaf reflectance only (SVR, PLSR, RFR and K-Nearest Neighbors) for the estimation of EWT and LMA. Overall, their results show that EWT was more accurately estimated with SVR. For LMA, results were not

unequivocal and mostly depended on the training dataset. In contrast, for EWT and LMA, we obtained an accurate estimation with linear MLRAs (ridge and PLSR), highlighting that the relationship between LOPs and EWT/LMA is approximately linear. These two MLRAs were followed by GPR. GPR also provided good results for C_{ab} and C_{xc} (only RFR stayed one step ahead for C_{xc}). While choosing an MLRA for statistical methods, GPR may be the best compromise, since it is more versatile and able to deal with linear and non-linear problems. For hybrid methods, RFR obtained the best accuracy for C_{ab} , EWT, and LMA and a very good accuracy for C_{xc} compared to other MLRAs. Therefore, RFR may provide more robust estimators to cope with the transition from synthetic data to measured data.

Each method includes numerous parameters that could be optimized. However, the idea of our study is to investigate a wide range of methods; therefore, we choose to optimize only major parameters which were always considered in previous studies. In contrast, some studies specifically tackled the optimization of other parameters whose effects are not evaluated in our work. Firstly, defining a trait-specific spectral range is a thorny question for all estimation methods. Some previous studies tackle this issue and search for optimal ranges of several leaf traits. But these investigations focus on iterative inversions of PROSPECT, such as those developed by Féret et al. [29] or Spafford et al. [37], who found optimized spectral subdomains for the four leaf traits (C_{ab} : 0.7–0.72 μm , C_{xc} : 0.52–0.56 μm , and EWT/LMA: 1.7–2.4 μm). It is not clear if using these spectral subdomains for statistical or hybrid methods would yield more accurate estimates. In our study, we used the same spectral ranges for statistical, hybrid, and LUT-based methods (C_{ab} : 0.45–0.76 μm , C_{xc} : 0.45–0.56 μm , EWT: 0.9–2.4 μm , and LMA: 0.75–2.4 μm) and they were built on sensitivity analysis results. These ranges differ from the optimal ranges found for iterative inversions of PROSPECT [29,37]. They also differ from those already used at the canopy level for oaks (C_{ab} : 0.5–0.75 μm and C_{xc} : 0.5–0.55 μm with a LUT-based method [64]; EWT/LMA: 1.5–2.4 μm with hybrid PLSR [24]). Nevertheless, despite potential for future improvements, good performance was obtained for each leaf trait of these four oak species.

Moreover, transformations of spectral data could be used in statistical and hybrid methods to extract features or reduce their number for MLRA inputs. Particularly, Yang et al. [63] compared statistical methods based on reflectance or spectral indices. They found that estimation accuracy was improved (reduced by 5.7%) when using spectral indices rather than reflectance. However, all our tested approaches were LOP-based and we did not apply transformations such as spectral indices or dimensionality reductions.

4.2.2. Estimation of Leaf Pigments

For leaf pigments, IO-PROSPECT was the best method after STAT-CSTARS-GPR with a higher accuracy for C_{ab} (RMSE of 7.8 and 5.0 $\mu\text{g}\cdot\text{cm}^{-2}$, respectively) than for C_{xc} (2.0 and 1.3 $\mu\text{g}\cdot\text{cm}^{-2}$). In particular, STAT-CSTARS-GPR estimates had a very low bias for both pigments (both 0.1 $\mu\text{g}\cdot\text{cm}^{-2}$) compared to IO-PROSPECT (4.9/0.4 $\mu\text{g}\cdot\text{cm}^{-2}$ for C_{ab}/C_{xc}). Generally, in the literature, IO-PROSPECT is the most widely used inversion method [26,30,31,62]. For C_{ab} , the results are in the same order of magnitude when compared to other studies. Demarez et al. [31] found an RMSE of 7.3 $\mu\text{g}\cdot\text{cm}^{-2}$ over phenological variations of oaks, beeches, and hornbeams. They had a bias that increased with crown leaf position: from 2 $\mu\text{g}\cdot\text{cm}^{-2}$ for sunlit leaves to 19 $\mu\text{g}\cdot\text{cm}^{-2}$ for shaded leaves for oaks. In comparison, we obtained a bias of 4.9 $\mu\text{g}\cdot\text{cm}^{-2}$. Qiu et al. [62] obtained an RMSE of 8.9 $\mu\text{g}\cdot\text{cm}^{-2}$ for broadleaf leaf samples by accounting for leaf surface reflection. Wang et al. [30] produced an RMSE of 13.1 and 10.9 $\mu\text{g}\cdot\text{cm}^{-2}$ for two large datasets including trees, shrubs, and grass from USA and China and from temperate to tropical climates. Féret et al. [26] reported an RMSE of 9.0 $\mu\text{g}\cdot\text{cm}^{-2}$ among several available datasets and [32] provided an RMSE of 6.3 $\mu\text{g}\cdot\text{cm}^{-2}$ for a temperate forest with vertical variability within the canopy. For C_{xc} , our results are also in line with previous studies ([26]: RMSE = 3 $\mu\text{g}\cdot\text{cm}^{-2}$; [30]: RMSE = 3.5/5.3 $\mu\text{g}\cdot\text{cm}^{-2}$).

Then, evaluating seasonal variations in estimation performance for C_{ab} , Gara et al. [32], using a LUT-based method, noticed that the lowest accuracy corresponds to the summer period when they pooled all leaf samples collected from the upper canopy (spring/summer/fall: RMSE

= 7.1/7.3/5.8 $\mu\text{g}\cdot\text{cm}^{-2}$). The same tendency occurred in our dataset (spring/summer/fall: RMSE = 7.0/9.2/7.0 $\mu\text{g}\cdot\text{cm}^{-2}$) and was also reported by Zhang et al. [65]. This can possibly be explained by a reorganization of the chloroplast (which contains the pigments) in the leaf cytoplasm from being clumped during peak vegetative growth to being more uniformly distributed when leaves start being senescent [32]. However, we also found that a statistical method such as PLSR [66] produced better estimations for summer than other seasons. For C_{xc} , we did not find a particular seasonal trend compared to C_{ab} (spring/summer/fall: RMSE = 2.2/2.0/1.9 $\mu\text{g}\cdot\text{cm}^{-2}$). To our knowledge, no study exists in the literature with which to compare our findings for C_{xc} . Differentiating by species and plant functional types, we observed better results for evergreen species for C_{ab} (RMSE twice lower, R^2 very significantly higher, low biases) but the opposite was found for C_{xc} to a lesser extent (higher RMSE and R^2 , similar biases).

At the canopy level, using the same dataset as ours combined with AVIRIS airborne hyperspectral images, Miraglio et al. [24,64] found that leaf pigments were correctly estimated with a LUT-based method for QUDO^(e) at the TONZ site (C_{ab} : RMSE = 5.2 $\mu\text{g}\cdot\text{cm}^{-2}$; C_{xc} : RMSE = 1.34 $\mu\text{g}\cdot\text{cm}^{-2}$) and with a statistical method for QUDO^(d) and QUWI^(e) at both the TONZ and SJER sites (C_{ab} : RMSE \approx 7.91 $\mu\text{g}\cdot\text{cm}^{-2}$; C_{xc} : RMSE \approx 1.73 $\mu\text{g}\cdot\text{cm}^{-2}$). This demonstrates that our results have potential for upscaling from the leaf to canopy level for oak woodland savannas. But in contrast to the leaf level, canopy estimations for C_{ab} during summer periods did not produce particularly worse results than those made for fall samples [64].

4.2.3. Estimation of Leaf Water Content

For EWT, statistical methods yielded more accurate estimates than PROSPECT-based methods. RMSE was reduced by 50% with STAT-ANGERS-Ridge compared to IO-PROSPECT or LUT-LH-SAM. On the other hand, Féret et al. [29] reached the opposite conclusion and showed that PROSPECT inversions could outperform statistics-based methods (using SVM as the MLRA) using an optimized spectral subdomain (1700 to 2400 nm).

PROSPECT inversions for EWT estimation lead to an RMSE of 0.0035 cm, which is similar to that obtained by Asner et al. [35] for heterogeneous humid tropical forests using an 800–2400 nm spectral range. However, regardless of the PROSPECT-based method, our estimates exhibit two major deficient trends: a multiplicative bias and underestimation for some QUKE^(d) samples.

Firstly, EWT is estimated with multiplicative bias, which is particularly noticeable for QUDO^(d), QUWI^(e), and QUCH^(e) samples, which have higher EWT. While such multiplicative bias was not systematically reported by previous studies, one can find some hints of such bias in the work of Gara et al. [32]. Indeed, using a LUT-based method, Gara et al. [32] found that higher values of EWT were overestimated, which reveals a similar multiplicative bias. However, EWT values in Gara et al. [32] only reach 0.012 cm; therefore, the bias is less noticeable than in our experiment, where some EWT values are over 0.015 cm. Similarly, a multiplicative bias was found by Pacheco-Labrador et al. [60] for IO-PROSPECT, which in their study tended to underestimate EWT. This bias was attenuated by removing leaf trichomes from *Quercus Ilex* prior to spectral measurement. Conversely, Wang et al. [30] did not find the same tendency in large datasets using PROSPECT iterative inversion and they obtained unbiased estimates of EWT with high accuracy ($R^2 = 0.74/0.77$, RMSE = 0.0022/0.0036). Different sources of errors could explain the bias observed in our results when using PROSPECT. On the one hand, the *Quercus* species present in our sites are not considered in the calibration databases used to set some parameters of PROSPECT-D (surface scattering, unique value of refractive index, etc.). On the other hand, some bias could exist in the leaf optical measurements [29].

Secondly, EWT is underestimated for some samples. These latter samples originate from QUKE^(d) oaks, almost exclusively from spring 2014 collections. Inaccurate estimations for QUKE^(d) in spring can have multiple sources of origin. (i) Most of the samples that exhibit an underestimation of EWT were collected at the BLOF site in the 2014 spring

campaign. Measurements from this campaign could have been biased. (ii) QUKE^(d) leaves are larger compared to those of the other species, which may have led to a poor representativeness of LOPs when considering the whole leaf area. Lastly, (iii) these samples also exhibited low N values (Figure 12). This range of values for N has not been fully studied, and in this range, N has more impact in NIR and SWIR (Figure 4) where EWT is spectrally sensitive.

However, both issues (multiplicative bias and underestimation for QUKE^(d) spring samples with low N) are not observed in estimates from statistics-based methods, including STAT-ANGERS methods (see Figure 12). This may also indicate that these estimation issues come from inaccurate modeling of PROSPECT for oak EWT and suggest that PROSPECT is not fully suited for our dataset.

4.2.4. Estimation of Leaf Dry Matter Content

Estimating LMA using PROSPECT, Asner et al. [35] found similar orders of magnitude as in our results ($0.0033 \text{ g}\cdot\text{cm}^{-2}$), although the forest types in their study are very different. Nevertheless, our statistical methods, including STAT-ANGERS methods, outperform PROSPECT-based methods. Similar to EWT, this leads to opposite conclusions than those made by Féret et al. [29]. However, results obtained with IO-PROSPECT are surprising since this method yielded equally or more accurate estimates than other PROSPECT-based methods for the other three leaf traits. In the case of LMA, LUT-based methods provided more accurate estimates. Particularly, using SAM as the distance function for LUT-based methods led to better result; with MSE, this difference was not as noticeable for other leaf traits. Considering hybrid methods, using RFR as the MLRA yielded more accurate estimates. Indeed, the difference between RFR and other MLRAs was more pronounced for LMA than for other leaf traits.

Generally, our estimation results showed global overestimations of LMA using PROSPECT-based methods (bias over $0.0014 \text{ g}\cdot\text{cm}^{-2}$) while statistical methods showed lower bias. Gara et al. [32] found underestimations regardless of the season. They found no particular seasonal trend in their dataset (spring/summer/fall: $R^2 = 0.67/0.82/0.78$, $\text{RMSE} = 0.0014/0.0013/0.0014 \text{ g}\cdot\text{cm}^{-2}$; global: $R^2 = 0.76$, $\text{RMSE} = 0.0014 \text{ g}\cdot\text{cm}^{-2}$). More particularly for evergreen oaks, Gonzáles-Cascón et al. [38] estimated the LMA of *Quercus Ilex* leaves with high performance ($R^2 = 0.90$) by using a PLSR statistical method. For comparison, for QUCH and QUWI, we obtained a mean R^2 of 0.62 and RMSE of $0.0012 \text{ g}\cdot\text{cm}^{-2}$ with STAT-CSTARS-GPR.

4.3. Transferability of Statistical Methods Trained on an Independent Dataset

Considering the transferability of statistical methods, similar trends are observed for all leaf traits when comparing STAT-ANGERS to STAT-CSTARS. The lowest RMSE obtained with STAT-ANGERS methods is around twice the value obtained by STAT-CSTARS-GPR for C_{ab} , C_{xc} , and EWT. For LMA, the difference is less important: the RMSE obtained with STAT-ANGERS-Ridge is around 1.3 times the size of the RMSE obtained with STAT-CSTARS-Ridge. The same trend is observed in the work of Wang et al. [30]. They evaluated the transferability of a PLSR statistical method to retrieve foliar traits across two datasets collected in a tropical and subtropical forest in China and a temperate and subtropical forest in the United States. Wang et al. demonstrated that their PLSR-based method yielded a lower accuracy when applied to an independent dataset, unused in training data. Similarly to our results, they found that a lower relative RMSE difference was reached for LMA (around 35%).

Féret et al. [29] and Yang et al. [30] evaluated the transferability of statistics-based methods for EWT and LMA. They performed a cross-dataset validation using two independent training and test datasets. They showed that the results are highly dependent on both the training and test datasets. Moreover, Féret et al. (2019) demonstrated that combining several datasets for training in order to increase the size of the training set improves the results. Consequently, the order of magnitude we found when comparing the

RMSE obtained with STAT-CSTARS and STAT-ANGERS depends on our datasets, and it is very likely that different RMSE variations would be observed using other datasets.

Both Féret et al. [29] and Wang et al. [30] also compared statistical methods to PROSPECT-based methods similar to our IO-PROSPECT. Wang et al. [30] estimated the same four leaf traits as in our study, while Féret et al. focused on EWT and LMA. In the work of Wang et al., the transferred PLSR-based method achieved better accuracy than their equivalent to our IO-PROSPECT method for LMA and C_{xc} . Féret et al. obtained better accuracy for LMA with statistical methods for half of the cases they studied, but these results were highly dependent on the datasets used for training and testing. These results are in line with the accuracy we obtained for LMA. However, both studies reached better accuracy with improved versions of IO-PROSPECT and demonstrated that our IO-PROSPECT method is not perfectly suited for the estimation of EWT and LMA. Therefore, the opposite conclusions could be drawn if we modified the IO-PROSPECT method.

5. Conclusions

This work aimed to compare several statistical, physical, and hybrid estimation methods for four foliar traits of leaves of California oak species collected from four sites in three different seasons.

We showed that the structural parameter N in PROSPECT depends little on the season for evergreen species, which was not the case for deciduous species. Our estimation methods had no prior knowledge of the N parameter, although trait estimates were obtained with good accuracy.

In conclusion, the most accurate estimation methods for all leaf traits are statistical methods built on a dataset that include the same species composition and are measured with the same protocol. Among the four MLRAs tested, GPR enabled the development of the most accurate estimator (i.e., STAT-CSTARS-GPR). However, we noticed that statistical linear methods deliver better results for EWT and LMA. On the contrary, non-linear ones are better for leaf pigments. However, deriving such data is very demanding in terms of time and resources (for instance, to account for seasonality and geographic sampling) and requires high laboratory measurement costs (e.g., for pigments).

Other than that, physical inversion methods yield more accurate estimates for leaf pigment contents. Indeed, this class of methods delivers a similar performance. We recommend using IO-PROSPECT for pigments and EWT because it estimates these traits with good accuracy and performs a joint estimation of the leaf traits. For LMA, HYBRID-RFR is the most powerful method.

We used our dataset to evaluate the transferability of statistical methods trained on an independent dataset (ANGERS). For EWT and LMA, we demonstrated that this type of statistical methods leads to better estimation accuracy than PROSPECT-based methods. Particularly, statistical methods using linear models (STAT-ANGERS-PLSR or -Ridge) provided more accurate estimates. The performance of STAT-ANGERS methods was inferior compared to physical methods for pigments. In particular, results for C_{xc} were inferior by 50%, but for C_{ab} , this occurred to a lesser extent. Therefore, we emphasize that statistical methods are promising estimation methods and a better understanding of their functioning could improve their transferability.

Considering the impact of seasons on each trait and its associated most accurate estimation method, estimation errors in terms of RMSE were similar. Estimation performance did not depend particularly on species but on plant functional type (evergreen or deciduous).

Finally, trait estimates were obtained from spectra averaged over several leaves and compared to the mean biochemical composition of this set of leaves. This constitutes an intermediary scale between the single-leaf and the canopy scales. Thus, this work provides insights into the upscaling of leaf trait estimation at the canopy level using imaging spectroscopy.

Author Contributions: Conceptualization, T.G., K.A., S.U. and X.B.; methodology, T.G.; software, T.G.; validation, T.G.; formal analysis, T.G.; investigation, T.G.; resources, M.H., K.A. and S.U.; data

curation, T.G. and M.H.; writing—original draft preparation, T.G., K.A., M.H. and X.B.; writing—review and editing, T.G., K.A., M.H., S.U. and X.B.; visualization, T.G.; supervision, S.U. and X.B.; project administration, S.U. and X.B.; funding acquisition, K.A., S.U. and X.B. All authors have read and agreed to the published version of the manuscript.

Funding: This work was funded by CNES (Centre National d’Études Spatiales), Région Occitanie, and by ONERA (Office National d’Études et de Recherches Aérospatiales).

Data Availability Statement: Restrictions apply to the availability of these data. Data was obtained from CSTARS, University of California, Davis, and are available from the author with the permission of CSTARS, University of California, Davis.

Acknowledgments: The authors are grateful to the CSTARS team (University of California, Davis) for collecting and processing the field data as part of the HypsIRI Preparatory Science Campaign (S.L. Ustin PI, NASA grant #NNX12AP87G, “Identification of Plant Functional Types by Characterization of Canopy Chemistry”).

Conflicts of Interest: The authors declare no conflict of interest.

References

- Carrero, C.; Jerome, D.; Beckman, E.; Byrne, A.; Coombes, A.J.; Deng, M.; Rodríguez, A.G.; Van Sam, H.; Khoo, E.; Nguyen, N.; et al. *The Red List of Oaks 2020*; The Morton Arboretum: Lisle, IL, USA, 2020.
- Stavi, I.; Thevs, N.; Welp, M.; Zdruli, P. Provisioning Ecosystem Services Related with Oak (*Quercus*) Systems: A Review of Challenges and Opportunities. *Agrofor. Syst.* **2022**, *96*, 293–313. [[CrossRef](#)]
- Nixon, K.C. *The Oak (Quercus) Biodiversity of California and Adjacent Regions*; USDA Forest Service General Technical Report PSW-GTR-184; USDA Forest Service: Washington, DC, USA, 2002; pp. 3–20.
- Gaman, T. California’s Oaks in the 21st Century: Mapping Oak Woodlands and Forests. *californiaoaks.org* 2022. Available online: <https://californiaoaks.org> (accessed on 1 September 2023).
- Gaman, T.; Firman, J. *Oaks 2040: The Status and Future of Oaks in California*; California Oak Foundation: Oakland, CA, USA, 2006.
- Dib, T.; Ait Said, S.; Krouchi, F. Monitoring Long-Term Cork Oak Forest Spatio-Temporal Dynamics Based on Aerial Photographs: A Case Study of Kiadi Corks Oak Forest in Akfadou Mountain (Algeria). *Analele Univ. Din Oradea Ser. Geogr.* **2022**, *32*, 26–38. [[CrossRef](#)]
- Meng, R.; Wu, J.; Zhao, F.; Cook, B.D.; Hanavan, R.P.; Serbin, S.P. Measuring Short-Term Post-Fire Forest Recovery across a Burn Severity Gradient in a Mixed Pine-Oak Forest Using Multi-Sensor Remote Sensing Techniques. *Remote Sens. Environ.* **2018**, *210*, 282–296. [[CrossRef](#)]
- Carreiras, J.M.B.; Pereira, J.M.C.; Pereira, J.S. Estimation of Tree Canopy Cover in Evergreen Oak Woodlands Using Remote Sensing. *For. Ecol. Manag.* **2006**, *223*, 45–53. [[CrossRef](#)]
- Yousefi, S.; Haghghian, F.; Naghdzadegan Jahromi, M.; Pourghasemi, H.R. Chapter 26—Pest-Infected Oak Trees Identify Using Remote Sensing-Based Classification Algorithms. In *Computers in Earth and Environmental Sciences*; Pourghasemi, H.R., Ed.; Elsevier: Amsterdam, The Netherlands, 2022; pp. 363–376. ISBN 978-0-323-89861-4.
- Kattenborn, T.; Schmidlein, S. Radiative Transfer Modelling Reveals Why Canopy Reflectance Follows Function. *Sci. Rep.* **2019**, *9*, 6541. [[CrossRef](#)] [[PubMed](#)]
- Violle, C.; Navas, M.-L.; Vile, D.; Kazakou, E.; Fortunel, C.; Hummel, I.; Garnier, E. Let the Concept of Trait Be Functional! *Oikos* **2007**, *116*, 882–892. [[CrossRef](#)]
- Lausch, A.; Erasmi, S.; King, D.J.; Magdon, P.; Heurich, M. Understanding Forest Health with Remote Sensing -Part I—A Review of Spectral Traits, Processes and Remote-Sensing Characteristics. *Remote Sens.* **2016**, *8*, 1029. [[CrossRef](#)]
- Croft, H.; Chen, J.M.; Wang, R.; Mo, G.; Luo, S.; Luo, X.; He, L.; Gonsamo, A.; Arabian, J.; Zhang, Y.; et al. The Global Distribution of Leaf Chlorophyll Content. *Remote Sens. Environ.* **2020**, *236*, 111479. [[CrossRef](#)]
- Pereira, H.M.; Ferrier, S.; Walters, M.; Geller, G.N.; Jongman, R.H.G.; Scholes, R.J.; Bruford, M.W.; Brummitt, N.; Butchart, S.H.M.; Cardoso, A.C.; et al. Essential Biodiversity Variables. *Science* **2013**, *339*, 277–278. [[CrossRef](#)]
- Gamon, J.A.; Qiu, H.-L.; Sanchez-Azofeifa, A. Ecological Applications of Remote Sensing at Multiple Scales. In *Functional Plant Ecology*; CRC Press: Boca Raton, FL, USA, 2007; pp. 655–684.
- Ustin, S.; Asner, G.; Gamon, J.; Huemmrich, K.; Jacquemoud, S.; Schaepman, M.; Zarco-Tejada, P. Retrieval of Quantitative and Qualitative Information about Plant Pigment Systems from High Resolution Spectroscopy. In Proceedings of the 2006 IEEE International Symposium on Geoscience and Remote Sensing, Denver, CO, USA, 31 July–4 August 2006; pp. 1996–1999.
- Colombo, R.; Busetto, L.; Meroni, M.; Rossini, M.; Panigada, C. Optical Remote Sensing of Vegetation Water Content. In *Hyperspectral Indices and Image Classifications for Agriculture and Vegetation*; CRC Press: Boca Raton, FL, USA, 2018; ISBN 978-1-315-15933-1.
- Féret, J.-B.; Berger, K.; de Boissieu, F.; Malenovsky, Z. PROSPECT-PRO for Estimating Content of Nitrogen-Containing Leaf Proteins and Other Carbon-Based Constituents. *Remote Sens. Environ.* **2021**, *252*, 112173. [[CrossRef](#)]

19. Gara, T.W.; Rahimzadeh-Bajgiran, P.; Darvishzadeh, R. Forest Leaf Mass per Area (LMA) through the Eye of Optical Remote Sensing: A Review and Future Outlook. *Remote Sens.* **2021**, *13*, 3352. [[CrossRef](#)]
20. Jacquemoud, S.; Ustin, S. *Leaf Optical Properties*; Cambridge University Press: Cambridge, UK, 2019.
21. Verrelst, J.; Malenovský, Z.; Van der Tol, C.; Camps-Valls, G.; Gastellu-Etchegorry, J.-P.; Lewis, P.; North, P.; Moreno, J. Quantifying Vegetation Biophysical Variables from Imaging Spectroscopy Data: A Review on Retrieval Methods. *Surv. Geophys.* **2019**, *40*, 589–629. [[CrossRef](#)] [[PubMed](#)]
22. Jacquemoud, S.; Ustin, S.L.; Verdebout, J.; Schmuck, G.; Andreoli, G.; Hosgood, B. Estimating Leaf Biochemistry Using the PROSPECT Leaf Optical Properties Model. *Remote Sens. Environ.* **1996**, *56*, 194–202. [[CrossRef](#)]
23. Ali, A.M.; Darvishzadeh, R.; Skidmore, A.K.; Duren, I.V.; Heiden, U.; Heurich, M. Estimating Leaf Functional Traits by Inversion of PROSPECT: Assessing Leaf Dry Matter Content and Specific Leaf Area in Mixed Mountainous Forest. *Int. J. Appl. Earth Obs. Geoinf.* **2016**, *45*, 66–76. [[CrossRef](#)]
24. Miraglio, T.; Adeline, K.; Huesca, M.; Ustin, S.; Briottet, X. Assessing Vegetation Traits Estimates Accuracies from the Future SBG and Biodiversity Hyperspectral Missions over Two Mediterranean Forests. *Int. J. Remote Sens.* **2022**, *43*, 3537–3562. [[CrossRef](#)]
25. Jacquemoud, S.; Baret, F. PROSPECT: A Model of Leaf Optical Properties Spectra. *Remote Sens. Environ.* **1990**, *34*, 75–91. [[CrossRef](#)]
26. Féret, J.-B.; François, C.; Asner, G.P.; Gitelson, A.A.; Martin, R.E.; Bidet, L.P.R.; Ustin, S.L.; le Maire, G.; Jacquemoud, S. PROSPECT-4 and 5: Advances in the Leaf Optical Properties Model Separating Photosynthetic Pigments. *Remote Sens. Environ.* **2008**, *112*, 3030–3043. [[CrossRef](#)]
27. Féret, J.-B.; Gitelson, A.A.; Noble, S.D.; Jacquemoud, S. PROSPECT-D: Towards Modeling Leaf Optical Properties through a Complete Lifecycle. *Remote Sens. Environ.* **2017**, *193*, 204–215. [[CrossRef](#)]
28. Allen, W.A.; Gausman, H.W.; Richardson, A.J.; Wiegand, C.L. Mean Effective Optical Constants of Thirteen Kinds of Plant Leaves. *Appl. Opt.* **1970**, *9*, 2573–2577. [[CrossRef](#)]
29. Féret, J.-B.; le Maire, G.; Jay, S.; Berveiller, D.; Bendoula, R.; Hmimina, G.; Cheraiet, A.; Oliveira, J.C.; Ponzoni, F.J.; Solanki, T.; et al. Estimating Leaf Mass per Area and Equivalent Water Thickness Based on Leaf Optical Properties: Potential and Limitations of Physical Modeling and Machine Learning. *Remote Sens. Environ.* **2019**, *231*, 110959. [[CrossRef](#)]
30. Wang, Z.; Féret, J.-B.; Liu, N.; Sun, Z.; Yang, L.; Geng, S.; Zhang, H.; Chlus, A.; Kruger, E.L.; Townsend, P.A. Generality of Leaf Spectroscopic Models for Predicting Key Foliar Functional Traits across Continents: A Comparison between Physically- and Empirically-Based Approaches. *Remote Sens. Environ.* **2023**, *293*, 113614. [[CrossRef](#)]
31. Demarez, V. Seasonal Variation of Leaf Chlorophyll Content of a Temperate Forest. Inversion of the PROSPECT Model. *Int. J. Remote Sens.* **1999**, *20*, 879–894. [[CrossRef](#)]
32. Gara, T.W.; Darvishzadeh, R.; Skidmore, A.K.; Wang, T.; Heurich, M. Evaluating the Performance of PROSPECT in the Retrieval of Leaf Traits across Canopy throughout the Growing Season. *Int. J. Appl. Earth Obs. Geoinf.* **2019**, *83*, 101919. [[CrossRef](#)]
33. Lu, B.; He, Y. Evaluating Empirical Regression, Machine Learning, and Radiative Transfer Modelling for Estimating Vegetation Chlorophyll Content Using Bi-Seasonal Hyperspectral Images. *Remote Sens.* **2019**, *11*, 1979. [[CrossRef](#)]
34. Noda, H.M.; Muraoka, H.; Nasahara, K.N. Phenology of Leaf Optical Properties and Their Relationship to Mesophyll Development in Cool-Temperate Deciduous Broad-Leaf Trees. *Agric. For. Meteorol.* **2021**, *297*, 108236. [[CrossRef](#)]
35. Asner, G.P.; Martin, R.E.; Tupayachi, R.; Emerson, R.; Martinez, P.; Sinca, F.; Powell, G.V.N.; Wright, S.J.; Lugo, A.E. Taxonomy and Remote Sensing of Leaf Mass per Area (LMA) in Humid Tropical Forests. *Ecol. Appl.* **2011**, *21*, 85–98. [[CrossRef](#)] [[PubMed](#)]
36. Cavender-Bares, J.; Meireles, J.E.; Couture, J.J.; Kaproth, M.A.; Kingdon, C.C.; Singh, A.; Serbin, S.P.; Center, A.; Zuniga, E.; Pilz, G.; et al. Associations of Leaf Spectra with Genetic and Phylogenetic Variation in Oaks: Prospects for Remote Detection of Biodiversity. *Remote Sens.* **2016**, *8*, 221. [[CrossRef](#)]
37. Spafford, L.; le Maire, G.; MacDougall, A.; de Boissieu, F.; Féret, J.-B. Spectral Subdomains and Prior Estimation of Leaf Structure Improves PROSPECT Inversion on Reflectance or Transmittance Alone. *Remote Sens. Environ.* **2021**, *252*, 112176. [[CrossRef](#)]
38. González-Cascón, R.; Pacheco-Labrador, J.; González-González, I.; Martín, M.P. Temporal Analysis of Fresh Leaf Spectroscopy and Chemical Properties in Quercus Ilex Trees. 2013. Available online: <https://digital.csic.es/handle/10261/141147> (accessed on 1 September 2023).
39. Niinemets, Ü. Is There a Species Spectrum within the World-Wide Leaf Economics Spectrum? Major Variations in Leaf Functional Traits in the Mediterranean Sclerophyll Quercus Ilex. *New Phytol.* **2015**, *205*, 79–96. [[CrossRef](#)]
40. Raddi, S.; Giannetti, F.; Martini, S.; Farinella, F.; Chirici, G.; Tani, A.; Maltoni, A.; Mariotti, B. Monitoring Drought Response and Chlorophyll Content in Quercus by Consumer-Grade, near-Infrared (NIR) Camera: A Comparison with Reflectance Spectroscopy. *New For.* **2022**, *53*, 241–265. [[CrossRef](#)]
41. Chlus, A.; Townsend, P.A. Characterizing Seasonal Variation in Foliar Biochemistry with Airborne Imaging Spectroscopy. *Remote Sens. Environ.* **2022**, *275*, 113023. [[CrossRef](#)]
42. Pavan, G.; Jacquemoud, S.; De Rosny, G.; Rambaut, J.; Frangi, J.; Bidet, L.; François, C. Ramis: A New Portable Field Radiometer to Estimate Leaf Biochemical Content. In Proceedings of the Seventh International Conference on Precision Agriculture and Other Precision Resources Management, Minneapolis, MN, USA, 25–28 July 2004; pp. 25–28.
43. Herrig, J. Preserving California’s Oak Trees: An Evaluation of Factors Impacting Oak Woodlands. Available online: https://ic.arc.losrios.edu/~veiszep/24fall2010/Herrig/G350_Herrig_Project.htm (accessed on 1 September 2023).
44. NASA. *HypSIRI Preparatory Airborne Activities and Associated Science and Applications Research—Abstracts of Selected Proposals (NNH11ZDA001N—HYSPIRI)*; NASA: Washington, DC, USA, 2011.

45. Ma, S.; Baldocchi, D.; Wolf, S.; Verfaillie, J. Slow Ecosystem Responses Conditionally Regulate Annual Carbon Balance over 15 Years in Californian Oak-Grass Savanna. *Agric. For. Meteorol.* **2016**, *228–229*, 252–264. [[CrossRef](#)]
46. Blodgett Forest Research Station. Available online: <https://forests.berkeley.edu/forests/blodgett> (accessed on 8 September 2023).
47. Soaproot Saddle NEON. Available online: <https://www.neonscience.org/field-sites/soap> (accessed on 8 September 2023).
48. Schaepman-Strub, G.; Schaepman, M.E.; Painter, T.H.; Dangel, S.; Martonchik, J.V. Reflectance Quantities in Optical Remote Sensing—Definitions and Case Studies. *Remote Sens. Environ.* **2006**, *103*, 27–42. [[CrossRef](#)]
49. LI-COR, Inc. *LI-1800-12 Integrating Sphere Instruction Manual*; LI-COR, Inc.: Lincoln, NE, USA, 1983.
50. Lichtenthaler, H.K. Chlorophylls and Carotenoids: Pigments of Photosynthetic Biomembranes. In *Methods in Enzymology*; Plant Cell Membranes; Academic Press: Cambridge, MA, USA, 1987; Volume 148, pp. 350–382.
51. Lichtenthaler, H.K.; Buschmann, C. Chlorophylls and Carotenoids: Measurement and Characterization by UV-VIS Spectroscopy. *Curr. Protoc. Food Anal. Chem.* **2001**, *1*, F4.3.1–F4.3.8. [[CrossRef](#)]
52. Sun, J.; Shi, S.; Yang, J.; Du, L.; Gong, W.; Chen, B.; Song, S. Analyzing the Performance of PROSPECT Model Inversion Based on Different Spectral Information for Leaf Biochemical Properties Retrieval. *ISPRS J. Photogramm. Remote Sens.* **2018**, *135*, 74–83. [[CrossRef](#)]
53. Powell, M.J.D. An Efficient Method for Finding the Minimum of a Function of Several Variables without Calculating Derivatives. *Comput. J.* **1964**, *7*, 155–162. [[CrossRef](#)]
54. Féret, J.-B.; François, C.; Gitelson, A.; Asner, G.P.; Barry, K.M.; Panigada, C.; Richardson, A.D.; Jacquemoud, S. Optimizing Spectral Indices and Chemometric Analysis of Leaf Chemical Properties Using Radiative Transfer Modeling. *Remote Sens. Environ.* **2011**, *115*, 2742–2750. [[CrossRef](#)]
55. Wold, S.; Sjöström, M.; Eriksson, L. PLS-Regression: A Basic Tool of Chemometrics. *Chemom. Intell. Lab. Syst.* **2001**, *58*, 109–130. [[CrossRef](#)]
56. Rasmussen, C.E.; Williams, C.K.I. *Gaussian Processes for Machine Learning*; Adaptive Computation and Machine Learning Series; MIT Press: Cambridge, MA, USA, 2005; ISBN 978-0-262-18253-9.
57. Breiman, L. Random Forests. *Mach. Learn.* **2001**, *45*, 5–32. [[CrossRef](#)]
58. Boren, E.J.; Boschetti, L.; Johnson, D.M. Characterizing the Variability of the Structure Parameter in the PROSPECT Leaf Optical Properties Model. *Remote Sens.* **2019**, *11*, 1236. [[CrossRef](#)]
59. Ceccato, P.; Flasse, S.; Tarantola, S.; Jacquemoud, S.; Grégoire, J.-M. Detecting Vegetation Leaf Water Content Using Reflectance in the Optical Domain. *Remote Sens. Environ.* **2001**, *77*, 22–33. [[CrossRef](#)]
60. Pacheco-Labrador, J.; González-Cascón, R.; Hernández-Clemente, R.; Martín, M.P.; Melendo de la Vega, J.R.; Zarco-Tejada, P. Impact of Trichomes in the Application of Radiative Transfer Models in Leaves of *Quercus Ilex*. In Proceedings of the VII Spanish Forestry Congress, Plasencia, Spain, 26 June 2017.
61. Barry, K.M.; Newnham, G.J.; Stone, C. Estimation of Chlorophyll Content in Eucalyptus Globulus Foliage with the Leaf Reflectance Model PROSPECT. *Agric. For. Meteorol.* **2009**, *149*, 1209–1213. [[CrossRef](#)]
62. Qiu, F.; Chen, J.M.; Croft, H.; Li, J.; Zhang, Q.; Zhang, Y.; Ju, W. Retrieving Leaf Chlorophyll Content by Incorporating Variable Leaf Surface Reflectance in the PROSPECT Model. *Remote Sens.* **2019**, *11*, 1572. [[CrossRef](#)]
63. Yang, B.; Lin, H.; He, Y. Data-Driven Methods for the Estimation of Leaf Water and Dry Matter Content: Performances, Potential and Limitations. *Sensors* **2020**, *20*, 5394. [[CrossRef](#)] [[PubMed](#)]
64. Miraglio, T.; Adeline, K.; Huesca, M.; Ustin, S.; Briottet, X. Monitoring LAI, Chlorophylls, and Carotenoids Content of a Woodland Savanna Using Hyperspectral Imagery and 3D Radiative Transfer Modeling. *Remote Sens.* **2020**, *12*, 28. [[CrossRef](#)]
65. Zhang, Y.; Chen, J.M.; Thomas, S.C. Retrieving Seasonal Variation in Chlorophyll Content of Overstory and Understory Sugar Maple Leaves from Leaf-Level Hyperspectral Data. *Can. J. Remote Sens.* **2007**, *33*, 406–415. [[CrossRef](#)]
66. Yang, X.; Tang, J.; Mustard, J.F.; Wu, J.; Zhao, K.; Serbin, S.; Lee, J.-E. Seasonal Variability of Multiple Leaf Traits Captured by Leaf Spectroscopy at Two Temperate Deciduous Forests. *Remote Sens. Environ.* **2016**, *179*, 1–12. [[CrossRef](#)]

Disclaimer/Publisher’s Note: The statements, opinions and data contained in all publications are solely those of the individual author(s) and contributor(s) and not of MDPI and/or the editor(s). MDPI and/or the editor(s) disclaim responsibility for any injury to people or property resulting from any ideas, methods, instructions or products referred to in the content.

Conclusion

The work conducted with the CSTARS-Leaf dataset and presented in the peer-reviewed article [Gaubert et al. 2024](#) aimed to compare several estimation methods, including statistical and PROSPECT-based methods, for the four key leaf traits and the four oak species from TONZ, SJER, BLOF and SOAP sites.

Comparing all the estimation methods, the statistical methods trained on the CSTARS-Leaf dataset outperformed the PROSPECT-based methods regardless of the leaf trait. Statistical methods built on CSTARS-Leaf dataset reach higher accuracy than PROSPECT-based methods regardless of the MLRA considered, but estimators based on GPR (*i.e.*, STAT-CSTARS-GPR) globally yielded more accurate estimates considering the four leaf traits (RMSE of $5.0 \mu\text{g} \cdot \text{cm}^{-2}$; $1.3 \mu\text{g} \cdot \text{cm}^{-2}$; 0.0009 cm ; $0.0009 \text{ g} \cdot \text{cm}^{-2}$ for C_{ab} , C_{xc} , EWT and LMA respectively). However, it can be noticed that nonlinear MLRAs achieved more accurate estimates for leaf pigments while linear MLRAs delivered more accurate estimates for EWT and LMA. Examining the existing literature it seems that this is the first time this result is highlighted. In conclusion, a statistical method built on a dataset that includes the same species composition and measured with the same protocol may be the most accurate estimation method for all leaf traits. Nonetheless, deriving data to build statistical methods from scratch can be very demanding in time, material and financial resources. Therefore, to estimate leaf traits in ecosystems, or for species, where leaf traits and leaf optical properties have never been sampled, a user may prefer to refer to a PROSPECT-based method or a transferred statistical method.

Comparing the PROSPECT-based methods, the iterative inversion of the leaf RTM may be recommended to a user. The iterative inversion of PROSPECT (*i.e.*, IO-PROSPECT) led to more accurate estimates for C_{ab} , C_{xc} and EWT (RMSE of and $7.8 \mu\text{g} \cdot \text{cm}^{-2}$, $2.0 \mu\text{g} \cdot \text{cm}^{-2}$, 0.0035 cm respectively). Additionally, IO-PROSPECT performs a joint estimation of the leaf traits which could ease its use in practice. Estimates for LMA show a distinct behavior and were more accurate for the hybrid method built with RFR (*i.e.*, HYBRID-RFR; $RMSE = 0.0030 \text{ g} \cdot \text{cm}^{-2}$).

The impact of sampling seasons and species were also investigated. According to the results, estimation accuracy seems to be little affected by the sampling season. Additionally, the estimation accuracy did not depend particularly on the species but rather on its plant functional type.

To assess the transferability of statistical methods, estimators were also built from an independent dataset (ANGERS). As expected, estimation accuracies were degraded for estimators built on the ANGERS database (STAT-ANGERS) compared to estimators built exclusively on the CSTARS-Leaf dataset (STAT-CSTARS). Using ANGERS, RMSE were degraded by a factor of around 2 for C_{ab} , C_{xc} and EWT, and a factor 1.3 for LMA. For EWT and LMA transferred statistical methods lead to more accurate estimates than PROSPECT-based methods. Similarly as STAT-CSTARS estimators, STAT-ANGERS estimators were more accurate for EWT and LMA when they were built from a linear MLRA. For C_{ab} and C_{xc} , the performance yielded by STAT-ANGERS estimator degraded compared to PROSPECT-based methods. Therefore, statistical methods are to some extent transferable. However, as highlighted in other studies ([Féret et al. 2019](#); [Yang et al. 2020](#)), the accuracies obtained by statistical strategies are highly dependent on both the trained and the test datasets. Therefore, RMSE variations would likely have been different if other training datasets had been used. To conclude on the transferability of statistical methods, future work should provide a better understanding of natural variability of leaf traits spectral signatures across species and ecosystems, and understand how MLRAs identify their spectral signatures. Future work could provide new ways to regularize MLRAs in order to achieve the transferability of statistical methods across species and ecosystems.

The distribution of the structural parameter N from the PROSPECT model has been studied for the four oak species under study. Retrieved N values lie in the 1.0 – 2.2 range which is in line with the previous ranges proposed in the literature (1.0 – 2.5 ; [Spafford et al. 2021](#)) and have an intraspecific dynamic range bigger than 0.5. Additionally, the results showed that N is strongly correlated to the LMA for these species. Consequently, N follows the same seasonal trends as LMA: N depends little on the season for evergreen species, and tends to increase over the year for deciduous species, which is consistent with previous observations ([Noda et al. 2021](#)). PROSPECT-based estimation methods had no prior knowledge on N to estimate the leaf traits, while such prior is often recommended in the state-of-the-art. Nevertheless, with PROSPECT-based methods the four leaf traits were estimated with suitable accuracies compared to past studies results.

Regarding the samples of conifer species that were originally present in the CSTARs-Leaf dataset, their reliability can be questioned. Indeed the protocol from [Mesarch et al. 1999](#) was used to perform the measurement of conifer needle-leaves reflectance and transmittance to by-pass the measurement issue with the wide opening of the integrating sphere. However the obtained measures were uncertain because a large number of them were physically unrealistic (e.g., negative transmittance) even after applying the correction protocol.

Not surprisingly, PROSPECT iterative inversions and ANGERS-based statistical strategies yielded poor accuracies and estimation errors that have a high variance and/or are highly biased ([Appendix B](#)). This experience does not allow to draw any conclusions on the applicability of the PROSPECT-based and ANGERS-based statistical methods considering potential intrinsic errors in the reflectance and transmittance data.

The statistical strategies using only these samples yielded coherent estimates with suitable accuracies and highlight that statistical algorithms learn the biases contained in the training data (see [Appendix B](#) Tables [B.1](#), [B.2](#), [B.3](#) and [B.4](#); RMSE of $13.4 \mu\text{g} \cdot \text{cm}^{-2}$, $3.1 \mu\text{g} \cdot \text{cm}^{-2}$, 0.0042 cm , $0.0044 \text{ g} \cdot \text{cm}^{-2}$; R^2 of 0.64, 0.58, 0.52, 0.46; for C_{ab} , C_{xc} , EWT and LMA respectively with Ridge). But again, considering measurement errors it is not possible to conclude that estimation uncertainties are intrinsic to the tested statistical strategies.

At least one other measurement protocol exists for needle-leaves reflectance measurement and requires the use of a special carrier ([Harron 2000](#)). Although, it is considered that the difference between [Mesarch et al. 1999](#) and [Harron 2000](#) protocols is approximately an offset because the use of the special carrier only eliminates the specular forward scattering ([Zarco-Tejada et al. 2004](#)).

Besides, several datasets gathering leaf optical properties and corresponding leaf traits are freely available for broadleaved species but only few of them for needle-leaved species. Such datasets are necessary to improve the analysis and accuracy of statistical methods.

The traits were estimated at the leaf scale from spectra averaged over several leaves and compared to the mean biochemical composition of this set of leaves. This scale constitutes an intermediary scale between the single leaf and the canopy scales: on the one hand, the leaf scale is able to represent the mean behavior of the tree rather than taking into account the variance from each single leaf ; on the other hand, this representation avoids the impacts of structure, geometry and non-photosynthetic parts of the trees that alter the optical properties at the canopy scale.

Nevertheless, with all these simplifications, the leaf scale is still far from being able to apply imaging spectroscopy to remote sensing of canopies. Although leaf traits are correctly estimated at the leaf scale, there is no guarantee that the results obtained at this scale can be transposed to the canopy scale. However, leaf scale estimates provide insight for canopy scale estimation where the effects of canopy geometry, non photosynthetic vegetation and background are taken into account.

As a continuation of this work, the [next chapter](#) will present estimation methods at the canopy scale. The difference of accuracies from leaf scale and canopy scale will be discussed.

Chapter 5

Estimation at the Canopy Scale

In the previous chapter, estimation methods for leaf traits were evaluated and compared at the leaf scale using spectral in-lab data. This work demonstrated that both statistical methods and PROSPECT-based methods could estimate leaf traits from oak leaf samples, all species and seasons included. Although, statistical methods yielded more accurate estimates.

In this chapter, the performance of leaf traits estimation methods are analyzed at the canopy scale for all the ecosystems, species, and seasons. Leaf traits are estimated in this chapter from AVIRIS-C airborne imaging spectroscopy with a GSD around 14 m. The chapter aims to compare statistical and hybrid methods using the CSTARS-Canopy dataset introduced in [Chapter 3](#). At canopy scale, many factors can impact canopy reflectance (understory, canopy geometry, woody elements) such as mentioned in [Chapter 1](#). As a result, spectral measurements are carried out in a less controlled environment than at the leaf scale. For this reason, this chapter also seeks to compare the accuracy of estimates between canopy scale and leaf scale. With AVIRIS-C spectral measurements, reflectance is sampled every 10 nm with a bandwidth of 10 nm, in contrast to leaf-scale measurements carried out with an ASD with a sampling step of 1 nm and a bandwidth of 3 nm in the visible and NIR range and with a sampling step of 2 nm and a 10 nm bandwidth in the SWIR range.

To assess the accuracy of the methods at the canopy scale, leaf traits are estimated with both statistical and hybrid methods from AVIRIS-C extracted spectra and compared to corresponding reference leaf traits measurements included in the CSTARS-Canopy dataset introduced in [Chapter 3](#). In the first step, leaf traits are estimated using the same statistical methods evaluated in [Chapter 4](#) at the leaf scale and using the same evaluation strategy. These statistical methods are built with four MLRA (Ridge, PLSR, GPR and RFR, detailed in [Chapter 2, Subsection 2.2.1](#)). As with all statistical methods, performance depends on the training and validation datasets (here, subsets of the CSTARS-Canopy dataset). Although, since statistical methods alleviate potential biases from measurements, the expected error from these methods provides a comparison point to benchmark hybrid methods evaluated in the second and third steps. In the second step, leaf traits are estimated using a hybrid method that does not depend on illumination geometry. This global approach uses a 1D-CNN as MLRA to build an estimator from radiative transfer simulations accounting the various illumination geometries from all the images.

[Section 5.1](#) presents the statistical methods and their evaluation. [Section 5.2](#) introduces the 1D-CNN based method, details the calibration of the 1D-CNN architecture and the estimation results. Finally, [Section 5.3](#) discusses the results obtained with the three canopy-scale methods and highlights the upscaling effects by comparison with results from [Chapter 4](#).

5.1 Assessment of statistical methods accuracy on the CSTARS-Canopy dataset

5.1.1 Methodology

Four statistical methods are proposed and differ by the MLRA used to build the estimators: Ridge, PLSR, GPR, and RFR. The approach is similar to STAT-CSTARS methods from [Chapter 4](#). The methods are evaluated through an iterative hold-out evaluation with shuffling such as detailed in [Chapter 2, Subsection 2.2.3](#). This evaluation strategy provides an assessment of the expected error for the four methods.

During the iterative hold-out evaluation with shuffling, the train/test split ratio is set to 75%/25% and the dataset is split randomly. The hold-out evaluation is repeated for 200 iterations. Since the test set is selected randomly, the number of times a sample is selected in the test set remains random and unpredictable. However, the number of times a sample would be selected in the test set follows a binomial law with parameters 200 trials and a probability of success of 0.25. Therefore the probability that a sample will be drawn in the test set more than 15 times is 98.89%, and 99.99% that it will be drawn more than 10 times. The evaluation metrics are computed at each iteration of the iterative hold-out evaluation and are saved. The expected value of each metric is the mean value of the metric over all the iterations.

To evaluate the specific expected error for a species or family of species, several subsets of the CSTARS-Canopy dataset were considered before applying the train/test split. Subsets were built to contain only samples with the same features (species, species family, plant functional types, ecosystems...). These subsets are given in [Table 5.1](#)

Subset name	Species	Sites
Oaks	QUCH ^(e) , QUDO ^(d) , QUKE ^(d) , QUWI ^(e)	BLOF, SJER, SOAP, TONZ
Woodland Savannas oaks	QUDO ^(d) , QUWI ^(e)	SJER, TONZ
Mid-Elev. Forests oaks	QUCH ^(e) , QUKE ^(d)	BLOF, SOAP
Conifers	PISA, PIPO, PILA, PIJE, ABCO, ABMA, CADE	BLOF, SJER, SOAP, TEAK, TONZ
<i>Pinus spp.</i>	PISA, PIPO, PILA, PIJE	BLOF, SJER, SOAP, TEAK, TONZ
<i>Abies spp.</i>	ABCO, ABMA	BLOF, SOAP, TEAK

Table 5.1: Subsets of species considered for the evaluation of estimation methods. The last columns provide the sites involved

5.1.2 Results

The expected values for RMSE, R^2 , bias and Kendall's Tau are given in Tables [5.2](#), [5.3](#), [5.4](#) and [5.5](#) for C_{ab} , C_{xc} , EWT, and LMA respectively. Results are given for several subsets of CSTARS-Canopy dataset including species, species pooled by families or species pooled by ecosystems.

Table 5.2: Accuracy metrics expected values of statistical methods for C_{ab} on several subsets of CSTARS-Canopy. The mean m and standard deviation σ of reference data are given in the first column.

	MLRA	RMSE $\mu\text{g.cm}^{-2}$	R^2 -	Bias $\mu\text{g.cm}^{-2}$	τ -
Oaks ($m = 31.6$) ($\sigma = 14.6$)	Ridge	13.6	0.08	0.1	0.25
	PLSR	13.7	0.05	0.1	0.24
	GPR	13.0	0.15	-0.2	0.24
	RFR	13.3	0.11	0.3	0.24
Woodland Savannas ($m = 35.2$) ($\sigma = 10.2$)	Ridge	10.5	-0.25	0.4	0.16
	PLSR	10.8	-0.36	0.5	0.15
	GPR	9.7	-0.06	-0.4	0.21
	RFR	9.6	-0.06	0.2	0.26
QUDO^(d) ($m = 36.2$) ($\sigma = 10.5$)	Ridge	11.2	-0.64	-0.3	0.07
	PLSR	12.0	-0.92	-0.3	0.10
	GPR	9.8	-0.24	-0.7	0.19
	RFR	9.7	-0.21	-0.0	0.26
QUWI^(e) ($m = 33.3$) ($\sigma = 9.8$)	Ridge	10.2	-1.71	-0.5	0.14
	PLSR	10.7	-2.22	-0.5	0.15
	GPR	8.9	-1.02	-1.0	0.32
	RFR	9.9	-1.59	-0.2	0.17
Mid-Elev. Forests ($m = 30.0$) ($\sigma = 16.0$)	Ridge	14.7	0.11	0.2	0.30
	PLSR	14.7	0.09	0.2	0.29
	GPR	14.2	0.16	0.1	0.29
	RFR	14.7	0.09	0.4	0.26
QUKE^(d) ($m = 23.3$) ($\sigma = 14.8$)	Ridge	9.0	0.60	-0.2	0.61
	PLSR	9.0	0.59	-0.2	0.61
	GPR	9.2	0.57	0.0	0.60
	RFR	10.3	0.45	-0.1	0.52
QUCH^(e) ($m = 39.8$) ($\sigma = 12.3$)	Ridge	11.5	-0.03	-0.7	0.24
	PLSR	12.0	-0.15	-0.8	0.23
	GPR	12.6	-0.22	-0.1	0.00
	RFR	13.2	-0.37	-0.7	0.07
Conifers ($m = 62.2$) ($\sigma = 23.8$)	Ridge	20.0	0.27	-0.3	0.41
	PLSR	20.4	0.23	-0.4	0.40
	GPR	20.2	0.26	-0.5	0.40
	RFR	20.6	0.22	-0.2	0.38
<i>Pinus spp.</i> ($m = 68.2$) ($\sigma = 24.8$)	Ridge	21.9	0.13	0.2	0.36
	PLSR	22.9	0.04	-0.1	0.33
	GPR	22.3	0.10	0.5	0.34
	RFR	21.9	0.12	1.2	0.36
<i>Abies spp.</i> ($m = 63.3$) ($\sigma = 15.9$)	Ridge	15.3	-0.13	-0.1	0.31
	PLSR	15.1	-0.11	-0.3	0.32
	GPR	16.2	-0.22	-0.3	0.15
	RFR	15.5	-0.19	-0.1	0.19
CADE ($m = 35.3$) ($\sigma = 10.3$)	Ridge	10.8	-0.50	0.3	0.15
	PLSR	11.1	-0.64	0.1	0.15
	GPR	11.3	-0.63	0.5	-0.08
	RFR	11.2	-0.72	1.2	0.08

For C_{ab} , RMSE ranges from 8.9 (with GPR for QUWI^(e)) to 22.9 $\mu\text{g} \cdot \text{cm}^{-2}$ (with PLSR for *Pinus spp.*). Although, computing the ratio of the RMSE with the mean of reference values, the results show less discrepancy between categories. For oaks, the overall rRMSE is equal to 40% percent. But the rRMSE is greater for QUKE^(d) (39%) than QUDO^(d), QUCH^(e) or QUWI^(e) (less than 30%). For conifers and each subset of conifers, the rRMSE is less important, rRMSE are around 30%.

All sRMSE vary between 85 and 95%, except for QUKE^(d) (61%) and CADE (105%). The trends observed for sRMSE also appear with the R^2 and Kendall's Tau. In fact R^2 ranges from -2.22 (QUWI^(e)) to 0.60 (QUKE^(d)), and most of them are negative or close to zero, highlighting that the MSE is close to the variance of reference data.

Tau ranges from -0.08 (with GPR for CADE) to 0.61 (with PLSR for QUKE^(d)). Tau is closer to zero when R^2 is negative. Tau around 0.6 and over are obtained for QUKE^(d), whose samples have a greater variance. Tau over 0.3 are obtained for pine and fir species.

For most of the categories the bias is negligible and ranges between -0.5 and $0.5 \mu\text{g} \cdot \text{cm}^{-2}$. Bias is larger for oaks species when considered separately: the bias is around $-0.7 \mu\text{g} \cdot \text{cm}^{-2}$ for QUCH^(e) with Ridge, PLSR and RFR, for QUWI^(e) it is $-1.0 \mu\text{g} \cdot \text{cm}^{-2}$ with GPR. RFR-based estimators reach a positive bias for pine species and CADE ($1.2 \mu\text{g} \cdot \text{cm}^{-2}$).

Considering all the results, none of the MLRA clearly stands out from the others. Overall, the difference between linear and non-linear MLRA is not pronounced. Estimates are slightly more accurate if they are provided by Ridge-based estimators since Ridge provides the most accurate results in 6 categories.

Table 5.3: Accuracy metrics expected values of statistical methods for C_{xc} on several subsets of CSTARS-Canopy. For reference the mean m and standard deviation σ of reference data are given.

	MLRA	RMSE $\mu g.cm^{-2}$	R ² -	Bias $\mu g.cm^{-2}$	tau -
Oaks ($m = 8.2$) ($\sigma = 3.2$)	Ridge	3.2	-0.04	0.0	0.14
	PLSR	3.2	-0.05	0.0	0.13
	GPR	3.0	0.06	-0.1	0.24
	RFR	3.1	0.01	0.0	0.24
Woodland Savannas ($m = 9.1$) ($\sigma = 2.1$)	Ridge	2.2	-0.35	0.0	-0.11
	PLSR	2.3	-0.41	0.0	-0.08
	GPR	2.1	-0.19	0.0	0.15
	RFR	2.3	-0.42	-0.1	0.10
QUDO^(d) ($m = 9.3$) ($\sigma = 2.2$)	Ridge	2.2	-0.55	0.0	-0.04
	PLSR	2.4	-0.78	0.0	-0.04
	GPR	2.2	-0.43	0.0	-0.04
	RFR	2.5	-0.98	-0.1	-0.04
QUWI^(e) ($m = 8.6$) ($\sigma = 2.1$)	Ridge	2.6	-33.65	-0.3	-0.01
	PLSR	2.8	-28.01	-0.4	-0.01
	GPR	2.0	-25.86	-0.2	0.14
	RFR	2.1	-24.01	-0.0	0.30
Mid-Elev. Forests ($m = 7.7$) ($\sigma = 3.6$)	Ridge	3.3	0.05	0.0	0.24
	PLSR	3.3	0.04	0.0	0.24
	GPR	3.4	0.03	0.0	0.25
	RFR	3.4	-0.01	0.0	0.25
QUKE^(d) ($m = 6.0$) ($\sigma = 2.4$)	Ridge	1.8	0.39	-0.1	0.49
	PLSR	1.8	0.35	-0.1	0.47
	GPR	2.1	0.17	0.0	0.39
	RFR	2.1	0.17	0.0	0.39
QUCH^(e) ($m = 10.3$) ($\sigma = 3.4$)	Ridge	2.5	0.32	0.0	0.44
	PLSR	2.5	0.27	-0.1	0.42
	GPR	3.1	0.00	0.0	0.27
	RFR	3.0	0.00	0.1	0.28
Conifers ($m = 16.0$) ($\sigma = 5.1$)	Ridge	4.3	0.28	-0.1	0.40
	PLSR	4.4	0.25	-0.1	0.39
	GPR	4.9	0.08	-0.2	0.24
	RFR	4.6	0.17	-0.2	0.33
<i>Pinus spp.</i> ($m = 17.8$) ($\sigma = 5.0$)	Ridge	4.4	0.13	0.0	0.34
	PLSR	4.6	0.07	0.0	0.32
	GPR	4.8	-0.03	0.0	0.21
	RFR	4.6	0.05	0.0	0.27
<i>Abies spp.</i> ($m = 15.6$) ($\sigma = 3.6$)	Ridge	3.6	-0.33	-0.1	0.19
	PLSR	3.6	-0.40	-0.1	0.17
	GPR	3.6	-0.19	-0.2	0.14
	RFR	3.6	-0.36	0.0	0.14
CADE ($m = 9.8$) ($\sigma = 2.4$)	Ridge	2.6	-1.14	0.1	-0.02
	PLSR	2.7	-1.86	0.2	-0.03
	GPR	2.5	-0.72	0.1	0.04
	RFR	2.5	-0.76	0.3	0.08

For C_{xc} , RMSE ranges from 1.8 (for QUKE^(d) with Ridge) to 4.9 (for Conifers with GPR) $\mu\text{g} \cdot \text{cm}^{-2}$. RMSE is globally higher for pine and fir species.

The rRMSE is equivalent to around 25% for all conifer categories, QUCH^(e) and woodland savanna oak species (QUDO^(d), QUWI^(e)). For QUKE^(d) the rRMSE is around 30%. The RMSE are close to the reference C_{xc} standard deviation for most of the categories (sRMSE above 90%), exceptions are QUKE^(d) (sRMSE=75%), QUCH^(e) (sRMSE=74%) and all conifers combined (sRMSE=84%).

Ratios between RMSE and standard deviation are mirrored by the R^2 and Tau values. In fact, R^2 close to 0.3 or above are obtained for all conifers, QUCH^(e) and QUKE^(d) with Ridge-based estimators (respectively 0.28, 0.32 and 0.39). Other categories obtain R^2 values close to zero or even negative values.

Tau ranges from -0.11 (for oaks of woodland savannas with Ridge) to 0.49 (for QUKE^(d) with Ridge). Values around 0.4 or above are obtained for QUCH^(e) (with Ridge and PLSR), QUKE^(d) (with the four MLRA), and all conifers combined (with Ridge and PLSR). Suitable performance is also obtained for pines with linear MLRAs (Tau above 0.3). Other categories show weaker correlation according to Kendall's Tau values.

Expected bias ranges from -0.4 (for QUWI^(e) with PLSR) to 0.3 (for CADE with RFR). Overall, estimates remain little biased because for all the categories and for the MLRA which minimizes RMSE, the absolute value of bias is less than $0.15 \mu\text{g} \cdot \text{cm}^{-2}$.

Considering all the categories, GPR and Ridge yield the most accurate estimates. In cases where Ridge-based estimators provide the more accurate estimates, PLSR-based estimators also provide estimates with the second best accuracy. This highlights the linearity of the problem.

Table 5.4: Accuracy metrics expected values of statistical methods for EWT on several subsets of CSTARS-Canopy. For reference the mean m and standard deviation σ of reference data are given.

	MLRA	RMSE <i>cm</i>	R ² -	Bias <i>cm</i>	tau -
Oaks ($m = 0.0111$) ($\sigma = 0.0040$)	Ridge	0.0040	-0.11	0.0001	-0.02
	PLSR	0.0041	-0.15	0.0001	-0.07
	GPR	0.0041	-0.18	0.0001	0.13
	RFR	0.0042	-0.23	0.0000	0.16
Woodland Savannas ($m = 0.0110$) ($\sigma = 0.0022$)	Ridge	0.0022	-0.28	0.0000	0.03
	PLSR	0.0023	-0.44	0.0000	0.04
	GPR	0.0022	-0.32	0.0000	0.03
	RFR	0.0022	-0.31	-0.0001	0.21
QUDO^(d) ($m = 0.0105$) ($\sigma = 0.0017$)	Ridge	0.0018	-0.52	-0.0001	0.10
	PLSR	0.0018	-0.58	-0.0001	0.11
	GPR	0.0018	-0.56	0.0000	0.04
	RFR	0.0017	-0.39	0.0000	0.12
QUWI^(e) ($m = 0.0122$) ($\sigma = 0.0026$)	Ridge	0.0027	-2.84	0.0002	-0.19
	PLSR	0.0033	-5.34	0.0005	-0.15
	GPR	0.0027	-2.60	0.0002	-0.04
	RFR	0.0028	-2.14	0.0003	-0.24
Mid-Elev. Forests ($m = 0.0111$) ($\sigma = 0.0047$)	Ridge	0.0047	-0.18	0.0001	0.07
	PLSR	0.0048	-0.26	0.0002	0.00
	GPR	0.0048	-0.27	0.0001	0.13
	RFR	0.0048	-0.28	0.0000	0.15
QUKE^(d) ($m = 0.00091$) ($\sigma = 0.0031$)	Ridge	0.0020	0.47	0.0001	0.51
	PLSR	0.0021	0.45	0.0001	0.51
	GPR	0.0029	-0.01	-0.0001	0.30
	RFR	0.0029	-0.01	0.0001	0.26
QUCH^(e) ($m = 0.0139$) ($\sigma = 0.0052$)	Ridge	0.0051	-0.49	0.0001	0.12
	PLSR	0.0052	-0.62	0.0002	0.11
	GPR	0.0055	-0.61	0.0001	0.02
	RFR	0.0062	-1.32	0.0004	-0.03
Conifers ($m = 0.0371$) ($\sigma = 0.0068$)	Ridge	0.0059	0.21	0.0001	0.39
	PLSR	0.0060	0.16	0.0001	0.38
	GPR	0.0064	0.05	0.0000	0.27
	RFR	0.0061	0.15	-0.0001	0.32
<i>Pinus spp.</i> ($m = 0.0376$) ($\sigma = 0.0062$)	Ridge	0.0058	0.06	0.0000	0.30
	PLSR	0.0061	-0.05	0.0000	0.28
	GPR	0.0057	0.10	-0.0003	0.32
	RFR	0.0060	0.03	-0.0003	0.23
<i>Abies spp.</i> ($m = 0.0401$) ($\sigma = 0.0063$)	Ridge	0.0064	-0.22	-0.0002	0.18
	PLSR	0.0066	-0.32	-0.0003	0.16
	GPR	0.0064	-0.18	-0.0001	0.07
	RFR	0.0061	-0.11	0.0001	0.21
CADE ($m = 0.0295$) ($\sigma = 0.0037$)	Ridge	0.0031	-0.02	-0.0001	0.48
	PLSR	0.0032	-0.12	-0.0001	0.49
	GPR	0.0030	0.08	0.0001	0.51
	RFR	0.0032	-0.07	0.0004	0.42

For EWT, the RMSE values are below 0.0025 cm for QUDO^(d) (with the four MLRA), QUKE^(d) (with Ridge and PLSR) and less specifically for oaks of woodland savannas (with the four MLRA). Highest RMSE values are obtained for pines and firs and are above 0.0060 cm.

However, rRMSE values for conifers, pines, firs and CADE is only around 15%. rRMSE equals more than 30% for all oaks combined, oaks of mid elevation forests and QUCH^(e). For all oak categories, the sRMSE is around 100%, except for QUKE^(d) (sRMSE is around 65%). The sRMSE ranges between 85% and 100% for conifer categories.

Most of R^2 scores are negative. Suitable R^2 scores are only obtained for QUKE^(d) with linear MLRAs (0.45 with PLSR and 0.47 with Ridge). Intermediate R^2 is obtained for conifers species with Ridge ($R^2 = 0.21$).

Expected bias values range from -0.0003 (*Abies spp.*) to 0.0005 cm (QUWI^(e)). Globally, the bias is more pronounced for conifers categories, but remains negligible and acceptable for all categories.

Tau ranges from -0.24 (for QUWI^(e) with RFR) to 0.51 (for CADE with GPR). Best tau values are obtained for QUKE^(d) (0.51 with Ridge), then for all conifers combined (0.39 with Ridge) and for pines (0.32 with GPR). For QUWI^(e), the four MLRA yield negative values for Tau, highlighting that estimators perform worse than a random guess from a normal distribution $\mathcal{N}(m, \sigma)$.

Ridge yields more accurate estimates for oaks or conifers. GPR or RFR provide more accurate estimates for smaller subsets but Ridge-based estimators are often the second most accurate. Ridge and PLSR yield almost equivalent results, but PLSR results are always slightly under those from Ridge.

Table 5.5: Accuracy metrics expected values of statistical methods for LMA on several subsets of CSTARS-Canopy. For reference the mean m and standard deviation σ of reference data are given.

	MLRA	RMSE $g.cm^{-2}$	R ² -	Bias $g.cm^{-2}$	tau -
Oaks ($m = 0.0119$) ($\sigma = 0.0047$)	Ridge	0.0044	0.07	0.0000	0.28
	PLSR	0.0046	-0.02	0.0000	0.23
	GPR	0.0042	0.19	-0.0002	0.32
	RFR	0.0038	0.32	0.0000	0.43
Woodland Savannas ($m = 0.0135$) ($\sigma = 0.0026$)	Ridge	0.0025	-0.12	0.0000	0.27
	PLSR	0.0026	-0.20	0.0000	0.26
	GPR	0.0025	-0.09	-0.0002	0.25
	RFR	0.0024	-0.07	0.0001	0.32
QUDO^(d) ($m = 0.0123$) ($\sigma = 0.0019$)	Ridge	0.0016	-0.06	0.0000	0.36
	PLSR	0.0016	-0.15	0.0000	0.33
	GPR	0.0016	-0.09	-0.0000	0.27
	RFR	0.0016	-0.07	0.0000	0.37
QUWI^(e) ($m = 0.0158$) ($\sigma = 0.0023$)	Ridge	0.0023	-1.36	-0.0002	0.25
	PLSR	0.0025	-2.33	-0.0002	0.24
	GPR	0.0021	-0.59	-0.0001	0.25
	RFR	0.0023	-1.31	-0.0002	0.14
Mid-Elev. Forests ($m = 0.0111$) ($\sigma = 0.0052$)	Ridge	0.0047	0.14	0.0002	0.37
	PLSR	0.0050	0.00	0.0002	0.32
	GPR	0.0045	0.21	0.0001	0.36
	RFR	0.0042	0.32	0.0000	0.42
QUKE^(d) ($m = 0.0071$) ($\sigma = 0.0016$)	Ridge	0.0015	-0.05	-0.0001	0.27
	PLSR	0.0015	-0.12	-0.0001	0.27
	GPR	0.0016	-0.17	0.0000	0.15
	RFR	0.0014	0.00	0.0000	0.30
QUCH^(e) ($m = 0.0171$) ($\sigma = 0.0020$)	Ridge	0.0021	-0.37	-0.0001	-0.13
	PLSR	0.0022	-0.63	-0.0001	-0.12
	GPR	0.0020	-0.28	0.0000	-0.05
	RFR	0.0025	-1.02	-0.0001	-0.14
Conifers ($m = 0.0328$) ($\sigma = 0.0058$)	Ridge	0.0053	0.14	0.0000	0.35
	PLSR	0.0055	0.08	0.0000	0.33
	GPR	0.0056	0.04	-0.0003	0.20
	RFR	0.0053	0.16	-0.0002	0.29
<i>Pinus spp.</i> ($m = 0.0338$) ($\sigma = 0.0050$)	Ridge	0.0041	0.22	0.0000	0.42
	PLSR	0.0043	0.13	0.0000	0.40
	GPR	0.0049	-0.05	-0.0001	0.14
	RFR	0.0048	-0.03	-0.0001	0.17
<i>Abies spp.</i> ($m = 0.0335$) ($\sigma = 0.0070$)	Ridge	0.0068	-0.18	-0.0001	0.23
	PLSR	0.0071	-0.29	-0.0001	0.19
	GPR	0.0073	-0.29	0.0000	0.06
	RFR	0.0067	-0.14	0.0001	0.28
CADE ($m = 0.0275$) ($\sigma = 0.0031$)	Ridge	0.0029	-0.23	-0.0001	0.25
	PLSR	0.0030	-0.34	-0.0001	0.24
	GPR	0.0030	-0.28	0.0001	0.29
	RFR	0.0025	0.11	0.0002	0.44

For LMA, lowest RMSE are obtained for the two deciduous oak species (QUKE^(d) and QUDO^(d), RMSE lower than $0.0016 \text{ g} \cdot \text{cm}^{-2}$) compared to evergreen oak species (QUCH^(e) and QUWI^(e), RMSE is around $0.0022 \text{ g} \cdot \text{cm}^{-2}$). LMA estimations combining all the oak species obtain higher RMSE values (around $0.40 \text{ g} \cdot \text{cm}^{-2}$), probably due to the more important errors with mid-elevation oak species. Similar RMSE values are obtained for pines. Highest RMSE values are obtained for fir species.

However LMA distributions are distinct considering the species, and considered categories have distinct means m and standard deviations σ . Therefore, rRMSE is the lowest for QUDO^(d), QUCH^(e), QUWI^(e), pines and CADE (rRMSE smaller than 15%) and is around 20% for QUKE^(d) and fir species. sRMSE is around 80% for all oak species combined, oak species of mid-elevation forests, and CADE. For all other categories, sRMSE values vary between 90% and 100% and reach 110% for oak species of woodland savannas.

Most of R^2 scores are negative or very close to zero. Best R^2 scores are obtained with RFR-based estimators for all oak species (0.32), oak species of mid-elevation forests (0.32) and all conifer species (0.16), and with Ridge-based estimators for pines (0.22).

Tau values emphasize that estimates are more correlated to reference combining all oak species, combining mid-elevation oak species, for QUDO^(d), pines and CADE (Tau is around 0.40).

For QUCH^(e), the four MLRA yield negative Tau values, highlighting that estimators perform worse than a random guess from a normal distribution $\mathcal{N}(m, \sigma)$.

Biases are negligible. With some exceptions, absolute bias values are smaller than $0.0001 \text{ g} \cdot \text{cm}^{-2}$.

RFR yields more accurate estimates than other MLRA for both oak and conifer species. Indeed, RFR-based estimators yield the most accurate results in 8 categories. Ridge-based estimators yield the most accurate results in 2 categories and the second most accurate in 7, which emphasizes that the LMA estimation is close to a linear problem.

5.1.3 Summary and conclusion

Regarding the choice of the MLRA to estimate leaf traits, RMSE, R^2 and Tau values mostly depend on the samples (*i.e.*, pixels and associated leaf traits measurements) considered and less on the MLRA chosen to build estimators. For C_{ab} , C_{xc} and EWT, Ridge and GPR often yield the better estimation performances while for LMA RFR achieved better estimates. Results for Ridge and PLSR follow the same trends, but in most cases the Ridge yields better results than PLSR.

Overall, RMSE values were higher for categories of conifer species, but hide the fact that mean and standard deviation of leaf traits are intrinsically higher for conifer species. As a result, R^2 and Kendall's Tau are more appropriate to compare estimation performances for oak and conifer species. R^2 scores are globally not significant and are often under 0.2 or even negative. Tau values show that estimated values are often correlated to reference data. However, correlations remain weak, with values under 0.4 in most of the cases. Since a 0.4 tau value equals a misclassification of 30% of pairs, such estimators remain limited to detect the intra-specific intra-group variability of leaf traits. For the four leaf traits and for all categories under consideration, the bias is negligible, regardless of the chosen MLRA.

For oak species, estimation performances are better for QUDO^(d), QUCH^(e) and QUKE^(d) compared to QUWI^(e). Fewer samples are in the CSTARS-Canopy dataset for QUWI^(e), and QUWI^(e) leaf traits have a narrow variance. This may explain why estimation performances for QUWI^(e) are lower. RMSE values are lower for oak species of woodland savannas. However, for oak species of the mid-elevation forests, better R^2 and Tau are obtained and demonstrate that the estimates are more representative of leaf traits variability.

For conifer species, regardless of the leaf trait, RMSE performances are lower for CADE compared to pine or fir species. But this hides the fact that average leaf trait values are greater for pine and fir species. Analyzing R^2 scores and Tau correlations, estimation performances are better for pine species compared to fir species.

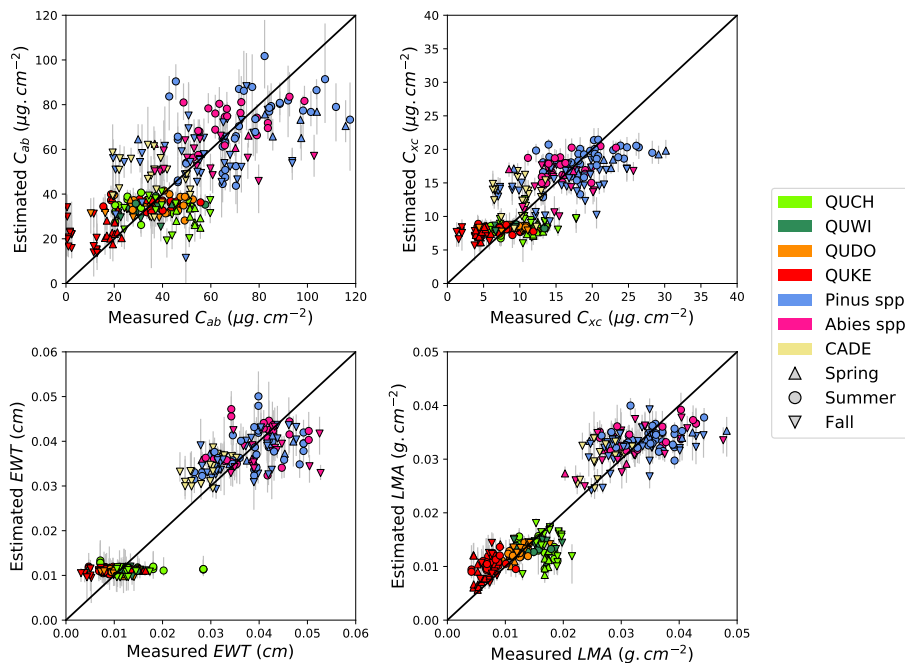


Figure 5.1: Mean leaf traits estimates compared to measured values. Gray vertical lines indicate the range between minimal and maximal estimated values for each sample. Results are given for the MLRA highlighted in Tables 5.2 to 5.5 (for oaks: GPR, GPR, Ridge, RFR; for conifers: Ridge, Ridge, Ridge, RFR; for C_{ab} , C_{xc} , EWT, and LMA respectively)

5.2 The Hybrid 1D-CNN Strategy

Most studies focused on classical MLRA including artificial neural networks (ANN) or multi-layer perceptrons. More recently, convolutional neural networks (CNN) have emerged and have the ability to deal with complex supervised learning problems, such as image classification problems. However, only a few studies have used it for vegetation analysis with spectroscopic data (Pulanagari et al. 2021; Shi et al. 2022; Cherif et al. 2023). Cherif et al. 2023 study represents the most advanced work on estimating leaf traits from canopy reflectance with the help of a 1D-CNN. However their work focuses on a purely statistical approach.

Sensitivity analysis (Chapter 1) demonstrates that canopy reflectance alone is mainly sensitive to variations in canopy geometry and background reflectance and only marginally to variations of leaf traits. However, CWT (Continuous Wavelet Transform) outputs could be highly sensitive to leaf traits, highlighting that well-chosen convolutional filters could extract and isolate information on leaf traits. In this frame, 1D-CNNs are promising algorithms to create inverse models to assess canopy foliar biochemistry since the first layer of a CNN acts as a set of filters, and could indeed extract features from the shape of the spectra.

Moreover, previous work on hybrid methods lead to suitable estimation performances but present two drawbacks: leaf traits are estimated separately from specific spectral ranges and they were usually trained and evaluated on a single site at a specific date.

The objective of this section is to perform a joint estimation of the four leaf traits from the whole range 400 – 2500 nm with a hybrid approach based on 1D-CNN and evaluate its performance. With this hybrid approach, the 1D-CNN model is trained on the illumination geometry considered in the synthetic dataset generation. Thus, the trained 1D-CNN provides a global estimator that could handle the estimation of the four leaf traits analyzed in this study for all the AVIRIS images.

In this section, the work is organized in two steps. Firstly, the 1D-CNN hyperparameters are calibrated and the model is trained on the synthetic dataset to build the 1D-CNN-based estimator. Secondly, the 1D-CNN-based estimator is applied on AVIRIS spectra from CStars-Canopy to evaluate its accuracy.

5.2.1 Synthetic dataset generation

A synthetic dataset was built to train and test MLRA in hybrid methods. Radiative transfer simulations are performed with a combination of PROSPECT DART-SFR RTMs (see Chapter 1 for detailed explanation on RTM functioning). Besides the four leaf traits, the PROSPECT-DART combination include as parameter: the leaf structure parameter (N), illumination parameters (sun zenith angle SZA, sun azimuth angle SAA), parameters related to the canopy geometry (canopy cover CC, leaf area index LAI, average leaf angle ALA) and soil reflectance (see Chapter 3, Subsection 3.4.3 for details on the extraction of background reflectance spectra).

Illumination angles were based on sun angles of the 32 AVIRIS images for the five study sites. Other simulation inputs were generated through a Latin hypercube sampling. Other model inputs include leaf traits, but also canopy geometry parameters (CC, LAI, ALA) and several types of soil reflectance. For each AVIRIS image, 1000 cases were generated and ranges used for Latin hypercube sampling are defined in Table 5.6. In total 32,000 canopy reflectance spectra were simulated.

Parameter	Unit	Min. Value	Max. Value
C_{ab}	$\mu g.cm^{-2}$	0.0	140
C_{xc}	$\mu g.cm^{-2}$	0.0	35
EWT	cm	0.001	0.055
LMA	$g.cm^{-2}$	0.001	0.050
N	-	1.0	3.0
LAI	$m^2.m^{-2}$	0.05	7.0
ALA	$^{\circ}$	0	90
CC	%	10	100

Table 5.6: Ranges of values used for Latin hypercube generation.

Table 5.7: Hyperparameter ranges for the TPE sampling experiment and optimal values found.

Hyperparameter	TPE sampling				Optimal Values
	Type	Min.	Max.	Scale	
Learning Rate	float	10^{-5}	10^{-2}	log	$5.6 \cdot 10^{-4}$
Batch Size	int	50	1000	linear	195
Number of conv. layers	int	1	3	linear	1
Kernel Size	int	3	159	linear	115
Number of channels	int	4	16	linear	16
Number of dense hidden layers	int	1	5	linear	2
Size of hidden layers	int	4	100	log	{86,90}

5.2.2 1D-CNN calibration

5.2.2.1 Architecture selection

The 1D-CNN is based on a classical CNN architecture detailed in [Chapter 2](#). The architecture includes: several one-dimensional convolution layers (each time followed by an activation layer and a maxpooling layer), a flatten layer, and several fully-connected layers. Inputs of the network are reflectance at 160 wavelengths to match AVIRIS data specifications (one wavelength every 10 nm between 400 nm and 2500 nm except for water absorption bands between 1270-1450 nm and 1800-1980 nm) and four outputs (the four leaf traits of interest).

The architecture was trained with a stochastic gradient descent which aims to minimize the MSE loss function. In the stochastic gradient descent, the weights were updated with the Adam optimizer ([Kingma and Ba 2014](#)). This architecture involves at least five hyperparameters: number of convolutional layers, size of convolutional kernels, number of kernels, number of dense layers, and size of hidden layers. We explore different combinations of hyperparameters with a TPE (Tree-structured Parzen Estimator) sampler ([Bergstra et al. 2011](#)) implemented in the optuna library ([Akiba et al. 2019](#)). Additionally, the batch size and learning rate were parameters included in the TPE sampling. TPE sampling is an adaptive sampling strategy and aims to reach the optimal hyperparameters that minimize the MSE loss on test data.

The training process is implemented on the synthetic PROSPECT-DART dataset. From the synthetic PROSPECT-DART dataset 5,000 simulations are selected randomly and saved as test data. Remaining simulations are used as train dataset for the stochastic gradient descent process. For the train dataset, a Gaussian noise is added to the simulated reflectance to increase the robustness of the model toward noisy input data (the variance of the noise is set to 0.01). The test dataset is kept noise-free. The 1D-CNN is trained with a mean squared error loss during 100 epochs. Training the 1D-CNN during 100 epochs was enough to reach convergence in the training process.

A learning rate between $5 \cdot 10^{-4}$ and $7 \cdot 10^{-4}$ leads to smaller mean square error loss after 100 epochs ([Figure 5.2](#)). Batch size was found optimal between 100 and 250, although the choice of batch size had less significant impact on the results.

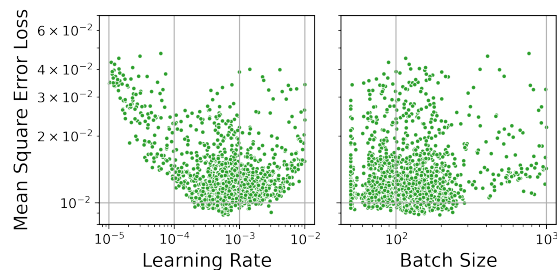


Figure 5.2: Distribution of the mean square error validation loss compared to the learning rate (left), and the batch size (right).

The following architecture leads to the minimal mean square error loss: a single convolution layer (16 kernels of size 115) and 3 dense layers (hidden layers of size 86 and 90).

More generally, the TPE experiment highlights that one convolution layer is enough to extract features to retrieve leaf traits on simulated spectra ([Figure 5.3](#)). Moreover, better results were reached with architectures that include a single convolution layer with a kernel size greater than

100. The MSE loss appears to decrease with the number of channels within convolution layers. By extrapolation, a number of channels greater than 16 seems to provide a smaller loss value, although these cases have not been tested in the experiment.

The MSE loss value is minimal for a number of 3 dense layers (Figure 5.4). The loss value seems to decrease with the size of the hidden layers and to saturate for greater sizes. However the saturation does not appear to be reached for the maximal value of 100 that was set in the TPE experiment.

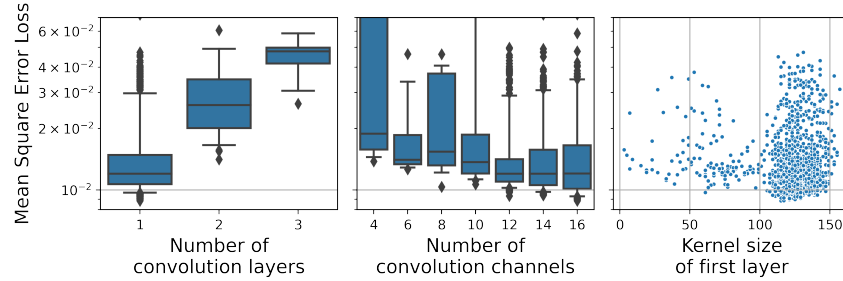


Figure 5.3: Distribution of the mean square error validation loss compared to numbers of convolution layers (left), number of channels (middle) and kernel size of the first layer (right).

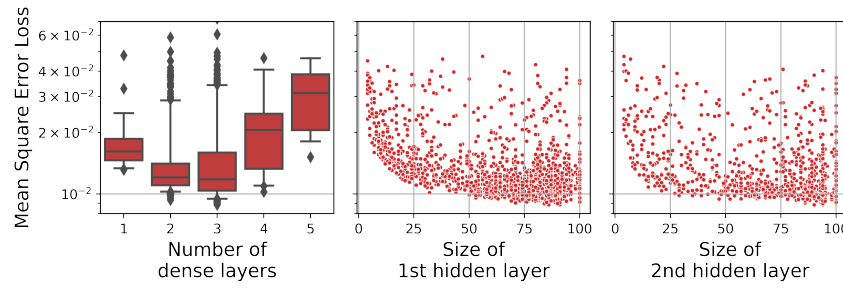


Figure 5.4: Distribution of the mean square error validation loss compared to numbers of dense layers (left), size of the first layer (middle), size of the second layer (right)

5.2.2.2 1D-CNN training process

During the training process, the 1D-CNN model is initialized randomly at the first iteration. Due to the complexity of the loss evolution in the parameters space (meaning that the loss is not likely a convex function in the parameters space) the parameter values on which the loss converges are dependent on the initial values (Li et al. 2018). To overcome the dependence of convergence values on initial values, 50 1D-CNN models are trained from distinct and randomly chosen initial values. This strategy also provides the variability of estimates and enables to study the reliability of the protocol. Indeed, each of the 50 models provides an estimation, meaning that one sample has 50 corresponding estimated values that can be summarized into basic statistics (mean, standard deviation, quantiles). The same goes for the accuracy metrics, 50 values are computed for each metrics and will be summarized into basic statistics. During the training process, the loss is computed at each epoch on the validation synthetic dataset. The parameters values that reach the best prediction accuracy on the validation synthetic dataset are saved to perform estimation on the measured data.

During training, both the train loss and the validation on synthetic data loss are decreasing along the epochs for all the 50 models (Figure 5.5, left). The decay of the validation loss highlights that the models are not overfitted on the train dataset compared to the validation synthetic dataset. Moreover, along the 100 epochs, the majority of most accurate models on the validation synthetic dataset occur on the 10 last epochs (epochs 90 to 100, see Figure 5.5, right).

When applied on the 5000 synthetic samples saved for validation, this architecture revealed the ability to estimate the leaf traits on the synthetic dataset. The mean R^2 ranges between 0.78 and 0.87 for the four traits, and the mean RMSE is respectively $14.8 \mu\text{g} \cdot \text{cm}^{-2}$, $4.8 \mu\text{g} \cdot \text{cm}^{-2}$, 0.0058 cm ; $0.0055 \text{ g} \cdot \text{cm}^{-2}$ for C_{ab} , C_{xc} , EWT and LMA. However the estimated values are not stable considering the initialisation of the training process. Indeed, the mean standard deviations of estimated values are $8.7 \mu\text{g} \cdot \text{cm}^{-2}$, $2.4 \mu\text{g} \cdot \text{cm}^{-2}$, 0.0035 cm , $0.0032 \text{ g} \cdot \text{cm}^{-2}$ for C_{ab} , C_{xc} , EWT

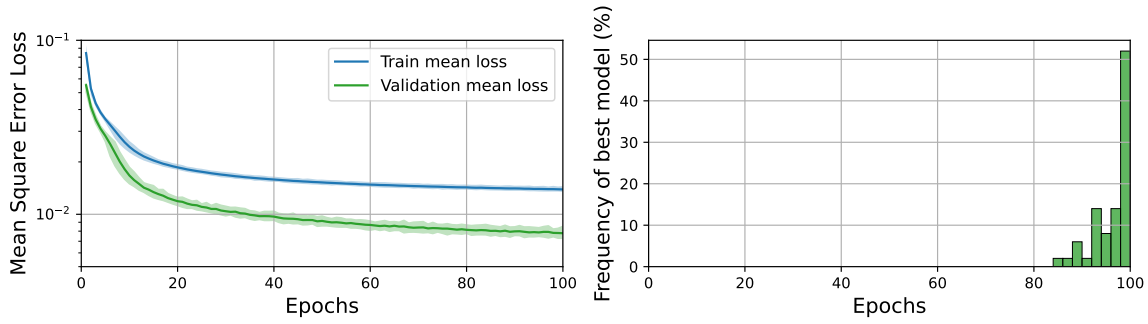


Figure 5.5: Left: Loss evolution for train and validation on synthetic data. Solid lines indicate the mean losses and filled areas indicate the 1st and 9th deciles ; Right: Distribution of best models for validation on synthetic data.

and LMA; they highlight the instability of the estimation (Figure 5.6). Moreover, the variance of errors is too large to indicate properly the small leaf traits variations. This can be noticed considering smaller ranges of leaf traits reference values and looking at the range of predicted values (Figure 5.6).

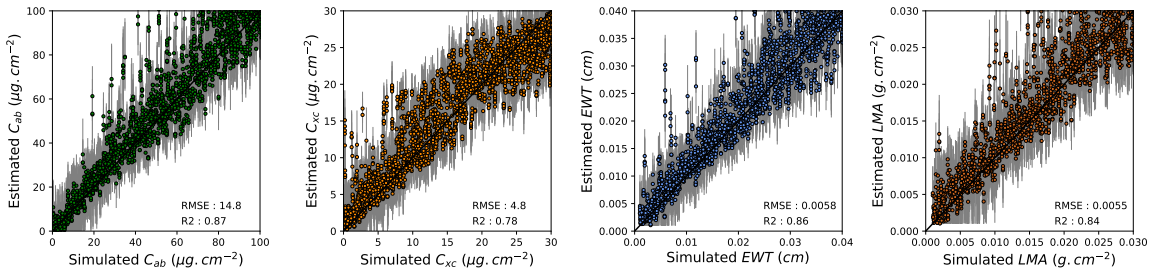


Figure 5.6: Scatter plot of leaf traits mean estimates compared to input values for validation synthetic data. Gray vertical lines indicate the 1st and 9th deciles of estimated values for each sample.

5.2.3 Evaluation of the 1D-CNN estimator performances

To evaluate its estimation accuracy on measured data, the 1D-CNN-based estimators are applied on AVIRIS spectra from CSTARS-Canopy dataset. For each AVIRIS spectrum included in CSTARS-Canopy, the 1D-CNN estimators are applied and the estimated values are compared to the reference measurements values.

Moreover, the MSE loss can be computed for all the epochs on CSTARS-Canopy and analyzed. The MSE for CSTARS-Canopy does not decrease along the epochs (Figure 5.7). Particularly, the loss increases strongly in the first 15 epochs and remains stable after the 20th epoch. The models with the most accuracy are all obtained before the 6th epoch.

Respective contributions of C_{ab} , C_{xc} , EWT and LMA to the MSE loss show the same behaviors (Figure 5.7, right). Although this behavior is less pronounced for LMA and C_{ab} , the loss decreases slightly from epoch 1 to 60.

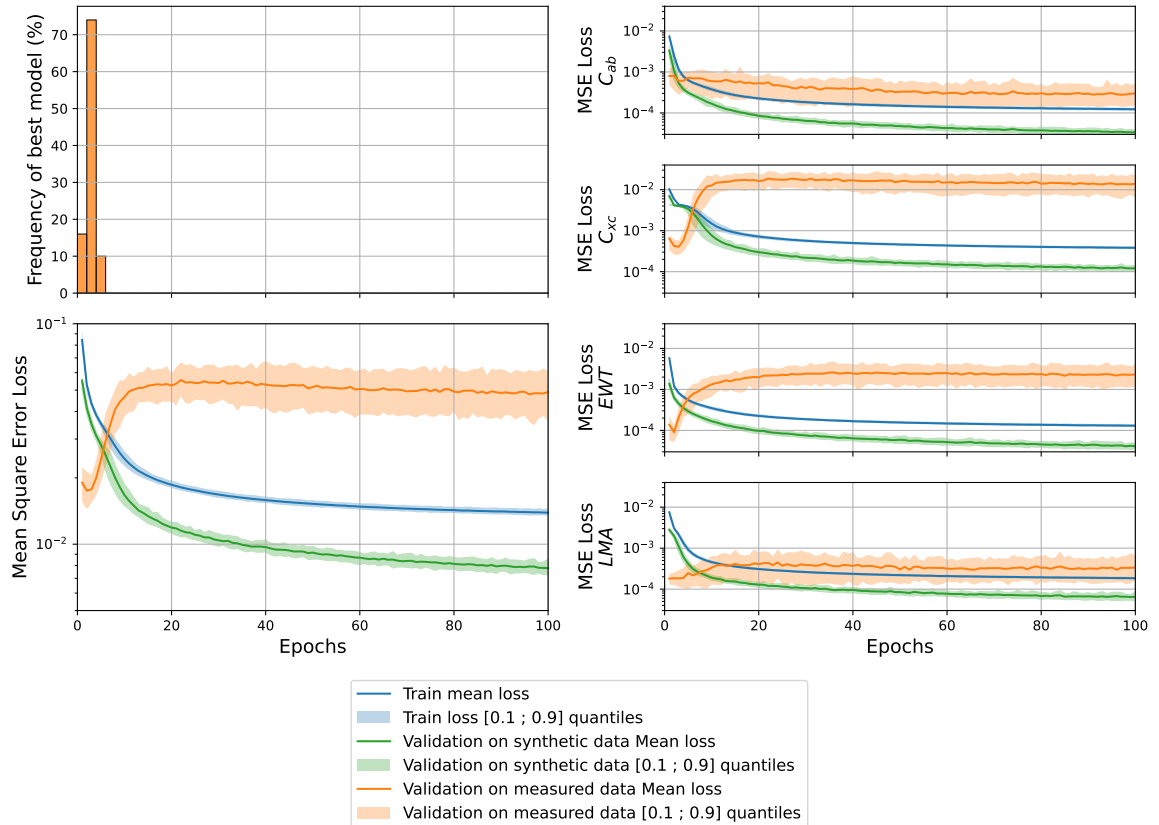


Figure 5.7: Top left: Distribution of best models for validation CSTARS-Canopy ; Bottom left: Loss evolution for train and validation on synthetic data and validation CSTARS-Canopy ; Right: Trait-specific loss evolutions for train, validation on synthetic data and validation on CSTARS-Canopy

The mean values for RMSE, R^2 , bias and Kendall's Tau are given in Tables 5.8, 5.9, 5.10 and 5.11 for C_{ab} , C_{xc} , EWT, and LMA respectively. Results are given for several subset of CSTARS-Canopy dataset including species, species pooled by families or species pooled by ecosystems.

Table 5.8: Mean values of accuracy metrics for the 1D-CNN estimator for C_{ab} on CSTARS-Canopy. The 5th and 95th percentiles are given in square brackets. For reference, the mean m and standard deviation σ of reference data are given for each CSTARS-Canopy subset.

	RMSE $\mu\text{g}\cdot\text{cm}^{-2}$	R^2 -	Bias $\mu\text{g}\cdot\text{cm}^{-2}$	tau -
Oak ($m = 31.6$; $\sigma = 14.6$)	19.8 [16.8 ; 24.0]	-0.37 [-1.72 ; -0.33]	8.4 [0.2 ; 13.0]	0.04 [-0.03 ; 0.17]
Woodland Savannas ($m = 35.2$; $\sigma = 10.2$)	15.9 [12.9 ; 18.7]	-1.52 [-2.42 ; -0.62]	1.5 [-6.9 ; 8.2]	0.05 [-0.12 ; 0.2]
QUDO^(d) ($m = 36.2$; $\sigma = 10.5$)	15.8 [12.8 ; 18.4]	-1.38 [-2.2 ; -0.55]	0.04 [-5.1 ; 10.9]	0.04 [-0.13 ; 0.23]
QUWI^(e) ($m = 33.3$; $\sigma = 9.8$)	16.1 [10.9 ; 20.9]	-2.00 [-3.89 ; -0.34]	-2.2 [-12.2 ; 6.5]	0.03 [-0.29 ; 0.32]
Mid-Elev. Forests ($m = 30.0$; $\sigma = 16.0$)	21.2 [17.3 ; 26.6]	-0.80 [-1.79 ; -0.17]	9.6 [2.5 ; 17.8]	0.13 [-0.01 ; 0.24]
QUKE^(d) ($m = 23.3$; $\sigma = 14.8$)	22.5 [16.4 ; 29.5]	-1.42 [-3.03 ; -0.24]	16.3 [9.3 ; 23.3]	0.27 [0.07 ; 0.41]
QUCH^(e) ($m = 39.8$; $\sigma = 12.3$)	18.8 [15.3 ; 23.4]	-1.46 [-2.73 ; -0.6]	-0.2 [-8.5 ; 9.5]	0.00 [-0.19 ; 0.21]
Conifers ($m = 62.2$; $\sigma = 23.8$)	35.9 [31.6 ; 39.7]	-1.31 [-1.81 ; -0.78]	-23.5 [-30.3 ; -17.1]	0.05 [-0.08 ; 0.15]
<i>Pinus spp.</i> ($m = 68.2$; $\sigma = 24.8$)	40.8 [36.1 ; 44.8]	-1.75 [-2.29 ; -1.14]	-30.5 [-36.5 ; -24.3]	0.10 [-0.02 ; 0.24]
<i>Abies spp.</i> ($m = 63.3$; $\sigma = 15.9$)	31.6 [25.6 ; 38.3]	-3.09 [-4.91 ; -1.65]	-22.9 [-30.9 ; -14.8]	0.02 [-0.13 ; 0.19]
CADE ($m = 35.3$; $\sigma = 10.3$)	16.7 [12.2 ; 20.9]	-1.80 [-3.29 ; -0.47]	-3.9 [-4.8 ; 11.7]	0.10 [-0.09 ; 0.28]

For C_{ab} , RMSE ranges from 10.9 for QUWI^(e) to 44.8 $\mu\text{g}\cdot\text{cm}^{-2}$ for pine species. Average RMSE is higher for pine and fir species (above 30 $\mu\text{g}\cdot\text{cm}^{-2}$) compared to oak species and CADE (all under 22.5 $\mu\text{g}\cdot\text{cm}^{-2}$). The average rRMSE ranges between 45% and 60% except for oaks of mid-elevation forest (70%) and QUKE^(d) (96%). R^2 scores are almost all negative and emphasize that the RMSE is greater than the standard deviation of the reference C_{ab} values ($sRMSE > 1$). Particularly, R^2 scores are strongly negative for fir species (mean $R^2 = -3.09$). R^2 scores are less negative for all oak species combined (mean $R^2 = -0.37$) and particularly for mid-elevation forest species (mean $R^2 = -0.80$). The bias varies widely from one category to another. Globally, the C_{ab} for conifers species is underestimated while C_{ab} is overestimated for QUKE^(d). Particularly, the bias is strongly negative for pine and fir species. The bias for QUDO^(d), QUCH^(e) and QUWI^(e) tend to be around zero. The positive bias for all oak species combined and mid-elevation forest species is mainly due to QUKE^(d). Kendall's Tau ranges from -0.29 for QUWI^(e) to 0.41 for QUKE^(d). Average values of Tau indicate that, overall, estimates misrepresent C_{ab} variations. QUKE^(d) appears as the exception with an average Tau of 0.27 and 90% of values within the interval [0.07 ; 0.41].

Table 5.9: Mean values of accuracy metrics for the 1D-CNN estimator for C_{xc} on CSTARS-Canopy. The 5th and 95th percentiles are given in square brackets. For reference, the mean m and standard deviation σ of reference data are given for each CSTARS-Canopy subset.

	RMSE $\mu\text{g}\cdot\text{cm}^{-2}$	R ² -	Bias $\mu\text{g}\cdot\text{cm}^{-2}$	tau -
Oak ($m = 8.2$; $\sigma = 3.2$)	12.3 [10.4 ; 14.3]	-13.66 [-18.76 ; -9.32]	9.7 [7.8 ; 11.6]	-0.08 [-0.11 ; -0.03]
Woodland Savannas ($m = 9.1$; $\sigma = 2.1$)	4.4 [3.5 ; 5.6]	-3.5 [-5.98 ; -1.66]	2.1 [0.2 ; 4.5]	0.05 [-0.12 ; 0.14]
QUDO^(d) ($m = 9.3$; $\sigma = 2.2$)	4.3 [3.4 ; 5.3]	-3.16 [-5.19 ; -1.58]	1.8 [-0.1 ; 4.4]	-0.04 [-0.18 ; 0.11]
QUWI^(e) ($m = 8.6$; $\sigma = 2.1$)	4.6 [2.9 ; 6.5]	-4.68 [-9.71 ; -1.18]	2.6 [0.0 ; 5.3]	0.14 [-0.14 ; 0.36]
Mid-Elev. Forests ($m = 7.7$; $\sigma = 3.6$)	14.5 [12.2 ; 17.0]	-15.95 [-22.21 ; -10.84]	13.2 [10.8 ; 15.6]	0.06 [-0.02 ; 0.14]
QUKE^(d) ($m = 6.0$; $\sigma = 2.4$)	15.5 [13.2 ; 17.8]	-40.91 [-53.3 ; -28.79]	14.5 [12.2 ; 16.7]	0.03 [-0.05 ; 0.13]
QUCH^(e) ($m = 10.3$; $\sigma = 3.4$)	12.7 [9.7 ; 16.0]	-13.77 [-21.91 ; -7.33]	11.2 [8.2 ; 14.3]	0.04 [-0.09 ; 0.2]
Conifers ($m = 16.0$; $\sigma = 5.1$)	11.3 [9.9 ; 13.1]	-3.98 [-5.58 ; -2.77]	4.5 [2.7 ; 6.5]	-0.14 [-0.2 ; -0.1]
<i>Pinus spp.</i> ($m = 17.8$; $\sigma = 5.0$)	10.2 [8.9 ; 11.7]	-3.25 [-4.53 ; -2.17]	1.2 [-0.9 ; 3.1]	-0.14 [-0.21 ; -0.06]
<i>Abies spp.</i> ($m = 15.6$; $\sigma = 3.6$)	11.1 [9.5 ; 13.1]	-9.01 [-12.66 ; -6.15]	7.0 [4.9 ; 9.3]	-0.17 [-0.29 ; -0.06]
CADE ($m = 9.8$; $\sigma = 2.4$)	15.2 [12.8 ; 18.0]	-43.33 [-60.56 ; -30.13]	13.1 [10.6 ; 15.3]	0.10 [-0.0 ; 0.2]

For C_{xc} , RMSE ranges from 2.9 for QUWI^(e) to 18 $\mu\text{g}\cdot\text{cm}^{-2}$ for CADE. RMSE is the lowest for oak species of woodland savannas (QUDO^(d) and QUWI^(e)) with an average around 4.5 $\mu\text{g}\cdot\text{cm}^{-2}$. Compared to the mean, RMSE is also lower for QUDO^(d) and QUWI^(e) (respectively 46% and 53%). The rRMSE is respectively 57% and 71% for pine and fir species, and is over 150% for other species (CADE, QUCH^(e) and QUKE^(d)). R² scores are all strongly negative and emphasize that the RMSE is greater than the standard deviation of the reference C_{xc} values. Average R² scores are above -4 only for QUDO^(d) and pine species. For all the categories, estimates of C_{xc} are positively biased. The bias follows roughly the same trend as RMSE and is the lowest for QUDO^(d), QUWI^(e) and pine species. Average Kendall's Tau is at most 0.14 for QUWI^(e). Values of Tau indicate that for all the cases C_{xc} estimates misrepresents the trends of C_{xc} reference values.

Table 5.10: Mean values of accuracy metrics for the 1D-CNN estimator for EWT on CSTARS-Canopy. The 5th and 95th percentiles are given in square brackets. For reference, the mean m and standard deviation σ of reference data are given for each CSTARS-Canopy subset.

	RMSE <i>cm</i>	R² -	Bias <i>cm</i>	tau -
Oak ($m = 0.0111$; $\sigma = 0.0040$)	0.0120 [0.0100 ; 0.0145]	-7.94 [-11.89 ; -5.21]	0.0097 [0.0078 ; 0.012]	0.01 [-0.08 ; 0.09]
Woodland Savannas ($m = 0.0110$; $\sigma = 0.0022$)	0.0094 [0.0077 ; 0.0110]	-18.69 [-25.8 ; -12.19]	0.0076 [0.0046 ; 0.0098]	-0.08 [-0.21 ; 0.04]
QUDO^(d) ($m = 0.0105$; $\sigma = 0.0017$)	0.0097 [0.0081 ; 0.0113]	-34.39 [-46.45 ; -23.0]	0.0081 [0.0055 ; 0.0100]	-0.05 [-0.22 ; 0.1]
QUWI^(e) ($m = 0.0122$; $\sigma = 0.0026$)	0.0086 [0.0062 ; 0.0111]	-11.14 [-18.65 ; -5.08]	0.0065 [0.0027 ; 0.0099]	-0.02 [-0.25 ; 0.18]
Mid-Elev. Forests ($m = 0.0111$; $\sigma = 0.0047$)	0.0129 [0.0104 ; 0.0160]	-6.91 [-10.81 ; -4.06]	0.0107 [0.0086 ; 0.0135]	0.05 [-0.04 ; 0.14]
QUKE^(d) ($m = 0.0091$; $\sigma = 0.0031$)	0.0132 [0.0110 ; 0.0162]	-17.92 [-27.02 ; -11.99]	0.0120 [0.0101 ; 0.0147]	0.07 [-0.14 ; 0.26]
QUCH^(e) ($m = 0.0139$; $\sigma = 0.0052$)	0.0124 [0.0089 ; 0.0166]	-5.17 [-9.58 ; -2.09]	0.0089 [0.0058 ; 0.013]	0.02 [-0.09 ; 0.12]
Conifers ($m = 0.0371$; $\sigma = 0.0068$)	0.0166 [0.0142 ; 0.0189]	-5.1 [-6.90 ; -3.43]	-0.0123 [-0.0160 ; -0.0092]	0.08 [-0.01 ; 0.16]
<i>Pinus spp.</i> ($m = 0.0376$; $\sigma = 0.0062$)	0.0168 [0.0148 ; 0.0190]	-6.49 [-8.52 ; -4.73]	-0.0129 [-0.0162 ; -0.0101]	0.06 [-0.02 ; 0.16]
<i>Abies spp.</i> ($m = 0.0401$; $\sigma = 0.0063$)	0.0173 [0.0145 ; 0.0206]	-6.96 [-10.17 ; -4.49]	-0.0128 [-0.0174 ; -0.0083]	-0.10 [-0.25 ; 0.02]
CADE ($m = 0.0295$; $\sigma = 0.0037$)	0.0135 [0.0099 ; 0.0166]	-13.6 [-20.4 ; -6.67]	-0.0090 [-0.0126 ; -0.0050]	-0.10 [-0.33 ; 0.13]

For EWT, RMSE ranges from 0.0077 cm for oaks of woodland savannas to 0.0206 cm for fir species. The rRMSE is around 45% for conifer species and the three subcategories. For oak species, the rRMSE is lower for QUWI^(e) (70%) compared to QUCH^(e), QUDO^(d) and QUKE^(d) (respectively 89%, 92% and 145%). For all the categories, R² scores are strongly negative. Average R² scores are above -6 only for QUCH^(e) and all conifer species pooled together. Bias is systematically positive for oak species and systematically negative for conifer species. Average values for Tau are all under 0.1 and the greatest value is reached with QUKE^(d) (0.26). Consequently, the EWT estimates are not correlated to the reference values.

Table 5.11: Mean values of accuracy metrics for the 1D-CNN estimator for LMA on CSTARs-Canopy. The 5th and 95th percentiles are given in square brackets. For reference, the mean m and standard deviation σ of reference data are given for each CSTARs-Canopy subset.

	RMSE $g \cdot cm^{-2}$	R² -	Bias $g \cdot cm^{-2}$	tau -
Oak ($m = 0.0119$; $\sigma = 0.0047$)	0.0069 [0.0059 ; 0.0085]	-1.24 [-2.29 ; -0.61]	0.0022 [0.0001 ; 0.0045]	0.09 [-0.05 ; 0.21]
Woodland Savannas ($m = 0.0135$; $\sigma = 0.0026$)	0.0058 [0.0045 ; 0.0079]	-4.39 [-8.78 ; -2.14]	0.0007 [-0.0022 ; 0.0037]	0.22 [0.10 ; 0.32]
QUDO^(d) ($m = 0.0123$; $\sigma = 0.0019$)	0.0057 [0.0046 ; 0.0069]	-8.88 [-13.4 ; -5.23]	0.0006 [-0.002 ; 0.0036]	0.16 [-0.07 ; 0.36]
QUWI^(e) ($m = 0.0158$; $\sigma = 0.0023$)	0.0060 [0.0043 ; 0.0092]	-6.93 [-16.63 ; -2.76]	0.0010 [-0.0032 ; 0.0041]	0.17 [-0.06 ; 0.40]
Mid-Elev. Forests ($m = 0.0111$; $\sigma = 0.0052$)	0.0074 [0.0061 ; 0.0093]	-1.04 [-2.17 ; -0.37]	0.0029 [0.0000 ; 0.0057]	0.07 [-0.12 ; 0.23]
QUKE^(d) ($m = 0.0071$; $\sigma = 0.0016$)	0.0081 [0.0058 ; 0.0110]	-26.7 [-47.11 ; -12.29]	0.0063 [0.0037 ; 0.0094]	0.09 [-0.23 ; 0.15]
QUCH^(e) ($m = 0.0171$; $\sigma = 0.0020$)	0.0059 [0.0047 ; 0.0072]	-7.86 [-11.95 ; -4.44]	-0.0022 [-0.0057 ; 0.0015]	0.04 [-0.13 ; 0.20]
Conifers ($m = 0.0328$; $\sigma = 0.0058$)	0.0209 [0.0182 ; 0.0241]	-12.1 [-16.21 ; -8.82]	-0.0192 [-0.0227 ; -0.0159]	0.02 [-0.05 ; 0.10]
Pinus spp. ($m = 0.0338$; $\sigma = 0.0050$)	0.0214 [0.0188 ; 0.0245]	-17.75 [-23.46 ; -13.33]	-0.0200 [-0.0235 ; -0.0169]	0.01 [-0.11 ; 0.11]
Abies spp. ($m = 0.0335$; $\sigma = 0.0070$)	0.0219 [0.0181 ; 0.0255]	-9.01 [-12.45 ; -5.81]	-0.0198 [-0.0241 ; -0.0153]	-0.05 [-0.17 ; 0.12]
CADE ($m = 0.0275$; $\sigma = 0.0031$)	0.0163 [0.0135 ; 0.0196]	-29.24 [-42.08 ; -19.28]	-0.0149 [-0.0186 ; -0.0113]	0.07 [-0.09 ; 0.23]

For LMA, RMSE ranges from $0.0043 \text{ g} \cdot \text{cm}^{-2}$ for QUWI^(e) to $0.0255 \text{ g} \cdot \text{cm}^{-2}$ for fir species. For oak species, the RMSE is higher for QUKE^(d) (average is $0.0081 \text{ g} \cdot \text{cm}^{-2}$) compared to QUDO^(d), QUCH^(e) and QUWI^(e). Compared to the mean of reference data, the same arrangement is found: rRMSE is under 45% for QUDO^(d), QUCH^(e) and QUWI^(e) and above 100% for QUKE^(d). The average RMSE is around $0.02 \text{ g} \cdot \text{cm}^{-2}$ for conifer species but represents a rRMSE of only 60 to 65%. R² score are all negative for all the categories. Best R² scores are achieved considering all the oaks together, or considering oaks of mid-elevation forests. The bias is systematically negative for conifer species. The biases are different considering the oak species: LMA is overestimated for QUKE^(d) and slightly underestimated for QUCH^(e). Tau for QUDO^(d) and QUWI^(e), mirrored in the Average Tau for oaks of woodland savanna category (0.22, 90% of values within the interval [0.10 ; 0.32]).

For C_{ab} , low C_{ab} values for QUKE^(d) are overestimated, these points correspond to samples collected in autumn. This misestimation of senescent leaves in fall may explain the particular results for QUKE^(d) samples. The range C_{ab} estimates match the range of reference values for QUWI^(e), QUCH^(e) and QUDO^(d). For conifers, C_{ab} is strongly underestimated, and the range of estimates does not match the range of measured C_{ab} . All estimated values are located in a small range centered around a mean value of $40 \mu\text{g} \cdot \text{cm}^{-2}$ (Figure 5.8).

C_{xc} for QUKE^(d) and QUCH^(e) (oak species of mid-elevation forests) is significantly overestimated for all seasons. C_{xc} Estimates for QUDO^(d) and QUWI^(e) are in the right order of magnitude. C_{xc} estimates for conifers are in the same order of magnitude as measured C_{xc} values, although there is no apparent link between estimated and measured values.

EWT is overestimated for oak species and underestimated for conifer species. For LMA, the measured range is smaller than the estimated range for all the species. LMA estimates are in the good order of magnitude for QUDO^(d). LMA is overestimated for QUKE^(d) and underestimated for QUCH^(e) and even more underestimated for conifer species. For conifers, LMA is strongly underestimated, and the range of estimates does not match the range of measured LMA. All estimated values are located in a small range centered around a mean value of $0.012 \text{g} \cdot \text{cm}^{-2}$.

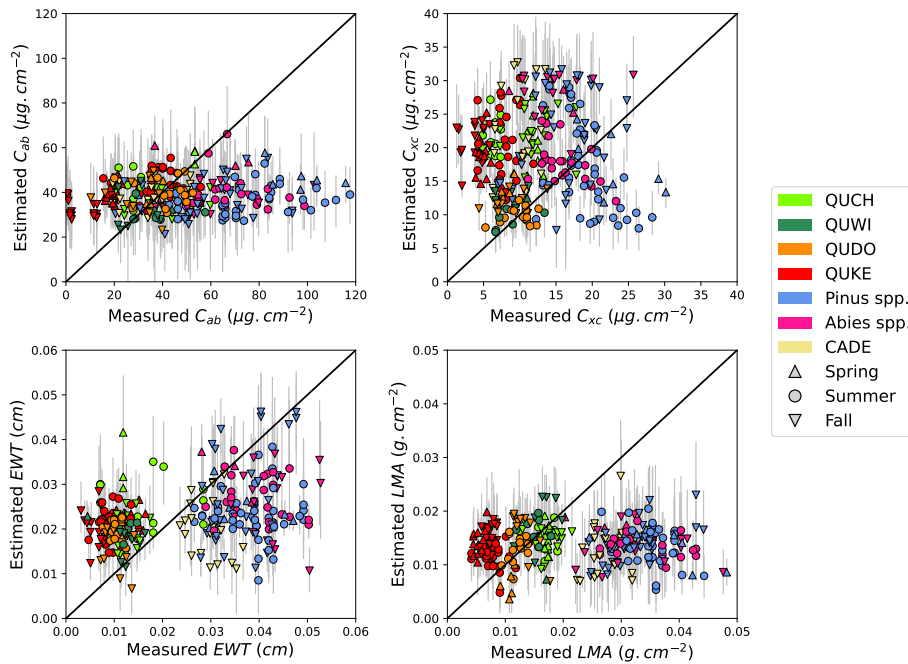


Figure 5.8: Mean leaf traits estimates compared to measured values for validation data. Gray vertical lines indicate the 1st and 9th deciles of estimated values for each sample.

Globally, for the four leaf traits, the estimates are highly uncertain. Indeed, for each sample, the range from the 1st decile to the 9th decile of estimated values is large compared with the total range of variation for each variable (greater than $20 \mu\text{g} \cdot \text{cm}^{-2}$ for C_{ab} , greater than 0.01cm for EWT). For the four leaf traits the performances do not significantly depend on the season and the site (Figure 5.8).

5.3 Discussions

5.3.1 Discussion on machine learning algorithms

Four MLRA were compared to build statistical estimation methods: Ridge, PLSR, GPR, and RFR. The four MLRA provide similar results. Specifically, linear MLRA (Ridge and PLSR) provided estimates close to non-linear MLRA (GPR and RFR). Similarities between linear and non-linear MLRA accuracy were already highlighted at the leaf scale for EWT and LMA for oak species (Chapter 4). At the canopy scale, these results may also highlight that estimation of leaf traits from canopy reflectance may be close to a linear problem and that it could be solved with simple linear MLRA. Although, the higher variance of errors at the canopy scale may also hide the non-linear behavior of the data.

Additionally, Ridge and PLSR achieve similar estimation performances for all the cases. This result is in line with previous studies that highlighted from experiments the almost identical behavior of Ridge and PLSR (Firinguetti et al. 2017; Jensen 2021). However, in the vast majority of cases, Ridge obtained slightly better performance than PLSR. This result may emphasize that estimation of leaf traits from canopy reflectance is a problem with high error variance since the Ridge algorithm performs better than PLSR in such types of problems (Firinguetti et al. 2017).

In the case of LMA estimation, RFR performs better estimation in most of the cases considered. The hypothesis is that LMA absorption signatures are more localized within the reflectance spectra and that RFR, which performs a feature selection, is more likely to isolate the specific spectral features for LMA.

During the search of optimal 1D-CNN architecture with the TPE sampling experiment, architectures with big kernel size (over 100 and corresponding to a 1000 nm length) were more efficient. Yet, choosing a kernel size almost as large as the size of signal (160) means that the cross-correlation is only computed on a few points. In the extreme case where the kernel size is identical to the size of the signal, the cross-correlation is computed only on one point and the convolution layer is equivalent to a fully connected layer from a classical neural network architecture. This means that the convolution kernel is not shifted, or only slightly, over the spectral dimension. This is a different behavior from other CNN use (e.g., object detection in images, image classification) where kernel size of the first layer remains usually very small compared to the signal total dimension. The reason for kernel size remaining smaller than images in such applications is that the targeted objects can be located anywhere in the image, so the convolution kernel needs to be translatable across the entire image. Therefore the hypothesis is that the patterns that activate the convolution layer in the estimation of leaf traits problem are spectrally localized and consequently do not require translation of the kernel.

The impact of hyperparameters and their optimal values for 1D-CNN in remote sensing problems based on spectral data has not been investigated in state-of-the-art studies or their range of variation or were restricted to a small subset of values.

In contrast with the kernel size optimization results obtained in Subsection 5.2.2, the past published studies usually consider a small kernel size for the first layer, by analogy to image processing problems. For example, in regression problems from reflectance, kernel size are equivalent to small windows narrower than 50 nm (3 nm equivalent window for Pullanagari et al. 2021, 30 nm for Annala et al. 2020, 20 nm for Ng et al. 2019). Wider equivalent windows of 100 nm have been investigated by Guidici and Clark 2017 for classification of reflectances on hyperspectral images. For the retrieval of C_{ab} and C_{xc} from synthetic spectra (PROSPECT-5) Shi et al. 2022 explored different kernel sizes. However, the maximal kernel size explored by Shi et al. 2022 corresponds to a 11 nm window, this window size is not enough to cover the wide band absorption features of chlorophylls and carotenoids.

Shi et al. 2022 also explored the number of convolution layers and showed that the accuracy error decreases with the number of layers, which is the opposite of the result found in Subsection 5.2.2. But, again, this result can be qualified because the proposed kernel sizes do not seem appropriately chosen.

Most studies used the same optimizer (Adam from Kingma and Ba 2014). However, some studies used an adaptive learning rate: Guidici and Clark 2017 used Adagrad, which is an optimizer with adaptive learning rate, for a classification problem of pixels of hyperspectral AVIRIS images; Ng et al. 2019 used a learning rate (geometric) decay to retrieve properties of soil samples from ASD reflectance measurements. An adaptive learning rate was not considered to train the 1D-CNN but this modification may improve the convergence of the network during the learning process.

For regression problems from reflectance data, all the review studies use a single output and build a specific model for each variable to be determined, except [Cherif et al. 2023](#). [Cherif et al. 2023](#) showed that a multi-output 1D-CNN model is more efficient than several models to estimate multiple traits. The hypothesis that would explain this result is that the multi-output 1D-CNN model incorporates traits' co-variation. The same multi-output strategy has been used in the Hybrid 1D-CNN approach. However in the Hybrid 1D-CNN approach problem the training set is derived from simulations built without traits' co-variation.

The loss curves exhibit different behavior between the train step, the validation on synthetic data step, and for CSTARS-Canopy dataset. As shown in ([Figure 5.5](#)) and ([Figure 5.7](#)) loss for the train and validation steps are continuously decreasing along the epoch. Moreover, most accurate models on the validation synthetic dataset occur after epoch 80 ([Figure 5.5](#), right). An opposite behavior is observed for the MSE loss for CSTARS-Canopy. This loss increases in the first epochs and remains constant after the 20th epoch, and models with the most accuracy are all obtained before the 6th epoch ([Figure 5.7](#)). These opposite behaviors highlight that the 1D-CNN learns patterns that are contained in the synthetic data but may not present in the CSTARS-Canopy dataset. Simulated data are likely not consistent with measured data from CSTARS-Canopy dataset.

5.3.2 Discussion on accuracy of estimations

5.3.2.1 Summary and comparison with literature

For oaks, the C_{ab} rRMSE is around 40% ($13.0 \mu\text{g} \cdot \text{cm}^{-2}$) for the statistical methods, and around 60% with the Hybrid-1D-CNN method. [Miraglio et al. 2022](#) estimated C_{ab} of QUCH^(e) and QUWI^(e) (woodland savanna sites) with an hybrid-PLSR method and obtained a RMSE of $7.9 \mu\text{g} \cdot \text{cm}^{-2}$ ($rRMSE = 22\%$). Mean rRMSE for these two species was around 26% with statistical methods and 43% with the Hybrid 1D-CNN method. [Wang et al. 2020](#) estimated C_{ab} over regions mainly composed of forests (Appalachian and Cumberland plateau, occupied with deciduous and evergreen forests and pasture, and Ozarks Complex occupied with deciduous/evergreen/mixed forests and woody wetlands). They found rRMSEs in the range 11.62% - 16.13%. In brief, RMSE obtained with STAT-GPR is 1.6 times higher compared to the state-of-the-art results. For conifers, C_{ab} is estimated over all the forests with a rRMSE of 30% ($20.0 \mu\text{g} \cdot \text{cm}^{-2}$) but with quite no bias. [Blackburn 2002](#) also estimated C_{ab} content of conifer forests with rRMSE of 24%. [Moorthy et al. 2008](#), estimated the C_{ab} of conifer forest with a rRMSE in the range 10 – 20% by coupling leaf and canopy models. [Schlerf et al. 2010](#) estimated a rRMSE of 8.1% over one spruce forest by comparing different preprocessing methods applied on a Hymap camera. [Zarco-Tejada et al. 2019](#) estimated C_{ab} over a sparse forest of conifers and reached a RMSE of $8.1 \mu\text{g} \cdot \text{cm}^{-2}$. Globally the RMSE results achieved by STAT-Ridge are two times higher compared to the state-of-the-art results.

For C_{xc} , the overall RMSE is around $3.0 \mu\text{g} \cdot \text{cm}^{-2}$ ($rRMSE = 37\%$). In comparison, [Miraglio et al. 2022](#) estimated C_{xc} with a hybrid-PLSR method and obtained a RMSE of $1.73 \mu\text{g} \cdot \text{cm}^{-2}$ ($rRMSE = 18\%$). For [Wang et al. 2020](#), C_{xc} from broadleaf/evergreen/mixed forest is estimated with rRMSE ranging from 16.13% to 11.62%.

For EWT, rRMSE are found above 20% for oak species (RMSE above 0.0020 cm) and are specifically degraded for QUCH^(e) and QUWI^(e). The accuracy remains lower than the one achieved by [Wang et al. 2020](#) (0.0036 cm). For conifers, rRMSE is around 15% (RMSE around 0.0060 cm). These results could be compared with results from the work of [Zhu et al. 2019](#). They estimated EWT over mixed forests of canopy cover in the range 70 – 100% and obtained a rRMSE around 16%.

For LMA, the RMSE is in the range 10 – 25% for oaks species (RMSE between 0.0015 and $0.0025 \text{g} \cdot \text{cm}^{-2}$). For conifers rRMSE is around 15% (RMSE around $0.0050 \text{g} \cdot \text{cm}^{-2}$). For oaks, the RMSE is equivalent to the results obtained on one site by [Chadwick and Asner 2016](#) ($0.0020 \text{g} \cdot \text{cm}^{-2}$) and lower than results from [Miraglio et al. 2022](#) ($0.0053 \text{g} \cdot \text{cm}^{-2}$) on QUDO^(d) and QUWI^(e) species. With a hybrid approach, [Ali et al. 2016](#) over mixed forest estimated LMA with a rRMSE of 4.39%.

Overall, the most accurate results from the statistical methods built from CSTARS-Canopy, exhibit lower estimation performances compared to the state-of-the-art results. The discrepancy between the results presented in this chapter and the state-of-the-art may have several origins, each of which is examined below.

5.3.2.2 Potential sources of errors and uncertainty

Sources of variability and uncertainty in the process of retrieving leaf traits from imaging spectroscopy data of vegetation canopies were reported by Malenovský et al. 2019. Malenovský et al. 2019 divide the source of variability and uncertainty into three classes. The first class is linked to the radiometric data acquisition and processing to deliver the surface reflectance. The second class includes the uncertainties of the process to retrieve the traits and assumptions embedded in the radiative transfer simulation. Finally, the last and third class integrates errors to the field data acquisition and to build the validation procedure. The potential sources of errors and uncertainty in the estimation and validation processes are further discussed following the classification from Malenovský et al. 2019.

The first class of sources of variations includes the quality of the acquisition system. The acquisition system can provide data containing error, but sensor calibration and atmospheric corrections are usually well controlled by the providers. For AVIRIS radiance acquisition, the absolute calibration of the sensor is accurate to 7%, and 2% with in-flight calibration (Boardman 2014).

As emphasized in Chapter 1, the impact of geometry and illumination condition are major factors of reflectance variance. This variability could be a source of error in the estimation process. To alleviate this issue, some authors add further processing steps to the canopy reflectance. For example, Feilhauer et al. 2010 or Wang et al. 2020 reduced the variability by normalizing the spectra before any retrieval process. Such preprocessing techniques were not considered in this thesis.

The second class deals with the quality of the retrieval process. There is no consensus on the recommendation for the selection of the proper retrieval method. Such a choice should depend on the type of forest, the present species, their architecture and organization, but also on the quality of the train dataset in the case of statistical approaches.

Regarding statistical approaches, the number of samples is critical to build robust estimators. Hoepfner et al. 2020 collected data over 40 plots in summer 2017 from coniferous, broadleaf, and mixed forest stands. Wang et al. 2020 collected about 108 samples in June and August and 140 in May. For comparison, the CStars-Canopy dataset contains 109 samples for oaks and 171 samples for conifers. However, CStars-Canopy samples are acquired over 5 sites and 3 forest types, at three seasons; these acquisition discrepancies must have increased variance of the CStars-Canopy samples.

Regarding hybrid approaches, it is required to provide physically accurate simulated reflectance. This point is crucial as simulated data are compared to sensor measurement expressed in the surface reflectance unit. A first control step is to check if the distribution of simulated reflectances overlap the distribution of measured reflectances. Here a comparison between spectra provides a relative confidence on the consistency between DART simulations and AVIRIS spectra, at least for oak species (Figure 5.9).

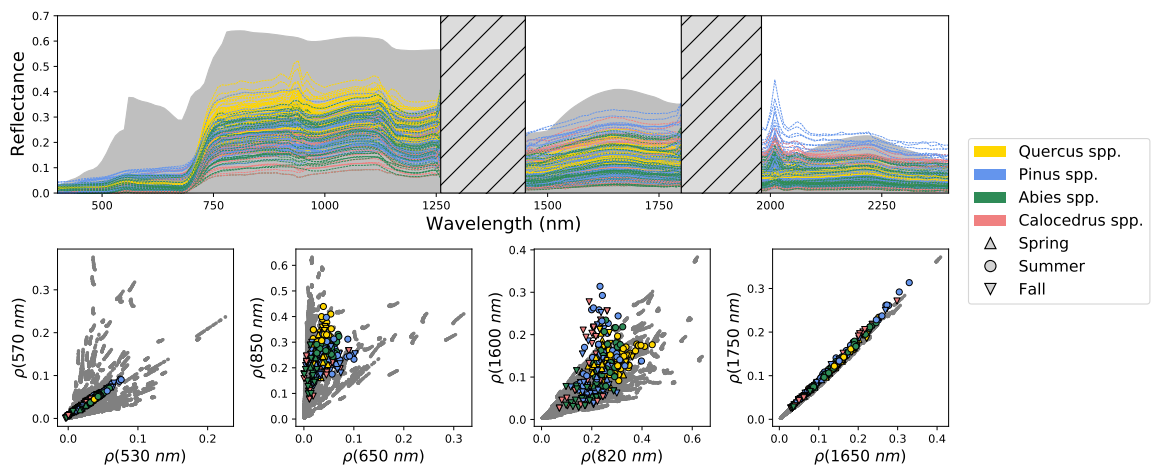


Figure 5.9: Reflectances of extracted AVIRIS pixels compared to reflectances computed with DART-SFR simulations. (top) Reflectances as a function of wavelength, gray area in the background shows the minimal and maximal reflectance simulated by DART-SFR. (bottom) Scatterplot for four pairs of bands, grey dots show the simulated reflectance values

The SFR scene used in this thesis may not be suitable to match the AVIRIS acquired signals.

The SFR scene gloss over the effects of several elements of the structure of the environment (*e.g.*, the effects of branches and woody elements reflectance). However, most of published studies focusing on hybrid methods also use simple representations of the vegetation within their chosen RTM. Complex and detailed representations of the vegetation are mostly used for evaluation of RTMs for solving the direct problem (*e.g.*, the RAMI-IV experiment, [Widlowski et al. 2015](#)).

The simulation issued from RTM should involve the elements that cause canopy reflectance variations. These elements are numerous, and are further discussed. A first element that is a source of variability of the canopy reflectance is the LAI and its combined effect with the background reflectance. As mentioned by [Gao et al. 2022](#), based on a lab experiment over wheat-like canopy, the spectral signature of the canopy varies considerably with the background reflectance, particularly for LAI less than 3 ([Barton and North 2001](#)). This threshold could depend on the type of vegetation as [Goel 1988](#) reported that a LAI over 3 or 4 has no impact on the spectral signature. Nonetheless, it seems that high LAI (> 6) do not have a significant impact on the spectral signature, their knowledge of LAI is necessary for low values (< 3) for a good estimation of forest traits ([Xiao et al. 2014](#)). Additionally, [Cheng et al. 2006](#) mentioned the retrieval of EWT was affected by vegetation canopy architecture causing over or under estimations. The canopy cover is another source of variability of the canopy reflectance, mainly because by definition lower canopy covers leave a larger fraction of soil and undergrowth visible. With high canopy cover levels, the canopy structure has a weaker impact on the spectral reflectance ([Xiao et al. 2014](#)). [Ali et al. 2016](#) also mentioned that the forest traits can be estimated from the spectral reflectance of a forest canopy without any information on the forest structure for a canopy cover higher than 50%. However, for lower canopy cover information on the canopy cover is required. Nonetheless, the tested methods with CSTARS-Canopy seem to be insensitive to the canopy cover regardless of the leaf trait. Indeed, the estimation absolute errors do not show any particular correlation to the canopy cover (Table [Table 5.12](#) and [Figure 5.10](#)).

Table 5.12: Non linear correlation (measured by Kendall’s Tau) between absolute estimation error and canopy cover.

	STAT methods		Hybrid 1D-CNN	
	Oaks	Conifers	Oaks	Conifers
C_{ab}	0.00	0.09	0.06	-0.04
C_{xc}	0.09	-0.07	0.34	0.01
EWT	0.07	-0.02	0.14	-0.02
LMA	0.07	0.04	0.05	-0.06

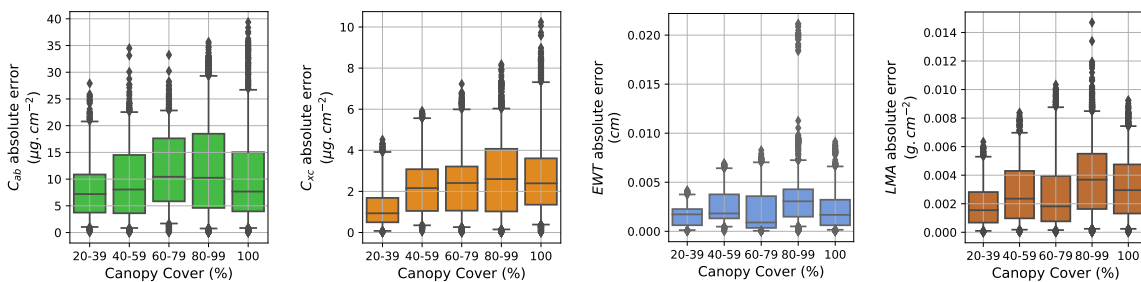


Figure 5.10: Evolution of the traits estimation errors as a function of the canopy cover, the best retrieval method of each trait is kept to graph each figure.

The tree structure and its woody elements can alter the canopy reflectance. By comparing two tree mockups, [Miraglio et al. 2021](#) showed that the impact of the 3D model of tree woody elements in the range $0.75 - 1.3 \mu\text{m}$ had an impact on the spectral reflectance but no influence was noted in the $1.5 - 2.4 \mu\text{m}$ range to estimate EWT and LMA.

Finally, the traits’ inter-correlation can be taken into account in the retrieval process, particularly between C_{ab} and C_{xc} that exhibit naturally strong linear correlation. For example, [Miraglio et al. 2022](#) and [Wocher et al. 2020](#) built such a relation between C_{ab} and C_{xc} , leading to a better estimation performance. Although, estimates from the Hybrid-1D-CNN estimator are obtained without any relation between C_{ab} and C_{xc} .

The third class of sources of errors integrates errors to the field data acquisition (from ground

or lab measurements) and the validation procedure. Firstly, the data acquisition for validation is performed at the leaf scale and on a unique branch. Therefore this reference for validation is not exactly at the same scale as the radiometric acquisition. Particularly, the ratio GSD- size of the object of interest is also crucial because if the GSD is too large in regard to the size of the object, this will introduce mixed pixels. In the case of CSTARS-Canopy, the radiometric acquisition is performed at a 14 m GSD over a landscape with a large range of canopy covers (20% to 100%). As a consequence, a larger number of pixels are a mix between several trees and/or canopy and background. This presence of mixed pixels is not the case for [Hoeppe et al. 2020](#) (who worked with a 3 m GSD) or [Wang et al. 2020](#) (1 m GSD).

Besides, an error can occur when the airborne acquisitions are not synchronized with the ground measurements. But, the estimation absolute errors do not show any particular correlation to the temporal shift ([Table 5.13](#) and [Figure 5.11](#)). This shows that a temporal shift between ground measurements and airborne acquisitions in CSTARS-Canopy has a limited influence on the estimates of the tested statistical methods and Hybrid-1DCNN.

Table 5.13: Non linear correlation (measured by Kendall’s Tau) between absolute estimation error and temporal shift.

	STAT methods		Hybrid 1D-CNN	
	Oaks	Conifers	Oaks	Conifers
C_{ab}	-0.03	0.02	0.01	-0.13
C_{xc}	0.00	0.01	0.05	0.08
EWT	0.17	0.01	0.03	-0.12
LMA	0.03	-0.06	0.01	-0.16

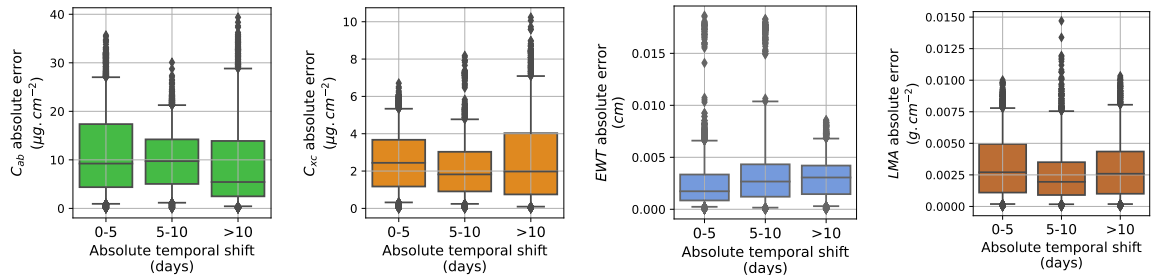


Figure 5.11: Evolution of the traits estimation errors as a function of the temporal shift between images and data collection, the best retrieval method of each trait is kept to graph each figure.

5.3.2.3 Upscaling leaf trait estimation from leaf to canopy scale

Globally, the traits estimates at canopy level exhibited a lower accuracy when compared to the estimates at leaf levels for deciduous forests. Regarding statistical methods, the RMSE degraded at least by a factor 2 for C_{ab} from $5.0 \mu\text{g} \cdot \text{cm}^{-2}$ to $13.0 \mu\text{g} \cdot \text{cm}^{-2}$, for C_{xc} from $1.3 \mu\text{g} \cdot \text{cm}^{-2}$ to $3.0 \mu\text{g} \cdot \text{cm}^{-2}$, and at least by a factor 4 for EWT from 0.0009 cm to 0.0040 cm and for LMA from $0.0009 \text{ g} \cdot \text{cm}^{-2}$ to $0.0038 \text{ g} \cdot \text{cm}^{-2}$. Several authors detailed the reason for accuracy losses. As mentioned by [Schlerf et al. 2010](#) the upscaling process introduced effects like architecture (canopy cover, LAI), and influence of soil and understory background. For low canopy cover (< 50%), the heterogeneity of the structural variables can also explain the dispersion of the results ([Ali et al. 2016](#)). [Ali et al. 2016](#) demonstrated by simulation that the spectral variation at canopy level is lower than that at leaf level, due to the structural variables effect and as a consequence lead to a highest estimation uncertainty. Several parameters have to be considered in the upscaling process which are sources of uncertainties. More particularly, [Wocher et al. 2020](#) mentioned that for low LAI the soil background affects the spectral signature in the VNIR and as a consequence the C_{ab} estimation. Further, the estimation of EWT degrades with a LAI increase which intensifies the 910 nm water absorption band but also in presence of moist soil leading to an underestimation of EWT ([Wocher et al. 2020](#)).

Conclusion

The work carried out in this chapter focused on the estimation of leaf traits at the canopy level from AVIRIS images. Two estimation strategies were evaluated: a statistical strategy where four MLRA were tested (Ridge, PLSR, RFR, GPR), and a hybrid strategy based on DART-SFR simulations and a 1D-CNN as MLRA. More specifically the two strategies estimated the leaf traits for all the AVIRIS images included in the dataset at the same time, covering several forest types and sites at three seasons.

The statistical methods considered separately the broadleaf species (oaks) and the conifer species. The four MLRA evaluated achieved similar accuracies (RMSE of $13.0 \mu\text{g} \cdot \text{cm}^{-2}$; $3.0 \mu\text{g} \cdot \text{cm}^{-2}$; 0.0040 cm ; $0.0038 \text{ g} \cdot \text{cm}^{-2}$ for C_{ab} , C_{xc} , EWT and LMA respectively for oaks; RMSE of $20.0 \mu\text{g} \cdot \text{cm}^{-2}$; $3.1 \mu\text{g} \cdot \text{cm}^{-2}$; 0.0042 cm ; $0.0044 \text{ g} \cdot \text{cm}^{-2}$ for C_{ab} , C_{xc} , EWT and LMA respectively for conifers). Although, estimation errors are too large compared to the natural infra-specific variations of leaf traits in the CSTARS-Canopy dataset and consequently these methods does not appear suitable to monitor leaf traits for those sites and species.

The hybrid 1D-CNN method provides unreliable estimates for both oaks and conifers. More specifically, the inverse model learned from the simulations does not match the reflectances extracted from the AVIRIS images. Indeed, MSE loss computed on the CSTARS-Canopy dataset did not decrease during the 1D-CNN training. This indicates that the radiative transfer simulation from the DART-SFR model are not suitable in this case. Yet, the results on the synthetic dataset highlight that 1D-CNN may be not a suitable algorithm to deal with spectroscopy. In fact, the 1D-CNN obtained a better accuracy with large kernels, behaving in this case as a simple multi-layer perceptron.

Therefore, the four statistical methods produced most accurate estimates than the hybrid method, whatever the trait and/or species considered. Nevertheless, statistical methods evaluated in this chapter obtained worse performances than methods evaluated in the state-of-the-art. This difference can be partially explained by the strategy employed here, combining data from different dates and sites while most of the published studies usually consider site- and period-specific data. The performances obtained in this chapter could also be explained by the type of data. Indeed, the resolution of AVIRIS likely covers several trees and background in the same pixel. Considering this, the signal is altered which act as noise in the dataset, and the validation protocol from this thesis protocol is not perfectly suited to the AVIRIS data. Conversely, studies that obtain better estimation accuracy in the state-of-the-art used images with a smaller GSD.

To cope with the limitations highlighted in this chapter, future works should focus on images with lower GSD or use more extensive reference data that assess the properties of the multiple trees detected in one pixel. Additionally, more knowledge on the preprocessing of imaging spectroscopy data to alleviate the effects of canopy structure or illumination variability would be necessary.

Conclusions and Perspectives

Conclusions

Forest ecosystems are important reservoirs of biodiversity and play important roles in regulating biogeochemical cycles and climate. As such, forest ecosystems provide numerous ecological functions and ecosystem services. However, these ecosystems are under threat from current and future climate change, which is leading to an increase in dry periods, the spread of pathogens and invasive species. As a result, the health of forests and their trees needs to be monitored. Leaf traits, defined in ecology, can be used to assess the health of vegetation. They can be estimated using hyperspectral optical remote sensing by solving an inverse problem, as they alter the optical properties of vegetation in the 0.4 – 2.5 μm optical range. The estimation of functional traits, of which leaf traits are a part, is one of the main challenges of environmental remote sensing, along with the classification of plant species to assess and monitor the evolution of species richness and their geographical extent. Spaceborne hyperspectral sensors have already been launched or are planned for the next decade. These sensors will provide massive and unprecedented flows of hyperspectral images of the Earth, making it possible to monitor forest ecosystems, but requiring automated processing methods.

In this context, it will be necessary to use generalizable methods for estimating leaf traits, *i.e.* capable of processing all forest images from a spatial sensor and therefore being robust to different temperate forest types and their temporal variations. The work in this thesis is part of this approach. The aim is to estimate four leaf traits - leaf concentrations of chlorophylls (C_{ab}), carotenoids (C_{xc}), water (EWT) and dry matter (LMA) - at five forest sites in California, covering three temperate forest types at three times of year. In addition, the development of a generalizable method rests upon two underlying scientific challenges and questions related to the scale of observation. To address these challenges, the thesis work has been divided into two main parts.

On the one hand, the different tree species of temperate forests have foliage with specific morphological and phenological characteristics linked to their adaptation to climates. It was therefore necessary to check whether the estimation methods based on spectroscopic measurements identified in the literature are applicable to the foliage of temperate forest species. At the leaf scale, the challenge was to determine the most accurate method for estimating each leaf trait, applicable to the species studied. At this scale, several estimation methods using spectroscopic measurements and from the literature were compared on the basis of leaf samples collected at the five sites. The methods selected include both physical and statistical approaches.

On the other hand, specific features are also visible at the canopy scale, modifying reflectance above the canopy, as well as landscape variations related to solar illumination and understory. It therefore appeared necessary to assess the extent to which the estimation accuracies obtained at leaf scale are transferable to canopy scale, taking into account variations due to canopy structure, solar illumination and understory. At the tree and canopy scale, the challenge was to identify an estimation method capable of coping with temporal changes in apparent forest reflectance, based on AVIRIS acquisitions made at the five sites in conjunction with leaf collections for laboratory measurements. At this scale, leaf traits were estimated using various statistical approaches based on the same algorithms employed at the leaf scale. A hybrid method, based on 1D-CNN and DART-SFR radiative transfer simulations, was also evaluated.

At the leaf scale, four categories of methods were considered for estimating the four leaf traits: iterative inversion of PROSPECT (IO-PROSPECT), LUT-based PROSPECT inversion, four MLRA-based PROSPECT inversions (hybrid approaches) and statistical approaches based on the same four MLRAs. The four MLRAs studied are Ridge, PLSR, GPR and RFR. For the statistical approaches, two training databases were used (CSTARS-Leaf and ANGERS), enabling us to assess

the transferability potential of these statistical methods. The accuracies of the estimation methods were compared using the CSTARS-Leaf dataset. This contains leaf trait measurements combined with hemispherical reflectance and directional transmittance measurements for coniferous and deciduous species over three distinct seasons.

Regarding conifer species, the experience did not allow drawing any conclusions on the applicability of the methods considered in this work. In fact, as the measurement tools used are poorly adapted to conifer needles, reflectance and transmittance measurements are highly uncertain, even after the application of a correction protocol. For these reasons, it was not possible to determine whether the estimation errors originate from the measurement or are intrinsic to the different estimation methods.

In particular, estimation methods were examined for the four hardwood species present in the CSTARS-Leaf dataset, which are four species of oak (*Quercus spp.*). For these four oak species, the main results show that statistical methods lead to the best performance for all four leaf traits, in particular using GPR as MLRA (RMSE of $5.0 \mu\text{g} \cdot \text{cm}^{-2}$; $1.3 \mu\text{g} \cdot \text{cm}^{-2}$; 0.0009 cm ; $0.0009 \text{ g} \cdot \text{cm}^{-2}$ for C_{ab} , C_{xc} , EWT and LMA respectively). Using the ANGERS database to assess the transferability potential of statistical methods, accuracies were degraded by a factor of 2 in terms of RMSE, for all four leaf traits. Without a representative database, IO-PROSPECT is the recommended method for estimating C_{ab} , C_{xc} and EWT. For LMA, a hybrid approach based on the RFR algorithm achieved better estimation accuracy. Performance seemed to depend little on the season. In addition, the accuracy of the estimate does not depend particularly on the species, but rather on the functional type of the plant (*i.e.*, deciduous or evergreen species). The distribution of PROSPECT's N structure parameter was also analyzed. It was observed that N was strongly correlated with LMA for the oak species studied. Moreover, the distribution of N appeared stable for evergreen species throughout the year, while N tended to increase over the year for deciduous species.

The results of the leaf-scale work highlight several limitations. On the one hand, the dataset shows that optical measurement lacks reliability for conifers due to the type of foliage: needles instead of broadleaves. To compare estimation methods reliably, it would be necessary to improve the precision of the protocols for physically reliable measurements. For example, [Harron 2000](#) proposed the use of a specific carrier to conduct reflectance measurements on needle-like foliage. On the other hand, it is commonly accepted that fine spectral resolution, *i.e.* below 10 nm, is sufficient to estimate leaf traits. However, the effect of changing spectral resolution on performance estimation at the leaf level has not been studied. Indeed, portable spectroradiometers commonly have a bandwidth of 3 nm, while airborne sensors, notably future space missions, have a bandwidth of 10 nm ([Rast et al. 2021](#); [Green et al. 2022](#)).

At the canopy scale, two strategies were evaluated: a statistical strategy for which the four algorithms already employed at the leaf scale were tested, and a hybrid strategy including DART-SFR simulations and a 1D-CNN algorithm. In particular, the results of the hybrid 1D-CNN method show that the inverse model learned from the simulations does not match the reflectances extracted from the AVIRIS images. Furthermore, the 1D-CNN hybrid method does not use any species-specific simulations (deciduous, coniferous), and in particular the RTMs used are calibrated for deciduous rather than coniferous species. Overall, the four statistical methods produced better estimates than the hybrid method, whatever the trait and/or species considered. The statistical methods achieved similar accuracies in terms of RMSE (RMSE of $13.0 \mu\text{g} \cdot \text{cm}^{-2}$; $3.0 \mu\text{g} \cdot \text{cm}^{-2}$; 0.0040 cm ; $0.0038 \text{ g} \cdot \text{cm}^{-2}$ for C_{ab} , C_{xc} , EWT and LMA respectively). Nevertheless, the estimation performances obtained here for the statistical methods remain of lower accuracy than the results presented in the state of the art. More specifically, estimation errors remain too large to detect seasonal and intra-specific variations in leaf traits for the species and sites considered in this thesis. The differences in estimation accuracy with the state of the art can be partly explained by the choice made in this work to combine different sites and different periods of the year at the same time, whereas the work carried out in the state of the art generally considers site- and period-specific data. However, the study conducted in this thesis is more realistic to actually measure real ecosystems.

The data processing and simulations presented in this document for work at the canopy scale reveal certain limitations. The following points are intended to remove or mitigate these limitations. In canopy-scale work, no pre-processing is carried out on reflectances measured at the top of the canopy. Nevertheless, pre-processing has been used in the state of the art by some authors and could be of interest in attenuating the effects of differences in illumination. Furthermore, the data used here do not include any relief-related corrections. The cases considered here are little affected by the effects of relief, and the collections were carried out on slight slopes for accessibility reasons (*i.e.*, less than 15°). Nevertheless, a generalizable method will have to take into account

the effects of more significant slopes.

In addition, it is important to take into account the influence of understory vegetation in future estimates. For variable forest densities, the resolutions used necessarily cover trees or portions of trees with portions of understory. Another point concerns woody elements, which are not taken into account in the simulation for hybrid methods. The resolution of future missions (*i.e.*, 30 m ; [Green et al. 2022](#); [Rast et al. 2021](#)) implies the collection of data on surfaces containing several trees and portions of understory. Pixels will therefore be mixed, covering several individuals, hence the interest in taking measurements, directly or indirectly, on an entire stand rather than a single tree.

The work presented in this thesis is limited to two ecoregions of the California floristic province. Even though the species and sites selected are similar to plant communities of other ecoregions of the temperate biomes, the study has been limited to this geographical area, and therefore it is not possible to simply generalize the conclusions at the global scale.

Perspectives

The work proposed in this thesis offers numerous prospects. Firstly, these prospects concern the improvement of estimation performance from a methodological point of view, and secondly, the monitoring of forest ecosystems in the context of future hyperspectral missions.

With the aim of developing a generalizable method, the validation datasets must cover a wider range of species and ecosystems, with a greater number of samples collected per tree group, in order to match the potential resolution and extent of future space-based sensors.

The new trend in machine learning is the explainability ([Schwalbe and Finzel 2023](#)). The field of explainable artificial intelligence (XAI) involves understanding how machine learning models work, in order to guarantee their reliability. The field of remote sensing, in particular for leaf trait estimation, could benefit from XAI advances to build estimation methods based on statistical and hybrid strategies. The aim would be to guarantee the reliability of these methods and the identification of key variables in the decision-making process of these models. In addition, transfer learning techniques can allow the use of several datasets with different distribution characteristics, and ease the transferability of statistically learned models ([Weiss et al. 2016](#)). At the end of the day, the generalization leaf traits estimations through a statistical strategy could drastically benefit from both XAI and transfer learning.

For hybrid methods, more insight are required regarding the complexity of the direct modeling. Addition of more elements in radiative transfer models might be necessary to provide more reliable simulated reflectances to feed statistical algorithms. The proper level of details required for leaf traits estimation should be assessed. It is expected that the proper level of details would vary as a function of the GSD. Besides, more details models can be provided from growth model developed for tree physiology studies ([Eloy et al. 2017](#)) or for computer graphics purposes ([Makowski et al. 2019](#)), including at the stand scale ([Dufour-Kowalski et al. 2012](#)). These growth models can also take into account environmental factors to deliver simulations adapted to a wide number of ecoregions.

The LMA comprises a large number of compounds (proteins, cellulose, hemicellulose and lignin ; [Féret et al. 2021](#)). To obtain more precise information on plant physiology, it is interesting to be able to estimate the concentration of each of these compounds. In particular, nitrogen-based compounds (proteins) can be spectrally distinguished from carbon-only elements, as the N-H bond has a specific spectral signature ([Curran 1989](#)).

At the leaf scale, several datasets, gathering leaf traits and optical measures, are freely available, but concern mainly broadleaved species. In order to improve the analysis of coniferous forests using statistical methods, it will be necessary to have more datasets of this kind for these types of species.

The datasets used here correspond to three collections at different seasons (spring, summer, autumn). A more complete validation of the methods requires work on data sets covering the whole year with the same frequency as a spatial sensor (*i.e.*, with an interval of 1 month or less). These observation frequencies would enable physiological processes to be monitored throughout the phenological cycle. In addition, it will be necessary to link the observations with plant physiology in order to monitor and predict the state of health of the forest ecosystem.

In the longer term, two major missions are planned: SBG (NASA ; [Green et al. 2022](#)) and CHIME (ESA ; [Rast et al. 2021](#)). These missions will make systematic acquisitions of all continental surfaces, similar to current multispectral observations (Sentinel-2, Landsat 8 and 9). These two sensors are planned to deliver hyperspectral images with a 30 GSD. With these large GSD, a single pixel will cover several trees, potentially encompassing a wide variety of species. Consequently, the validation protocol of leaf traits estimation methods needs to be adapted. One solution could

be to take measurements for the main trees of a whole stand included in the pixel, but would tremendously time consuming and require a large work force. Another solution could be to gradually upscale the estimation methods: a first validation method from low GSD airborne images would be validated in a first time, and then be used to produce reliable leaf traits maps that will be the reference values for estimation methods using a larger GSD.

Besides, hyperspectral data, especially space-borne data, could be coupled with multispectral data with a higher spatial resolution and therefore provide more information on canopies.

The signal received by a sensor will be sensitive to both vegetation features and the amount of foliage defined by LAI . This raises the question, particularly for larger GSD, of whether it is preferable to estimate canopy contents defined by the product of foliage traits and LAI, as opposed to foliage traits alone. Moreover, canopy contents will be directly related to the amount of chlorophyll per square meter, which directly gives the carbon dioxide absorption capacity per hectare.

Conclusions et Perspectives

Conclusions

Les écosystèmes forestiers sont d'importants réservoirs de biodiversité et jouent un rôle important dans la régulation des cycles biogéochimiques et du climat. En tant que tels, les écosystèmes forestiers assurent de nombreuses fonctions écologiques et de nombreux services écosystémiques. Toutefois, ces écosystèmes sont menacés par le changement climatique actuel et futur, qui entraîne une augmentation des périodes de sécheresse, la propagation de pathogènes et d'espèces envahissantes. Par conséquent, la santé des forêts et de leurs arbres doit être surveillée. Les caractéristiques foliaires, définies en écologie, peuvent être utilisées pour évaluer la santé de la végétation. Ils peuvent être estimés par télédétection optique hyperspectrale en résolvant un problème inverse, car ils modifient les propriétés optiques de la végétation dans la gamme optique $0,4 - 2,5 \mu\text{m}$. L'estimation des traits fonctionnels, dont les traits foliaires font partie, est l'un des principaux défis de la télédétection environnementale, avec la classification des espèces végétales pour évaluer et suivre l'évolution de la richesse des espèces et leur étendue géographique. Des capteurs hyperspectraux spatiaux ont déjà été lancés ou sont prévus pour la prochaine décennie. Ces capteurs fourniront des flux massifs et sans précédent d'images hyperspectrales de la Terre, ce qui permettra de surveiller les écosystèmes forestiers, mais nécessitera des méthodes de traitement automatisées.

Dans ce contexte, il sera nécessaire d'utiliser des méthodes généralisables pour l'estimation des traits foliaires, *i.e.* capables de traiter toutes les images forestières à partir d'un capteur spatial et donc d'être robustes aux différents types de forêts tempérées et à leurs variations temporelles. Le travail de cette thèse s'inscrit dans cette approche. L'objectif est d'estimer quatre caractéristiques foliaires - les concentrations foliaires de chlorophylles (C_{ab}), de caroténoïdes (C_{xc}), d'eau (EWT) et de matière sèche (LMA) - sur cinq sites forestiers en Californie, couvrant trois types de forêts tempérées à trois périodes de l'année. De plus, le développement d'une méthode généralisable repose sur deux défis scientifiques sous-jacents et des questions liées à l'échelle d'observation. Pour relever ces défis, le travail de thèse a été divisé en deux parties principales.

D'une part, les différentes espèces d'arbres des forêts tempérées ont un feuillage avec des caractéristiques morphologiques et phénologiques spécifiques liées à leur adaptation aux climats. Il a donc été nécessaire de vérifier si les méthodes d'estimation basées sur des mesures spectroscopiques identifiées dans la littérature sont applicables au feuillage des espèces forestières tempérées. A l'échelle de la feuille, l'enjeu était de déterminer la méthode d'estimation de chaque caractère foliaire la plus précise et applicable aux espèces étudiées. A cette échelle, plusieurs méthodes d'estimation utilisant des mesures spectroscopiques et issues de la littérature ont été comparées sur la base d'échantillons de feuilles collectés sur les cinq sites. Les méthodes sélectionnées comprennent à la fois des approches physiques et statistiques.

D'autre part, des caractéristiques spécifiques sont également visibles à l'échelle de la canopée, modifiant la réflectance au-dessus de la canopée, ainsi que les variations du paysage liées à l'illumination solaire et au sous-étage. Il est donc apparu nécessaire d'évaluer dans quelle mesure les précisions d'estimation obtenues à l'échelle de la feuille sont transférables à l'échelle de la canopée, en tenant compte des variations dues à la structure de la canopée, à l'illumination solaire et au sous-étage. A l'échelle de l'arbre et de la canopée, le défi était d'identifier une méthode d'estimation capable de faire face aux changements temporels de la réflectance apparente de la forêt, en se basant sur les acquisitions AVIRIS réalisées sur les cinq sites en conjonction avec des collectes de feuilles pour des mesures en laboratoire. À cette échelle, les caractéristiques des feuilles ont été estimées à l'aide de diverses approches statistiques basées sur les mêmes algorithmes que ceux utilisés à l'échelle des feuilles. Une méthode hybride, basée sur des simulations de transfert radiatif 1D-CNN et DART-SFR, a également été évaluée.

À l'échelle de la feuille, quatre catégories de méthodes ont été envisagées pour estimer les quatre caractères foliaires : l'inversion itérative de PROSPECT (IO-PROSPECT), l'inversion de PROSPECT basée sur la LUT, quatre inversions de PROSPECT basées sur les MLRA (approches hybrides) et des approches statistiques basées sur les mêmes quatre MLRA. Les quatre MLRA étudiés sont Ridge, PLSR, GPR et RFR. Pour les approches statistiques, deux bases de données d'entraînement ont été utilisées (CSTARS-Leaf et ANGERS), ce qui nous a permis d'évaluer le potentiel de transférabilité de ces méthodes statistiques. Les précisions des méthodes d'estimation ont été comparées à l'aide de l'ensemble de données CSTARS-Leaf. Cette base de données contient des mesures de caractéristiques foliaires combinées à des mesures de réflectance hémisphérique et de transmittance directionnelle pour des espèces de conifères et de feuillus au cours de trois saisons distinctes.

En ce qui concerne les espèces de conifères, l'expérience n'a pas permis de tirer des conclusions sur l'applicabilité des méthodes considérées dans ce travail. En effet, les outils de mesure utilisés étant mal adaptés aux aiguilles de conifères, les mesures de réflectance et de transmittance sont très incertaines, même après l'application d'un protocole de correction. Pour ces raisons, il n'a pas été possible de déterminer si les erreurs d'estimation proviennent de la mesure ou sont intrinsèques aux différentes méthodes d'estimation.

En particulier, les méthodes d'estimation ont été examinées pour les quatre espèces de feuillus présentes dans l'ensemble de données CSTARS-Leaf, qui sont quatre espèces de chênes (*Quercus spp.*). Pour ces quatre espèces de chênes, les principaux résultats montrent que les méthodes statistiques donnent les meilleurs résultats pour les quatre caractères foliaires, en particulier en utilisant le GPR comme MLRA (RMSE de $5.0 \mu\text{g} \cdot \text{cm}^{-2}$; $1.3 \mu\text{g} \cdot \text{cm}^{-2}$; 0.0009 cm ; $0.0009 \text{ g} \cdot \text{cm}^{-2}$ pour C_{ab} , C_{xc} , EWT et LMA respectivement). En utilisant la base de données ANGERS pour évaluer le potentiel de transférabilité des méthodes statistiques, les précisions ont été dégradées par un facteur de 2 en termes de RMSE, pour les quatre caractères foliaires. En l'absence d'une base de données représentative, IO-PROSPECT est la méthode recommandée pour estimer C_{ab} , C_{xc} et EWT. Pour la LMA, une approche hybride basée sur l'algorithme RFR a permis d'obtenir une meilleure précision d'estimation. Les performances semblent peu dépendre de la saison. En outre, la précision de l'estimation ne dépend pas particulièrement de l'espèce, mais plutôt du type fonctionnel de la plante (*i.e.*, espèces à feuilles caduques ou à feuilles persistantes). La distribution du paramètre de structure N de PROSPECT a également été analysée. Il a été observé que N était fortement corrélé avec LMA pour les espèces de chênes étudiées. De plus, la distribution de N semble stable pour les espèces à feuilles persistantes tout au long de l'année, alors que N a tendance à augmenter au cours de l'année pour les espèces à feuilles caduques.

Les résultats du travail à l'échelle de la feuille mettent en évidence plusieurs limites. D'une part, l'ensemble des données montre que les mesures optiques manquent de fiabilité pour les conifères en raison du type de feuillage : des aiguilles au lieu de feuilles larges. Pour comparer les méthodes d'estimation de manière fiable, il serait nécessaire d'améliorer la précision des protocoles pour obtenir des mesures physiquement fiables. Par exemple, [Harron 2000](#) a proposé l'utilisation d'un support spécifique pour effectuer des mesures de réflectance sur un feuillage en forme d'aiguille. D'autre part, il est communément admis qu'une résolution spectrale fine, *i.e.* inférieure à 10 nm, est suffisante pour estimer les caractéristiques des feuilles. Cependant, l'effet d'une modification de la résolution spectrale sur l'estimation des performances au niveau des feuilles n'a pas été étudié. En effet, les spectroradiomètres portables ont généralement une largeur de bande de 3 nm, tandis que les capteurs aéroportés, notamment les futures missions spatiales, ont une largeur de bande de 10 nm ([Rast et al. 2021](#); [Green et al. 2022](#)).

A l'échelle de la canopée, deux stratégies ont été évaluées : une stratégie statistique pour laquelle les quatre algorithmes déjà utilisés à l'échelle de la feuille ont été testés, et une stratégie hybride comprenant des simulations DART-SFR et un algorithme 1D-CNN. En particulier, les résultats de la méthode hybride 1D-CNN montrent que le modèle inverse appris à partir des simulations ne correspond pas aux réflectances extraites des images AVIRIS. En outre, la méthode hybride 1D-CNN n'utilise pas de simulations spécifiques aux espèces (feuillus, conifères) et, en particulier, les RTM utilisés sont calibrés pour les feuillus plutôt que pour les conifères. Dans l'ensemble, les quatre méthodes statistiques ont produit de meilleures estimations que la méthode hybride, quels que soient le caractère et/ou l'espèce considérés. Les méthodes statistiques ont atteint des précisions similaires en termes de RMSE (RMSE de $13.0 \mu\text{g} \cdot \text{cm}^{-2}$; $3.0 \mu\text{g} \cdot \text{cm}^{-2}$; 0.0040 cm ; $0.0038 \text{ g} \cdot \text{cm}^{-2}$ pour C_{ab} , C_{xc} , EWT et LMA respectivement). Néanmoins, les performances d'estimation obtenues ici pour les méthodes statistiques restent moins précises que les résultats présentés dans l'état de l'art. Plus précisément, les erreurs d'estimation restent trop importantes pour détecter les variations saisonnières et intraspécifiques des caractéristiques des feuilles pour

les espèces et les sites considérés dans cette thèse. Les différences de précision d'estimation avec l'état de l'art peuvent être partiellement expliquées par le choix fait dans ce travail de combiner différents sites et différentes périodes de l'année en même temps, alors que le travail effectué dans l'état de l'art considère généralement des données spécifiques au site et à la période. Cependant, l'étude menée dans cette thèse est plus réaliste pour mesurer réellement des écosystèmes réels.

Les traitements de données et les simulations présentés dans ce document pour les travaux à l'échelle de la canopée révèlent certaines limites. Les points suivants ont pour but de supprimer ou d'atténuer ces limitations. Dans les travaux à l'échelle de la canopée, aucun prétraitement n'est effectué sur les réflectances mesurées au sommet de la canopée. Néanmoins, le prétraitement a été utilisé dans l'état de l'art par certains auteurs et pourrait être intéressant pour atténuer les effets des différences d'illumination. Par ailleurs, les données utilisées ici ne comportent pas de corrections liées au relief. Les cas considérés ici sont peu affectés par les effets du relief, et les collectes ont été réalisées sur des pentes faibles pour des raisons d'accessibilité (*i.e.*, moins de 15°). Néanmoins, une méthode généralisable devra prendre en compte les effets de pentes plus importantes.

En outre, il est important de prendre en compte l'influence de la végétation de sous-bois dans les estimations futures. Pour des densités forestières variables, les résolutions utilisées couvrent nécessairement des arbres ou des portions d'arbres avec des portions de sous-bois. Un autre point concerne les éléments ligneux, qui ne sont pas pris en compte dans la simulation pour les méthodes hybrides. La résolution des futures missions (*i.e.*, 30 m ; Green et al. 2022; Rast et al. 2021) implique la collecte de données sur des surfaces contenant plusieurs arbres et des portions de sous-bois. Les pixels seront donc mélangés, couvrant plusieurs individus, d'où l'intérêt de prendre des mesures, directement ou indirectement, sur un peuplement entier plutôt que sur un seul arbre.

Le travail présenté dans cette thèse se limite à deux écorégions de la province floristique de Californie. Même si les espèces et les sites sélectionnés sont similaires aux communautés végétales d'autres écorégions des biomes tempérés, l'étude a été limitée à cette zone géographique et il n'est donc pas possible de généraliser simplement les conclusions à l'échelle mondiale.

Perspectives

Les travaux proposés dans cette thèse offrent de nombreuses perspectives. Ces perspectives concernent d'une part l'amélioration des performances d'estimation d'un point de vue méthodologique, et d'autre part le suivi des écosystèmes forestiers dans le cadre des futures missions hyperspectrales.

Dans le but de développer une méthode généralisable, les jeux de données de validation doivent couvrir une plus large gamme d'espèces et d'écosystèmes, avec un plus grand nombre d'échantillons collectés par groupe d'arbres, afin de correspondre à la résolution et à l'étendue potentielles des futurs capteurs spatiaux.

La nouvelle tendance en matière d'apprentissage automatique est l'explicabilité (Schwalbe and Finzel 2023). Le domaine de l'intelligence artificielle explicable (eXplanable Artificial Intelligence - XAI) consiste à comprendre le fonctionnement des modèles d'apprentissage automatique afin de garantir leur fiabilité. Le domaine de la télédétection, en particulier pour l'estimation des caractéristiques des feuilles, pourrait bénéficier des avancées de l'XAI pour construire des méthodes d'estimation basées sur des stratégies statistiques et hybrides. L'objectif serait de garantir la fiabilité de ces méthodes et l'identification des variables clés dans le processus de décision de ces modèles. En outre, les techniques d'apprentissage par transfert (transfer learning) peuvent permettre l'utilisation de plusieurs ensembles de données présentant des caractéristiques de distribution différentes, et faciliter la transférabilité des modèles appris statistiquement (Weiss et al. 2016). En fin de compte, la généralisation des estimations de traits de feuilles par le biais d'une stratégie statistique pourrait bénéficier considérablement de l'XAI et de l'apprentissage par transfert.

Pour les méthodes hybrides, il est nécessaire de mieux comprendre la complexité de la modélisation directe. L'ajout d'autres éléments dans les modèles de transfert radiatif pourrait être nécessaire pour fournir des réflectances simulées plus fiables afin d'alimenter les algorithmes statistiques. Il convient d'évaluer le niveau de détail requis pour l'estimation des caractéristiques des feuilles. On s'attend à ce que le niveau de détail approprié varie en fonction du GSD. En outre, des modèles plus détaillés peuvent être fournis par des modèles de croissance développés pour des études de physiologie des arbres (Eloy et al. 2017) ou à des fins d'infographie (Makowski et al. 2019), y compris à l'échelle du peuplement (Dufour-Kowalski et al. 2012). Ces modèles de croissance peuvent également prendre en compte des facteurs environnementaux pour fournir des simulations adaptées à un grand nombre d'écorégions.

La LMA comprend un grand nombre de composés (protéines, cellulose, hémicellulose et lignine ; Féret et al. 2021). Pour obtenir des informations plus précises sur la physiologie des plantes, il est intéressant de pouvoir estimer la concentration de chacun de ces composés. En particulier, les composés à base d'azote (protéines) peuvent être distingués spectralement des éléments uniquement carbonés, car la liaison N-H possède une signature spectrale spécifique (Curran 1989).

A l'échelle de la feuille, plusieurs jeux de données, rassemblant des traits foliaires et des mesures optiques, sont librement disponibles, mais concernent principalement des espèces dicotylédones. Afin d'améliorer l'analyse des forêts de conifères à l'aide de méthodes statistiques, il sera nécessaire de disposer de plus de jeux de données de ce type pour ces types d'espèces.

Les jeux de données utilisés ici correspondent à trois collectes à des saisons différentes (printemps, été, automne). Une validation plus complète des méthodes nécessite de travailler sur des jeux de données couvrant l'ensemble de l'année avec la même fréquence qu'un capteur spatial (*i.e.*, avec un intervalle de 1 mois ou moins). Ces fréquences d'observation permettraient de suivre les processus physiologiques tout au long du cycle phénologique. En outre, il sera nécessaire de relier les observations à la physiologie des plantes afin de surveiller et de prédire l'état de santé de l'écosystème forestier.

À plus long terme, deux grandes missions sont prévues : SBG (NASA ; Green et al. 2022) et CHIME (ESA ; Rast et al. 2021). Ces missions feront des acquisitions systématiques de toutes les surfaces continentales, similaires aux observations multispectrales actuelles (Sentinel-2, Landsat 8 et 9). Ces deux capteurs sont prévus pour fournir des images hyperspectrales avec un GSD de 30. Avec ces grandes dimensions, un seul pixel couvrira plusieurs arbres, englobant potentiellement une grande variété d'espèces. Par conséquent, le protocole de validation des méthodes d'estimation des caractéristiques des feuilles doit être adapté. Une solution pourrait consister à prendre des mesures pour les principaux arbres d'un peuplement entier inclus dans le pixel, mais cela prendrait énormément de temps et nécessiterait une main-d'œuvre importante. Une autre solution pourrait consister à augmenter progressivement l'échelle des méthodes d'estimation : une première méthode de validation à partir d'images aéroportées à faible GSD serait validée dans un premier temps, puis utilisée pour produire des cartes de caractéristiques foliaires fiables qui constitueront les valeurs de référence pour les méthodes d'estimation utilisant une GSD plus importante.

En outre, les données hyperspectrales, en particulier les données spatiales, pourraient être couplées à des données multispectrales avec une résolution spatiale plus élevée et fournir ainsi davantage d'informations sur les couverts.

Le signal reçu par un capteur sera sensible à la fois aux caractéristiques de la végétation et à la quantité de feuillage définie par le LAI. Cela soulève la question de savoir s'il est préférable d'estimer le contenu du couvert défini par le produit des caractéristiques du feuillage et du LAI, plutôt que par les seules caractéristiques du feuillage, en particulier pour les GSD les plus importantes. En outre, le contenu de la canopée sera directement lié à la quantité de chlorophylle par mètre carré, qui donne directement la capacité d'absorption du dioxyde de carbone par hectare.

Appendix A

June 2022 field campaign

This appendix presents the fieldwork that occurred in June 2022 (from June 13th to June 20th) on two study sites SOAP and TEAK, already introduced in [Chapter 3](#). This fieldwork aims to assess the health status of forest plots in the context of an extended drought and bark beetle outbreaks.

The appendix reports the proceedings of the fieldwork, the measured data, the processing of the data and the first analysis and results. Fieldwork focuses on the estimation of health status from the ground through visual assessments and noticing pathogens presence. Measurement protocols and basic statistics of the data are presented in this document. This fieldwork leads to a ground truth health status of small-forested plots. At the same time, the PRISMA satellite acquired spectral characteristics of the forest. The end of the section presents acquisitions from PRISMA and the processing of the images.

A.1 Fieldwork

The team was comprised of five people, including three students from the University of California in Davis who volunteered for this fieldwork. For fieldwork, the team was split into two groups: one group of 3 people and one group of two.

Fieldwork aims to perform forest inventories on 40 meter-sided square plots (1600 m² area) to evaluate locally the forest health status. The size of the plot was defined in order to include a full pixel of PRISMA images (30 m GSD) and with the smallest possible area to reduce time consumption. Squares of 40 m by 40 m seemed to be the best compromise. Selected plots are shown on [Figure A.1](#) for SOAP and [Figure A.2](#) for TEAK.

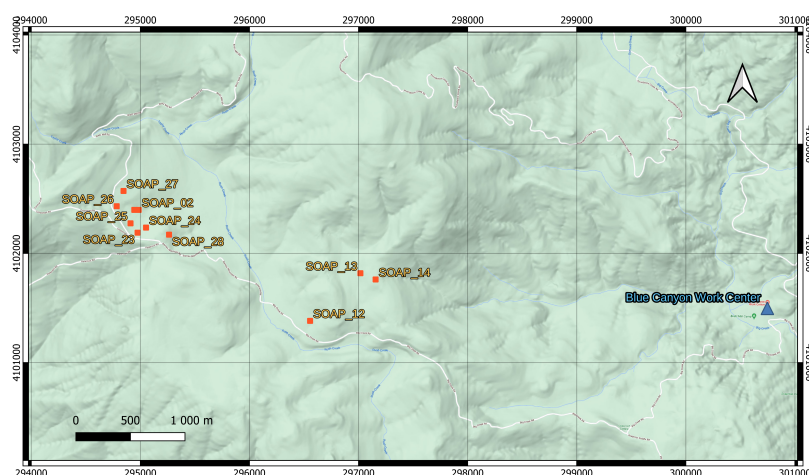


Figure A.1: Map of SOAP site (coordinates given in meter in the UTM 11N system (EPSG 32611), Google terrain as map background). Orange squares represent sampled forest plots and the blue triangle highlights the location of the base camp.

While performing inventories, the groups took note of the tree species, the stress status of the trees (qualitative assessment) and signs of pathogens (see details of the inventory protocol further in this section). Basic measurements were performed on each tree such as measurement of DBH

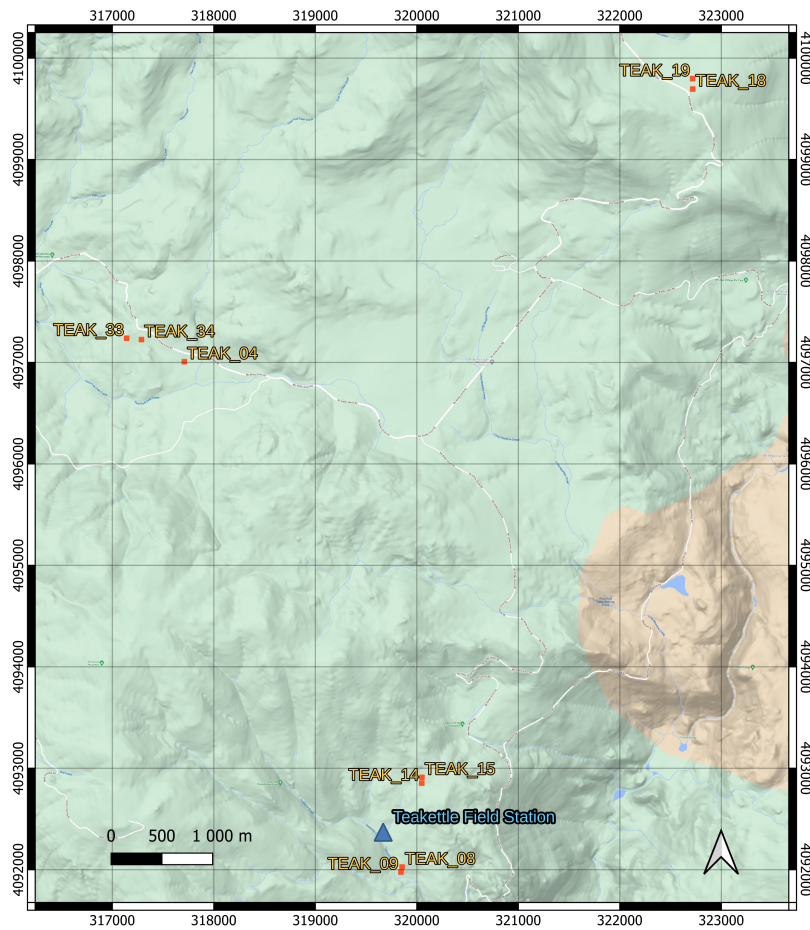


Figure A.2: Map of TEAK site (coordinates given in meter in the UTM 11N system (EPSG 32611), Google terrain as map background). Orange squares represents sampled forest plots and the blue triangle highlight the location of the based camp

(Diameter at Breast Height of the trunk) and record of GPS positions. Details of the sampling protocol are given at the end of this section.

Each plot is defined by a 40m by 40m square. For each plot, we define a regular grid of 25 points (5 rows, 5 columns). We use two numbers to refer to each point: its row number and its column number. The 25 points grid defines 16 subplots. The southwest point gives the subplot number (see Figure A.3). GPS units embedded the 25 points regular grid coordinates for each plot under a waypoint file. In the field, we put a flag at each point coordinate to delimit the subplots.

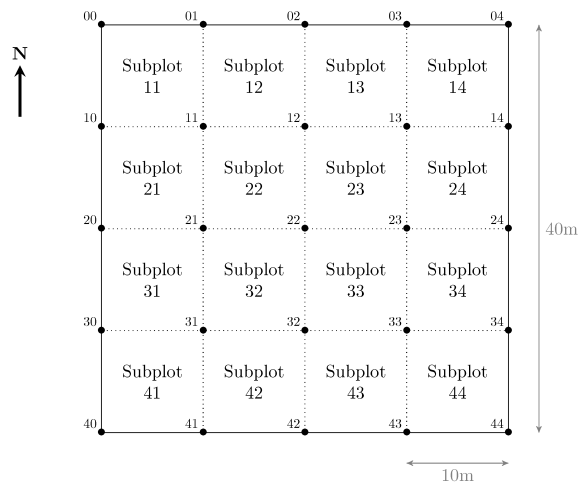


Figure A.3: Naming convention of subplots numbers and plot grid.

For each point of the regular grid, the type of ground cover (among ten categories, considered

types are listed below) and the type of canopy cover (whether or not there is canopy above the point and which tree species) were observed.

A.2 Measurements of tree-scale metrics

This part details the protocol used to perform the tree inventories inside plots. The protocol is designed to provide basic information on the stress level and growth status of the trees in the plot. The DBH is an indicator to assess the height, the age, and the total biomass of the tree. The Global Health index, the Chlorosis index and the Defoliation index provide information on the state and stress level of the tree. Signs of pathogens presence aim to give hypothetical explanatory factors on the health status observed. The inventory only considers trees with a DBH larger than 20 cm, smaller trees were rejected from the census.

Protocol:

- Record of the position of the tree (GPS measurement, taken on the north side of the tree),
- Identification of the tree species (written down with species code),
- Measurement of the DBH (taken at 1.3 m height),
- Evaluation of the global health status of the tree (through Global Health index, see details below),
- Evaluation of chlorosis level and defoliation level (through Chlorosis index and Defoliation index, see details below),
- Visual identification of pathogens and their signs of presence (for bark beetles, mistletoe and cankers, see details below).

After measuring a tree in our inventory, the team put a railroad chalk mark on the bark (always on the north side) in order to prevent measuring the tree twice or forgetting a tree.

Global Health Index: The Global Health Index rates each tree between 1 and 10. The evaluator rates the tree on its global visual aspect. For 1, the tree seems perfectly healthy. For 10 the tree is dead.

Chlorosis and defoliation indices are adaptations of Hawksworth's 1977 protocol designed to evaluate the invasion on dwarf mistletoe (Hawksworth 1977). The protocol separates the crown in tree parts with an independent rating for each part.

Chlorosis index: This index rates the chlorotic aspect of a tree. For the rating: we divide the crown in three parts (bottom, middle, top). For each third, the chlorosis is rated between 0 and 4 according to the number of branches affected by chlorosis:

- 0 => 0% of branches,
- 1 => 0-25% of branches,
- 2 => 25-50% of branches,
- 3 => 50-75% of branches,
- 4 => >75% of branches.

The final index is the sum of the three rates. Hence, this index ranges from 0 to 12.

NB: The Chlorosis index presented here does not discriminate between chlorosis due to a partial or full decay of the leaf going along with desiccation (brown leaves) and chlorosis only due to a lack of chlorophylls (unusual light green leaves) often caused by lack of some nutrients.

Defoliation index: This index rates the defoliated aspect of a tree. We proceed the same way as the chlorosis index.

During the ten days of fieldwork, 20 plots were sampled: 11 plots on SOAP and 9 plots on TEAK. The location of the 20 plots are illustrated in [Figure A.1](#) and [Figure A.2](#). At the end of fieldwork our teams census 1034 trees on the nine different species living on the two sites.

A.3 Plot-scale metrics

During data processing, plot-scaled metrics are derived by averaging these tree-scaled metrics. Comparison of plot-scaled metrics highlight the structural diversity and health status variability among sampled forest plots.

Statistics on measurements highlight the diversity of the 20 visited plots.

First, statistics on DBH measurements mirror the structural differences between plots. As an indicator of the age of trees, the DBH, and more precisely its distribution, show the diversity of vegetation types (Figure A.4). Some of the visited plots can be considered as young forest (low DBH with little variance) but most are older plots undergoing a renewal process (high and low DBH present on the plot).

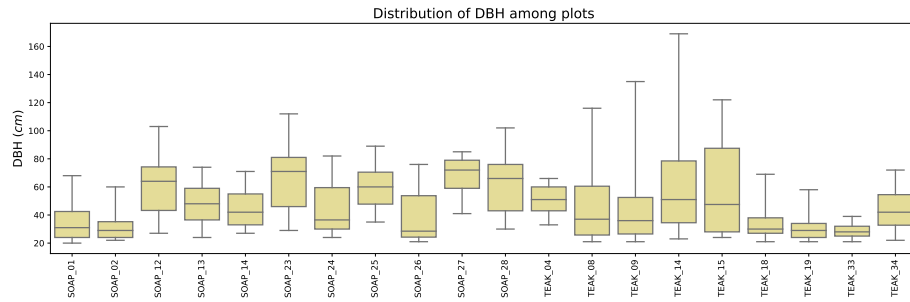


Figure A.4: Distribution of DBH for each visited plot.

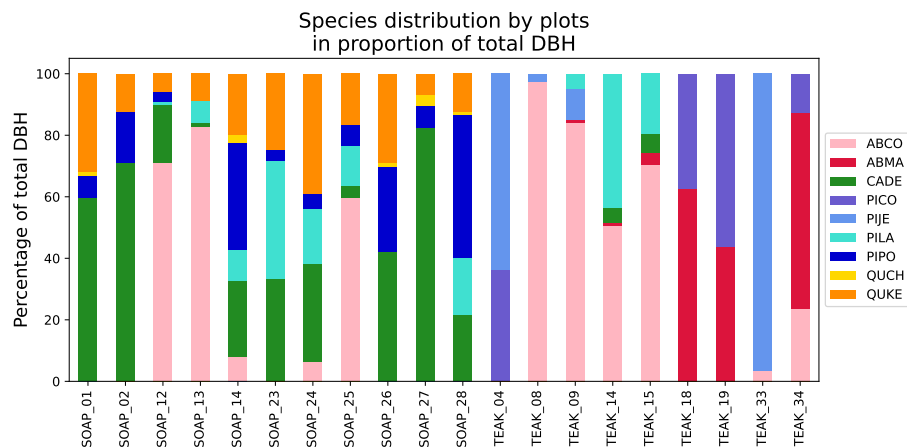


Figure A.5: Species distribution for each plot in proportion of total DBH.

All measurements are tree-scaled metrics, but it is possible to derive plot-scaled metrics by averaging all tree-scaled metrics from one plot. Averages can be computed considering each tree or stem equally or by weighting tree-scaled metrics with DBH. Since DBH is a good proxy for the total biomass of a tree, DBH-weighted averages provide information taking account for the size of each tree and should better match with what a spaceborne sensor can see.

Statistics the Global Health index emphasize gaps between the health status of all the plots (Figure A.6). The part of trees in decline (index of 6 or higher) is not the same for all plots. Some plots seem stable with few decaying trees compensated by natural renewal such as SOAP_24 and TEAK_04. For other plots, the high level of decaying trees jeopardizes the forest's future (TEAK_09 and TEAK_18).

More particularly, the mortality rate (index of 10) is included in these data. Figure A.6 shows directly this mortality rate in dark red.

From the data analysis, we are able to select five plot-scaled metrics (or indices). First, there are health indices which take account of all the trees and their health status. These indices are respectively derived from global health index, chlorosis index and defoliation index by computing the DBH-weighted averages:

- Plot global index

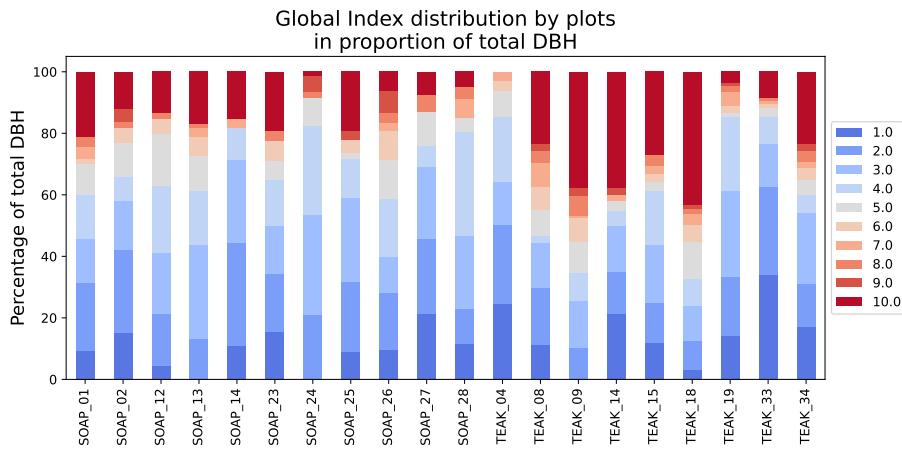


Figure A.6: Global Health index distribution by plots in proportion of total DBH.

- Plot chlorosis index
- Plot defoliation index

Secondly, there are two mortality indices:

- Plot stem mortality: number of dead trees (10 as global index) on the plot
- Plot biomass mortality: sum of DBH of all dead trees (10 as global index)

A.4 Remote sensing data

PRISMA is an experimental satellite from ASI (Italian spatial agency). Its payload is an imaging spectrometer (30 m GSD and 30 km swath). Vegetation traits can be estimated from PRISMA hyperspectral data.

PRISMA pre-feasibility service¹ on May 30th 2022, forecasted 12 overflights of SOAP and TEAK sites by the PRISMA satellite during June and July 2022. For each overflight, an acquisition was requested from the PRISMA web application. Two acquisitions succeeded in June at the same time as fieldwork (RGB images shown in Figure A.7).

Acquisition from 2022-06-11 on SOAP shows good quality, without any clouds over the area.

Acquisition from 2022-06-23 on TEAK is less reliable. The weather over the TEAK area was cloudy that day. The image contains several clouds, including clouds over some sampled plots.

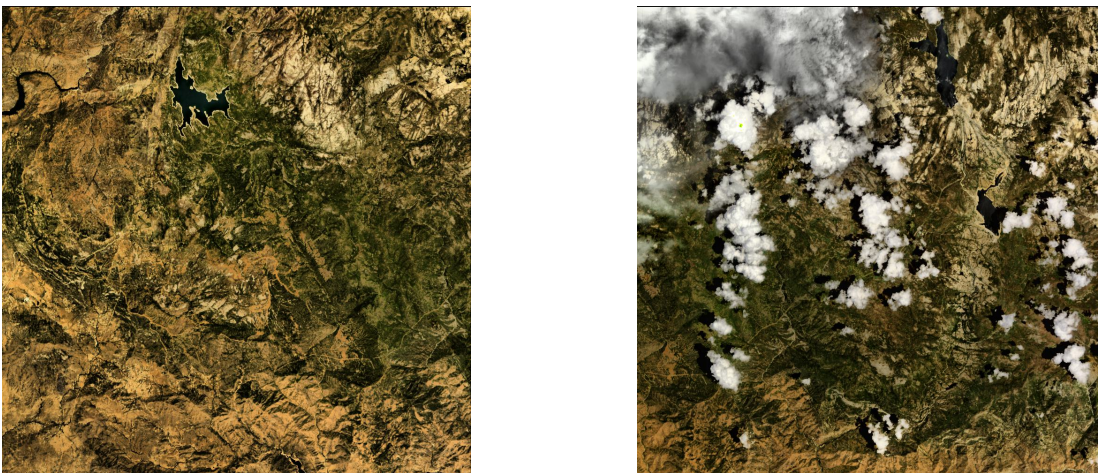


Figure A.7: PRISMA images (RGB extraction) acquired over Soaproot Saddle on 2022-06-11 (left) and Teakettle Experimental Range on 2022-06-23 (right).

Processing of PRISMA images includes their geo-referencing and extraction of pixels matching the plots' locations. PRISMA images already include a geo-referencing when downloaded from the

¹<http://prisma-prefeasibility.asi.it/>

PRISMA server, but a visual quality check showed that this geo-referencing is not reliable. They show shifts that are up to 6 pixels (180 m). Therefore, the first processing step was to perform a new registration for both PRISMA images. Gefolki (Brigot et al. 2016) algorithm performed a reliable geo-referencing. Reference images are RGB images from Maxar Technology, extracted from Google Earth service and resampled at a 30 m GSD. Coordinate reference system of the reference images is EPSG:32611 (UTM 11N). The reference band used for geo-referencing is Band 30 of the PRISMA VNIR sensor, at 641 nm. After registration, the second step is to extract data from pixels with ground truth. The ground sampling distance of the PRISMA sensor is 30 m, therefore during processing one pixel was extracted for each plot. Geographic position of plots' centroids defines the list of pixels to extract. Pixels of interest are extracted from the hyperspectral datacubes with rasterio python library. Figure A.8 illustrates the location of extracted pixels on correctly georeferenced images. Figure A.9 illustrates the reflectance data from all extracted pixels.

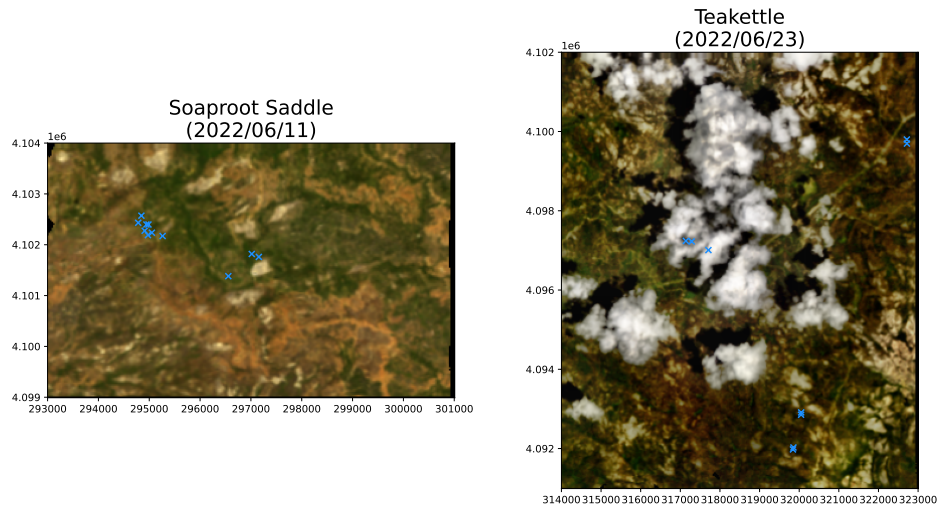


Figure A.8: RGB representation of PRISMA images correctly georeferenced for the SOAP (*left*) and TEAK (*right*). Each cross shows the location of a plot and the extracted pixels (coordinates given in meters in the UTM 11N system (EPSG 32611)).

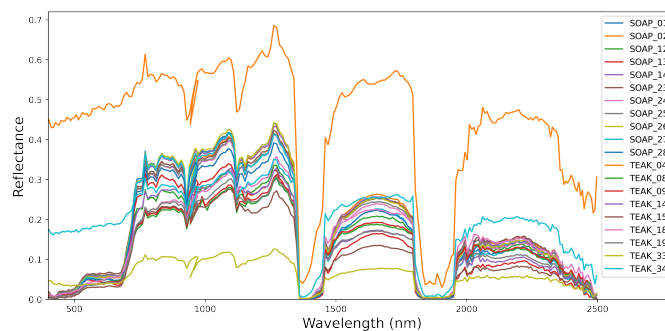


Figure A.9: Reflectance spectra extracted from PRISMA images (one spectrum for each plot).

It is important to notice that the PRISMA sensor acquired the image over TEAK while the sky was cloudy. For three plots, the extracted pixels are reflectance of cloudy atmosphere and will be rejected for the following steps of the study. These three spectra are noticeable on Figure A.9 (plot TEAK_04, TEAK_33, TEAK_34 respectively in orange, green and light blue).

Appendix B

Leaf scale estimation for needle-leaf species

The measurement protocol from Mesarch et al. 1999 provide two equation to derive the true reflectance ρ and transmittance τ of needle-leaves from the measured reflectance ρ_{meas} and transmittance τ_{meas} . The computation ρ and τ correct the effect of the gap fraction f_g between needle-leaves. The computation of τ take also into account the reflectance of the integrating sphere surface ρ_w . The computation of ρ and τ are respectively given by equations B.1 and B.2.

$$\rho = \frac{\rho_{meas}}{(1 - f_g)} \quad (B.1)$$

$$\tau = \frac{\tau_{meas} - \rho_w f_g}{(1 - f_g)} \quad (B.2)$$

Equations B.1 and B.2 can be reversed to assess the impact of the gap fraction on the apparent reflectance ρ_{meas} and transmittance τ_{meas} . These effects are shown in Figure B.1. Globally, when the gap fraction increase, ρ_{meas} increase while τ_{meas} decrease, possibly below zero.

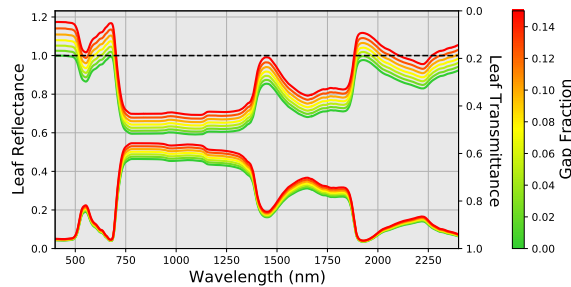


Figure B.1: Influence of gap fraction on measured reflectance ρ_{meas} (lower lines) and transmittance τ_{meas} (upper lines) following equations from Mesarch et al. 1999

Tables B.1, B.2, B.3 and B.4 and Figures B.2, B.3, B.4 and B.5 provides the results of leaf traits estimation on the needles-leaf species at the leaf scale.

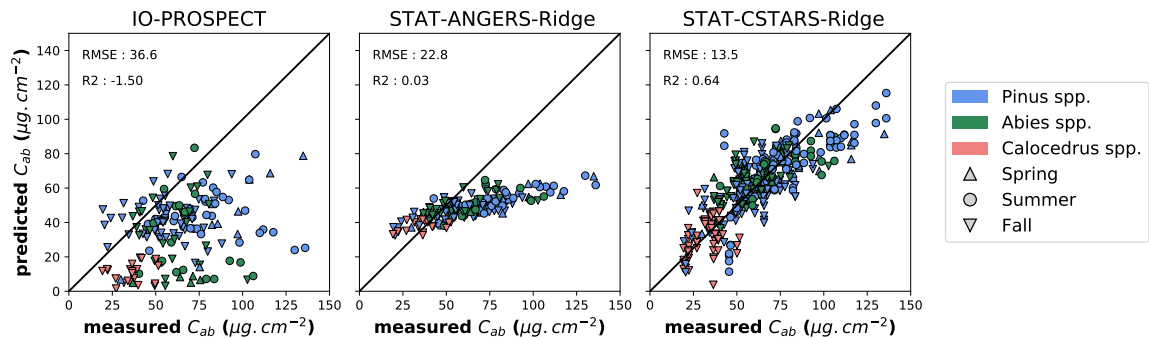


Figure B.2: Validation plots for C_{ab} for the methods highlighted in Table B.1

Table B.1: Performance of methods for the estimation of C_{ab} (in each subcategory, the most accurate method is highlighted in bold).

Category	Method	RMSE $\mu\text{g.cm}^{-2}$	R ² -	Bias $\mu\text{g.cm}^{-2}$
Physical	IO-PROSPECT	36.6	-1.50	-26.8
	STAT-ANGERS-Ridge	22.8	0.03	-14.1
	STAT-ANGERS-PLSR	24.3	-0.10	-16.6
	STAT-ANGERS-GPR	27.5	-0.41	-21.2
Statistical	STAT-ANGERS-RFR	30.3	-0.71	-13.1
	STAT-CSTARS-Ridge	13.4	0.64	-0.1
	STAT-CSTARS-PLSR	14.0	0.61	-0.2
	STAT-CSTARS-GPR	13.6	0.63	0.4
	STAT-CSTARS-RFR	17.0	0.42	0.5

Table B.2: Performance of methods for the estimation of C_{xc} (in each subcategory, the most accurate method is highlighted in bold).

Category	Method	RMSE $\mu\text{g.cm}^{-2}$	R ² -	Bias $\mu\text{g.cm}^{-2}$
Physical	IO-PROSPECT	14.0	-6.99	-12.5
	STAT-ANGERS-Ridge	5.6	-0.30	-2.7
	STAT-ANGERS-PLSR	5.4	-0.18	-2.0
	STAT-ANGERS-GPR	7.5	-1.28	-5.7
Statistical	STAT-ANGERS-RFR	8.0	-1.63	-5.6
	STAT-CSTARS-Ridge	3.1	0.58	0.0
	STAT-CSTARS-PLSR	3.2	0.54	-0.1
	STAT-CSTARS-GPR	3.4	0.48	0.0
	STAT-CSTARS-RFR	3.6	0.42	0.1

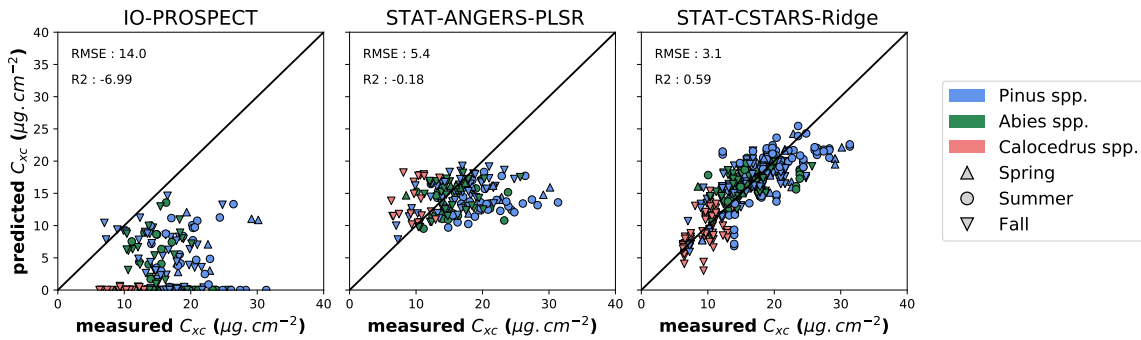


Figure B.3: Validation plots for C_{xc} for the methods highlighted in Table B.2

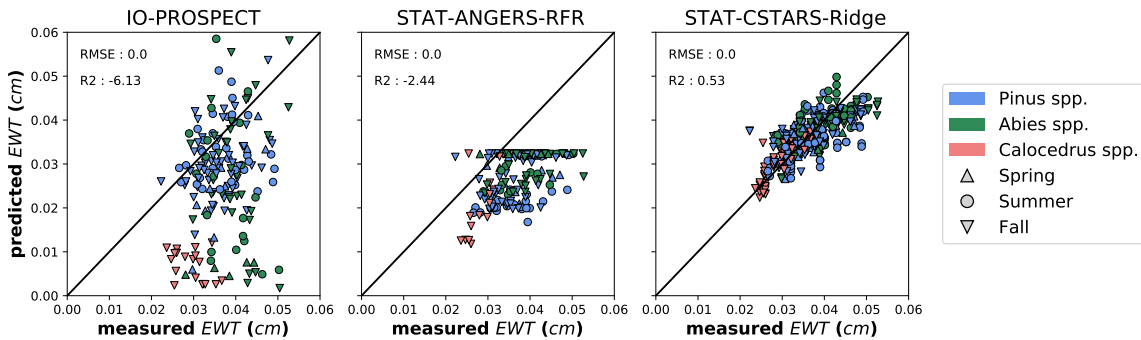


Figure B.4: Validation plots for EWT for the methods highlighted in Table B.3

Table B.3: Performance of methods for the estimation of EWT (in each subcategory, the most accurate method is highlighted in bold).

Category	Method	RMSE <i>cm</i>	R ² -	Bias <i>cm</i>
Physical	IO-PROSPECT	0.0165	-6.13	-0.0105
Statistical	STAT-ANGERS-Ridge	0.0158	-5.49	-0.0147
	STAT-ANGERS-PLSR	0.0155	-5.25	-0.0144
	STAT-ANGERS-GPR	0.0138	-3.96	-0.0129
	STAT-ANGERS-RFR	0.0115	-2.44	-0.0098
	STAT-CSTARS-Ridge	0.0042	0.52	-0.0004
	STAT-CSTARS-PLSR	0.0043	0.48	-0.0005
	STAT-CSTARS-GPR	0.0043	0.50	-0.0005
	STAT-CSTARS-RFR	0.0047	0.41	-0.0006

Table B.4: Performance of methods for the estimation of LMA (in each subcategory, the most accurate method is highlighted in bold).

Category	Method	RMSE <i>g.cm⁻²</i>	R ² -	Bias <i>g.cm⁻²</i>
Physical	IO-PROSPECT	0.0222	-13.61	0.0097
Statistical	STAT-ANGERS-Ridge	0.0133	-4.26	-0.0118
	STAT-ANGERS-PLSR	0.0134	-4.35	-0.0119
	STAT-ANGERS-GPR	0.0195	-10.24	-0.0166
	STAT-ANGERS-RFR	0.0149	-5.59	-0.0123
	STAT-CSTARS-Ridge	0.0044	0.46	-0.0002
	STAT-CSTARS-PLSR	0.0045	0.41	-0.0002
	STAT-CSTARS-GPR	0.0043	0.46	0.0000
	STAT-CSTARS-RFR	0.0055	0.14	-0.0002

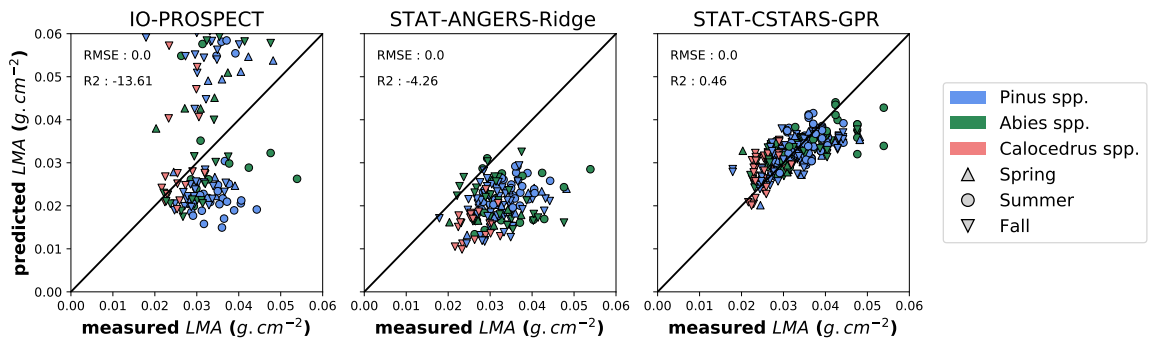


Figure B.5: Validation plots for LMA for the methods highlighted in Table B.4

Bibliography

- Akiba, Takuya et al. (2019). "Optuna: A Next-generation Hyperparameter Optimization Framework". In: *Proceedings of the 25th ACM SIGKDD International Conference on Knowledge Discovery & Data Mining*. KDD '19. New York, NY, USA: Association for Computing Machinery, pp. 2623–2631. DOI: [10.1145/3292500.3330701](https://doi.org/10.1145/3292500.3330701) (cit. on p. 128).
- Ali, Abebe Mohammed et al. (2016). "Effects of Canopy Structural Variables on Retrieval of Leaf Dry Matter Content and Specific Leaf Area From Remotely Sensed Data". In: *IEEE Journal of Selected Topics in Applied Earth Observations and Remote Sensing* 9.2. Number: 2 Conference Name: IEEE Journal of Selected Topics in Applied Earth Observations and Remote Sensing, pp. 898–909. DOI: [10.1109/JSTARS.2015.2450762](https://doi.org/10.1109/JSTARS.2015.2450762) (cit. on pp. 138, 140, 141).
- Allen, W. A. et al. (1970). "Mean Effective Optical Constants of Thirteen Kinds of Plant Leaves". EN. In: *Applied Optics* 9.11. Number: 11 Publisher: Optical Society of America, pp. 2573–2577. DOI: [10.1364/AO.9.002573](https://doi.org/10.1364/AO.9.002573) (cit. on pp. 32–34).
- Allen, William A. et al. (1969). "Interaction of Isotropic Light with a Compact Plant Leaf". EN. In: *JOSA* 59.10. Number: 10 Publisher: Optical Society of America, pp. 1376–1379. DOI: [10.1364/JOSA.59.001376](https://doi.org/10.1364/JOSA.59.001376) (cit. on p. 33).
- Annala, Leevi et al. (2020). "Chlorophyll Concentration Retrieval by Training Convolutional Neural Network for Stochastic Model of Leaf Optical Properties (SLOP) Inversion". en. In: *Remote Sensing* 12.2. Number: 2 Publisher: Multidisciplinary Digital Publishing Institute, p. 283. DOI: [10.3390/rs12020283](https://doi.org/10.3390/rs12020283) (cit. on pp. 56, 137).
- Arno, Stephen F. (1973). *Discovering Sierra Trees*. en. Google-Books-ID: DDTm1_9Pdy8C. Yosemite Natural History Association (cit. on p. 64).
- Atzberger, Clement (2000). "Development of an invertible forest reflectance model: The INFOR-model". In: *A decade of trans-european remote sensing cooperation. Proceedings of the 20th EARSeL Symposium Dresden, Germany*. Vol. 14. Issue: 16, pp. 39–44 (cit. on p. 35).
- Baranoski, Gladimir Valerio Guimarães and Jon Rokne (2004). *Light Interaction with Plants: A Computer Graphics Perspective*. en. Horwood Pub. (cit. on p. 33).
- Baret, Frédéric and Samuel Buis (2008). "Estimating Canopy Characteristics from Remote Sensing Observations: Review of Methods and Associated Problems". en. In: *Advances in Land Remote Sensing: System, Modeling, Inversion and Application*. Ed. by Shunlin Liang. Dordrecht: Springer Netherlands, pp. 173–201. DOI: [10.1007/978-1-4020-6450-0_7](https://doi.org/10.1007/978-1-4020-6450-0_7) (cit. on pp. 22, 28, 51–53).
- Barton, C. V. M and P. R. J North (2001). "Remote sensing of canopy light use efficiency using the photochemical reflectance index: Model and sensitivity analysis". In: *Remote Sensing of Environment* 78.3, pp. 264–273. DOI: [10.1016/S0034-4257\(01\)00224-3](https://doi.org/10.1016/S0034-4257(01)00224-3) (cit. on p. 140).
- Baudin, Michaël et al. (2017). "OpenTURNS: An Industrial Software for Uncertainty Quantification in Simulation". en. In: *Handbook of Uncertainty Quantification*. Ed. by Roger Ghanem et al. Cham: Springer International Publishing, pp. 2001–2038. DOI: [10.1007/978-3-319-12385-1_64](https://doi.org/10.1007/978-3-319-12385-1_64) (cit. on pp. 43, 53).
- Berger, Katja et al. (2018). "Evaluation of the PROSAIL Model Capabilities for Future Hyperspectral Model Environments: A Review Study". en. In: *Remote Sensing* 10.1. Number: 1 Publisher: Multidisciplinary Digital Publishing Institute, p. 85. DOI: [10.3390/rs10010085](https://doi.org/10.3390/rs10010085) (cit. on p. 36).
- Bergstra, James et al. (2011). "Algorithms for Hyper-Parameter Optimization". In: *Advances in Neural Information Processing Systems*. Vol. 24. Curran Associates, Inc. (cit. on p. 128).
- Bioucas-Dias, Jose M. et al. (2013). "Hyperspectral Remote Sensing Data Analysis and Future Challenges". In: *IEEE Geoscience and Remote Sensing Magazine* 1.2. Number: 2 Conference Name: IEEE Geoscience and Remote Sensing Magazine, pp. 6–36. DOI: [10.1109/MGRS.2013.2244672](https://doi.org/10.1109/MGRS.2013.2244672) (cit. on pp. 22, 27, 28, 51, 52).
- Blackburn, George Alan (2002). "Remote sensing of forest pigments using airborne imaging spectrometer and LIDAR imagery". In: *Remote Sensing of Environment* 82.2, pp. 311–321. DOI: [10.1016/S0034-4257\(02\)00049-4](https://doi.org/10.1016/S0034-4257(02)00049-4) (cit. on p. 138).
- Blodgett Forest Research Station (2023). en (cit. on p. 65).

- Boardman, Joseph W. (2014). *Precision Geocoding of Low-Altitude AVIRIS Data* (cit. on p. 139).
- Breiman, Leo (2001). "Random Forests". en. In: *Machine Learning* 45.1. Number: 1, pp. 5–32. DOI: [10.1023/A:1010933404324](https://doi.org/10.1023/A:1010933404324) (cit. on p. 55).
- Brigot, Guillaume et al. (2016). "Adaptation and Evaluation of an Optical Flow Method Applied to Coregistration of Forest Remote Sensing Images". In: *IEEE Journal of Selected Topics in Applied Earth Observations and Remote Sensing* 9.7. Conference Name: IEEE Journal of Selected Topics in Applied Earth Observations and Remote Sensing, pp. 2923–2939. DOI: [10.1109/JSTARS.2016.2578362](https://doi.org/10.1109/JSTARS.2016.2578362) (cit. on pp. 71, 157).
- Brondizio, E. S. et al. (2019). *IPBES (2019): Global assessment report on biodiversity and ecosystem services of the Intergovernmental Science-Policy Platform on Biodiversity and Ecosystem Services*. Bonn, Germany: IPBES secretariat (cit. on pp. 19, 20, 25).
- Campbell, G. S. (1986). "Extinction coefficients for radiation in plant canopies calculated using an ellipsoidal inclination angle distribution". en. In: *Agricultural and Forest Meteorology* 36.4. Number: 4, pp. 317–321. DOI: [10.1016/0168-1923\(86\)90010-9](https://doi.org/10.1016/0168-1923(86)90010-9) (cit. on p. 35).
- Chadwick, K. Dana and Gregory P. Asner (2016). "Organismic-Scale Remote Sensing of Canopy Foliar Traits in Lowland Tropical Forests". en. In: *Remote Sensing* 8.2. Number: 2 Publisher: Multidisciplinary Digital Publishing Institute, p. 87. DOI: [10.3390/rs8020087](https://doi.org/10.3390/rs8020087) (cit. on p. 138).
- Cheng, Yen-Ben et al. (2006). "Estimating vegetation water content with hyperspectral data for different canopy scenarios: Relationships between AVIRIS and MODIS indexes". In: *Remote Sensing of Environment* 105.4, pp. 354–366. DOI: [10.1016/j.rse.2006.07.005](https://doi.org/10.1016/j.rse.2006.07.005) (cit. on p. 140).
- Cherif, Eya et al. (2023). "From spectra to plant functional traits: Transferable multi-trait models from heterogeneous and sparse data". In: *Remote Sensing of Environment* 292, p. 113580. DOI: [10.1016/j.rse.2023.113580](https://doi.org/10.1016/j.rse.2023.113580) (cit. on pp. 56, 127, 138).
- Cogliati, S. et al. (2021). "The PRISMA imaging spectroscopy mission: overview and first performance analysis". en. In: *Remote Sensing of Environment* 262, p. 112499. DOI: [10.1016/j.rse.2021.112499](https://doi.org/10.1016/j.rse.2021.112499) (cit. on pp. 22, 27).
- Curran, Paul J (1989). "Remote sensing of foliar chemistry". en. In: *Remote Sensing of Environment* 30.3. Number: 3, pp. 271–278. DOI: [10.1016/0034-4257\(89\)90069-2](https://doi.org/10.1016/0034-4257(89)90069-2) (cit. on pp. 21, 145, 150).
- Curtis, Philip G. et al. (2018). "Classifying drivers of global forest loss". In: *Science* 361.6407. Number: 6407 Publisher: American Association for the Advancement of Science, pp. 1108–1111. DOI: [10.1126/science.aau3445](https://doi.org/10.1126/science.aau3445) (cit. on pp. 20, 26).
- Dawson, Terence P. et al. (1998). "LIBERTY—Modeling the Effects of Leaf Biochemical Concentration on Reflectance Spectra". en. In: *Remote Sensing of Environment* 65.1. Number: 1, pp. 50–60. DOI: [10.1016/S0034-4257\(98\)00007-8](https://doi.org/10.1016/S0034-4257(98)00007-8) (cit. on p. 33).
- Demmig-Adams, Barbara and William W. Adams (1996). "The role of xanthophyll cycle carotenoids in the protection of photosynthesis". en. In: *Trends in Plant Science* 1.1. Number: 1, pp. 21–26. DOI: [10.1016/S1360-1385\(96\)80019-7](https://doi.org/10.1016/S1360-1385(96)80019-7) (cit. on pp. 21, 27).
- Domenzain, Luis Mario et al. (2019). *jgomezdans/prosail: Pip package*. DOI: [10.5281/zenodo.2574925](https://doi.org/10.5281/zenodo.2574925) (cit. on p. 37).
- Dufour-Kowalski, Samuel et al. (2012). "Copsis: an open software framework and community for forest growth modelling". en. In: *Annals of Forest Science* 69.2, pp. 221–233. DOI: [10.1007/s13595-011-0140-9](https://doi.org/10.1007/s13595-011-0140-9) (cit. on pp. 145, 149).
- Earth, One (2023a). *California Interior Chaparral and Woodlands*. en (cit. on p. 64).
- (2023b). *Sierra Nevada Forests*. en (cit. on p. 64).
- Eloy, Christophe et al. (2017). "Wind loads and competition for light sculpt trees into self-similar structures". en. In: *Nature Communications* 8.1. Bandiera_abtest: a Cc_license_type: cc_by Cg_type: Nature Research Journals Number: 1 Primary_atype: Research Publisher: Nature Publishing Group Subject_term: Computational models;Plant ecology;Plant evolution Subject_term_id: computational-models;plant-ecology;plant-evolution, p. 1014. DOI: [10.1038/s41467-017-00995-6](https://doi.org/10.1038/s41467-017-00995-6) (cit. on pp. 145, 149).
- FAO (2020). *Global Forest Resources Assessment 2020: Main report*. en. Rome, Italy: FAO. DOI: [10.4060/ca9825en](https://doi.org/10.4060/ca9825en) (cit. on pp. 19, 25).
- FAO (2020). *Global Forest Resources Assessment 2020: Terms and definitions*. Tech. rep. Rome, Italy: FAO (cit. on pp. 19, 25).
- Feilhauer, Hannes et al. (2010). "Brightness-normalized Partial Least Squares Regression for hyperspectral data". In: *Journal of Quantitative Spectroscopy and Radiative Transfer* 111.12, pp. 1947–1957. DOI: [10.1016/j.jqsrt.2010.03.007](https://doi.org/10.1016/j.jqsrt.2010.03.007) (cit. on p. 139).
- Firinguetti, Luis et al. (2017). "Study of partial least squares and ridge regression methods". In: *Communications in Statistics - Simulation and Computation* 46.8. Number: 8 Publisher: Taylor & Francis _eprint: <https://doi.org/10.1080/03610918.2016.1210168>, pp. 6631–6644. DOI: [10.1080/03610918.2016.1210168](https://doi.org/10.1080/03610918.2016.1210168) (cit. on p. 137).

- Féret, J. B. et al. (2008). "PROSPECT-4 and 5: Advances in the leaf optical properties model separating photosynthetic pigments". en. In: *Remote Sensing of Environment* 112.6. Number: 6, pp. 3030–3043. DOI: [10.1016/j.rse.2008.02.012](https://doi.org/10.1016/j.rse.2008.02.012) (cit. on p. 35).
- Féret, J. B. et al. (2017). "PROSPECT-D: Towards modeling leaf optical properties through a complete lifecycle". en. In: *Remote Sensing of Environment* 193, pp. 204–215. DOI: [10.1016/j.rse.2017.03.004](https://doi.org/10.1016/j.rse.2017.03.004) (cit. on pp. 35, 77).
- Féret, J. B. et al. (2019). "Estimating leaf mass per area and equivalent water thickness based on leaf optical properties: Potential and limitations of physical modeling and machine learning". en. In: *Remote Sensing of Environment* 231, p. 110959. DOI: [10.1016/j.rse.2018.11.002](https://doi.org/10.1016/j.rse.2018.11.002) (cit. on pp. 52, 53, 77, 113).
- Féret, Jean-Baptiste et al. (2011). "Optimizing spectral indices and chemometric analysis of leaf chemical properties using radiative transfer modeling". en. In: *Remote Sensing of Environment* 115.10. Number: 10, pp. 2742–2750. DOI: [10.1016/j.rse.2011.06.016](https://doi.org/10.1016/j.rse.2011.06.016) (cit. on pp. 52, 53).
- Féret, Jean-Baptiste et al. (2021). "PROSPECT-PRO for estimating content of nitrogen-containing leaf proteins and other carbon-based constituents". en. In: *Remote Sensing of Environment* 252, p. 112173. DOI: [10.1016/j.rse.2020.112173](https://doi.org/10.1016/j.rse.2020.112173) (cit. on pp. 21, 27, 35, 145, 150).
- Gallery, William et al. (n.d.). "NEON ALGORITHM-THEORETICAL BASIS DOCUMENT: NEON IMAGING SPECTROMETER (NIS) LEVEL 1B CALIBRATED RADIANCE". en. In: () (cit. on p. 72).
- Gamon, J. A. et al. (2019). "Assessing Vegetation Function with Imaging Spectroscopy". en. In: *Surveys in Geophysics* 40.3. Number: 3, pp. 489–513. DOI: [10.1007/s10712-019-09511-5](https://doi.org/10.1007/s10712-019-09511-5) (cit. on pp. 23, 28).
- Gao, Bo-Cai et al. (1993). "Derivation of scaled surface reflectances from AVIRIS data". en. In: *Remote Sensing of Environment. Airbone Imaging Spectrometry* 44.2. Number: 2, pp. 165–178. DOI: [10.1016/0034-4257\(93\)90014-0](https://doi.org/10.1016/0034-4257(93)90014-0) (cit. on p. 71).
- Gao, Lin et al. (2022). "Hyperspectral response of agronomic variables to background optical variability: Results of a numerical experiment". In: *Agricultural and Forest Meteorology* 326, p. 109178. DOI: [10.1016/j.agrformet.2022.109178](https://doi.org/10.1016/j.agrformet.2022.109178) (cit. on p. 140).
- Gascon, F. et al. (2004). "Retrieval of forest biophysical variables by inverting a 3-D radiative transfer model and using high and very high resolution imagery". In: *International Journal of Remote Sensing* 25.24. Number: 24 Publisher: Taylor & Francis, pp. 5601–5616. DOI: [10.1080/01431160412331291305](https://doi.org/10.1080/01431160412331291305) (cit. on pp. 38, 39).
- Gastellu-Etchegorry, J. P. et al. (1996). "Modeling radiative transfer in heterogeneous 3-D vegetation canopies". en. In: *Remote Sensing of Environment* 58.2. Number: 2, pp. 131–156. DOI: [10.1016/0034-4257\(95\)00253-7](https://doi.org/10.1016/0034-4257(95)00253-7) (cit. on pp. 33, 35, 36).
- Gastellu-Etchegorry, J. P. et al. (2003). "An interpolation procedure for generalizing a look-up table inversion method". en. In: *Remote Sensing of Environment* 87.1. Number: 1, pp. 55–71. DOI: [10.1016/S0034-4257\(03\)00146-9](https://doi.org/10.1016/S0034-4257(03)00146-9) (cit. on p. 38).
- Gaubert, Thierry et al. (2024). "Estimation of Oak Leaf Functional Traits for California Woodland Savannas and Mixed Forests: Comparison between Statistical, Physical, and Hybrid Methods Using Spectroscopy". en. In: *Remote Sensing* 16.1. Number: 1 Publisher: Multidisciplinary Digital Publishing Institute, p. 29. DOI: [10.3390/rs16010029](https://doi.org/10.3390/rs16010029) (cit. on pp. 77, 113).
- GEO BON (n.d.). en-US (cit. on pp. 20, 26).
- Goel, Narendra S. (1988). "Models of vegetation canopy reflectance and their use in estimation of biophysical parameters from reflectance data". In: *Remote Sensing Reviews* 4.1. Publisher: Taylor & Francis _eprint: <https://doi.org/10.1080/02757258809532105>, pp. 1–212. DOI: [10.1080/02757258809532105](https://doi.org/10.1080/02757258809532105) (cit. on p. 140).
- Goodfellow, Ian et al. (2016). *Deep Learning*. en. Google-Books-ID: omivDQAAQBAJ. MIT Press (cit. on pp. 55, 56).
- Govaerts, Y.M. and M.M. Verstraete (1998). "Raytran: a Monte Carlo ray-tracing model to compute light scattering in three-dimensional heterogeneous media". In: *IEEE Transactions on Geoscience and Remote Sensing* 36.2. Conference Name: IEEE Transactions on Geoscience and Remote Sensing, pp. 493–505. DOI: [10.1109/36.662732](https://doi.org/10.1109/36.662732) (cit. on pp. 33, 34, 36).
- Green, Robert O et al. (1998). "Imaging Spectroscopy and the Airborne Visible/Infrared Imaging Spectrometer (AVIRIS)". en. In: *Remote Sensing of Environment* 65.3. Number: 3, pp. 227–248. DOI: [10.1016/S0034-4257\(98\)00064-9](https://doi.org/10.1016/S0034-4257(98)00064-9) (cit. on pp. 22, 27, 64, 70).
- Green, Robert O. et al. (2020). "The Earth Surface Mineral Source Investigation: An Earth Science Imaging Spectroscopy Mission". In: *2020 IEEE Aerospace Conference*. ISSN: 1095-323X, pp. 1–15. DOI: [10.1109/AERO47225.2020.9172731](https://doi.org/10.1109/AERO47225.2020.9172731) (cit. on pp. 22, 27).
- Green, Robert O. et al. (2022). "Surface Biology and Geology (SBG) Visible to Short Wavelength Infrared (VSWIR) Wide Swath Instrument Concept". In: *2022 IEEE Aerospace Conference (AERO)*.

- ISSN: 1095-323X, pp. 1–10. DOI: [10.1109/AERO53065.2022.9843676](https://doi.org/10.1109/AERO53065.2022.9843676) (cit. on pp. 22, 27, 144, 145, 148–150).
- Guanter, Luis et al. (2015). “The EnMAP Spaceborne Imaging Spectroscopy Mission for Earth Observation”. en. In: *Remote Sensing* 7.7. Number: 7 Publisher: Multidisciplinary Digital Publishing Institute, pp. 8830–8857. DOI: [10.3390/rs70708830](https://doi.org/10.3390/rs70708830) (cit. on pp. 22, 27).
- Guidici, Daniel and Matthew L. Clark (2017). “One-Dimensional Convolutional Neural Network Land-Cover Classification of Multi-Seasonal Hyperspectral Imagery in the San Francisco Bay Area, California”. en. In: *Remote Sensing* 9.6. Number: 6 Publisher: Multidisciplinary Digital Publishing Institute, p. 629. DOI: [10.3390/rs9060629](https://doi.org/10.3390/rs9060629) (cit. on p. 137).
- Hapke, Bruce (2012). *Theory of Reflectance and Emittance Spectroscopy*. en. Cambridge University Press (cit. on p. 31).
- Harron, JW (2000). “Optical properties of phytoelements in conifers.” Master of Science. North York, Ontario, Canada: York University (cit. on pp. 114, 144, 148).
- Hartmann, Henrik et al. (2022). “Climate Change Risks to Global Forest Health: Emergence of Unexpected Events of Elevated Tree Mortality Worldwide”. In: *Annual Review of Plant Biology* 73.1. Number: 1_eprint: <https://doi.org/10.1146/annurev-arplant-102820-012804>, pp. 673–702. DOI: [10.1146/annurev-arplant-102820-012804](https://doi.org/10.1146/annurev-arplant-102820-012804) (cit. on pp. 20, 26).
- Hastie, Trevor et al. (2009). *Elements of Statistical Learning*. en (cit. on pp. 52, 56).
- Hawksworth, Frank G (1977). *The 6-class dwarf mistletoe rating system*. Vol. 48. Rocky Mountain Forest and Range Experiment Station, Forest Service, US ... (cit. on p. 154).
- Hill, Joachim et al. (2019). “Imaging Spectroscopy of Forest Ecosystems: Perspectives for the Use of Space-borne Hyperspectral Earth Observation Systems”. en. In: *Surveys in Geophysics* 40.3. Number: 3, pp. 553–588. DOI: [10.1007/s10712-019-09514-2](https://doi.org/10.1007/s10712-019-09514-2) (cit. on pp. 22, 28).
- Hoepfner, J. Malin et al. (2020). “Mapping Canopy Chlorophyll Content in a Temperate Forest Using Airborne Hyperspectral Data”. en. In: *Remote Sensing* 12.21. Number: 21 Publisher: Multidisciplinary Digital Publishing Institute, p. 3573. DOI: [10.3390/rs12213573](https://doi.org/10.3390/rs12213573) (cit. on pp. 139, 141).
- Homolová, Lucie et al. (2013). “Review of optical-based remote sensing for plant trait mapping”. en. In: *Ecological Complexity* 15, pp. 1–16. DOI: [10.1016/j.ecocom.2013.06.003](https://doi.org/10.1016/j.ecocom.2013.06.003) (cit. on pp. 23, 28).
- Hornik, Kurt et al. (1989). “Multilayer feedforward networks are universal approximators”. en. In: *Neural Networks* 2.5. Number: 5, pp. 359–366. DOI: [10.1016/0893-6080\(89\)90020-8](https://doi.org/10.1016/0893-6080(89)90020-8) (cit. on p. 55).
- Huemmrich, K. F. (2001). “The GeoSail model: a simple addition to the SAIL model to describe discontinuous canopy reflectance”. en. In: *Remote Sensing of Environment* 75.3. Number: 3, pp. 423–431. DOI: [10.1016/S0034-4257\(00\)00184-X](https://doi.org/10.1016/S0034-4257(00)00184-X) (cit. on p. 35).
- Jacquemoud, S. and F. Baret (1990). “PROSPECT: A model of leaf optical properties spectra”. en. In: *Remote Sensing of Environment* 34.2. Number: 2, pp. 75–91. DOI: [10.1016/0034-4257\(90\)90100-Z](https://doi.org/10.1016/0034-4257(90)90100-Z) (cit. on pp. 33–35).
- Jacquemoud, S. et al. (1996). “Estimating leaf biochemistry using the PROSPECT leaf optical properties model”. en. In: *Remote Sensing of Environment* 56.3. Number: 3, pp. 194–202. DOI: [10.1016/0034-4257\(95\)00238-3](https://doi.org/10.1016/0034-4257(95)00238-3) (cit. on p. 34).
- Jacquemoud, Stéphane and Susan Ustin (2019). *Leaf Optical Properties*. Cambridge University Press. DOI: [10.1017/9781108686457](https://doi.org/10.1017/9781108686457) (cit. on pp. 33, 34).
- Jacquemoud, Stéphane et al. (2009). “PROSPECT+SAIL models: A review of use for vegetation characterization”. en. In: *Remote Sensing of Environment*. Imaging Spectroscopy Special Issue 113, S56–S66. DOI: [10.1016/j.rse.2008.01.026](https://doi.org/10.1016/j.rse.2008.01.026) (cit. on p. 36).
- Jensen, Henrik (2021). “BRIDGING THE GAP: ANALYZING RIDGE REGRESSION VS. PLS REGRESSION”. en. In: *Top Academic Journal of Engineering and Mathematics* 6.3. Number: 3, pp. 1–23 (cit. on p. 137).
- Kattenborn, Teja et al. (2021). “Review on Convolutional Neural Networks (CNN) in vegetation remote sensing”. In: *ISPRS Journal of Photogrammetry and Remote Sensing* 173, pp. 24–49. DOI: [10.1016/j.isprsjprs.2020.12.010](https://doi.org/10.1016/j.isprsjprs.2020.12.010) (cit. on p. 55).
- Kawamura, Kensuke et al. (2021). “Using a One-Dimensional Convolutional Neural Network on Visible and Near-Infrared Spectroscopy to Improve Soil Phosphorus Prediction in Madagascar”. en. In: *Remote Sensing* 13.8. Number: 8 Publisher: Multidisciplinary Digital Publishing Institute, p. 1519. DOI: [10.3390/rs13081519](https://doi.org/10.3390/rs13081519) (cit. on p. 56).
- Kingma, Diederik P and Jimmy Ba (2014). “Adam: A method for stochastic optimization”. In: *arXiv preprint arXiv:1412.6980* (cit. on pp. 128, 137).
- Kubelka, Paul and Franz Munk (1931). “An article on optics of paint layers”. In: *Z. Tech. Phys* 12.593-601, pp. 259–274 (cit. on pp. 32, 33).

- Lausch, Angela et al. (2016). "Understanding Forest Health with Remote Sensing -Part I—A Review of Spectral Traits, Processes and Remote-Sensing Characteristics". en. In: *Remote Sensing* 8.12. Number: 12 Publisher: Multidisciplinary Digital Publishing Institute, p. 1029. DOI: [10.3390/rs8121029](https://doi.org/10.3390/rs8121029) (cit. on pp. 20, 26).
- LeCun, Yann et al. (2010). "Convolutional networks and applications in vision". In: *Proceedings of 2010 IEEE International Symposium on Circuits and Systems*. ISSN: 2158-1525, pp. 253–256. DOI: [10.1109/ISCAS.2010.5537907](https://doi.org/10.1109/ISCAS.2010.5537907) (cit. on p. 55).
- Lee, Christine M. et al. (2015). "An introduction to the NASA Hyperspectral InfraRed Imager (HyspIRI) mission and preparatory activities". en. In: *Remote Sensing of Environment*. Special Issue on the Hyperspectral Infrared Imager (HyspIRI) 167, pp. 6–19. DOI: [10.1016/j.rse.2015.06.012](https://doi.org/10.1016/j.rse.2015.06.012) (cit. on pp. 64, 67).
- Lewis, P. and M. Disney (2007). "Spectral invariants and scattering across multiple scales from within-leaf to canopy". en. In: *Remote Sensing of Environment* 109.2. Number: 2, pp. 196–206. DOI: [10.1016/j.rse.2006.12.015](https://doi.org/10.1016/j.rse.2006.12.015) (cit. on pp. 32, 36).
- Li, Hao et al. (2018). "Visualizing the Loss Landscape of Neural Nets". In: *Advances in Neural Information Processing Systems*. Vol. 31. Curran Associates, Inc. (cit. on p. 129).
- LI-COR (1983). *LI-1800-12 Integrating Sphere Instruction Manual*. Tech. rep. Pub. No. 8305-0034. Issue: Pub. No. 8305-0034. Lincoln, NE: LI-COR, Inc. (cit. on p. 70).
- Liang, Shunlin (2005). *Quantitative Remote Sensing of Land Surfaces*. en. John Wiley & Sons (cit. on p. 32).
- Lichtenthaler, Hartmut K. (1987). "Chlorophylls and carotenoids: Pigments of photosynthetic biomembranes". en. In: *Methods in Enzymology*. Vol. 148. Plant Cell Membranes. Academic Press, pp. 350–382. DOI: [10.1016/0076-6879\(87\)48036-1](https://doi.org/10.1016/0076-6879(87)48036-1) (cit. on p. 69).
- Lillesand, Thomas et al. (2015). *Remote Sensing and Image Interpretation*. en. John Wiley & Sons (cit. on pp. 20, 26).
- LuxCoreRender – Open Source Physically Based Renderer* (n.d.) (cit. on p. 36).
- Ma, Siyan et al. (2016). "Slow ecosystem responses conditionally regulate annual carbon balance over 15 years in Californian oak-grass savanna". In: *Agricultural and Forest Meteorology* 228-229, pp. 252–264. DOI: [10.1016/j.agrformet.2016.07.016](https://doi.org/10.1016/j.agrformet.2016.07.016) (cit. on p. 65).
- Makowski, Miłosz et al. (2019). "Synthetic silviculture: multi-scale modeling of plant ecosystems". In: *ACM Transactions on Graphics* 38.4. Number: 4, 131:1–131:14. DOI: [10.1145/3306346.3323039](https://doi.org/10.1145/3306346.3323039) (cit. on pp. 145, 149).
- Malenovský, Z. et al. (2006). "Applicability of the PROSPECT model for Norway spruce needles". In: *International Journal of Remote Sensing* 27.24. Number: 24 Publisher: Taylor & Francis _eprint: <https://doi.org/10.1080/01431160600762990>, pp. 5315–5340. DOI: [10.1080/01431160600762990](https://doi.org/10.1080/01431160600762990) (cit. on p. 35).
- Malenovský, Zbyněk et al. (2007). "Scaling dimensions in spectroscopy of soil and vegetation". en. In: *International Journal of Applied Earth Observation and Geoinformation*. Advances in airborne electromagnetics and remote sensing of agro-ecosystems 9.2. Number: 2, pp. 137–164. DOI: [10.1016/j.jag.2006.08.003](https://doi.org/10.1016/j.jag.2006.08.003) (cit. on p. 35).
- Malenovský, Zbyněk et al. (2019). "Variability and Uncertainty Challenges in Scaling Imaging Spectroscopy Retrievals and Validations from Leaves Up to Vegetation Canopies". en. In: *Surveys in Geophysics* 40.3. Number: 3, pp. 631–656. DOI: [10.1007/s10712-019-09534-y](https://doi.org/10.1007/s10712-019-09534-y) (cit. on p. 139).
- Mallat, Stephane (1999). *A Wavelet Tour of Signal Processing*. en. Elsevier (cit. on p. 43).
- Martin, M. E. et al. (2008). "A generalizable method for remote sensing of canopy nitrogen across a wide range of forest ecosystems". In: *Remote Sensing of Environment* 112.9, pp. 3511–3519. DOI: [10.1016/j.rse.2008.04.008](https://doi.org/10.1016/j.rse.2008.04.008) (cit. on pp. 23, 29).
- Masson-Delmotte, V. et al. (2021). *IPCC, 2021: Climate Change 2021: The Physical Science Basis. Contribution of Working Group I to the Sixth Assessment Report of the Intergovernmental Panel on Climate Change*. Vol. Cambridge University Press. doi:10.1017/9781009157896. Cambridge, United Kingdom and New York, NY, USA (cit. on pp. 19, 20, 25).
- McKay, M. D. et al. (1979). "A Comparison of Three Methods for Selecting Values of Input Variables in the Analysis of Output from a Computer Code". In: *Technometrics* 21.2. Publisher: [Taylor & Francis, Ltd., American Statistical Association, American Society for Quality], pp. 239–245. DOI: [10.2307/1268522](https://doi.org/10.2307/1268522) (cit. on p. 53).
- Melamed, N. T. (1963). "Optical Properties of Powders. Part I. Optical Absorption Coefficients and the Absolute Value of the Diffuse Reflectance. Part II. Properties of Luminescent Powders". In: *Journal of Applied Physics* 34.3. Number: 3 Publisher: American Institute of Physics, pp. 560–570. DOI: [10.1063/1.1729309](https://doi.org/10.1063/1.1729309) (cit. on pp. 32, 33).

- Mesarch, Mark A. et al. (1999). "A Revised Measurement Methodology for Conifer Needles Spectral Optical Properties: Evaluating the Influence of Gaps between Elements". en. In: *Remote Sensing of Environment* 68.2. Number: 2, pp. 177–192. DOI: [10.1016/S0034-4257\(98\)00124-2](https://doi.org/10.1016/S0034-4257(98)00124-2) (cit. on pp. 78, 114, 159).
- Millar, Constance I. and Nathan L. Stephenson (2015). "Temperate forest health in an era of emerging megadisturbance". In: *Science* 349.6250. Number: 6250 Publisher: American Association for the Advancement of Science, pp. 823–826. DOI: [10.1126/science.aaa9933](https://doi.org/10.1126/science.aaa9933) (cit. on pp. 20, 26).
- Miraglio, Thomas et al. (2021). "Impact of Modeling Abstractions When Estimating Leaf Mass per Area and Equivalent Water Thickness over Sparse Forests Using a Hybrid Method". en. In: *Remote Sensing* 13.16, p. 3235. DOI: [10.3390/rs13163235](https://doi.org/10.3390/rs13163235) (cit. on p. 140).
- Miraglio, Thomas et al. (2022). "Assessing vegetation traits estimates accuracies from the future SBG and biodiversity hyperspectral missions over two Mediterranean Forests". In: *International Journal of Remote Sensing* 43.10, pp. 3537–3562. DOI: [10.1080/01431161.2022.2093143](https://doi.org/10.1080/01431161.2022.2093143) (cit. on pp. 138, 140).
- Moorthy, Inian et al. (2008). "Estimating chlorophyll concentration in conifer needles with hyperspectral data: An assessment at the needle and canopy level". en. In: *Remote Sensing of Environment* 112.6. Number: 6, pp. 2824–2838. DOI: [10.1016/j.rse.2008.01.013](https://doi.org/10.1016/j.rse.2008.01.013) (cit. on pp. 35, 138).
- Musinsky, John and Kate Thibault (n.d.). "AOP FLIGHT PLAN BOUNDARIES DESIGN". en. In: () (cit. on p. 72).
- Myers, Norman et al. (2000). "Biodiversity hotspots for conservation priorities". en. In: *Nature* 403.6772. Number: 6772 Publisher: Nature Publishing Group, pp. 853–858. DOI: [10.1038/35002501](https://doi.org/10.1038/35002501) (cit. on pp. 19, 25, 63).
- NASA (2011). *HyspIRI Preparatory Airborne Activities and Associated Science and Applications Research - Abstracts of selected proposals (NNH11ZDA001N - HYSPIRI)*. en. Tech. rep. NASA (cit. on pp. 67, 68).
- NEON (2023a). *Lower Teakettle NEON* (cit. on p. 66).
- (2023b). *Soaproot Saddle NEON* (cit. on p. 65).
- Ng, Wartini et al. (2019). "Convolutional neural network for simultaneous prediction of several soil properties using visible/near-infrared, mid-infrared, and their combined spectra". en. In: *Geoderma* 352, pp. 251–267. DOI: [10.1016/j.geoderma.2019.06.016](https://doi.org/10.1016/j.geoderma.2019.06.016) (cit. on pp. 56, 137).
- Noda, Hibiki M. et al. (2021). "Phenology of leaf optical properties and their relationship to mesophyll development in cool-temperate deciduous broad-leaf trees." en. In: *Agricultural and Forest Meteorology* 297, p. 108236. DOI: [10.1016/j.agrformet.2020.108236](https://doi.org/10.1016/j.agrformet.2020.108236) (cit. on pp. 77, 113).
- North, Malcolm et al. (2016). "Montane forests". en. In: *In: Mooney, Harold; Zavaleta, Erika, eds. Ecosystems of California: Berkeley, CA: University of California Press: 553-577. Chapter 27, pp. 553–577* (cit. on pp. 64, 66).
- North, P.R.J. (1996). "Three-dimensional forest light interaction model using a Monte Carlo method". In: *IEEE Transactions on Geoscience and Remote Sensing* 34.4. Number: 4 Conference Name: IEEE Transactions on Geoscience and Remote Sensing, pp. 946–956. DOI: [10.1109/36.508411](https://doi.org/10.1109/36.508411) (cit. on pp. 33, 36).
- Olson, David M. et al. (2001). "Terrestrial Ecoregions of the World: A New Map of Life on Earth: A new global map of terrestrial ecoregions provides an innovative tool for conserving biodiversity". In: *BioScience* 51.11. Number: 11, pp. 933–938. DOI: [10.1641/0006-3568\(2001\)051\[0933:TEOTWA\]2.0.CO;2](https://doi.org/10.1641/0006-3568(2001)051[0933:TEOTWA]2.0.CO;2) (cit. on pp. 19, 25, 63).
- Oreskes, Naomi (2004). "The Scientific Consensus on Climate Change". In: *Science* 306.5702. Publisher: American Association for the Advancement of Science, pp. 1686–1686. DOI: [10.1126/science.1103618](https://doi.org/10.1126/science.1103618) (cit. on pp. 20, 25).
- Patow, Gustavo and Xavier Pueyo (2003). "A Survey of Inverse Rendering Problems". en. In: *Computer Graphics Forum* 22.4. Number: 4 eprint: <https://onlinelibrary.wiley.com/doi/pdf/10.1111/j.1467-8659.2003.00716.x>, pp. 663–687. DOI: [10.1111/j.1467-8659.2003.00716.x](https://doi.org/10.1111/j.1467-8659.2003.00716.x) (cit. on p. 22).
- Pedregosa, Fabian et al. (2011). "Scikit-learn: Machine learning in Python". In: *the Journal of Machine Learning Research* 12, pp. 2825–2830 (cit. on p. 54).
- Pereira, H. M. et al. (2013). "Essential Biodiversity Variables". In: *Science* 339.6117, pp. 277–278. DOI: [10.1126/science.1229931](https://doi.org/10.1126/science.1229931) (cit. on pp. 20, 26).
- Pharr, Matt et al. (2023). *Physically Based Rendering, fourth edition: From Theory to Implementation*. en. MIT Press (cit. on p. 36).
- Pinty, B. et al. (2004). "Radiation Transfer Model Intercomparison (RAMI) exercise: Results from the second phase". en. In: *Journal of Geophysical Research: Atmospheres* 109.D6. DOI: <https://doi.org/10.1029/2003JD004252> (cit. on p. 36).

- Pinty, Bernard et al. (2001). "Radiation transfer model intercomparison (RAMI) exercise". en. In: *Journal of Geophysical Research: Atmospheres* 106.D11, pp. 11937–11956. DOI: <https://doi.org/10.1029/2000JD900493> (cit. on pp. 35, 36).
- Powell, M. J. D. (1964). "An efficient method for finding the minimum of a function of several variables without calculating derivatives". In: *The Computer Journal* 7.2. Number: 2, pp. 155–162. DOI: [10.1093/comjnl/7.2.155](https://doi.org/10.1093/comjnl/7.2.155) (cit. on p. 53).
- Pullanagari, R. R. et al. (2021). "Field spectroscopy of canopy nitrogen concentration in temperate grasslands using a convolutional neural network". en. In: *Remote Sensing of Environment* 257, p. 112353. DOI: [10.1016/j.rse.2021.112353](https://doi.org/10.1016/j.rse.2021.112353) (cit. on pp. 56, 127, 137).
- Pörtner, H.-O. et al. (2022). *IPCC, 2022: Climate Change 2022: Impacts, Adaptation, and Vulnerability. Contribution of Working Group II to the Sixth Assessment Report of the Intergovernmental Panel on Climate Change. Technical Summary*. Cambridge, UK and New York, NY, USA: Cambridge University Press (cit. on pp. 19, 25).
- Rasmussen, Carl Edward and Christopher K. I. Williams (2005). *Gaussian Processes for Machine Learning*. en. Ed. by Francis Bach. Adaptive Computation and Machine Learning series. Series Editors: _:n7103 Series Editors: _:n7213. Cambridge, MA, USA: MIT Press (cit. on p. 55).
- Rast, M. et al. (2021). "Copernicus Hyperspectral Imaging Mission for the Environment (Chime)". In: *2021 IEEE International Geoscience and Remote Sensing Symposium IGARSS*. ISSN: 2153-7003, pp. 108–111. DOI: [10.1109/IGARSS47720.2021.9553319](https://doi.org/10.1109/IGARSS47720.2021.9553319) (cit. on pp. 22, 27, 144, 145, 148–150).
- Rast, Michael and Thomas H. Painter (2019). "Earth Observation Imaging Spectroscopy for Terrestrial Systems: An Overview of Its History, Techniques, and Applications of Its Missions". en. In: *Surveys in Geophysics* 40.3. Number: 3, pp. 303–331. DOI: [10.1007/s10712-019-09517-z](https://doi.org/10.1007/s10712-019-09517-z) (cit. on pp. 21, 27).
- Riano, D. et al. (2005). "Estimation of fuel moisture content by inversion of radiative transfer models to simulate equivalent water thickness and dry matter content: analysis at leaf and canopy level". In: *IEEE Transactions on Geoscience and Remote Sensing* 43.4. Number: 4 Conference Name: IEEE Transactions on Geoscience and Remote Sensing, pp. 819–826. DOI: [10.1109/TGRS.2005.843316](https://doi.org/10.1109/TGRS.2005.843316) (cit. on pp. 21, 27).
- Richter, Katja et al. (2012). "Derivation of biophysical variables from Earth observation data: validation and statistical measures". In: *Journal of Applied Remote Sensing* 6.1. Number: 1 Publisher: International Society for Optics and Photonics, p. 063557. DOI: [10.1117/1.JRS.6.063557](https://doi.org/10.1117/1.JRS.6.063557) (cit. on pp. 57, 58).
- Saltelli, Andrea et al. (2004). *Sensitivity analysis in practice: a guide to assessing scientific models*. Vol. 1. Wiley Online Library (cit. on pp. 42, 43).
- Saltelli, Andrea et al. (2010). "Variance based sensitivity analysis of model output. Design and estimator for the total sensitivity index". en. In: *Computer Physics Communications* 181.2. Number: 2, pp. 259–270. DOI: [10.1016/j.cpc.2009.09.018](https://doi.org/10.1016/j.cpc.2009.09.018) (cit. on p. 43).
- Savitzky, Abraham. and M. J. E. Golay (1964). "Smoothing and Differentiation of Data by Simplified Least Squares Procedures." In: *Analytical Chemistry* 36.8. Publisher: American Chemical Society, pp. 1627–1639. DOI: [10.1021/ac60214a047](https://doi.org/10.1021/ac60214a047) (cit. on p. 70).
- Sawyer, John O and Todd Keeler-Wolf (1995). "A manual of California vegetation". In: (cit. on p. 64).
- Schaepman, Michael E (2009). "Imaging spectrometers". In: *The SAGE handbook of remote sensing*. Publisher: Sage, pp. 166–178 (cit. on pp. 21, 27).
- Schlerf, Martin et al. (2010). "Retrieval of chlorophyll and nitrogen in Norway spruce (*Picea abies* L. Karst.) using imaging spectroscopy". en. In: *International Journal of Applied Earth Observation and Geoinformation* 12.1. Number: 1, pp. 17–26. DOI: [10.1016/j.jag.2009.08.006](https://doi.org/10.1016/j.jag.2009.08.006) (cit. on pp. 138, 141).
- Schwalbe, Gesina and Bettina Finzel (2023). "A comprehensive taxonomy for explainable artificial intelligence: a systematic survey of surveys on methods and concepts". en. In: *Data Mining and Knowledge Discovery*. DOI: [10.1007/s10618-022-00867-8](https://doi.org/10.1007/s10618-022-00867-8) (cit. on pp. 145, 149).
- Seymour, Frances et al. (2022). "Not Just Carbon: Capturing All the Benefits of Forests for Stabilizing the Climate from Local to Global Scales". en. In: (cit. on pp. 19, 25).
- Shen, Zefang and R. A. Viscarra Rossel (2021). "Automated spectroscopic modelling with optimised convolutional neural networks". en. In: *Scientific Reports* 11.1. Number: 1 Publisher: Nature Publishing Group, p. 208. DOI: [10.1038/s41598-020-80486-9](https://doi.org/10.1038/s41598-020-80486-9) (cit. on p. 56).
- Shi, Shuo et al. (2022). "A convolution neural network for forest leaf chlorophyll and carotenoid estimation using hyperspectral reflectance". en. In: *International Journal of Applied Earth Observation and Geoinformation* 108, p. 102719. DOI: [10.1016/j.jag.2022.102719](https://doi.org/10.1016/j.jag.2022.102719) (cit. on pp. 56, 127, 137).

- Shultis, J. Kenneth and R. B. Myneni (1988). "Radiative transfer in vegetation canopies with anisotropic scattering". In: *Journal of Quantitative Spectroscopy and Radiative Transfer* 39.2, pp. 115–129. DOI: [10.1016/0022-4073\(88\)90079-9](https://doi.org/10.1016/0022-4073(88)90079-9) (cit. on p. 35).
- Sims, Daniel A and John A Gamon (2002). "Relationships between leaf pigment content and spectral reflectance across a wide range of species, leaf structures and developmental stages". en. In: *Remote Sensing of Environment* 81.2. Number: 2, pp. 337–354. DOI: [10.1016/S0034-4257\(02\)00010-X](https://doi.org/10.1016/S0034-4257(02)00010-X) (cit. on p. 43).
- Singh, Aditya et al. (2015). "Imaging spectroscopy algorithms for mapping canopy foliar chemical and morphological traits and their uncertainties". en. In: *Ecological Applications* 25.8. _eprint: <https://onlinelibrary.wiley.com/doi/pdf/10.1890/14-2098.1>, pp. 2180–2197. DOI: [10.1890/14-2098.1](https://doi.org/10.1890/14-2098.1) (cit. on pp. 23, 29).
- Skidmore, Andrew K. et al. (2021). "Priority list of biodiversity metrics to observe from space". en. In: *Nature Ecology & Evolution* 5.7. Number: 7 Publisher: Nature Publishing Group, pp. 896–906. DOI: [10.1038/s41559-021-01451-x](https://doi.org/10.1038/s41559-021-01451-x) (cit. on pp. 20, 26).
- Spafford, Lynsay et al. (2021). "Spectral subdomains and prior estimation of leaf structure improves PROSPECT inversion on reflectance or transmittance alone". en. In: *Remote Sensing of Environment* 252, p. 112176. DOI: [10.1016/j.rse.2020.112176](https://doi.org/10.1016/j.rse.2020.112176) (cit. on pp. 34, 52, 113).
- Stein, Michael (1987). "Large Sample Properties of Simulations Using Latin Hypercube Sampling". In: *Technometrics* 29.2, pp. 143–151. DOI: [10.1080/00401706.1987.10488205](https://doi.org/10.1080/00401706.1987.10488205) (cit. on p. 53).
- Stokes, George Gabriel (1862). "On the intensity of the light reflected from or transmitted through a pile of plates". In: *Proceedings of the Royal Society of London* 11. Publisher: Royal Society, pp. 545–556. DOI: [10.1098/rsp1.1860.0119](https://doi.org/10.1098/rsp1.1860.0119) (cit. on p. 33).
- Taiz, Lincoln and E Zeiger (2010). *Plant physiology 5th Ed* (cit. on pp. 20, 26, 27).
- Tarantola, Albert (2005). *Inverse problem theory and methods for model parameter estimation*. SIAM (cit. on p. 22).
- Thompson, Richard L. and Narendra S. Goel (1998). "Two models for rapidly calculating bidirectional reflectance of complex vegetation scenes: Photon spread (PS) model and statistical photon spread (SPS) model". In: *Remote Sensing Reviews* 16.3. Publisher: Taylor & Francis _eprint: <https://doi.org/10.1080/02757259809532351>, pp. 157–207. DOI: [10.1080/02757259809532351](https://doi.org/10.1080/02757259809532351) (cit. on p. 36).
- Tucker, Compton J. and Michael W. Garratt (1977). "Leaf optical system modeled as a stochastic process". EN. In: *Applied Optics* 16.3. Publisher: Optica Publishing Group, pp. 635–642. DOI: [10.1364/AO.16.000635](https://doi.org/10.1364/AO.16.000635) (cit. on p. 33).
- USDA PLANTS Database (2021) (cit. on p. 66).
- Ustin, Susan L (2004). "Remote sensing of environment: State of the science and new directions". In: *Remote sensing of natural resources management and environmental monitoring*. Publisher: John Wiley & Sons (cit. on p. 33).
- Ustin, Susan L. and Elizabeth M. Middleton (2021). "Current and near-term advances in Earth observation for ecological applications". In: *Ecological Processes* 10.1. Number: 1, p. 1. DOI: [10.1186/s13717-020-00255-4](https://doi.org/10.1186/s13717-020-00255-4) (cit. on pp. 22, 27).
- Verhoef, W. (1984). "Light scattering by leaf layers with application to canopy reflectance modeling: The SAIL model". en. In: *Remote Sensing of Environment* 16.2. Number: 2, pp. 125–141. DOI: [10.1016/0034-4257\(84\)90057-9](https://doi.org/10.1016/0034-4257(84)90057-9) (cit. on pp. 32, 35, 36).
- Verhoef, Wout et al. (2007). "Unified Optical-Thermal Four-Stream Radiative Transfer Theory for Homogeneous Vegetation Canopies". In: *IEEE Transactions on Geoscience and Remote Sensing* 45.6. Number: 6 Conference Name: IEEE Transactions on Geoscience and Remote Sensing, pp. 1808–1822. DOI: [10.1109/TGRS.2007.895844](https://doi.org/10.1109/TGRS.2007.895844) (cit. on pp. 35, 36).
- Verrelst, Jochem et al. (2019). "Quantifying Vegetation Biophysical Variables from Imaging Spectroscopy Data: A Review on Retrieval Methods". en. In: *Surveys in Geophysics* 40.3. Number: 3, pp. 589–629. DOI: [10.1007/s10712-018-9478-y](https://doi.org/10.1007/s10712-018-9478-y) (cit. on pp. 22, 23, 28, 29, 51).
- Violle, Cyrille et al. (2007). "Let the concept of trait be functional!" en. In: *Oikos* 116.5. Number: 5 _eprint: <https://onlinelibrary.wiley.com/doi/pdf/10.1111/j.0030-1299.2007.15559.x>, pp. 882–892. DOI: <https://doi.org/10.1111/j.0030-1299.2007.15559.x> (cit. on pp. 20, 26).
- Wang, Yingjie et al. (2022). "DART-Lux: An unbiased and rapid Monte Carlo radiative transfer method for simulating remote sensing images". en. In: *Remote Sensing of Environment* 274, p. 112973. DOI: [10.1016/j.rse.2022.112973](https://doi.org/10.1016/j.rse.2022.112973) (cit. on pp. 33, 36, 40).
- Wang, Zhihui et al. (2020). "Foliar functional traits from imaging spectroscopy across biomes in eastern North America". en. In: *New Phytologist* 228.2, pp. 494–511. DOI: <https://doi.org/10.1111/nph.16711> (cit. on pp. 22, 23, 28, 29, 138, 139, 141).
- Wang, Zhihui et al. (2023). "Generality of leaf spectroscopic models for predicting key foliar functional traits across continents: A comparison between physically- and empirically-based ap-

- proaches". en. In: *Remote Sensing of Environment* 293, p. 113614. DOI: [10.1016/j.rse.2023.113614](https://doi.org/10.1016/j.rse.2023.113614) (cit. on pp. 52, 77).
- Weiss, Karl et al. (2016). "A survey of transfer learning". en. In: *Journal of Big Data* 3.1, p. 9. DOI: [10.1186/s40537-016-0043-6](https://doi.org/10.1186/s40537-016-0043-6) (cit. on pp. 145, 149).
- Whittaker, RH (1975). "Communities and ecosystems." In: (cit. on pp. 19, 25).
- Widlowski, J.-L. et al. (2007). "Third Radiation Transfer Model Intercomparison (RAMI) exercise: Documenting progress in canopy reflectance models". en. In: *Journal of Geophysical Research: Atmospheres* 112.D9. DOI: <https://doi.org/10.1029/2006JD007821> (cit. on p. 36).
- Widlowski, J.-L. et al. (2013). "The fourth radiation transfer model intercomparison (RAMI-IV): Proficiency testing of canopy reflectance models with ISO-13528". en. In: *Journal of Geophysical Research: Atmospheres* 118.13, pp. 6869–6890. DOI: <https://doi.org/10.1002/jgrd.50497> (cit. on p. 36).
- Widlowski, Jean-Luc et al. (2006). "Rayspread: A Virtual Laboratory for Rapid BRF Simulations Over 3-D Plant Canopies". en. In: *Computational Methods in Transport*. Ed. by Frank Graziani. Berlin, Heidelberg: Springer, pp. 211–231. DOI: [10.1007/3-540-28125-8_10](https://doi.org/10.1007/3-540-28125-8_10) (cit. on p. 36).
- Widlowski, Jean-Luc et al. (2015). "The fourth phase of the radiative transfer model intercomparison (RAMI) exercise: Actual canopy scenarios and conformity testing". en. In: *Remote Sensing of Environment* 169, pp. 418–437. DOI: [10.1016/j.rse.2015.08.016](https://doi.org/10.1016/j.rse.2015.08.016) (cit. on pp. 36, 140).
- Wocher, Matthias et al. (2020). "RTM-based dynamic absorption integrals for the retrieval of biochemical vegetation traits". en. In: *International Journal of Applied Earth Observation and Geoinformation* 93, p. 102219. DOI: [10.1016/j.jag.2020.102219](https://doi.org/10.1016/j.jag.2020.102219) (cit. on pp. 140, 141).
- Wold, Svante et al. (2001). "PLS-regression: a basic tool of chemometrics". en. In: *Chemometrics and Intelligent Laboratory Systems*. PLS Methods 58.2. Number: 2, pp. 109–130. DOI: [10.1016/S0169-7439\(01\)00155-1](https://doi.org/10.1016/S0169-7439(01)00155-1) (cit. on p. 54).
- WWF (2023a). *Sierra Nevada forests | Ecoregions | WWF*. en-US (cit. on p. 64).
- (2023b). *Terrestrial Ecoregions of the World | Publications | WWF*. en-US (cit. on p. 63).
- Xiao, Yanfang et al. (2014). "Sensitivity Analysis of Vegetation Reflectance to Biochemical and Biophysical Variables at Leaf, Canopy, and Regional Scales". In: *IEEE Transactions on Geoscience and Remote Sensing* 52.7. Number: 7 Conference Name: IEEE Transactions on Geoscience and Remote Sensing, pp. 4014–4024. DOI: [10.1109/TGRS.2013.2278838](https://doi.org/10.1109/TGRS.2013.2278838) (cit. on p. 140).
- Yang, Bin et al. (2020). "Data-Driven Methods for the Estimation of Leaf Water and Dry Matter Content: Performances, Potential and Limitations". en. In: *Sensors* 20.18. Number: 18 Publisher: Multidisciplinary Digital Publishing Institute, p. 5394. DOI: [10.3390/s20185394](https://doi.org/10.3390/s20185394) (cit. on p. 113).
- Yáñez-Rausell, Lucia et al. (2014). "Minimizing Measurement Uncertainties of Coniferous Needle-Leaf Optical Properties, Part I: Methodological Review". In: *IEEE Journal of Selected Topics in Applied Earth Observations and Remote Sensing* 7.2. Number: 2 Conference Name: IEEE Journal of Selected Topics in Applied Earth Observations and Remote Sensing, pp. 399–405. DOI: [10.1109/JSTARS.2013.2272890](https://doi.org/10.1109/JSTARS.2013.2272890) (cit. on p. 78).
- Zarco-Tejada, P. J. et al. (2019). "Chlorophyll content estimation in an open-canopy conifer forest with Sentinel-2A and hyperspectral imagery in the context of forest decline". en. In: *Remote Sensing of Environment* 223, pp. 320–335. DOI: [10.1016/j.rse.2019.01.031](https://doi.org/10.1016/j.rse.2019.01.031) (cit. on p. 138).
- Zarco-Tejada, Pablo J. et al. (2004). "Needle chlorophyll content estimation through model inversion using hyperspectral data from boreal conifer forest canopies". en. In: *Remote Sensing of Environment*. BOREAS Remote Sensing Science 89.2. Number: 2, pp. 189–199. DOI: [10.1016/j.rse.2002.06.002](https://doi.org/10.1016/j.rse.2002.06.002) (cit. on pp. 35, 114).
- Zhu, Xi et al. (2019). "Estimation of forest leaf water content through inversion of a radiative transfer model from LiDAR and hyperspectral data". en. In: *International Journal of Applied Earth Observation and Geoinformation* 74, pp. 120–129. DOI: [10.1016/j.jag.2018.09.008](https://doi.org/10.1016/j.jag.2018.09.008) (cit. on p. 138).

Publications and Communications

Peer-Reviewed Publications

T. Gaubert, K. Adeline, M. Huesca, S. Ustin, and X. Briottet, "Estimation of Oak Leaf Functional Traits for California Woodland Savannas and Mixed Forests: Comparison between Statistical, Physical, and Hybrid Methods Using Spectroscopy," *Remote Sensing*, vol. 16, no. 1, Art. no. 1, Jan. 2024, doi: [10.3390/rs16010029](https://doi.org/10.3390/rs16010029).

Communications

T. Gaubert, K. Adeline, M. Huesca, S. Ustin, and X. Briottet, "Assessing the robustness of inversion methods to estimate leaf traits from leaf spectra of mixed broadleaf/conifer ecosystems," 40th EARSeL Symposium, Jun. 2021.

T. Gaubert, K. Adeline, M. Huesca, S. Ustin, and X. Briottet, "Inversion of Radiative Transfer Model Through One-Dimensional Convolutional Neural Network To Retrieve Foliar Traits of Temperate Forest Canopies With Imaging Spectroscopy," in *IGARSS 2023 - 2023 IEEE International Geoscience and Remote Sensing Symposium*, Jul. 2023, pp. 4903–4906. doi: [10.1109/IGARSS52108.2023.10282458](https://doi.org/10.1109/IGARSS52108.2023.10282458).